Ocean ventilation at the mesoscale

Yanxu Chen

To cite this version:

Yanxu Chen. Ocean ventilation at the mesoscale. Oceanography. Université Paris sciences et lettres, 2022. English. NNT : 2022UPSLE048 . tel-04613096

HAL Id: tel-04613096
https://theses.hal.science/tel-04613096
Submitted on 15 Jun 2024

PSL UNIVERSITÉ PARIS

THÈSE DE DOCTORAT
DE L'UNIVERSITÉ PSL

Préparée à l'École Normale Supérieure

Ocean ventilation at the mesoscale

Soutenue par

Yanxu Chen

Le 18 juillet 2022

École doctorale n°129

Sciences de l'Environnement

Spécialité

Physique de l'Océan

Préparée au

Laboratoire de Météorologie Dynamique

Composition du jury :

Xavier CARTON Laboratoire d'Oceanographie Physique et Spatiale, Université de Bretagne Occidentale	*Président du jury* *Rapporteur*
Lynne TALLEY Scrippts Institution of Oceanography, University of California San Diego	*Rapporteuse*
Laurent BOPP Département de Géosciences, École Normale Supérieure	*Examinateur*
Rosemary MORROW Laboratoire d'Etudes en Géophysique et Océanographie Spatiales, Université Toulouse III	*Examinatrice*
George NURSER National Oceanography Centre	*Examinateur*
Nicolas KOLODZIEJCZYK Laboratoire d'Oceanographie Physique et Spatiale, Université de Bretagne Occidentale	*Examinateur*
Sabrina SPEICH Laboratoire de Météorologie Dynamique, École Normale Supérieure	*Directrice de thèse*

ENS | PSL IPSL LMD

Acknowledgements

I sincerely thank my advisor Prof. Sabrina Speich for supporting this study and many other perspectives of my PhD life in Paris. It is an invaluable journal to study and work with her since she takes over many concerns to let me purely focus on my research. I also appreciate the opportunity to work under a grant from Prof. Laurent Bopp in our Department of Geosciences (the grant of Chaire Chanel devoted to climate studies). Academically and personally, I would like to thank Prof. David Straub for ongoing exchanges of thoughts that contribute in several ways to this thesis and my research in general. In the history of this PhD study, several scientists also provide their comments that I feel grateful for. They are Drs. Johannes Karstensen (on mode water formation), Rémi Laxenaire (on mesoscale eddies), Artemis Ioannou (on subsurface eddy detection), Gilles Reverdin (on ocean ventilation processes), Lynne Talley (on global mode water characteristics) and Bruno Blanke (on subduction rate calculation). Lastly, I would like to thank my parents for their complete support to let me pursue my studies in ocean physics and other personal objectives, my friends for their company either in Paris or electronically, and Mr. Friedrich Nietzsche for his inspiring philosophical thinking that penetrates into every aspect of my life.

Abstract

Within the Earth's climate system, the ocean is engaged as a huge reservoir of important properties such as heat and carbon, predominantly resulting from exchanges with the atmosphere on timescales from hours to millennia. Such large volume of storage in the ocean interior thus questions the mechanisms of water property transport and distribution, leading to the concept of ocean ventilation, a process that connects ocean surface waters with the interior. Commonly associated with an increase in density of surface waters, ventilation is typically interpreted as a downward transfer of water masses due to stability and other fine-scale processes. Understanding the dynamics and thermodynamics of water mass formation, ventilation and dissipation, is therefore one of the key scientific challenges confronting the entire climate community.

In this thesis, several processes related to ventilation have been discussed and a specific attention has been given to the mesoscale whose typical length is less than 100 km and timescale spans on the order of a month. The largest proportion of mesoscale kinetic energy is contained by coherent vortices, known as mesoscale eddies, which are nearly geostrophic and can have the vertical extent down to the thermocline. Aimed at a combination between the ventilation theory and mesoscale dynamics, the first part of this thesis has been devoted to a revisit to the theory of subduction at the bottom of mixed layer that quantifies long-term (permanent) transport of surface water masses into the main thermocline. Interpreted as a transient state in the subduction process, mode waters are a specific type of water mass homogeneous in properties (i.e., characterized by low potential vorticity) and residing between the seasonal and main thermoclines. Such transiency of mode waters is associated with their formation mechanism largely due to surface buoyancy forcing that is season-dependent. The second part of this thesis is thus related to an algorithm development to detect more precisely than other available methods the surface mixed layers and mode waters from several profiling databases. By co-locating mode waters with mesoscale eddies identified from the satellite altimetry, it is possible to quantify 1) the percentage of mode waters carried by eddies in an Eulerian sense, and 2) anomalies of temperature, salinity and others transported within eddies in a Lagrangian framework. Accordingly, a revisit to global mode water distribution has been provided, in terms of their dynamics and thermodynamics at the mesoscale. The South Atlantic

Subtropical Mode Water has been considered as a special example and brought into details in the last chapter, since it is not only formed according to the typical baroclinity at the western boundary, but also develops due to a large amount of inter-basin transport carried by anticyclonic Agulhas Rings shedding from the Indian Ocean.

Apart from the thermohaline perspective of ocean circulation and ventilation, i.e., surface convection and its significance on mode water formation and renewal, this thesis also provides an assessment on the wind-driven aspect and a combination of these two components. In specific, we extended the Ekman dynamics to allow for an influence from geostrophic motions and self-advection. A brief discussion on diapycnal and more complex physics of ventilation at the mesoscale is also presented.

Keywords : ocean ventilation theory, mesoscale dynamics, mode water, heat uptake

Résumé

Dans le système climatique de la Terre, l'océan constitue un énorme réservoir de chaleur et carbone, résultant principalement des échanges avec l'atmosphère sur des échelles de temps allant des heures aux millénaires. Les mécanismes d'absorption de la chaleur et du carbone, leur transport et distribution dans l'océan intérieur sont conceptualisés en tant que ventilation de l'océan, un processus qui relie la formation des masses d'eau à la surface de l'océan et leur propagation et transformation en profondeur. Typiquement associée à une augmentation de la densité des eaux de surface, la ventilation est généralement interprétée comme un transfert verticale des masses d'eau dû à la stabilité de la colonne d'eau, à leur transport horizontal et à d'autres processus à petite échelle. Comprendre la dynamique et la thermodynamique sous-jacentes à la formation, transport et transformation des masses d'eau est donc l'un des principaux défis scientifiques en sciences du climat.

Dans cette thèse, l'accent a été mis sur plusieurs processus liés à la ventilation avec un focus particulier sur la dynamique à méso-échelle de l'océan caractérisée par des échelles horizontales de l'ordre de 100 km et des échelles de temps de l'ordre des mois. La plus grande partie de l'énergie cinétique à méso-échelle est contenue dans des tourbillons cohérents, connus sous le nom de tourbillons de méso-échelle, dont les écoulements sont proches de l'équilibre géostrophique et peuvent avoir une étendue verticale allant de la surface jusqu'à la thermocline. Visant une combinaison entre la théorie de la ventilation et la dynamique à méso-échelle, la première partie de cette thèse a été consacrée à une revisite de la théorie de la subduction au fond de la couche de mélange qui quantifie le transport à long terme des masses d'eau de surface dans le thermocline principale. Interprétées comme un état transitoire dans le processus de ventilation, les eaux modales sont des masses d'eau aux propriétés homogènes (c'est-à-dire caractérisées par une faible vorticité potentielle) et résidant entre les thermoclines saisonnières et principales. Cette éphémérité des eaux modales est associée à leur mécanisme de formation dû au forçage saisonnier de flottabilité de surface. La deuxième partie de cette thèse porte donc sur le développement d'un algorithme permettant de détecter les couches de mélange de surface et les eaux modales avec plus de précision que les autres méthodes disponibles. En associant les eaux modales aux tourbillons de méso-échelle identifiés par altimétrie satellitaire, c'était possible de quantifier 1) le pourcentage d'eaux modales transportées par les tourbillons au sens eulérien, et 2) les anomalies de température, de salinité et d'autres transportées dans les tourbillons dans un cadre lagrangien. Par conséquent, une révision de la distribution globale des eaux modales a été proposée, en termes de leur dynamique et thermodynamique à la méso-échelle. Les eaux modales subtropicales de l'Atlantique Sud ont été considérées comme un exemple particulier et détaillées dans le dernier chapitre, parce qu'elles ne se forment pas seulement selon la baroclinité typique à la limite ouest, mais elles se développent également en raison d'une grande quantité de transport interbassin transporté par des tourbillons anticycloniques se déversant de l'océan Indien.

Outre la perspective thermohaline de la circulation et de la ventilation océanique, c'est-à-dire la convection de surface et son importance sur la formation et le renouvellement des eaux modales, cette thèse fournit également une évaluation du forçage par vent de la circulation océanique et une combinaison de ces deux composantes. C'est-à-dire la théorie d'Ekman et son couplage avec la dynamique géostrophique de l'océan. Une brève discussion sur les processus de mélange diapycnal et d'autres processus plus complexe de la ventilation à la méso-échelle a également été fournie.

Mots clés : théorie de la ventilation océanique, dynamique à méso-échelle, eaux modales, absorption de chaleur

Contents

List of figures

List of tables

Acronyms

AABW *Antarctic Bottom Water*

AAIW *Antarctic Intermediate Water*

ACC *Antarctic Circumpolar Current*

ADT *Absolute Dynamic Topography*

AMOC *Atlantic Meridional Overturning Circulation*

CLT *Core Layer Temperature*

CTD *Conductivity-Temperature-Depth*

EDW *Eighteen Degree Water*

EKE *Eddy Kinetic Energy*

HCA *Heat Content Anomaly*

IDW *Indian Deep Water*

LCDW *Lower Circumpolar Deep Water*

MDT *Mean Dynamic Topography*

MLD *Mixed Layer Depth*

MOC *Meridional Overturning Circulation*

NADW *North Atlantic Deep Water*

NAEMW *North Atlantic Eastern Mode Water*

NAMOW *North Atlantic Mediterranean Outflow Water*

NASPMW *North Atlantic Subpolar Mode Water*

NASTMW *North Atlantic Subtropical Mode Water*

NPCMW *North Pacific Central Mode Water*

NPIW *North Pacific Intermediate Water*

NPSTMW *North Pacific Subtropical Mode Water*

PDW *Pacific Deep Water*

PV *Potential Vorticity*

SAF *Subantarctic Front*

SAMW *Subantarctic Mode Water*

SASTMW *South Atlantic Subtropical Mode Water*

SHA *Steric Height Anomaly*

SHSTMW *Southern Hemisphere Subtropical Mode Water*

SLA *Sea Level Anomaly*

SPMW *Subpolar Mode Water*

SPSTMW *South Pacific Subtropical Mode Water*

SSS *Sea Surface Salinity*

SST *Sea Surface Temperature*

STF *Subtropical Front*

STMW *Subtropical Mode Water*

THC *Thermohaline Circulation*

WMT *Water Mass Transformation*

XBT *Bathythermograph*

Chapter 1

General introduction

Objectives

Ocean motions can extend over a great variety of scales in both time and space. At one end, we find turbulence at the Kolmogorov microscales, and at the other, the large-scale circulation, which encompasses several ocean basins and evolves over climatic timescales (see Figure 1.1 of spatial and temporal scales of major oceanic processes). Due to mass conservation, circulation at the horizontal plane provides implications for vertical movements of water masses that further outline the overturning cells in the ocean interior. Ventilation, defined as a communication between the sea surface and interior, is thus inseparable from the ocean general circulation and its continuous extensions of theories. In this chapter, a brief introduction is presented concerning several physical processes of the ocean ventilation theory from the large scale down to submesoscale, which follows the history of this PhD research progression.

Contents

1 Large scale: ocean ventilation theory

The primary question concerning the large-scale ocean physics is: what drives ocean circulation? There are multiple mechanisms to think of, counting 1) the gravitational force exerted by the moon (and sun), 2) spatial differences in atmospheric pressures at the sea level, 3) wind forcing acting over the ocean surface layer, and 4) convection resulting mainly from cooling and evaporation processes at the air-sea boundary layers. Both 1) and 2) generate negligible permanent circulation, whereas the last two mechanisms take separate responsibilities in setting water masses in motion at the large scale. Ocean ventilation, if viewed as a vertical process of communicating surface water properties to the ocean interior, is thus inseparable from ocean general circulation due to continuity. Combined together, this is the most fundamental question of ocean physics that has been extended over 100 years from a quasi-steady viewpoint to the state-of-the-art turbulent representation [Wunsch, 2018]. Figure 1.1 provides a comprehensive view of physical processes at several spatial and time scales that are regarded in the entire climate system. The mesoscale features of the ocean that constitute the most content of this thesis study are at spatial scales of 10 to 100 km and time scales of weeks to months.

From a vertical perspective, the water column can be generally divided into four segments in the classic theory (Figure 1.2). At the top lies the mixed layer that is stirred by the surface wind stress and buoyancy exchanges with the atmosphere. With a depth on the order of several tens of meters, this layer was assimilated by the purely wind-driven Ekman layer for large-scale circulation back to the history of early circulation theory, and is characterized by $\partial\rho/\partial z = 0$ (with ρ the seawater density). Below lies the seasonal thermocline, a layer where the vertical stratification is reduced every winter by surface convective mixing that can penetrate into a depth on the order of 100 m. Below the maximum depth that winter convection is able to enter is the main/permanent thermocline, which is fed by water left behind whenever the seasonal thermocline retreats, and is thus permanently stratified (i.e., $\partial\rho/\partial z \neq 0$). The rest of the water column, which comprises most of the ocean water, is the abyssal layer that moves very slowly. When combined together, the main thermocline and abyssal layer are referred to as the ocean interior that, in the first approximation, are independent of small-scale and high-frequency processes (regardless of bottom frictions and interactions with bathymetry). In general, this thesis focuses on the physical processes of the upper ocean, especially vertical and horizontal movements of water masses that are relocated constantly between the surface mixed layer and permanent thermocline, which are commonly defined as ocean ventilation processes.

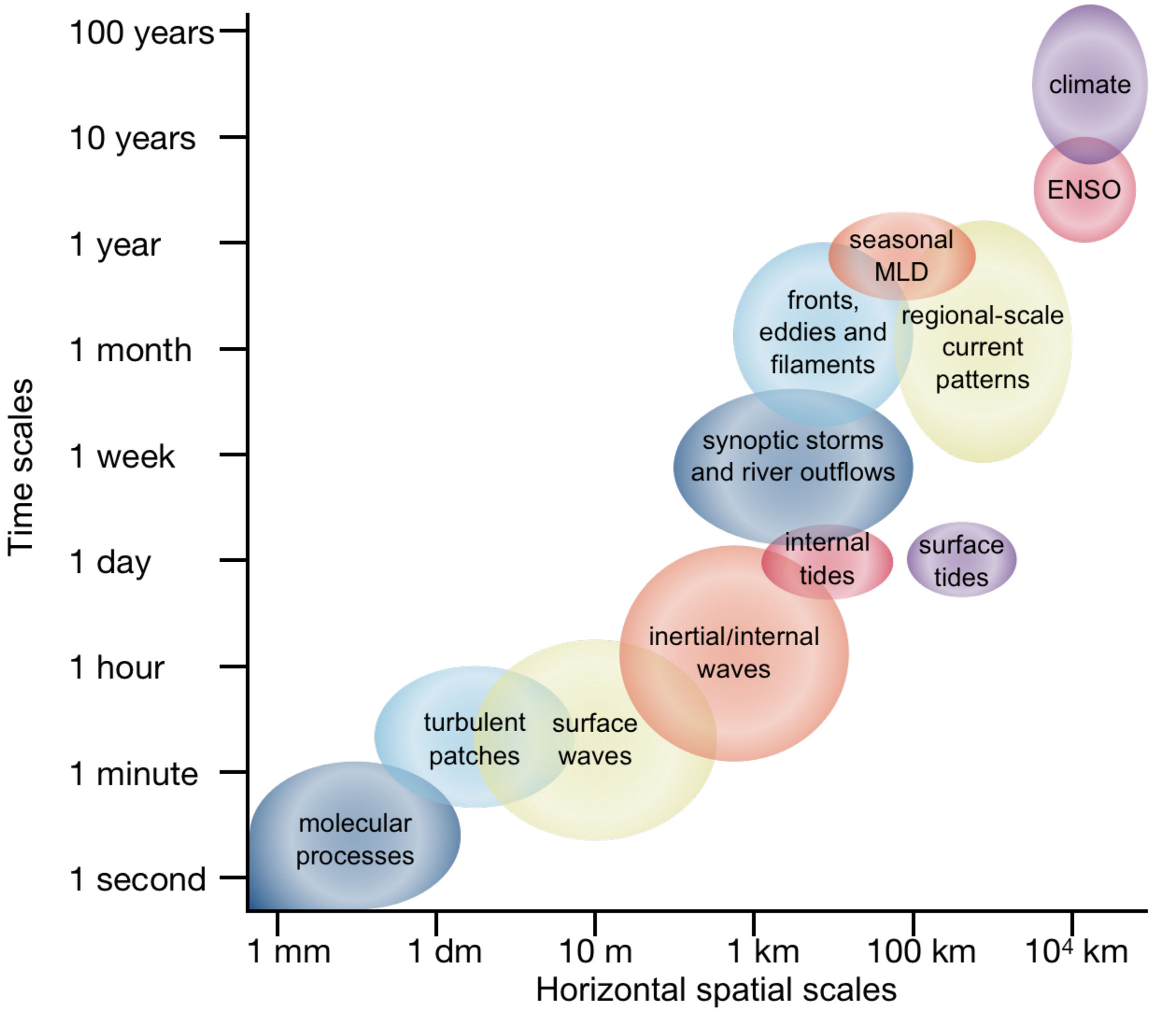

Figure 1.1: Spatial and temporal scales that characterize several important physical processes in the ocean (and atmosphere).

Intuitively, winds can only drive currents approximately in the upper 100 m of the ocean surface. As we move from the surface down to the deepest layers, sea water density increases. Constant density surfaces are known as isopycnals, along which the flow tends to move. In this regard, if we switch from depth to density as the vertical coordinate and accordingly treat depth as a dependent variable instead, it is possible to map the horizontal variation of depths for any given isopycnal which indicates the flow field in the ocean interior. Since water's density is controlled by temperature and salinity that are both highly related to surface convection, this process is widely known as the thermohaline circulation.

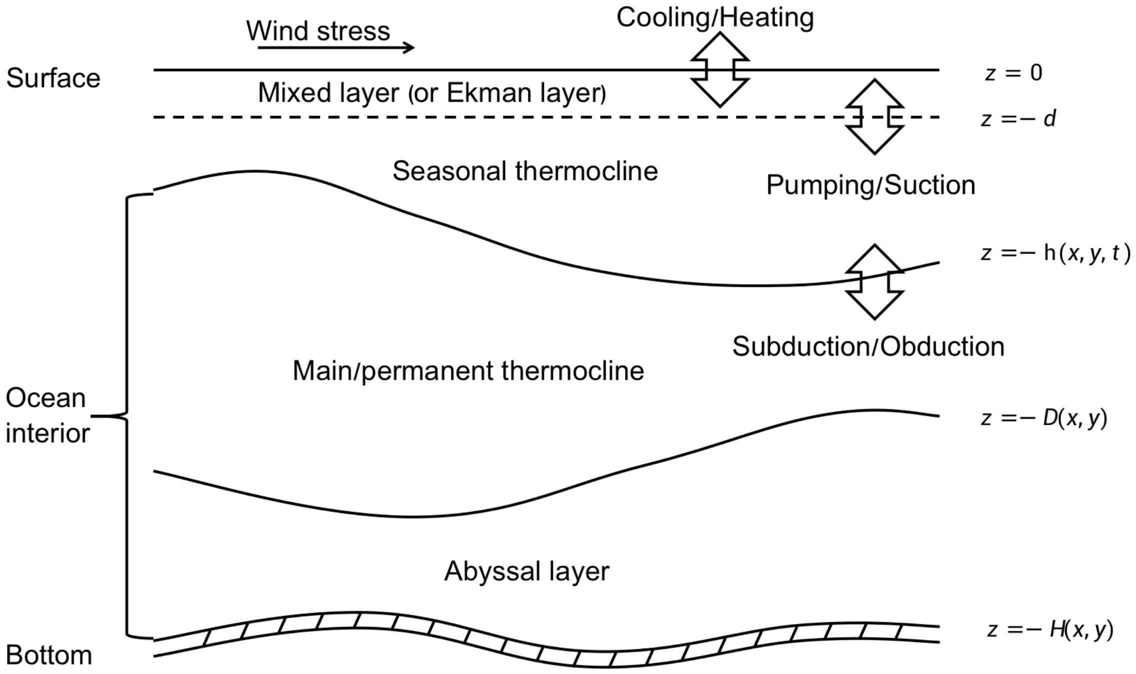

Figure 1.2: Vertical structure of the ocean from the viewpoint of large-scale circulation. There are four layers in general from the top to bottom, i.e., surface mixed layer (considered to be in wind-driven Ekman balance for a while), seasonal thermocline, permanent thermocline and abyssal layer.

This chapter is then focused on the different roles that wind-driven and thermohaline circulations play in the global ocean ventilation. Though such separation is artificial, it can still help to simplify the problems and obtain a clear picture of the physical processes involved in each of these components. This chapter thus begins with the classic seminal work associated with the wind-driven Ekman theory and its connection to the interior flow balance [Ekman, 1905; Sverdrup, 1947; Stommel, 1948; Munk, 1950b].

1.1 Wind-driven circulation and the Ekman theory

1.1.1 Surface wind forcing

Since the Ekman dynamics at the sea surface is driven by mechanical forcing (i.e., wind), it is important to draw a picture of wind at the first step. The common way of quantifying the effect of wind on the upper-ocean dynamics is to treat wind stress as an imposed frictional force for the surface layer, i.e., by applying the bulk formula $\boldsymbol{\tau} = \rho_a C_d |\boldsymbol{u_a}| \boldsymbol{u_a}$ (where ρ_a is the air density, C_d the drag coefficient and $\boldsymbol{u_a}$ the wind velocity at 10 m above the sea surface). However, surface waves and turbulence in the ocean boundary layer play an important role in regulating the vertical fluxes of momentum, heat, freshwater and gases, not to mention other dynamical aspects in its counterpart of the atmospheric boundary layer. A more complicated representation of wind stress $\boldsymbol{\tau}$ considers the air-sea velocity difference [Duhaut, 2006; Dawe, 2006; Zhai, 2012], and the dependence of drag coefficient C_d on ocean surface waves and stability of the atmospheric boundary layer [Large, 1981; Trenberth, 1989], e.g., $\boldsymbol{\tau} = \rho_a C_d |\boldsymbol{u_a} - \boldsymbol{u_o}|(\boldsymbol{u_a} - \boldsymbol{u_o})$ where C_d is a function of air-sea temperature difference and ocean current velocity $\boldsymbol{u_o}$. Furthermore, the distribution of wind stress on the upper ocean should be a final product of the atmosphere–ocean coupled system, and such interaction involves complex dynamical processes that are the subject of air–sea interactions and are beyond the scope of this thesis. In this chapter, the wind stress is thus treated as an external forcing for the ocean circulation.

Figure 1.3 depicts surface wind vectors for one specific month which occupy broad spectra in space. The primary feature of the surface wind stress is the strong westerlies associated with the jet stream at mid latitudes of both hemispheres, and easterlies at low latitudes. Owing to the Earth's rotation, the near-surface branch of the equatorward flow of the Hadley Cell is turned westward and appears as the northeast trade wind in the Northern Hemisphere. Under other dynamical constraints, e.g., topographic blocking, the wind stress pattern at the sea surface takes complicated forms. Strong circulation is induced by wind stress in the upper kilometer of the ocean. The most outstanding features of wind-driven circulation include gigantic anticyclonic gyres in subtropical basins, and cyclonic gyres in subpolar basins, as well as the strong circumpolar current system in the Southern Ocean.

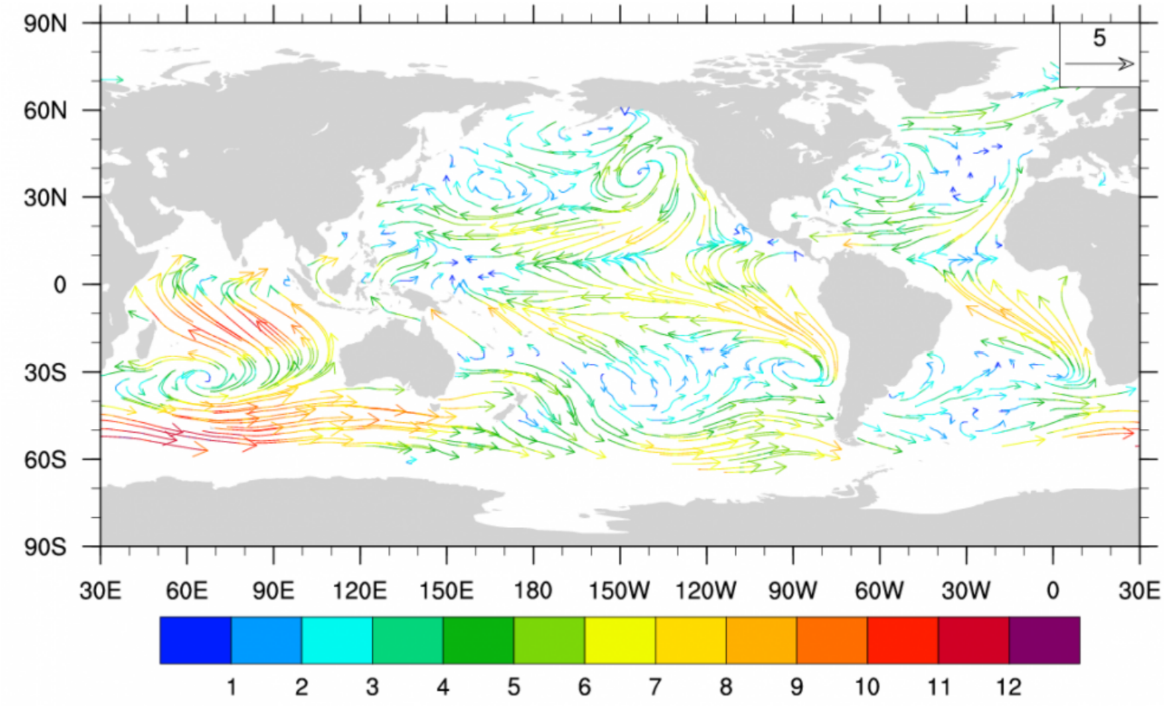

Figure 1.3: Near surface wind vectors colored by wind magnitude for September 2003. The magnitude maximum is located along the ACC in the Southern Indian Ocean for this season. (Source: the QuikSCAT project [Hoffman, 2005]).

Animation: time-dependent wind stress overlying air-sea CO_2 flux

Also available by clicking here.

1.1.2 Ekman layer at the ocean surface

Intuitively, one expects the frictional wind forcing to push a thin layer of water in the same direction as the wind. In a similar manner, this uppermost layer pushes the layer just below, and so forth. In other words, it is plausible to anticipate a vertical structure of the upper ocean with each layer in the same direction of the wind and with slower speeds further down.

However, if the wind persists, fairly commensurate with the Earth's rotation, we must recast the ocean dynamics from a rotating reference frame to describe any flow relative to the moving surface of Earth. In this frame, a fictitious force (the Coriolis force) modifies the picture above, which transforms into a balance between the Coriolis effect and the frictional forcing on each vertical layer. But since the Coriolis force is perpendicular to the current velocity, the uppermost layer responds by deflecting at some angle (to the right in the Northern Hemisphere) relative to the surface wind. Consequently, this layer pushes on the next one down not in the same direction as the wind, but in a direction determined by its motion.

Similarly, each layer of water driven by the layer above shifts direction as well and, for an ideal case where a steady horizontal wind blows across an ocean of unlimited depth, a spiral is formed (see panel (b) in Figure 1.4). That is, each successive layer moves more towards the right and at a slower speed [Ekman, 1905]. The range of depths from the surface to the depth at which this spiral velocity becomes negligible is known as the Ekman layer. Typically, the Ekman-layer thickness is $\sim O\ (10^2\ \text{m})$ or even less, compared with the average ocean depth around 3 km. Thus, the direct effects of the wind are confined to the upper few meters of the ocean. Integrating over the entire Ekman spiral results in a net horizontal transport that is termed as the Ekman transport.

A brief review of important work related to Ekman dynamics will be given in this thesis (specifically the interaction between Ekman dynamics and geostrophic flows or near-inertial waves) in that vertical velocities at the base of the Ekman layer are believed to be one component of ocean ventilation. Classic Ekman theory assumes friction and the Coriolis force to be the only terms in the relevant horizontal balance of forces. This results in a net mass transport perpendicular to the wind stress and has a magnitude given by the ratio of the wind stress to the Coriolis parameter, f,

$$\boldsymbol{U}_{Ek} = \frac{\boldsymbol{\tau} \times \hat{\boldsymbol{z}}}{\rho_0 f}. \tag{1.1}$$

Here, $\boldsymbol{\tau}$ is surface wind stress and $\boldsymbol{U}_{Ek}$ is the mass transport integrated over the Ekman layer (with unit kg m^{-1} s^{-1}). And ρ_0 is the density of seawater and we can assume its magnitude to be $\sim 10^3$ kg m^{-3} in a simple incompressible fluid context.

Beyond the implications for horizontal flows and transport, spatial variability in the Ekman transport also generates vertical velocities across the base of the Ekman layer. From the perspective of mass conservation, convergent transport drives downward vertical motion (Ekman pumping) and divergent transport drives upward vertical motion from beneath (Ekman suction). In this thesis, Ekman pumping is also used to represent the general effect of both upward and downward motions (i.e., the concept itself). We see from Eqn 1.1 that the structure of Ekman transport is determined by the structure of the wind stress and the dependence of f on latitude. From many applications, the latter can be considered small so that Ekman pumping is dominated by spatial variability of the wind stress. To be more specific, vertical Ekman pumping velocities turn out to be proportional to the wind stress curl. To see this, consider the non-divergence constraint integrated over the Ekman layer,

$$\int_{-h}^{0} (\frac{\partial u}{\partial x} + \frac{\partial v}{\partial y} + \frac{\partial w}{\partial z})\, dz = 0, \tag{1.2}$$

where h marks the depth at the base of the Ekman layer. Consider the boundary condition $w = 0$ at the surface,

$$\frac{\partial}{\partial x}\int_{-h}^{0} u\, dz + \frac{\partial}{\partial y}\int_{-h}^{0} v\, dz = -\int_{-h}^{0} \frac{\partial w}{\partial z}\, dz = w(-h) = w_{Ek}, \tag{1.3}$$

which can be reshaped as,

$$w_{Ek} = \frac{\partial}{\partial x}(U_{Ek}) + \frac{\partial}{\partial y}(V_{Ek}) = \frac{\partial}{\partial x}(\frac{\tau_y}{\rho_0 f}) - \frac{\partial}{\partial y}(\frac{\tau_x}{\rho_0 f}) = \nabla \times (\frac{\boldsymbol{\tau}}{\rho_0 f}). \tag{1.4}$$

The Ekman pumping velocity, defined by Eqn 1.4, provides a boundary condition for the interior flow that is central to theories of the general ocean circulation. In the Northern Hemisphere where $f > 0$, a clockwise wind pattern (negative curl) generates a downwelling, whereas a counterclockwise wind pattern causes upwelling. Figure 1.5 shows global maps of wind stress curl and the Ekman pumping velocities, linking boundary conditions of the interior ocean to the global wind stress pattern. In general, Ekman pumping/downwelling is generated in the subtropics while suction/upwelling occurs at the subpolar regions. A comparison between panels (a) and (c) refers to an intensification of wind stress curl in the winter season. This is also evident in the comparison between (b) and (d) of pumping velocities that the difference between upwelling at the subpolar region and downwelling at the subtropics is intensified in winter.

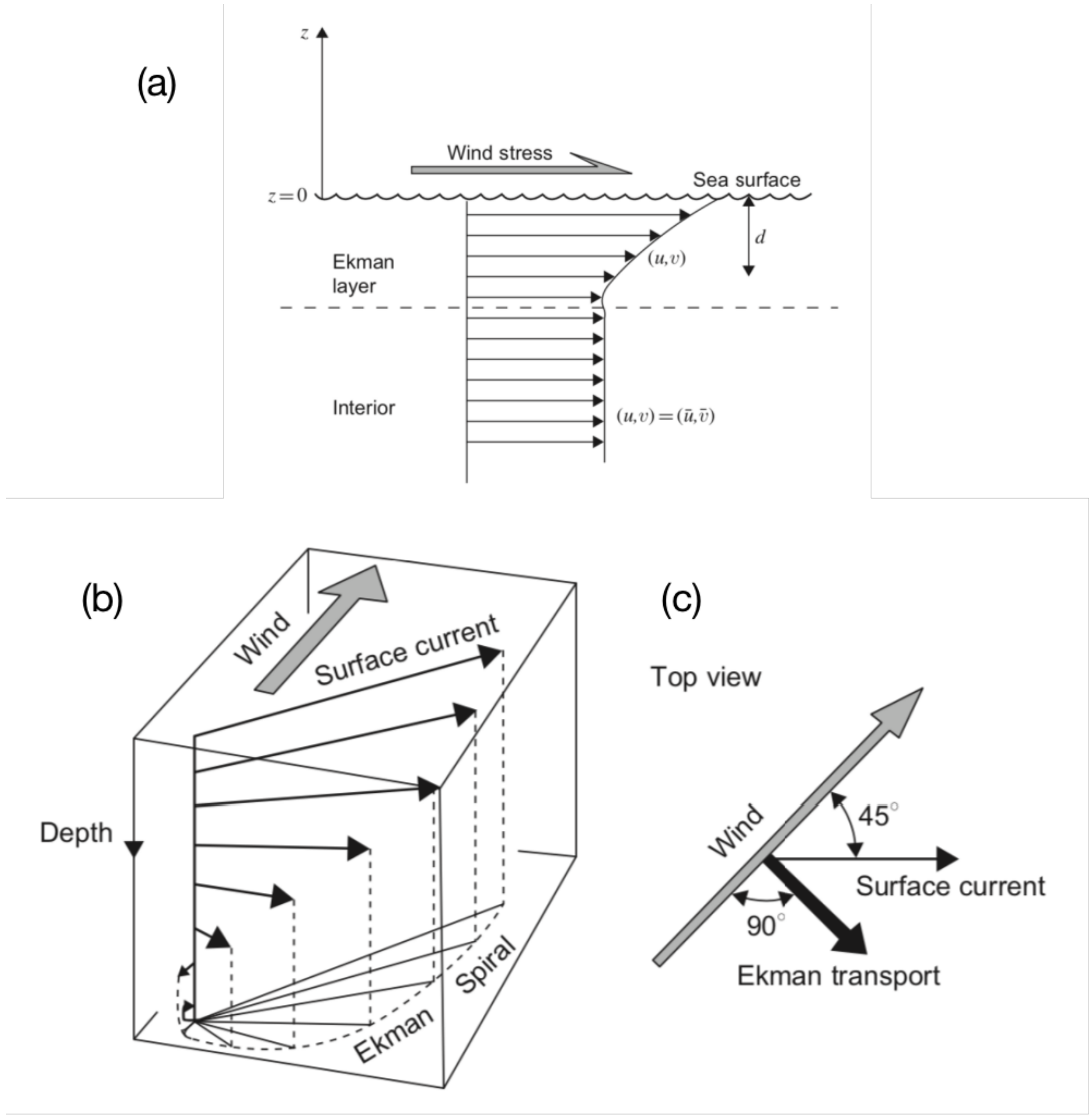

Figure 1.4: The surface Ekman layer generated by a wind forcing over the ocean (Source: [Cushman-Roisin, 2011b]). (a) 1D Ekman layer on top of the ocean interior that is approximately geostrophic. (b) Ekman spiral. (c) The classic theory predicts that the integrated Ekman transport over the entire Ekman spiral is perpendicular to the wind stress and directs towards its right side in the Northern Hemisphere.

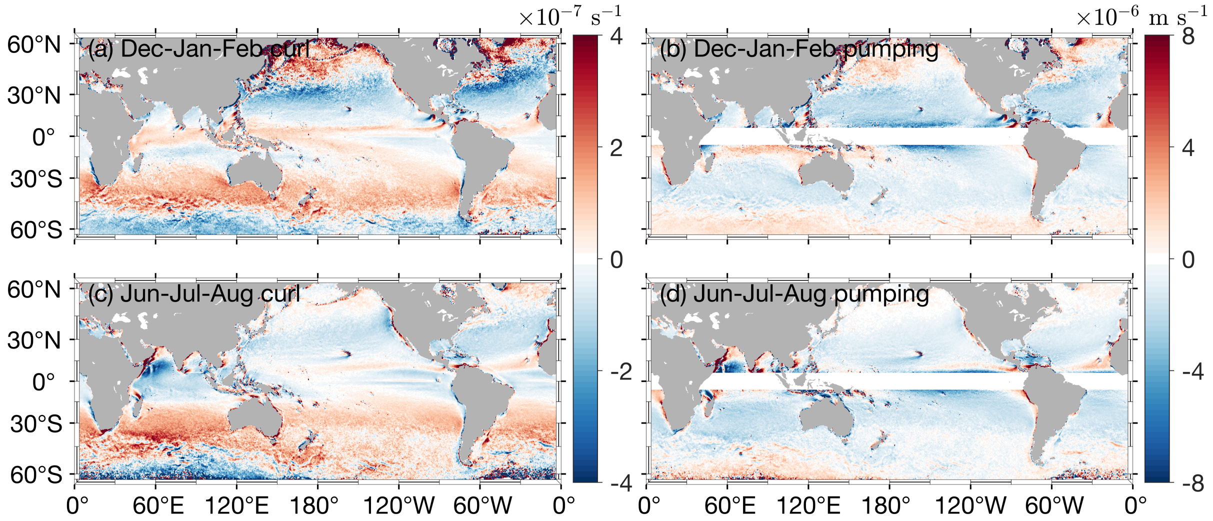

Figure 1.5: The global pattern of wind stress curl and Ekman vertical velocity for two seasons, December-to-February and June-to-August respectively (plotting with the dataset of QuikSCAT [Hoffman, 2005]). The Ekman pumping velocity w_{Ek} is not computed over the white strip along the equator because f is zero there.

1.1.3 Closure of the wind-driven circulation: response of the interior ocean to Ekman pumping

Once stirred into motion by wind or other extra forcing, the surface currents flow according to the geostrophic balance in approximation, $f\hat{\boldsymbol{k}} \times \boldsymbol{u}_g = -\frac{1}{\rho}\nabla p$ where ∇p represents the pressure gradient. To interpret, geostrophic currents flow along isobars, resulting from a balance between the Coriolis force and pressure gradient force. The principle of geostrophy is useful because it allows to infer ocean currents from measurements of the sea surface height (by combined satellite altimetry and gravimetry) or from vertical profiles of seawater density taken by ships or autonomous buoys. The major currents of the world's oceans, such as the Gulf Stream and Kuroshio Extensions, the Agulhas Current, and the Antarctic Circumpolar Current (ACC), are all approximately in geostrophic balance. In addition, this balance is especially useful for the detection of nearly-geostrophic mesoscale eddy fields from satellite images based on the sea surface height anomalies.

If the wind persists, there is a constant horizontal frictional stress that simply results in an Ekman layer at the ocean surface. The wind-driven theory can thus be interpreted as a decomposition into a surface Ekman layer and a geostrophic flow below, which embeds this Ekman layer. An equivalent regime appears at the lower atmosphere, where the wind approaches a geostrophic value with increasing height. Taking the horizontal divergence of the geostrophic flow,

$$\nabla_h \cdot \boldsymbol{u}_g = \frac{\partial}{\partial x}(-\frac{1}{\rho_0 f}\frac{\partial p}{\partial y}) + \frac{\partial}{\partial y}(\frac{1}{\rho_0 f}\frac{\partial p}{\partial x}) = -\frac{\beta}{f}v_g, \tag{1.5}$$

where the variation of f with latitude is considered and the meridional gradient of f is denoted by β. The resulting horizontal divergence of geostrophic flow is thus associated with vertical stretching of water columns:

$$\nabla_h \cdot \boldsymbol{u}_g + \frac{\partial w}{\partial z} = 0. \tag{1.6}$$

Combining Eqns 1.5 and 1.6 one can obtain an expression for the interior geostrophic flow:

$$\beta v_g = f\frac{\partial w}{\partial z}, \tag{1.7}$$

which relates horizontal and vertical currents. If vertical velocity magnitude in the abyss is much smaller than surface Ekman pumping velocities, then ocean currents in the interior will have a southward component in regions where $w_{Ek} < 0$ and northward where $w_{Ek} > 0$.

By integrating Eqn 1.7 from the bottom of Ekman layer to a depth of no motion (e.g., around 1000 m), we can obtain a Sverdrup balance [Sverdrup, 1947],

$$V_g = \frac{f}{\beta}\hat{\boldsymbol{k}} \cdot \nabla \times (\frac{\boldsymbol{\tau}}{\rho_0 f}), \tag{1.8}$$

which is the first model of general ocean circulation. Here, V_g is the meridional component of the geostrophic transport. In 1948, Stommel [Stommel, 1948] used the same basic equations but integrated to the bottom of the ocean and allowed for bottom friction that is a simple linear function of velocity, and the results showed that the variation in Coriolis parameter with latitude leads to a narrow western boundary current in ocean basins. Munk [Munk, 1950b] proposed a complete solution for the ocean circulation, by further adding a lateral eddy diffusion term associated with the horizontal exchange of large eddies. These are pictures drawn for a steady-state ocean circulation followed by more extensions on the theories of western boundary current [Munk, 1950a] and abyssal solutions [Stommel, 1957], while the first time-dependent circulation has been proposed and formulated mathematically by Rossby [Rossby, 1939] that is nowadays known as the "Rossby wave".

Figure 1.6 panel (a) displays the wind-derived geostrophic transport, averaged over the entire QuikSCAT period, exhibiting the expected large-scale pattern of equatorward flow in the subtropics and poleward flow in the high latitudes. The line of zero wind-derived transport is approximately aligned with the axes of the Kuroshio and Gulf Stream Extensions in the Northern Hemisphere and with the ACC in the Southern Hemisphere. While the largest wind-derived transports are located in the higher latitudes, there are also local maxima in the eastern parts of most gyres. Panel (b) indicates the relative error of this Sverdrup approximation compared with Argo measurements, where yellow represents perfect agreement. Here, it is apparent that the Sverdrup balance provides a quantitative description of meridional transport for a large fraction of the global ocean, primarily in the subtropics and tropics. However, it fails to accurately represent meridional transports all along the ACC and in the subpolar North Pacific and North Atlantic.

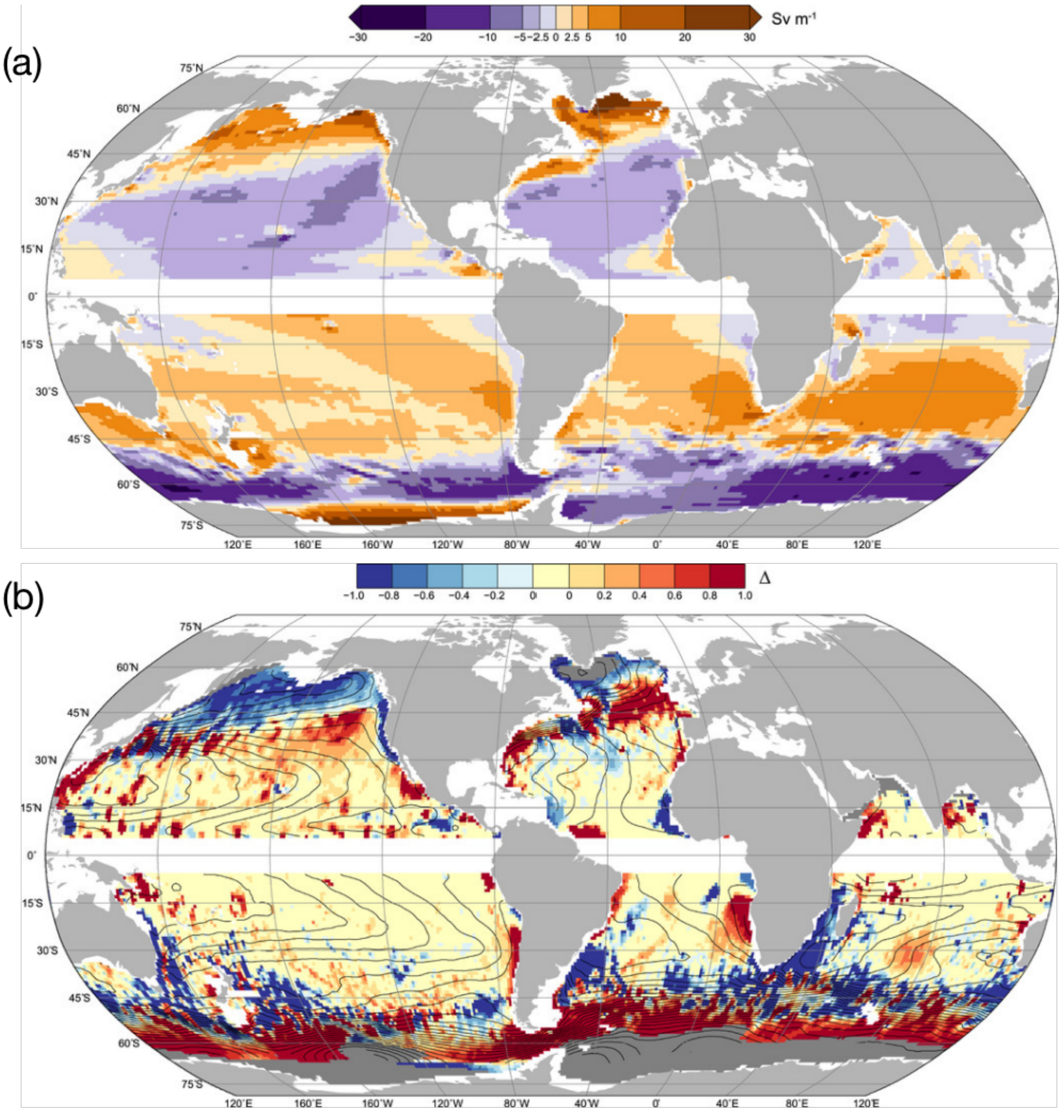

Figure 1.6: (a) Interior geostrophic transport predicted from the Sverdrup theory using the QuikSCAT dataset. Positive (negative) values indicate northward (southward) transport. (b) Relative error with respect to Argo measurements (Source: [Gray, 2014]).

1.2 Thermohaline circulation and convection

Thermohaline circulation (THC) describes the movement of ocean currents due to differences in temperature and salinity (that also induce differences in density) of separate locations in the global ocean. Since it must be driven by mechanical stirring which transports mass, heat, freshwater and other properties in the meridional/zonal direction, the THC is not an individual process of the large scale, but rather supported by external sources of mechanical energy, e.g., the wind stress and tidal dissipation, in addition to surface heat and freshwater fluxes.

Since the thermocline/pycnocline specifies the maximal stratification of the ocean that is important in setting up and controlling the THC, spatial variations of the thermoclines are shown in Figure 1.7. In contrast to the abyss whose water mass formation is due to deep water convection at high latitudes, the main thermocline is the region in which the circulation is primarily caused by the wind-driven Ekman pumping received from the surface layer and is most pronounced at mid-latitudes. Figure 1.7 summarizes the meridional distribution of potential density in the Atlantic, Pacific and Indian Oceans down to 5000 m from three World Ocean Circulation Experiment (WOCE) sections. WOCE is a comprehensive global hydrographic survey of physical and chemical properties, and it represents the state of the oceans during the 1990s. These example sections reveal similar patterns that the pycnocline is very strong and shallow (100 to 200 m) at the equator (only the pink-colored portions in these figures); from there, it spreads into the Northern and Southern Hemispheres differently: it reaches the surface around 25 ° in the Northern Hemisphere, and plunges down to 1000 m around 35 ° before heading upward again and surfacing around 45 ° in the Southern Hemisphere.

Another simple approach to derive the depth of the thermocline can be followed by a scaling analysis to the Sverdrup balance shown in Eqn 1.7. From the hydrostatic balance, the scale for pressure is $\Delta P = gh\Delta\rho$, with h indicating the thermocline depth. Considering the scale of $v_g \sim \Delta P/(\rho f L_x)$ according to geostrophic balance (with L_x the length scale in the x-direction), we have

$$\beta \frac{gh\Delta\rho}{\rho f L_x} = f \frac{w_{Ek}}{h}, \tag{1.9}$$

from which the depth scale h can be estimated at each latitude. For example at 45 ° in the North Atlantic, this estimate of thermocline reaches 500 m, which is consistent with observations.

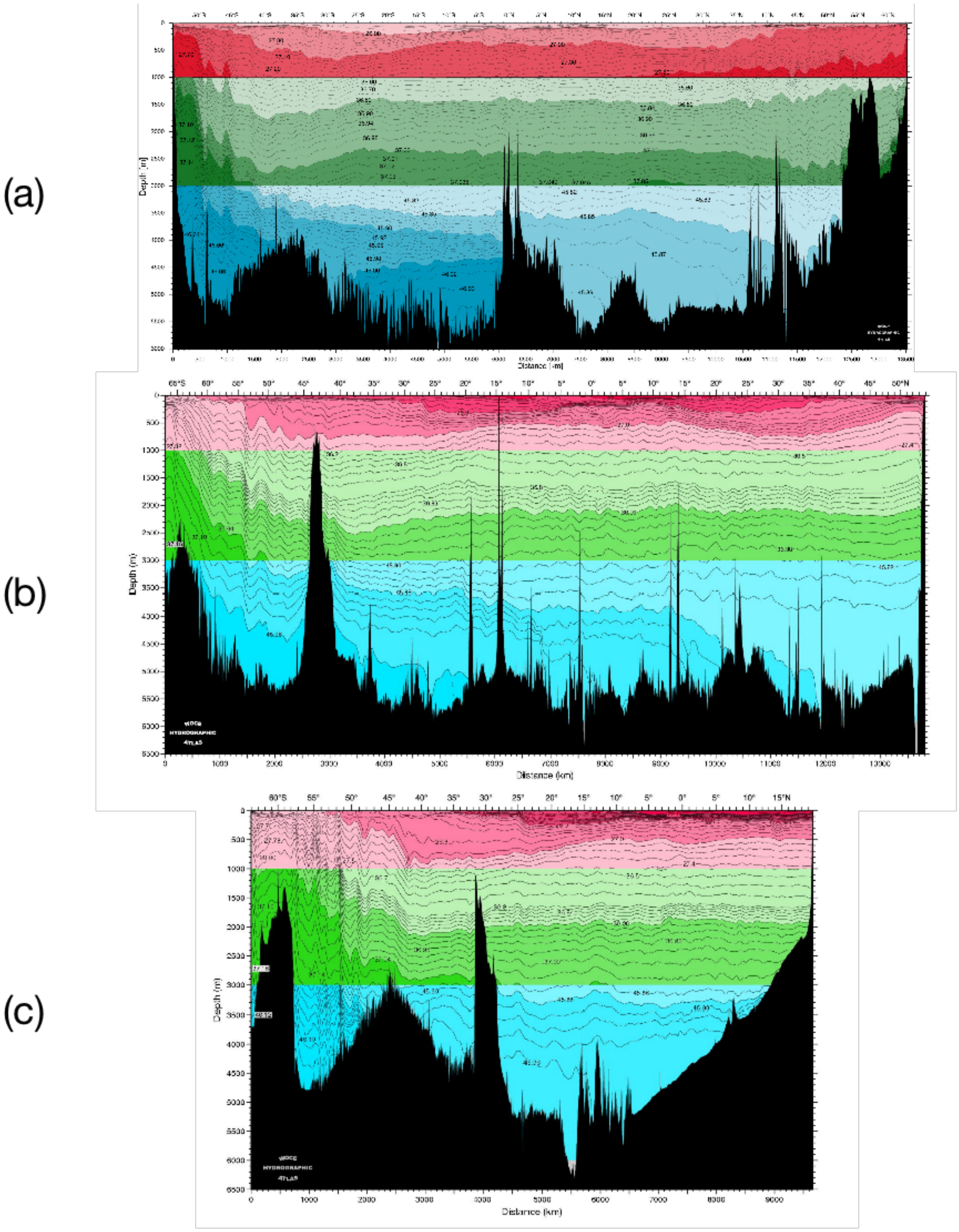

Figure 1.7: Meridional structure of potential density along three WOCE sections, namely (a) A16 for the Atlantic, (b) P15 for the Pacific and (c) I08I09 for the Indian Ocean. A clear version of figures can be found here.

1.2.1 Surface buoyancy forcing

With reference to the temperature and salinity distribution in the ocean, we can specifically relate circulation and transport of these natural tracers to gains/losses of heat and freshwater at boundaries, primarily at the ocean surface. Below listed some processes that are associated with heat and freshwater budget.

Surface gain or loss of heat involves:

- The Sun warms the ocean surface (gain);
- Evaporation cools the ocean surface (loss);
- The ocean radiates more infrared longwave radiation upward than it receives (loss);
- Sensible heat exchanges between the ocean and atmosphere depending on which is warmer (gain or loss);
- Geothermal heating at the seabed (small amount of gain).

Surface gain or loss of freshwater involves:

- Precipitation freshens the ocean surface (gain);
- Evaporation raises surface salinity (loss);
- River runoff (gain);
- Sea ice freezing (loss) or melting (gain);
- Glacial processes like ice shelf melting and iceberg melting (gain).

The balance of these processes in terms of heat (freshwater) determines when and where the ocean is gaining or losing heat (freshwater), and the consequences for temperature (salinity). The combined effects of surface heating/cooling and freshwater exchanges adjust the level of surface density (or buoyancy) forcing that in turn shapes the 3D density structure in the ocean interior. The associated density gradients with their maximal values at the main pycnocline support baroclinity of the ocean (i.e., the difference between surface and deep ocean flow fields) that contributes to the formation of Meridional Overturning Circulation (MOC). Referring to surface heat fluxes as thermal forcing and surface freshwater fluxes as haline forcing, the combined density forcing is thus defined as thermohaline. For this reason, the MOC is alternatively referred to as the THC.

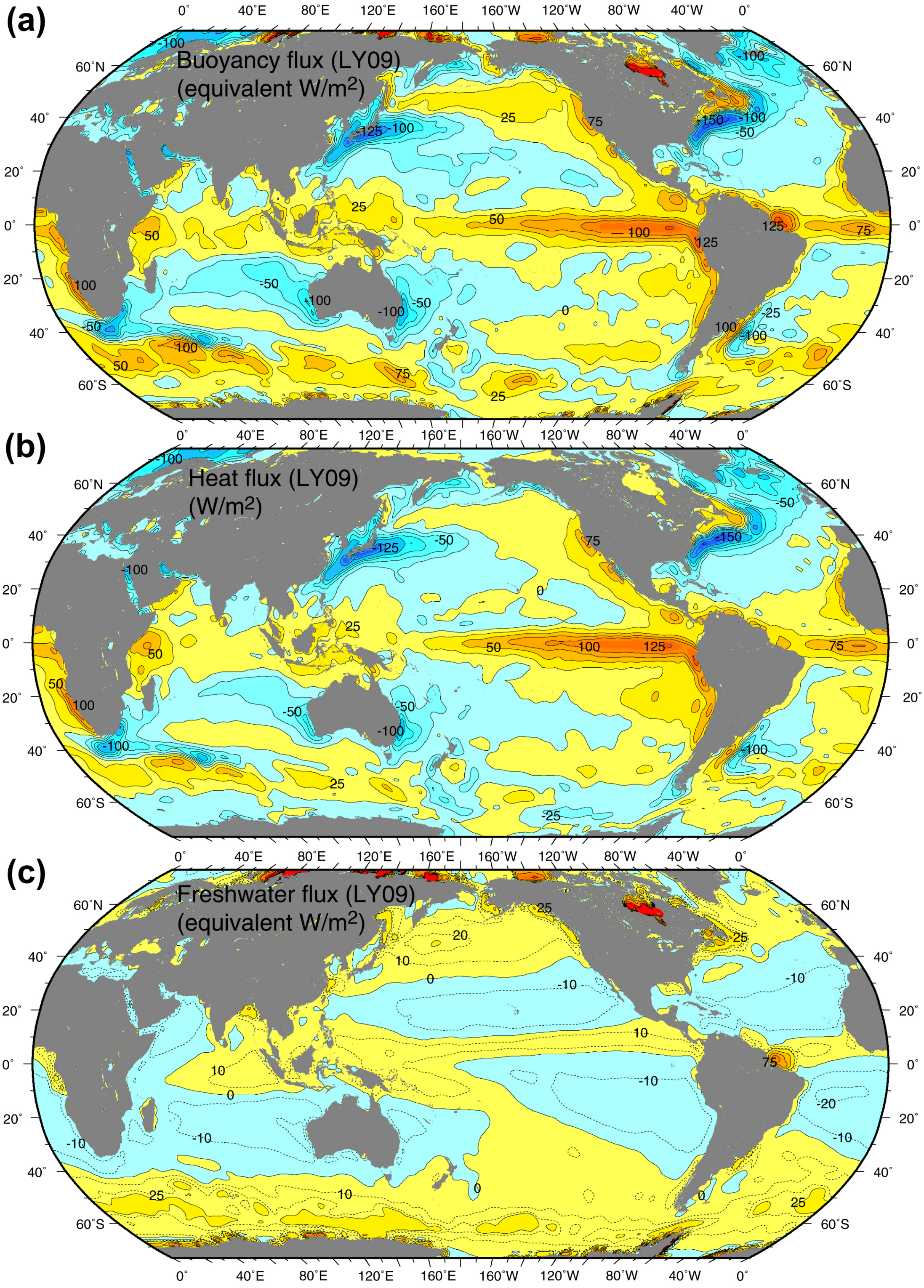

Figure 1.8: Annual mean air–sea (a) buoyancy flux, (b) heat flux, and (c) freshwater flux, with (a) and (c) converted to equivalent heat fluxes (W m^{-2}). Positive values indicate that the ocean is becoming lighter, warmer, and fresher in the respective maps. (Source: [Talley, 2011]).

Figure 1.8 displays the heat, freshwater and buoyancy fluxes for the global ocean. The distribution of net air–sea heat flux shown in (b) implies that the ocean gains heat in the tropics and loses heat at higher latitudes. Interestingly, the maximum value of heat loss is in accordance with western boundary currents (especially along the Gulf Stream and Kuroshio Extensions in the Northern Hemisphere in that these warm waters carried northward encounter dry and cold air blowing from the continent in winter). The associated northward transport of heat and hence buoyancy in the Atlantic is related to the MOC. Though smaller in terms of amount, heat loss is also obvious at each western boundary current system in the Southern Hemisphere, especially nearby the Agulhas Current that both retroflects along the ACC and potentially leaks water into the South Atlantic Ocean. Such heat loss can also be found in the vicinity of Brazil and East Australian Currents as the western boundary system respectively in the South Atlantic and Pacific. It is also worthwhile noting the Leeuwin Current that is the only southward flowing eastern boundary current associated with heat loss to the atmosphere. The hotspot of heat gain is located at the eastern Pacific near the equator.

Although freshwater fluxes generally contribute much less than heat fluxes to the total buoyancy flux (e.g., the resemblance between panels (a) and (b) in Figure 1.8), freshwater fluxes in the Southern Ocean and subpolar North Pacific result in stronger buoyancy gain by the ocean. Freshwater fluxes also make a difference where heat fluxes are small, such as throughout the subtropical gyres outside the western boundary currents, where contributions from both fluxes are on the same order.

After showing the surface forcing from the heat and freshwater fluxes, it is of interest to investigate how these fluxes drive the THC. Figure 1.9 provides three theories that explain the THC in terms of its vertical loop.

1. **Theory of pushing**: In this theory, surface cooling produces dense water that sinks to a great depth (i.e., deep water formation), which pushes the deep current and then maintains the THC. The high-latitude ocean is filled up with cold and dense water from surface to bottom. Combining with the warm and light water in the upper ocean at low latitudes, this creates a pressure force in the abyssal ocean which causes cold bottom water to push towards low latitudes that maintains the meridional circulation. The major problem of this theory is that, due to the lack of an external source of mechanical energy to sustain mixing, cold water piles up in the ocean, and the solution is eventually reduced to a very weak circulation.

2. **Theory of pulling by deep mixing**: To maintain a sizable circulation, the cold water in the abyss should be removed. Deep mixing sustained by tidal mixing can transform cold water into warm water in the deep ocean, creating room for newly formed deep water and thus pulling the THC [Munk, 1998].

3. **Theory of pulling by wind stress**: In this regime, the Southern Ocean westerlies pull cold water from the deep ocean and thus maintain the global THC. Under the present climatic conditions and modern geographic and topographic distribution, a strong Ekman upwelling around the latitude band of 50–60 °S exists, in the vicinity of ACC. Due to this strong upwelling, North Atlantic Deep Water (NADW) at depth is pulled up to the upper ocean, where water properties are gradually modified in the surface mixed layer on its way northward. In the upper ocean, wind stress continues to input mechanical energy through Ekman layer and surface waves. Theoretically, wind-driven upwelling and mixing in the upper ocean can build up the major parts of the THC and water mass transformation in the world ocean, while the remaining parts of the transformation in the deep ocean are relatively small and can be accomplished by external mechanical energy from tidal mixing.

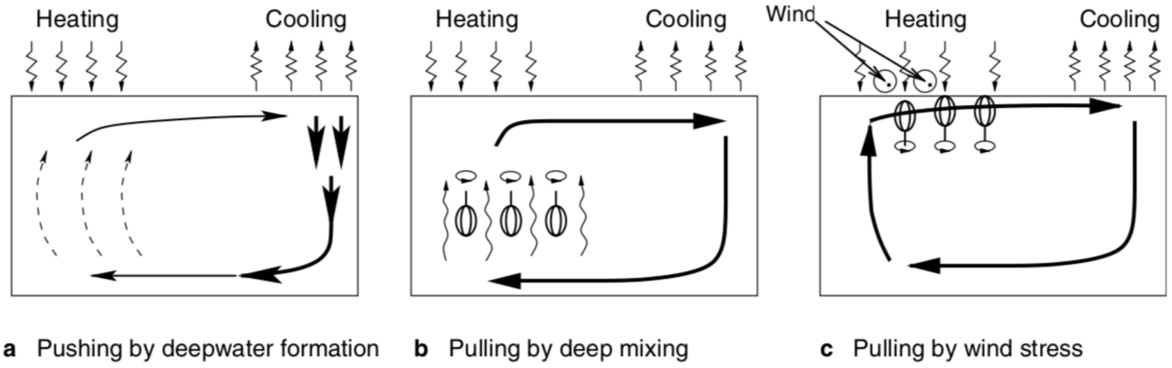

Figure 1.9: Three theories of thermohaline circulation. (Source: [Huang, 2009]).

1.2.2 Equation of state and important variables in ocean thermodynamics

In any description of the fluid system, it is necessary to have the momentum budgets (for three directions in the Cartesian coordinate) in addition to a mass conservation. These four equations are complete and solvable for an incompressible fluid with a constant density ρ_0. In the ocean, however, water density is a complicated function of pressure, temperature, and salinity, and this relation is called the equation of state that determines the THC in many aspects. The two diagrams in Figure 1.10 show density contours in the temperature-salinity and temperature-pressure fields respectively. These isolines indicate that the relation between density and the combination of temperature, salinity and pressure is slightly nonlinear, which will be discussed shortly.

With the Boussinesq approximation, which has the assumption that seawater density does not depart much from a mean value, it has allowed a replacement of the actual density ρ by its reference value ρ_0 for every term in these equations, except for the gravitational acceleration in momentum. This approximation also eliminates the need to infer density from salinity and temperature, since the energy equation has become an equation governing density variations instead of temperature. More generally and for most applications, it can be assumed that the density of seawater is independent of pressure (incompressibility) and linearly dependent upon both temperature and salinity according to:

$$\rho = \rho_0[1 - \alpha(T - T_0) + \beta(S - S_0)], \tag{1.10}$$

where T is the temperature, and S is the salinity (defined by the so-called practical salinity unit psu, derived from measurements of conductivity and having no units). The constants ρ_0, T_0, and S_0 are reference values of density, temperature, and salinity respectively, whereas α is the coefficient of thermal expansion, and β is the coefficient of saline contraction by analogy. Typical seawater values are $\rho_0 = 1028$ kg m^{-3}, $T_0 = 10$ °C, $S_0 = 35$ (psu), $\alpha = 1.7 \times 10^{-4}$ K^{-1}, and $\beta = 7.6 \times 10^{-4}$.

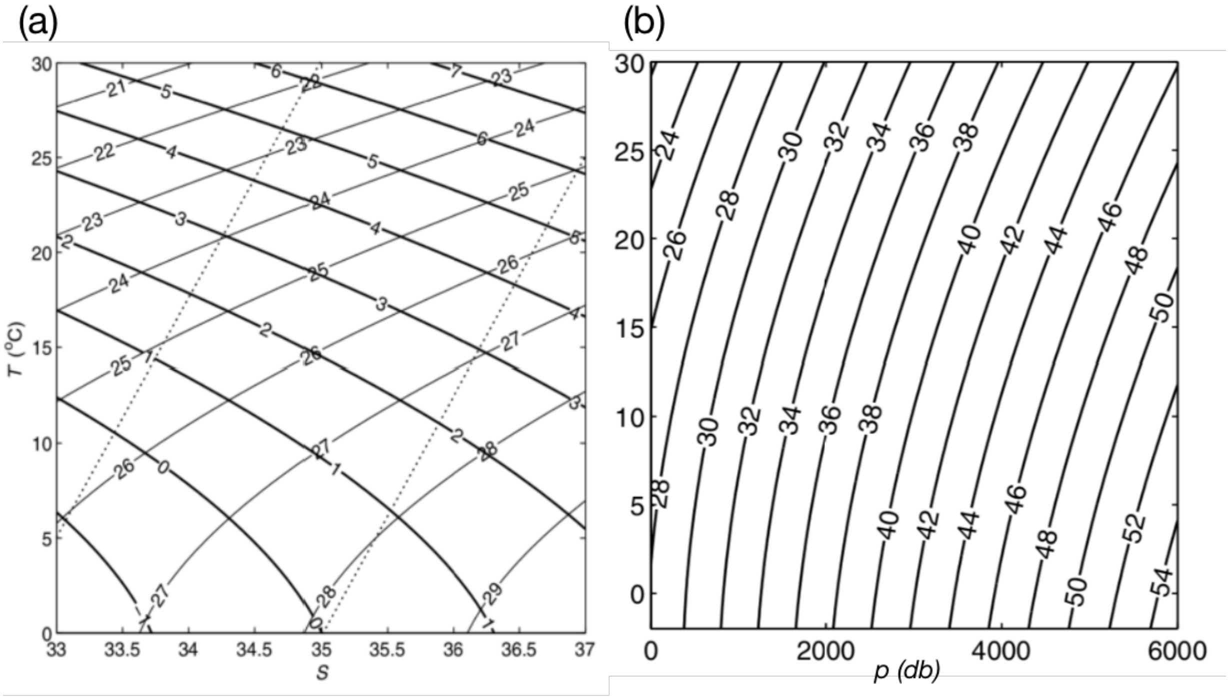

Figure 1.10: (a) Isopycnals (thin lines) and spiciness isolines (heavy lines) at sea surface; (b) Seawater density as a function of pressure and temperature.

Accounting that several important variables/concepts used to infer ocean circulation and ventilation have been linked to temperature, salinity and density properties of water masses, they are listed here to avoid any repeated introductions later in the main text.

Potential density Panel (b) in Figure 1.10 shows that some proportion of the vertical density gradient in the ocean is due to the increase of pressure. However, it is often more desirable to identify density changes due to other physical factors, such as temperature and salinity. Potential density is thus introduced and defined as the density of a seawater parcel if it is moved adiabatically and without changing its salinity from an initial pressure p to a reference pressure p_r. Potential density has been widely used in the study of water column stability and relevant issues, such as in the definition of Rossby radius. The most frequently used potential density sets the sea surface as the reference level. Owing to the nonlinearity of the equation of state, however, stratification inferred from potential density defined in this way, denoted as σ_0 here, can display some artefact of unstable conditions in the depth range of 4–4.5 km. To be more precise, the calculation of potential density at different depths is thus dependent on several reference pressures. For example, σ_0 is used for the upper ocean while σ_4 (using 4000 db as the reference pressure) is used for analyzing the deep circulation. In this thesis, since only the upper ocean until 2000 m has been considered, most calculations related to potential density take the surface as its reference level.

Neutral density and neutral surface To overcome the issue of artefact associated with potential density discussed above and to bridge the gap of density over depths, we can use the local pressure as the reference pressure to define the potential density, σ_r, where the subscript r indicates the local reference pressure. Therefore, the neutral surface is defined and constructed as a surface whose normal is in the direction of $-\alpha\nabla\theta + \beta\nabla S$, where θ is the potential temperature defined in a similar manner to the potential density. However, such a surface turns out to be a helical surface that a trajectory beginning from one location (x, y) at depth z and going around the basin cannot come back to the same depth z but with a small discrepancy of depth. An algorithm [Jackett, 1997] has been developed to overcome this issue, which provides the corresponding neutral density variable γ_n for any given location in the world ocean in addition to its in-situ observed temperature, salinity and pressure.

Spiciness A reversed thought of plotting density as a function of temperature and salinity is to have temperature and salinity on the same isopycnal. To represent the thermodynamic properties on an isopycnal surface more concisely (since temperature and salinity on an isopycnal surface are not independent), another thermodynamic function which is perpendicular to density surfaces has been introduced that is called spiciness. Since its introduction in ocean physics, spiciness has been used as a tool in the study of double diffusion and other processes in the ocean. A scale-invariant constraint for defining spiciness is to require that, at any given point in the (θ, S) space, the slopes of the isopycnals and spiciness isolines are equal and of opposite sign (see Figure 1.10 panel (a)). In the study of water mass identification and ventilation, spiciness is important in that water masses in the same density class are sometimes difficult to distinguish from each other due to a compensation between temperature and salinity.

Stability and Brunt-Väisälä frequency Consider a water parcel that has density ρ_0, in an environment where the density is a function of depth $\rho = \rho(z)$. If the parcel is displaced by a small vertical distance z', its vertical momentum becomes

$$\rho_0 \frac{\partial^2 z'}{\partial t^2} = -g[\rho(z) - \rho(z + z')] = g\frac{\partial \rho(z)}{\partial z} z', \tag{1.11}$$

which has a straightforward solution ($z' = z'_0 e^{i\sqrt{N^2}t}$) with its frequency N as

$$N = \sqrt{-\frac{g}{\rho_0}\frac{\partial \rho(z)}{\partial z}}. \tag{1.12}$$

The displacement z' has oscillating solutions if $\partial\rho(z)/\partial z$ in the square root is negative, while there is an unstable growth if it is positive. This frequency is of importance in terms of vertical movements of water parcels in the ocean that indicates possible convection sites for water mass transformation.

Potential vorticity Friction is essential for the transfer of momentum in a fluid. For example, wind inputs momentum through the thin frictional Ekman layer at the sea surface, with a similar momentum transfer found at the sea floor. In the vast interior ocean, however, the flow is frictionless and thus conservative in its angular momentum. Potential vorticity (PV) is one indicator of such conservation, defined as $q = \frac{f+\zeta}{H}$ in a barotropic approximation, where ζ is the relative vorticity and H denotes the thickness of an ocean layer. For baroclinic flows in a continuously stratified fluid, the potential vorticity can be written as $q = \frac{f+\zeta}{\rho} \cdot \nabla\lambda$ where λ is any conserved quantity for each fluid element. In particular, if $\lambda = \rho$ and assume that $f \gg \zeta$,

$$q \approx \frac{f+\zeta}{\rho}\frac{\partial \rho}{\partial z} \approx \frac{f}{\rho}\frac{\partial \rho}{\partial z}. \tag{1.13}$$

This approximation results from an assumption that the horizontal gradients of density are small compared with the vertical gradients, which is useful within the thermocline. Such approximation also allows the PV of various layers of the ocean to be determined directly from hydrographic data without knowledge of the velocity field. For example, an algorithm developed to detect mode waters (one type of homogeneous water masses in the upper ocean) from profiling datasets depends on this simplified PV, and will be thoroughly introduced in Chapter 3.

1.2.3 Water mass (trans)formation

The concept of tracer has been applied to the definition and detection of water masses for a long time that is to trace any water mass back to its origin and infer a circulation without measurement of circulation itself. This concept is useful since there are relatively few direct measurements of dynamical ocean fields such as currents on a scale sufficient to quantify the global ocean circulation. Consequently, oceanographers seek indirect methods to gain a conceptual and quantitative understanding of ocean circulation.

Natural tracers include temperature, salinity, oxygen and other biogeochemical compounds. The study of Walin [Walin, 1982] focused on the heat budget for the North Atlantic by using temperature to mark water masses. Salinity is a key scalar property when studying the river outflow or hydrological cycle. The most common scalar property for tracing water masses is buoyancy, or its approximation as provided by potential density [Speer, 1992]. The PV discussed previously has been considered as a very important dynamical tracer as well [Haynes, 1990], especially for idealized numerical modeling studies with simplifications in temperature and salinity equations, since PV is a materially conserved property that is related to both the velocity and the stratification as shown in Eqn 1.13. To interpret, if how the PV field evolves in time is available, we can derive the evolution of circulation given any specific velocity field at one time step.

A key feature of this tracer analysis is the development of an understanding of how water masses (denoted by tracers) are both transported by the circulation and modified, or transformed, through processes such as mixing and biogeochemical activities. The understanding of these processes, combined with observational estimates of water mass transformation (WMT), leads to the construction of a global conveyor belt circulation that provides an important step towards perceiving the globally interconnected ocean circulation. Therefore, the WMT is briefly introduced here (see Large et al. [Large, 2001] and Marshall et al. [Marshall, 1999] for a comprehensive summary).

A fluid element is exposed to various processes, including property exchanges with the atmosphere (air–sea fluxes) or adjacent seawater elements (mixing). These processes are the main causes for the transformation of water masses. Walin [Walin, 1982] developed a framework that combines different aspects of Eulerian and Lagrangian kinematics, in order to characterize and quantify the transformation of water masses due to these processes. Most seawater properties experience strong changes near the surface and bottom boundaries, whereas interior property changes (i.e., mixing) are relatively weak. However, interior changes generally act over larger volumes and therefore make an important contribution to ocean property distributions.

The WMT framework links transformation rates due to boundary-layer fluxes and mixing, offering the means to infer one from the other. That is, one can use the WMT framework to infer interior transformation from direct measurements of boundary-layer fluxes in models and observations, or to infer boundary-layer fluxes from direct measurements of interior transformation. For example, if the tracer is potential density [Speer, 1992], the diapycnal flow is linked with diabatic forcing of density. In other words, the water mass (trans)formation rate — the convergence of the diapycnic flow — can be diagnosed from only the diabatic forcing without requiring any additional information about the circulation or dynamics. More generally speaking, the flow across surfaces of any property (tracer) can be linked to the forcing of that property in the framework of water mass transformation. The transformation rates in the temperature-salinity space further link the surface flux-induced water mass properties to the observed mode water properties [Speer, 1993; Hieronymus, 2014].

Figure 1.11 compares global WMT rates due to air–sea fluxes (G_{bdy}) and mixing (G_{mix}) in neutral density space. The mixing is split into mesoscale mixing (G_{meso}) and small-scale mixing (G_{iso}). Air–sea fluxes generally add buoyancy to light water and remove buoyancy from dense water, thus producing the extremes in the globally observed water mass distribution [Large, 2001]. Mixing acts to reduce extremes, therefore generally showing an opposite structure. Panel (b) shows the corresponding Atlantic meridional overturning circulation (AMOC). The AMOC indicates both a shallow and deep overturning, with light water entering the domain and transforming into Subtropical Mode Water (STMW) and North Atlantic Deep Water (NADW). The peak NADW transport is located at approximately 50 °N.

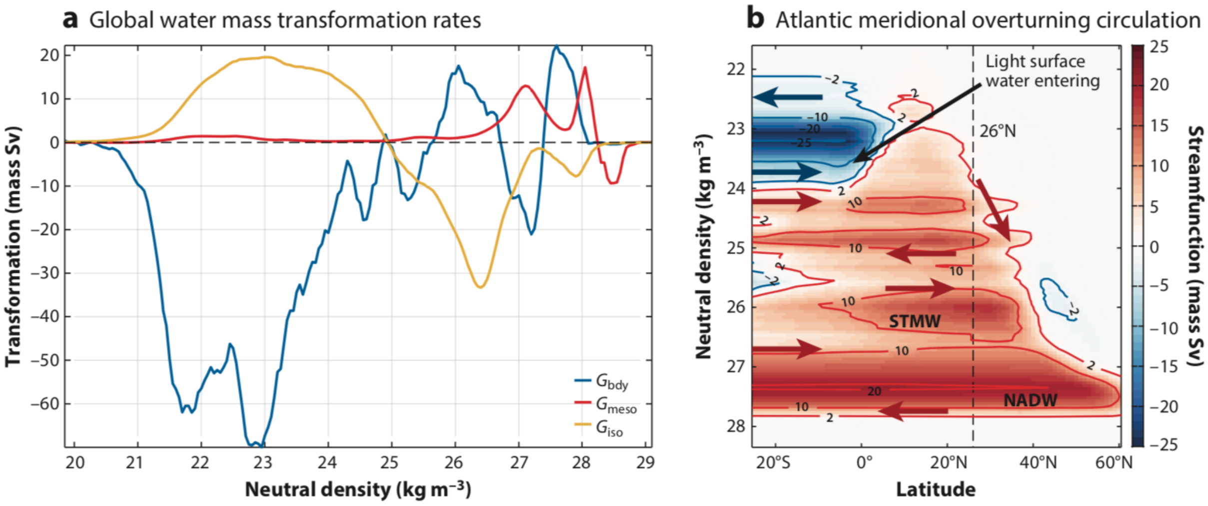

Figure 1.11: (a) Global annual mean water mass transformation for air–sea fluxes (G_{bdy}, blue line), mesoscale mixing (G_{meso}, red line), and isotropic small-scale mixing (G_{iso}, yellow line). (b) The Atlantic meridional overturning circulation as calculated. (Source: [Groeskamp, 2019]).

1.3 Ventilation and thermocline theory

The permanent thermocline in classic theories is regarded as a local equilibrium between advection (upwelling of cold abyssal water) and diffusion (downward heat transfer from the sea surface). This paradigm changes with a theory [Luyten, 1983] that combines subduction of water masses from the mixed layer with advective descent into the stratified thermocline. In specific, mixed-layer waters at the mid-latitude are subducted into the main thermocline where Ekman pumping is downward (see Figure 1.5). At the thermocline, these water masses slide along isopycnals, carrying with them their surface properties such as density and potential vorticity. That is to say, layers of thermocline water that can be traced back to the base of the mixed layer where Ekman pumping is downward are already ventilated, and their intersection with the mixed layer where they are supplied is named as the outcrop line. As will be discussed in more details in the next chapter, the vertical structure of the main thermocline in the ventilated area thus contains and indicates the density distribution at the surface in late winter [Iselin, 1939].

Under these premises, the thermocline problem is reduced to solving for the vertical distribution of density by tracking individual density layers upstream to their relative outcrop lines, where the surface density distribution is known. As the idea of subduction and subsequent sliding along isopycnals suggests a thermocline controlled by advection, there is not much work done by diffusion. An extension to this theory considered a separation between waters that can be traced back to outcrops and those (re-)circulating without any contact to the surface [Huang, 1991; Marshall, 1992]. The latter has been speculated that is is characterized by a slow but effective homogenization of potential vorticity. In this thesis, the next chapter will focus on the vertical movement of water parcels at the base of the mixed layer (i.e., surface water mass subduction), while the other chapters are related to mode waters that might shed some light on the recirculating components of this thermocline theory.

Now, we have seen two theories that are associated with the changes of volume and properties of surface-layer water masses: (trans)formation and subduction. While they are clearly related to one another, the difference between them must be clarified (see Figure 1.12).

Subduction is associated with a rate at which fluid passes between the seasonal boundary layer (i.e., mixed layer) of the ocean and the ocean's stratified interior [Marshall, 1992; Marshall, 1993]. It is of interest because the mixed layer acts as a rectifier at the surface due to seasonality of forcing, so that water masses transmitted into the main thermocline are also time-dependent.

Formation is an integral calculation about the rate of creation (and destruction) of water masses at the sea surface by air—sea fluxes. In specific, it is concerned with fluid passing laterally across outcropping isopycnals at the sea surface, of which the convergence is determined by the air-sea forcing.

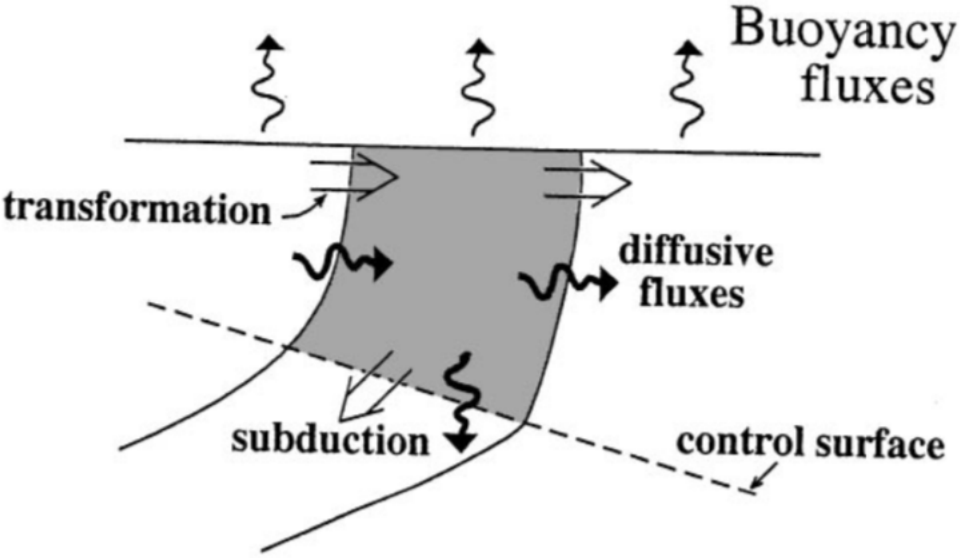

Figure 1.12: A schematic of the upper ocean showing the sea surface, two outcropping isopycnals and a fixed control surface across which the subduction is monitored. Buoyancy fluxes at the sea surface and diffusive fluxes in the interior transform water masses from one density class to another. (Source: [Marshall, 1999]).

Another perspective of the thermocline theory is to consider the continuity of the entire ocean, as shown in Figure 1.13 that displays a global overturning streamfunction. Note that the formation and stabilization of thermocline are not separable from the thermohaline circulation as discussed. This streamfunction of overturning is constructed by summing the layer transports for each latitude. The major features are i) shallow tropical and subtropical overturning cells with sinking at about 30 ° and rising in the tropics; ii) the large deep cell of NADW with sinking in the north, occupying most of Northern Hemisphere water column and extending southward to about 35 °S; iii) the deep cell centered in the Southern Hemisphere at 3000 m, with a northward flow of Antarctic Bottom Water (AABW) and southward deep flow, mainly as Pacific Deep Water (PDW) and Indian Deep Water (IDW); iv) a top-to-bottom overturn in the southern boundary that forms AABW; and v) the surface-intensified Deacon Cell that sinks around 50 °S and upwells between 35 and 50 °S.

The first four cells are principally connected to diapycnal processes, while the Deacon Cell almost disappears when the overturning is instead calculated in isopycnal layers, which means that this cell is not associated with a large amount of diapycnal flux. In the Southern Ocean, there is a large component of adiabatic northward flow that returns southward at the same density but at greater depth that leads to the formation of Deacon Cell. However, the diabatic component of the Deacon Cell includes northward Ekman transport across the ACC, which is meanwhile fed by adiabatic upwelling from deep layers [Speer, 2000]. Buoyancy gain at the sea surface then allows these upwelled waters to move northward, decreasing in density. They are mostly deposited into the Subantarctic Mode Water (SAMW) layer just north of the ACC and then move into the Southern Hemisphere gyre circulations to the north [Jones, 2016].

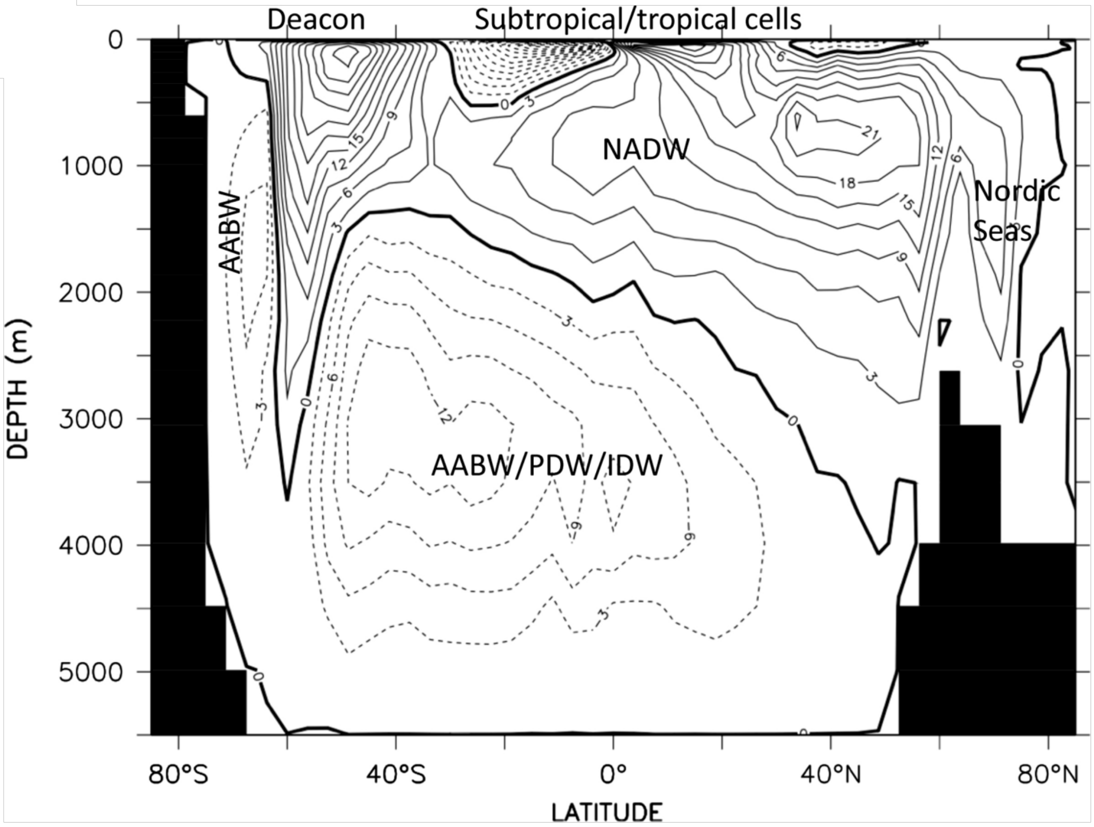

Figure 1.13: Global meridional overturning streamfunction from a high-resolution global coupled climate model. (Source: [Talley, 2011]).

To summarize the elements of the global overturning circulation, Figure 1.14 shows two schematics associated with the movement of each water mass in the large-scale ocean [Talley, 2011]. The global overturning can be divided into two major connected global cells, one with dense water formation around the North Atlantic and the other around Antarctica. These are the NADW and AABW cells, respectively. These two cells are interconnected especially in the Southern Ocean. Another weak overturning cell is found in the North Pacific, forming a small amount of intermediate water (NPIW), which is mostly separated from the other two large cells. The features of each water mass are listed below:

North Atlantic Deep Water The NADW cell begins with warm water entering the Atlantic from the Indian via the Agulhas, and from the Pacific via Drake Passage. This warm water then moves northward through the entire Atlantic and then sinks at several sites in the northern North Atlantic (Nordic Seas, Labrador Sea, and Mediterranean Sea). These denser waters flow south and exit the Atlantic as NADW. Bottom water (AABW) also enters the Atlantic from the south, which upwells into the bottom of the NADW layer in a diffusive process. When the NADW leaves the Atlantic, part of it enters the Indian Ocean around the southern tip of Africa, and most enters the ACC to be the source water for deep water formation (AABW) around Antarctica.

Antarctic Bottom Water The AABW cell begins with the upwelling of NADW nearby Antarctica. The densest waters accordingly formed will sink and become the AABW, that further move northward at the bottom of the Atlantic, Indian and Pacific Oceans. In all three oceans, AABW then upwells into the local deep water, i.e., the NADW, IDW and PDW. Because there are no volumetrically important surface sources of dense water in the northern Indian and Pacific Oceans, this upwelled AABW is the primary volumetric source of the IDW and PDW, whereas AABW is only a minor component of NADW.

Indian and Pacific Deep Water The IDW and PDW can be traced by low oxygen since they are composed of old upwelled waters. They flow southward into the Southern Ocean above the NADW layer because they are lighter in density. As a result, compared with the upwelling region of NADW, these two deep waters upwell farther north in the Southern Ocean. The upwelled IDW/PDW in the Antarctic feeds two cells: one is associated with a northward flux of surface water across the ACC that joins the upper-ocean circulation, accomplished initially by Ekman transport; and the second is related to the dense AABW formation that recycles back through the deep water routes, along with the NADW.

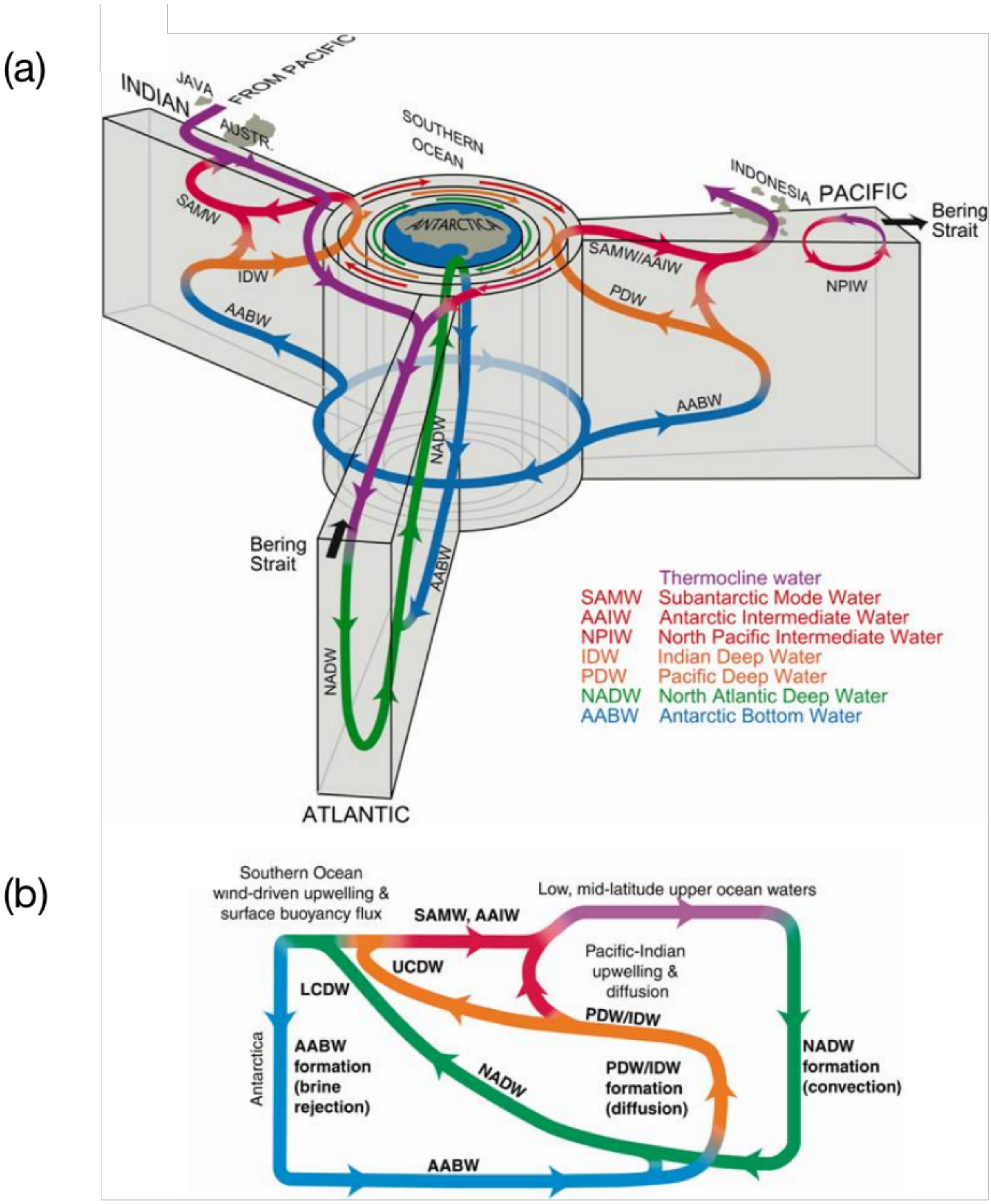

Figure 1.14: Global overturning circulation schematics. (a) Overturn from a Southern Ocean perspective. (b) Two-dimensional schematic of the interconnected water cells. (Source: [Talley, 2011]).

1.3.1 A potential state of subduction: mode water

The subduction process of surface water masses was briefly introduced in the context of ventilated thermocline previously and will be narrated in details in Chapter 2. As discussed previously, ventilation of the ocean interior occurs when fluid is subducted, or pushed down, from the ocean surface. The initial view dates back to [Iselin, 1939], who proposed that water would be pushed downwards along sloping isopycnals from the base of the Ekman layer by the wind-induced vertical Ekman pumping velocity. [Stommel, 1979] recognized that only the fluid leaving the deep winter mixed layer irreversibly enters the permanent pycnocline (the Stommel's demon hypothesis), and this biases the temperature and salinity properties of the main thermocline toward those of the deep winter mixed layer. Consequently, it is actually the flow through the base of the winter mixed layer (rather than the Ekman layer) that ventilates the underlying ocean, and, as pointed out by [Woods, 1985], the absence of a mixed layer in idealized models precludes lateral influence of other water columns across the sloping base of the mixed layer. These perspectives of ocean ventilation have shown that the studies of water mass subduction primarily care about water masses that can permanently subduct into the main thermocline from the sea surface.

The theory of Stommel's demon indicates that the seasonality of surface buoyancy forcing leads to a shoaling of the mixed layer from winter to summer, and a deepening from summer to winter. This seasonal bias forms a homogeneous water mass — mode water — commonly situated between the seasonal and permanent thermoclines (i.e., the demon itself). In specific, the deepest mixed layer formed in winter is later capped by a near-surface restratification due to buoyancy gain. The residual component of the winter mixed layer that is not re-entrained into this surface restratification is defined as mode water. In this regard, mode water is a nearly homogeneous water mass and can be found within or near the top of the permanent thermocline and hence is visible through the contrast in stratification with the thermocline waters [Hanawa, 2001]. Compared with the "permanent" subduction rate that the ventilation theories try to quantify, mode waters, by contrast, can either subduct into the ocean interior or be re-entrained into the surface layer. Thus, these special water masses represent a state with potential to be permanently subducted. In terms of their vertical position, mode waters are pushed down from the surface layer. However, since the common definition of subduction refers to surface water masses entering the main thermocline, whether mode waters represent such permanent process needs further studies. On the other hand, the transport and recirculation of mode waters do represent as the lateral influence discussed by Woods [Woods, 1985], though in a different perspective, since mode waters are generally distributed far beyond their formation areas.

Identified in every ocean basin and over a large geographical area, mode waters are always found on the warm side of a current or front. In the Northern Hemisphere, subtropical mode waters (STMWs) are associated with every separated western boundary current of the subtropical gyres, and also located on the eastern side of the basin albeit a smaller amount [Hautala, 1998]. For example, [Masuzawa, 1969] first introduced the term "Subtropical Mode Water" (STMW) in reference to the thick layer of temperature 16–18 °C on the southern side of the Kuroshio Extention in the subtropical North Atlantic. This STMW is the counterpart of the previously identified Eighteen Degree Water (EDW) associated with the Gulf Stream Extension in the North Atlantic [Worthington, 1958].

In the Southern Ocean, the Subantarctic Front is the southern boundary of the subtropical gyres. Since isopycnals plunge rapidly towards the north across the ACC, a very thick mode water is found at the northern periphery of the front — the Subantarctic Mode Water (SAMW) [McCartney, 1977; Herraiz-Borreguero, 2011; Hartin, 2011]. McCartney et al. [McCartney, 1982] then applied the term "Subpolar Mode Water" (SPMW) to the thick near-surface mixed layers in the subpolar gyre of the North Atlantic.

In a volumetric census (as in a θ-S diagram), this homogeneity of mode waters in comparison with surrounding higher stratification produces a maximum inventory [Speer, 2013]. The term "mode water" now is nearly ubiquitous for describing any thick, broadly distributed, near-surface layer. Figure 1.15 shows a broad distribution of mode waters in all ocean basins. Generally speaking, subtropical mode waters can be divided into three varieties in terms of formation zones and thermodynamic characteristics: the one that has a western-boundary origin of formation (red), the one linked to the downstream transport and subduction along the poleward boundary of the subtropical gyre (brown), and a third variety that appears in the eastern extremity of gyres, which is sometimes influenced by inter-basin exchanges of water masses (pink). These different types of mode waters will be discussed in details in Chapter 3 where an algorithm is developed to detect their presence from profiling datasets.

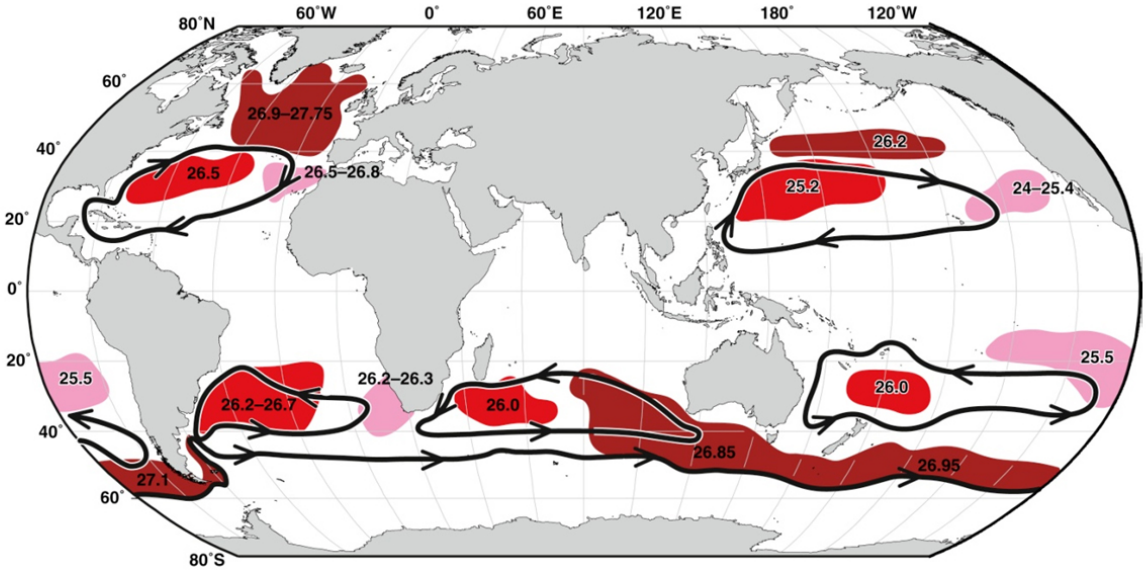

Figure 1.15: A schematic of mode waters: brown—Subantarctic and Subpolar Mode Waters; red—Subtropical Mode Waters; pink—Eastern Subtropical Mode Waters. (Source: [Hanawa, 2001]).

Mode water studies are therefore useful in terms of different aspects. First, mode water reflects temporal variations of oceanic and climatic conditions. Variations in mode water properties, distribution and circulation manifest variations in wintertime air–sea interaction (surface cooling) in the formation area, oceanic heat transport to the formation area, eddy activity in the formation area and spin-up/spin-down of the gyre. Second, mode water simulation is a good target for numerical models. In order to model mode waters and their variations accurately, various processes must be correctly simulated, including: plausible separation of western boundary currents and their extensions, frontal systems, mixed-layer processes given proper surface forcing, eddy activity in the formation area, advection and subduction processes, and isopycnal/diapycnal mixing. Third, mode water in the sense of its potential vorticity signal is a good tracer of subtropical ventilation, as useful as chemical tracers. This could be particularly useful in the case of the eastern subtropical mode waters and the SAMW, which are subducted in the eastern parts of the gyres. The Chapters 2 and 3 of this thesis thus focus on all the points listed above.

2 Mesoscale: role of eddies in ocean circulation

Scaling down from the large-scale ocean circulation and ventilation (though some processes extend across scales and are resulted in part due to nonlinear interactions among scales), the mesoscale receives much attention in the next. Ocean mesoscale features are the "weather" of the ocean, with typical horizontal lengths of less than 100 km and time scales on the order of a month. A large amount of energy in the mesoscale field is contained by coherent vortices, known as mesoscale eddies. They are characterized by temperature and salinity anomalies with associated flow anomalies that are nearly geostrophic. Although only the surface expression of mesoscale eddies is visible in satellite images of sea surface height or temperature, they are in fact three dimensional structures that reach down into the thermocline. In this section, a brief introduction is provided considering the difference between perspectives from theories and observations.

2.1 Mesoscale eddies: theoretical perspective

In theory, a vortex, or eddy, is often defined as a closed circulation that is relatively persistent (i.e., the turnaround time of a fluid parcel embedded in the structure is much shorter than the time during which the structure remains identifiable). A cyclone is a vortex in which the rotary motion is in the same sense as the Earth's rotation, counterclockwise in the Northern Hemisphere and clockwise in the Southern Hemisphere. An anticyclone rotates the other way, clockwise in the Northern Hemisphere and counterclockwise in the Southern Hemisphere.

In cylindrical coordinates, the balance of forces of a steady circular motion can be expressed as

$$-\frac{v^2}{r} - fv = -\frac{1}{\rho_0}\frac{\partial p}{\partial r}, \tag{1.14}$$

where v is the orbital velocity (positive as counterclockwise), r is the radial direction (measured outward) and p is the pressure. Both v and p can be dependent on the vertical coordinate (depth z or density ρ). This equation, named as the gradient wind balance, represents an equilibrium between three forces, the centrifugal force, the Coriolis force and the pressure force. Although the centrifugal force is always directed outward, the Coriolis and pressure forces can be directed either inward or outward, depending on the direction of the orbital flow and on the center pressure.

Following a scaling analysis, these three terms of Eqn 1.14 are respectively $\frac{U^2}{L}$, fU, and $\frac{\Delta P}{\rho_0 L}$. At low Rossby numbers ($R_o = U/fL \ll 1$), where the first term is negligible relative to the second, the balance is nearly geostrophic, providing

$$fU = \frac{\Delta P}{\rho_0 L}, \tag{1.15}$$

and thus $U = \Delta P/(\rho_0 f L)$. Since the pressure difference is most likely the result of a density anomaly $\Delta\rho$, the hydrostatic balance provides $\Delta P = \Delta\rho g H = \rho_0 g' H$, where H is the appropriate height scale (thickness of vortex), and $g' = g\Delta\rho/\rho_0$ is the reduced gravity.

This leads to $U = g'H/fL$ and

$$R_o = \frac{U}{fL} = \frac{g'H}{f^2L^2} = (\frac{R_d}{L})^2, \tag{1.16}$$

in which the deformation radius is $R_d = \sqrt{g'H)}/f$. Thus, a small Rossby number occurs as a consequence of a horizontal scale larger than the deformation radius. This is typically the case in large-scale oceanic gyres as shown in top panels of Figure 1.16 and many discussions associated with the previous section on the large scale. This small R_o implies that the vorticity in large gyres is mostly constrained by vertical stretching rather than relative vorticity. Accordingly, the energy of such gyres is dominated by available potential energy rather than kinetic energy.

At scales on the order of the deformation radius, L can be equal to R_d, the Rossby number is on the order of unity, the velocity scale is $U = \sqrt{g'H}$, and the centrifugal force is comparable with the Coriolis force. Around a low pressure, the outward centrifugal force partially balances the inward pressure force, leaving the Coriolis force to bridge the difference. By contrast, the Coriolis force acting on the flow around a high pressure must balance both the outward pressure force and the outward centrifugal force (middle panels of Figure 1.16). Consequently, the orbital velocity in an anticyclone is greater than that in a cyclone of identical size and equivalent pressure anomaly. In the ocean system, rings shed by the Gulf Stream fall in the category of vortices with length scale on the order of the deformation radius.

For a even shorter radius, the centrifugal force becomes increasingly important, and for $L \ll R_d$, the Coriolis force becomes negligible, so that the force balance of anticyclones does not differentiate from the cyclones. The inward force around a low pressure is balanced by the outward centrifugal force regardless of the direction of rotation (bottom panel in Figure 1.16). The scale of this vortex type will be found in the bathtub and thus does not fall into the discussion scope of this thesis.

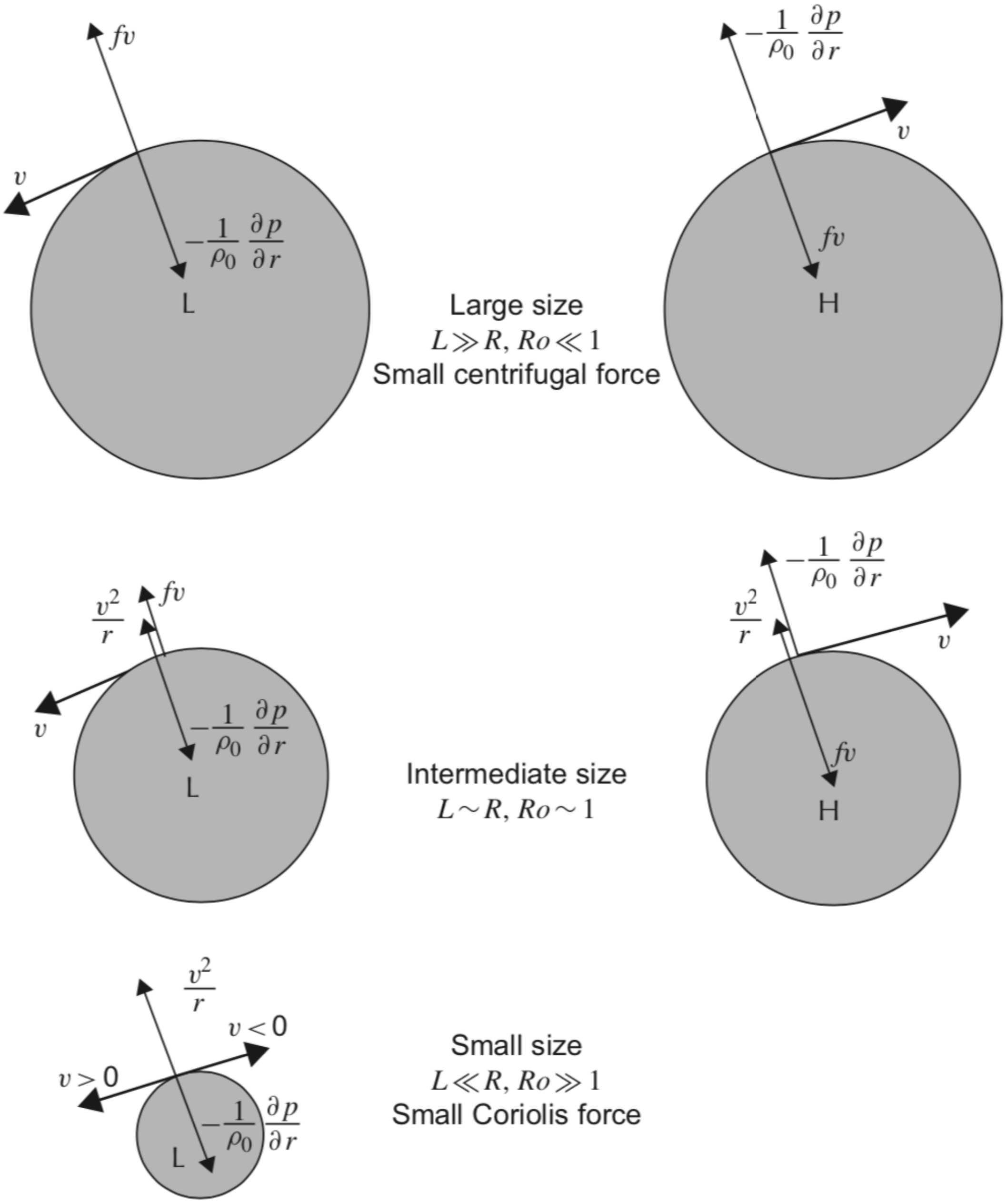

Figure 1.16: Balances between pressure gradient, Coriolis and centrifugal forces in the Northern Hemispheric circular vortices. The letters L and H indicate low and high pressures, respectively. (Source: [Cushman-Roisin, 2011a]).

Following the simple description of balanced vortex in the fluid, the theory goes further to discuss the first-order approximation of mesoscale eddies in a more complex context. As discussed, two main physical parameters that influence mesoscale variability are the Earth's rotation and vertical stratification. At the mesoscale, the Rossby number R_o is small, i.e., $R_o = U/fL \sim O(10^{-1})$, for typical velocities U of 0.1 m s^{-1} and spatial scales L of 10 km. This means that the flow obeys the geostrophic relation and the horizontal velocity, being non-divergent, can be described by a streamfunction ψ. A simplified system of equations, the quasigeostrophic (QG) equations, can be derived by further assuming a small ratio H/L, with H being the ocean depth, and a small Froude number $Fr = U/NH$, with $N = \sqrt{-\frac{g}{\rho_0}\frac{\partial \rho}{\partial z}}$ being the buoyancy frequency. The fundamental principles of mesoscale dynamics have been established using the QG framework, both in the linear (wave) regime and in the nonlinear regime.

Within these parameters above, the QG prognostic equation for the relative vorticity, $\nabla^2\psi$, is obtained by taking the curl of the horizontal momentum equations. The vertical dimension of the flow field can be described either by a superposition of layers at different densities, or by a decomposition into vertical modes structured by the stratification. In both cases, the barotropic streamfunction describes the depth-integrated transport, and the flow field is the sum of the barotropic and baroclinic modes [Vallis, 2006]. In a continuously stratified ocean, the QG potential vorticity equation can be written as

$$\begin{aligned} \frac{dq}{dt} &= G + D, \\ q &= \nabla^2\psi + f + \frac{\partial}{\partial z}(F\frac{\partial \psi}{\partial z}), \end{aligned} \tag{1.17}$$

where $\frac{d}{dt} = \frac{\partial}{\partial t} + J(\psi)$ is the total derivative and J is the Jacobian, $F = \frac{f_0^2}{N^2}$ is the stretching parameter, G represents the forcing, and D is the dissipation. Note that the variation of f with latitude, the β-effect, has to be taken into account in the mesoscale regime for a realistic representation of eddy anisotropy and westward propagation.

To see the horizontal movement of eddies, the easiest way is to consider the balance of forces (other interpretations of eddy drift include dynamics of potential vorticity etc). On the northern side of an anticyclonic eddy in the Northern Hemisphere, geostrophic velocity is smaller than on the southern side under identical Coriolis force balancing the pressure gradient (see Figure 1.17), mainly due to the β-effect. The velocity difference then yields a convergence (divergence) on the western (eastern) flank of the vortex. This in turn causes a vertical displacement of the density interface, leading the vortex volume to slide sideways with upwelling in its eastern flank and downwelling on its western flank. For the cyclone, similar reasoning yields again a westward displacement.

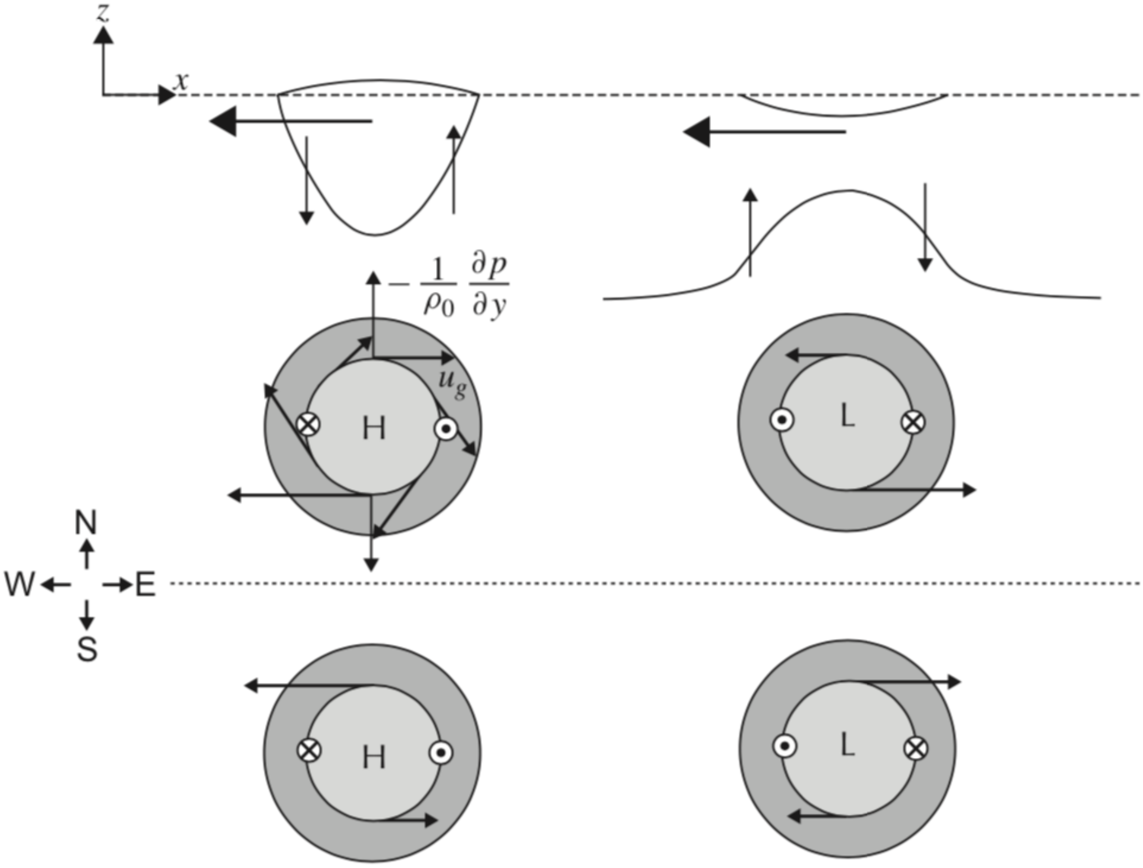

Figure 1.17: An explication of the westward drift for an anticyclone (left side) and cyclone (right side). The vertical section at top shows an anticyclone's core of lighter fluid (top-left) and the reduced layer thickness associated with a cyclone (top-right). The plots below represent top views spanning the equator (dotted line) and show the velocity fields. The convergence and divergence pattern associated with north–south velocity differences cause the vortex to move westward regardless of its sense of rotation. (Source: [Cushman-Roisin, 2011a]).

Theoretically commensurate with the westward eddy movements, the free solutions of the linear QG equations in an unbounded domain are westward-propagating Rossby waves. However, these waves are unstable that means nonlinearity should not be ignored. Numerical solutions of the QG system in its simplest form, the 2D barotropic equation, made the first successful atmospheric weather forecasts possible [Charney, 1950]. Numerical solutions of the QG equations in their baroclinic form later demonstrated the feasibility of oceanic forecasts at the mesoscale [Robinson, 1984].

The key to understanding mesoscale variability lies in the theory of baroclinic instability, which was established by Charney [Charney, 1947] and Eady [Eady, 1949], who demonstrated that a vertically sheared current can feed mesoscale disturbances. When the mean flow is baroclinically unstable, small perturbations grow by tapping into the available potential energy, which is related to the vertical shear of geostrophic currents (i.e., the thermal wind balance). Baroclinic instability is the source of synoptic disturbances in the atmosphere as well as the source of the most energetic mesoscale structures in the world ocean. Because it involves the characteristic scale of R_d, this theory explains why a large amount of energy is found at the mesoscale (at mid-latitudes, the peak in energy density at wavenumbers of order 30–50 km^{-1} has been described using satellite altimetry data). In a baroclinically unstable flow, the maximum growth rate for a linear perturbation is achieved at a scale related to R_d. With constant stratification N and ocean depth H, the first internal Rossby radius is given by $R_d = NH/\pi f$ that is the characteristic scale of the first baroclinic mode. This first Rossby radius varies from more than 200 km in the tropics to 20 km at 50 ° and just a few kilometers in the weakly stratified polar regions.

In many regions of the world ocean, the vertical shear associated with the main thermocline is the largest source of baroclinic instability and thus mesoscale energy. This explains why the first Rossby radius R_d is a relevant scale for the mesoscale flows we observe. Considering a baroclinically unstable two-layer flow, a small perturbation is visible first in the bottom layer and the wave at wavelength of R_d grows at the fastest rate and becomes dominant until it triggers a cascade towards larger scales to barotropize the two-layer system. Note that such a two-layer model is a crude representation of the vertical structure of the ocean. In the case of complex vertical shears (in the presence of a seasonal thermocline or with strong surface intensification), higher baroclinic modes might have the largest growth rate.

A horizontally sheared geostrophic current is also subject to instability; the shear instability at the mesoscale, where the β-effect is important, is called barotropic instability. Contrary to baroclinic instabilities, which feed on the available potential energy of the mean flow, barotropic instabilities grow from the mean kinetic energy. In reality, ocean current instabilities are often mixed (baroclinic and barotropic) with both the mean available potential energy and the mean kinetic energy being the main sources of eddies in different regions or at different times.

2.2 Mesoscale eddies: observational perspective

From an observational perspective, the most revealing maps of mesoscale eddy activity have been obtained by satellite altimetry [Morrow, 2012] (see Le Traon et al. [Le Traon, 2001] for a broad review of how eddies are detected from satellite images). As expected, because it results from flow instabilities, the surface eddy kinetic energy displays the same inhomogeneity as the time-mean ocean circulation. There are regions of high eddy activity near strong currents, such as the Gulf Stream, the Kuroshio, the ACC and the equatorial currents. Mesoscale motions exist in a variety of forms: meanders develop, sometimes leading to the formation of detached eddies or rings; isolated eddies coexist with zonal jets and wavelike motions. Mesoscale flows are part of a continuous spectrum of ocean turbulence, ranging from the basin scale to submesoscale filaments and internal waves.

The westward drifting of eddies is also evident, in comparison to the theoretical derivations. In the zonal direction, apart from in the ACC and separated western boundary currents, mesoscale eddies are found to propagate ubiquitously westward at speeds close to the long baroclinic Rossby wave, varying from 20 cm s^{-1} near the equator to 1 cm s^{-1} near the polar regions [Chelton, 2011]. In the meridional direction, anticyclonic eddies and cyclonic eddies tend to drift slightly equatorward and poleward, respectively, as a result of combined effects of β and nonlinear self-advection [Morrow, 2004]. These characteristics of eddy movement are particularly observed for isolated eddies [McWilliams, 1979]. Figure 1.18 displays global maps of individual eddy trajectories identified by an eddy detection algorithm TOEddies [Laxenaire, 2018], which shows that anticyclonic eddies tend to propagate westward and equatorward, whereas cyclonic eddies are prone to propagate westward and poleward.

Figure 1.19 instead shows a visualization of several eddy paths from a computer engineering perspective. Such eddy paths were detected from a numerical simulation of the northwest Atlantic Ocean off the coast generated by the Regional Ocean Modeling System (ROMS), and their techniques allow a dataset to be summarized into a single concise view but also enable structural understanding of the eddies and their dynamics. This figure is included here to intuitively present that eddy structures are even more complicated in the real ocean. The current techniques in terms of eddy tracking are all based on sea surface data visible from the satellite, however, they can subduct into the ocean interior along their paths which imprint little or none signatures on the sea surface. A more precise method to detect subsurface eddies is developed upon the calculation of potential vorticity anomaly from high-resolution hydrographic data [Meunier, 2021].

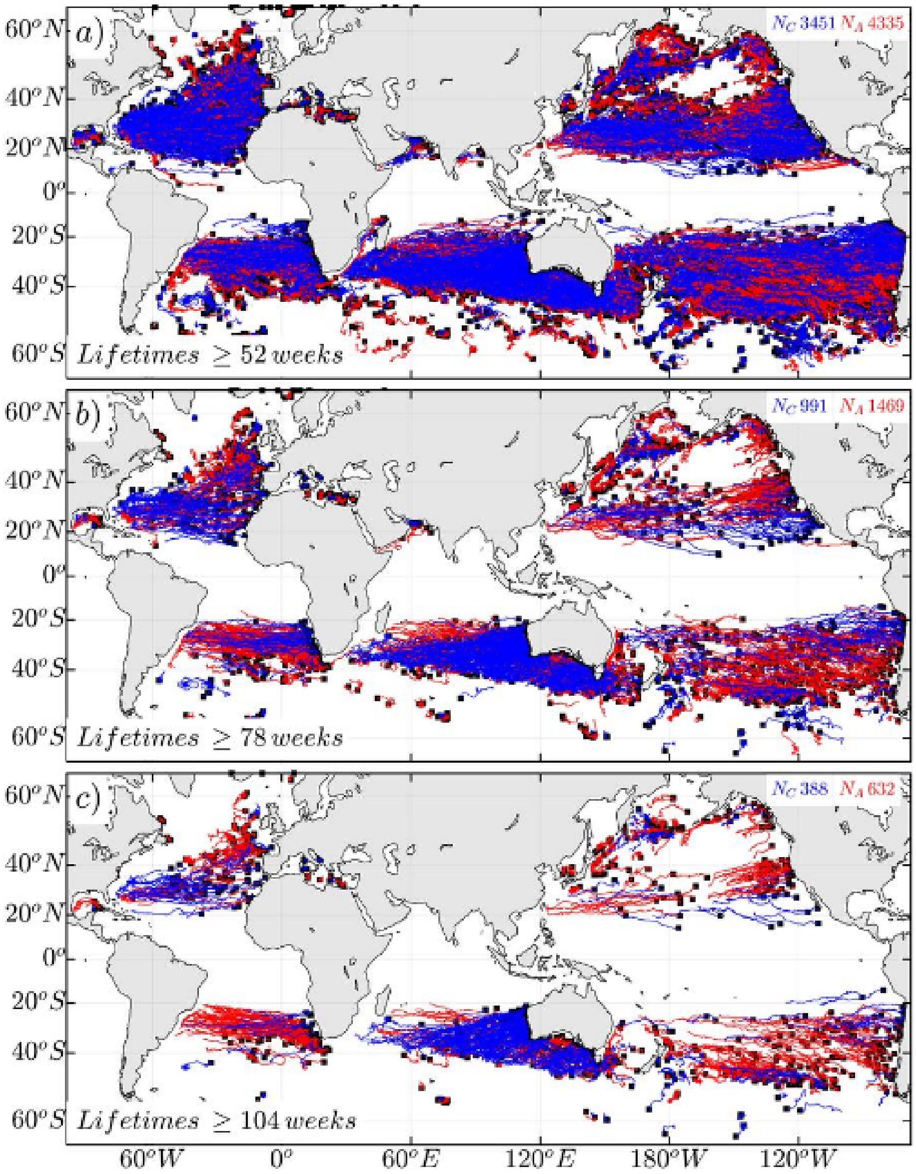

Figure 1.18: Trajectories of cyclonic (blue lines) and anticyclonic (red lines) eddies detected from TOEddies algorithm over a 24-year period (1993-2017), having a lifetime longer than (a) 52 weeks, (b) 78 weeks and (c) 104 weeks. The numbers of detected eddies are labeled at the top of each panel for each eddy polarity. (Source: Ioannou et al. (In prep)).

Animation: mesoscale eddy trajectories at the Agulhas Leakage

Also available by clicking here.

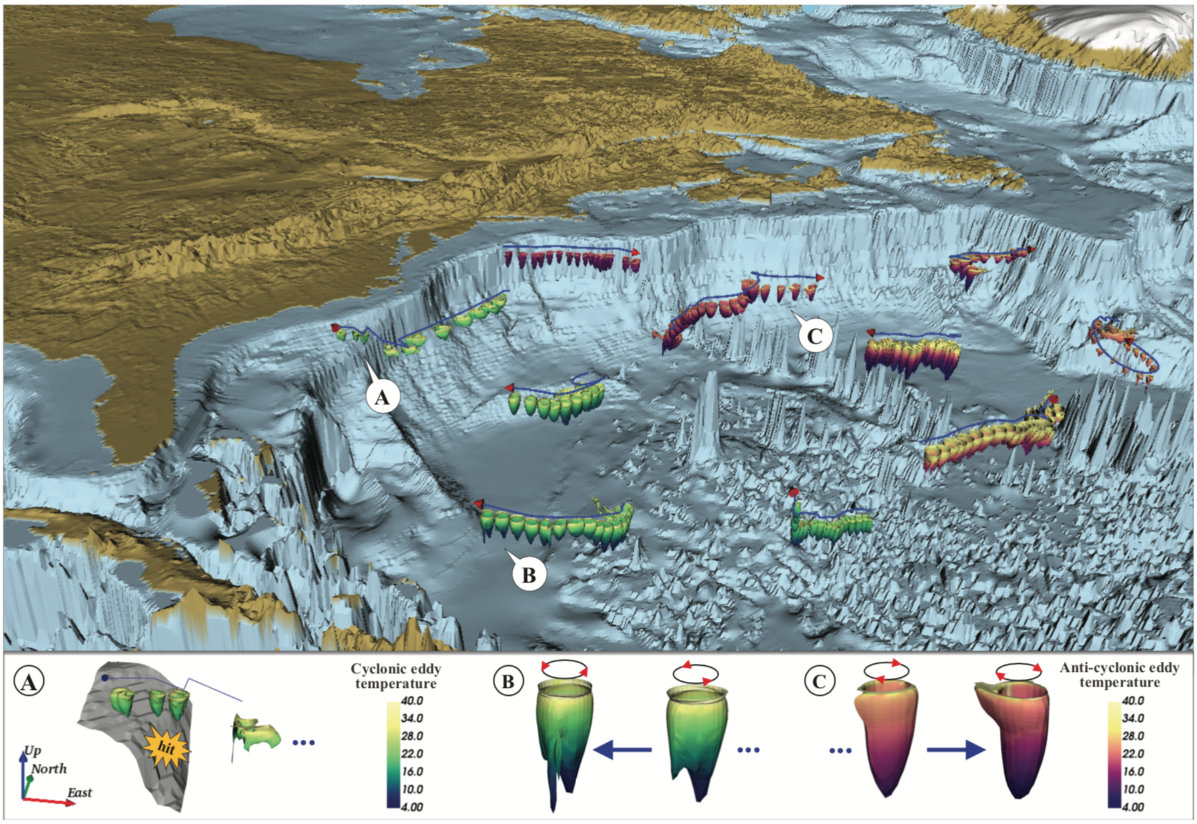

Figure 1.19: Three-dimensional eddy paths that last at least fifty days in 2006 and 2007 at the Gulf Stream Extension. The physical and kinematic changes in an eddy over its life cycle are illustrated by the depiction of its three-dimensional color-coded isosurface in successive time steps. Directional lines above each eddy path highlight eddy motion. Colors convey variations in ocean temperature. Three typical scenarios are observed from the map: (A) An eddy propagates onto the shelf, then bumps it before splitting. (B) A cyclonic eddy propagates to the west. (C) An anticyclonic eddy propagates to the east. (Source: [Liu, 2017]).

3 Submesoscale and nonlinear effects in ventilation

Previous arguments for the large scale and mesoscale show that the ocean's surface mixed layer is a vital component of the climate system, as it mediates the exchanges of physical and biogeochemical tracers between the atmosphere and the ocean interior. The spatial and temporal variability of the mixed layer thickness is also important in determining the water mass formation at the surface, subduction at the base of the mixed layer, and further the vertical structure of oceanic properties.

Apart from the large scale and mesoscale, submesoscale processes nowadays receive much attention in controlling the evolution of the mixed layer and its connection with the interior ocean. In the context of tracer analysis, submesoscale features can flux PV through the mixed layer, enhance communication between the thermocline and surface, and thus play a crucial role in changing the upper-ocean stratification and mixed-layer structure. Specifically in the presence of lateral buoyancy gradients, upper-ocean submesoscale processes arise and always play a counter-intuitive role in the ventilation processes. For example, these include the development of narrow elongated regions through frontogenesis (i.e.,the intensification of horizontal tracer gradients by a strain field), intense vertical velocities with a downward bias at these sites, and secondary circulations that redistribute buoyancy to stratify the mixed layer.

Therefore, these processes at the submesoscale often lead to localized phenomena, e.g., eddy-driven subduction of particulate organic carbon [Omand, 2015], upwelling of chlorophyll at the light side of the front [Zhang, 2019], and anomalous upward heat transport at ocean fronts [Siegelman, 2020; Su, 2020]. In terms of scaling, submesoscale flows are ubiquitous within the mixed layer throughout the global ocean [McWilliams, 2016]. They are manifested at horizontal scales of 0.1–10 km and time scales of several hours to several days, and are dynamically associated with Rossby and Richardson numbers of unity [Thomas, 2008b]. Table 1.1 listed several dimensionless numbers and their typical values for the mesoscale and submesoscale in comparison and Figure 1.20 illustrates the variety of mesoscale and submesoscale features associated with the Gulf Stream.

Table 1.1: Important dimensionless numbers for ocean flows.

Dimensionless numbers	*Expressions*	*Definitions*	*Mesoscale*	*Submesoscale*
Froude Number	$Fr = \frac{U}{NH}$	$\frac{\text{inertia}}{\text{stratification}}$	< 1	~ 1
Rossby Number	$Ro = \frac{U}{fL}$	$\frac{\text{inertia}}{\text{rotation}}$	< 1	~ 1
Richardson Number	$Ri = \frac{N^2}{(\partial u/\partial z)^2}$	$\frac{\text{stratification}}{\text{velocity shear}}$	> 1	~ 1
Burger Number	$Bu = (\frac{NH}{fL})^2$	$\frac{\text{stratification}}{\text{rotation}}$	~ 1	~ 1

* The Richardson Number of the ocean is a measure of relative importance of mechanical and density effects, associated with the Kelvin-Helmholtz instability. In other words, it is a measure of turbulence.

* The Burger Number can be calculated with a combination of Froude Number and Rossby Number, and thus it is to be determined in most cases and has been used to monitor how (sub)mesoscale fields evolve over time.

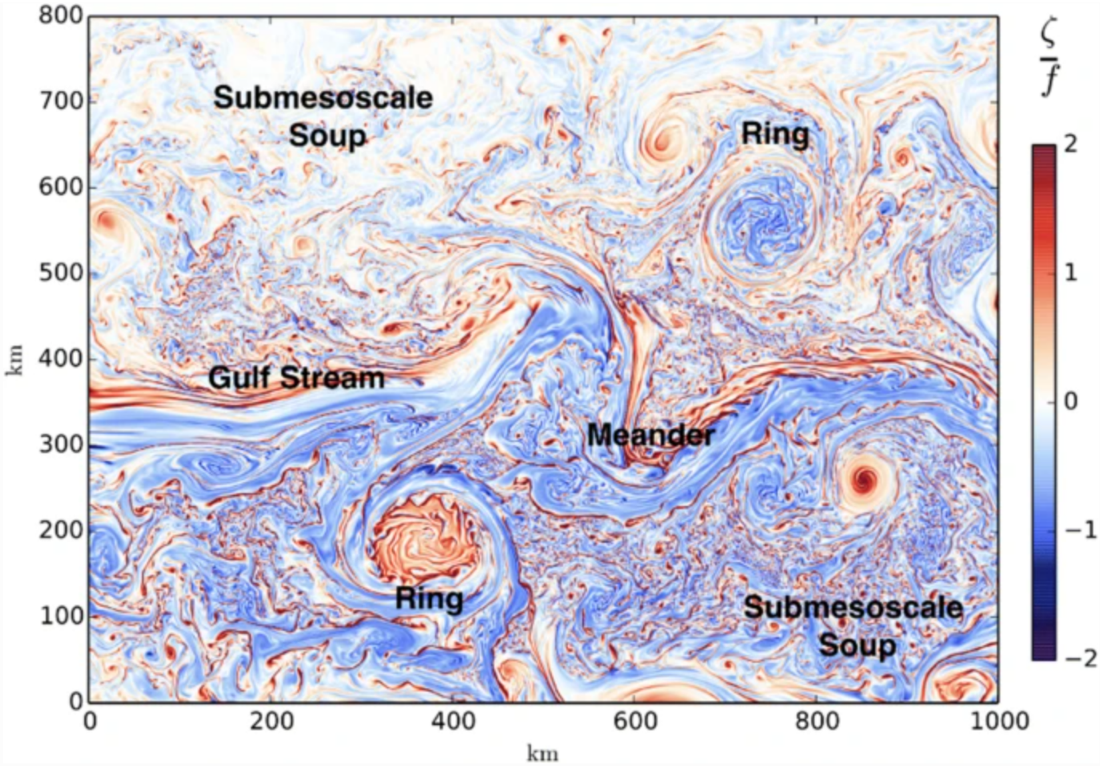

Figure 1.20: Simulated offshore Gulf Stream relative vorticity normalized by f at the surface in the wintertime Gulf Stream after separation from the western boundary in a nested-subdomain simulation. Notice the meandering Gulf Stream in the center, the northern warm anticyclonic and southern cold cyclonic mesoscale rings, and the nearly ubiquitous submesoscale features of many different types, including the typical open-sea "soup" away from strong mesoscale current. (Source: [McWilliams, 2019]).

Submesoscale processes are emerging as vital for the transport of biogeochemical properties, for generating spatial heterogeneity that is critical for biogeochemical processes and mixing, and for the transfer of energy from meso to small scales [Levy, 2013]. Several studies are in progress to measure, understand, model and parameterize these motions. This section will introduce several processes at the submesoscale that contribute counter-intuitively to the classic viewpoint of ocean ventilation. They include 1) nonlinear Ekman theory that retains the self-advection in the Ekman equation, 2) nonlinearity in the equation of state, and 3) instabilities associated with frontogenesis. Though submesoscale studies are often linked to the third topic associated with frontogenetic processes at the relevant scales, nonlinearities in the Ekman dynamics and nonlinear modifications to the equation of state are nonetheless contingent on high-frequency and ageostrophic features.

3.1 Nonlinear Ekman theory

At scales near the deformation radius and larger, near-surface ocean flow can be thought of as a superposition of geostrophic, Ekman and near-inertial components, and each of these can interact with the other two. Geostrophic modification of Ekman transport and pumping is the subject of nonlinear Ekman theory. Pioneering work by Stern [Stern, 1965] considered a uniform wind stress, $\boldsymbol{\tau}$, blowing over a geostrophic vortex and found the pumping velocity to go like $\nabla \cdot [(\boldsymbol{\tau} \times \hat{\boldsymbol{z}})/(f + \zeta)]$, where ζ is the relative vorticity associated with the vortex. Other work has focused on straight jets and has extended solutions to higher orders [Niiler, 1969], compared along- and across-stream stresses [Lee, 1994], used vorticity dynamics to examine interactions with stratification [Thomas, 2002], and examined higher-order Rossby number effects on the pumping velocity [Hart, 2000] and the vertical thickness of the Ekman layer [Pedlosky, 2008].

More recently, Wenegrat et al. [Wenegrat, 2017] revisited solutions for curvilinear flows such as vortices and meandering jets. Somewhat counter-intuitively, they pointed out that Stern's result above does not imply that the transport goes like $(\boldsymbol{\tau} \times \hat{\boldsymbol{z}})/(f + \zeta)$. Their solutions also produced complex and interesting structures that could not be expressed in terms of spatially local fields such as $\boldsymbol{\tau}$ and ζ. Instead, nonlocal effects influence the solution. (Nonlocality has also been suggested by Hart [Hart, 2000] and Pedlosky [Pedlosky, 2008].) Apart from these nonlinear Ekman effects, geostrophic currents can also impact Ekman transport more directly in that the stress itself depends on both current velocities, e.g., Duhaut et al. [Duhaut, 2006], Dawe et al. [Dawe, 2006], and Zhai et al. [Zhai, 2012] and sea surface temperature, e.g., Small et al. [Small, 2008], Chelton et al. [Chelton, 2010], O'Neill et al. [ONeill, 2012], and Grooms et al. [Grooms, 2016]. A series of studies has compared and discussed these effects in the context of eddy-wind interactions [McGillicuddy, 2007; Mahadevan, 2008; McGillicuddy, 2008; Gaube, 2015].

In our recent study [Chen, 2021], we have revisited the interaction between the geostrophic and Ekman flows (i.e., the nonlinear Ekman theory), as well as the near-inertial oscillations and Ekman dynamics. Here, the former is highlighted. Figure 1.21 shows two versions of a slab Ekman layer on top of a stand-alone balanced vortex that is to study the impact of geostrophic flow fields on Ekman solutions [Chen, 2021]. Specifically, the response of this slab Ekman layer to a uniform wind stress blowing over a horizontally non-divergent circular eddy was considered. The wind stress $\boldsymbol{\tau}$ is uniform in the x-direction, and produces a leading order southward Ekman transport of about 1.4 $\mathrm{m}^2\ \mathrm{s}^{-1}$. Results at steady state are similar to those described by Wenegrat et al. [Wenegrat, 2017] (see their Figure 3), who used a similar set-up. That is, nonlinear Ekman effects produce divergent zones on the northern and southern sides of the eddy, with the sign dependent on the vortex polarity. Two model regimes are considered. The first version of the slab-layer model, S1, is given by

$$\frac{\partial}{\partial t}\boldsymbol{U}_{Ek} + (\boldsymbol{U}_{Ek} \cdot \nabla)\boldsymbol{u}_1 + (\boldsymbol{u}_1 \cdot \nabla)\boldsymbol{U}_{Ek} + f\hat{\boldsymbol{z}} \times \boldsymbol{U}_{Ek} \quad = \quad \boldsymbol{\tau}/\rho_0 + \boldsymbol{D}_{Ek}, \qquad \text{(S1)}$$

and the second version, S2, is given by

$$\frac{\partial}{\partial t}\boldsymbol{U}_{Ek} + \frac{1}{H_{Ek}}(\boldsymbol{U}_{Ek}\cdot\nabla)\boldsymbol{U}_{Ek} + (\boldsymbol{U}_s\cdot\nabla)\boldsymbol{u}_1 + (\boldsymbol{u}_1\cdot\nabla)\boldsymbol{U}_{Ek} + f\hat{\boldsymbol{z}}\times\boldsymbol{U}_{Ek} \quad = \quad \boldsymbol{\tau}/\rho_0 + \boldsymbol{D}_{Ek}. \qquad \text{(S2)}$$

Here, $\boldsymbol{U}_{Ek}$ is the Ekman transport while $\boldsymbol{u}_1$ is the velocity of geostrophic vortex. $\boldsymbol{D}_{Ek}$ is a dissipation term and H_{Ek} is the thickness of the slab Ekman layer.

The S1 and S2 models produce similar results in the long time limit. They both also produce fast timescale transients, which are robust, long-lived and different between the two models. The transients are evident even in simulations for which the forcing is ramped up over several inertial periods. In the S1 simulations, the transients appear as clockwise whirling rings confined to the eddy, whereas in the S2 simulations these rings are pushed away by the leading order southward Ekman drift. Animations of these simulations also show other differences between cyclones and anticyclones. For example, in the cyclones, phase propagation is outward near the center and inward on the periphery, whereas these signs are reversed in anticyclones.

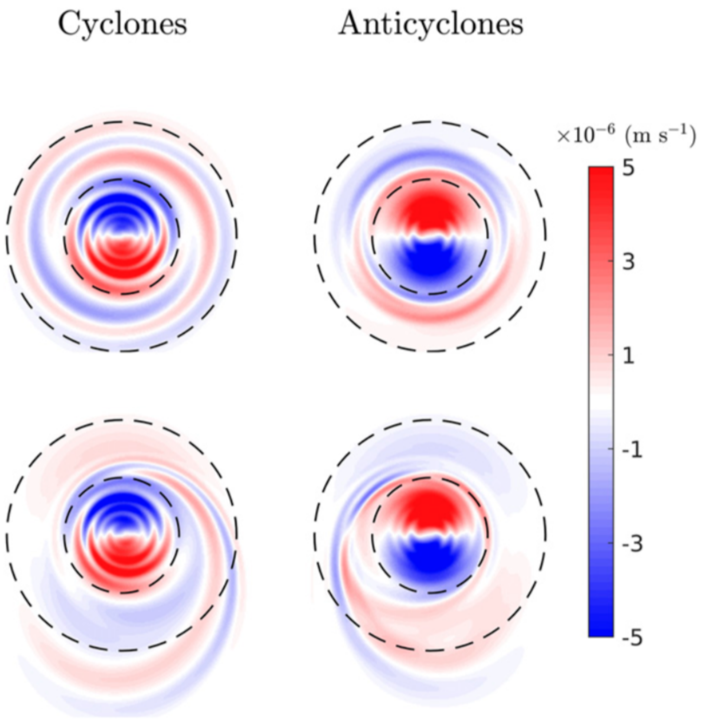

Figure 1.21: Pumping velocities in slab models with prescribed circular vortices forced by steady wind stress for (top row) the S1 model and (bottom row) the S2 model. The vortices are described by a Gaussian streamfunction with an 80 km decay scale. Shown is a subdomain centered on the vortices with dashed lines corresponding to circles with radii of 100 and 200 km.

Animation: different regimes of nonlinear Ekman layer (scroll down)

Also available by clicking here.

This nonlinearity of the Ekman dynamics is of particular importance for the calculation of water mass subduction, since Ekman pumping dominates the large-scale spatial pattern of subduction over the temporal evolution of the mixed layer depth and lateral induction (i.e., the advection of water masses at a neighboring column). Allowing for the background geostrophic flows to modify the Ekman dynamics might produce spatial variations similar to the lateral induction. This work has also been extended to a two-layer shallow water regime as the background field that can interact with the nonlinear slab Ekman layer.

Our publication: Interaction of Nonlinear Ekman Pumping, Near-Inertial Oscillations, and Geostrophic Turbulence in an Idealized Coupled Model

Also available by clicking here.

3.2 Nonlinearity in the equation of state

As introduced, mode waters are distinguished from other water masses by their defining characteristic—weak stratification and anomalously low potential vorticity. Mode water formation requires a convergent diapycnal mass flux that can fill isopycnal layers and reduce the stratification. The mechanism that selects the density class where a diapycnal mass flux converges and mode water forms is not well understood. The classical explanation involves air–sea fluxes, as shown in the discussions on water mass formation and winter mixed layer development [Speer, 1992]. In this paradigm, mode waters form on isopycnal layers that outcrop in regions where the net buoyancy loss to the atmosphere decreases with increasing density. Fronts and their associated currents play a role in this process by shaping the outcrop locations and by bringing relatively warm waters in contact with cold air during the winter. The entire process greatly relies on the geometry of the isopycnal outcrop areas that are determined by the distribution of mode waters themselves, because their weak stratification preconditions for the convective mixing that lifts isopycnals to the surface. Thus, this classic formation mechanism has a causality dilemma [Thomas, 2015]: air–sea fluxes generate mode water where outcrop areas are expansive because of the underlying pool of mode water they renew.

Several studies have extended the classic picture of mode water formation by taking into account the nonlinearity in the equation of state which is highly correlated with frontal motions. In specific, they are the thermobaric and cabbeling effects. Thermobaricity is the process in which the mixing of two water parcels with different temperature and pressure, but equal density, results in a water parcel which is either lighter or denser than the two original water parcels. Cabbeling is the process in which the mixing of two water parcels with different temperature and salinity, but equal density, results in a water parcel denser than the two original water parcels. Hence, both these processes can occur when mesoscale or submesoscale processes mix temperature and salinity along isopycnal surfaces [Groeskamp, 2019]. Figure 1.22 shows two temperature-salinity diagrams that display the process of cabbeling. Due to the curvature of each isopycnal, two water masses on the same isopycnal but with distance in their spiciness field can mix and result in a water mass with higher density.

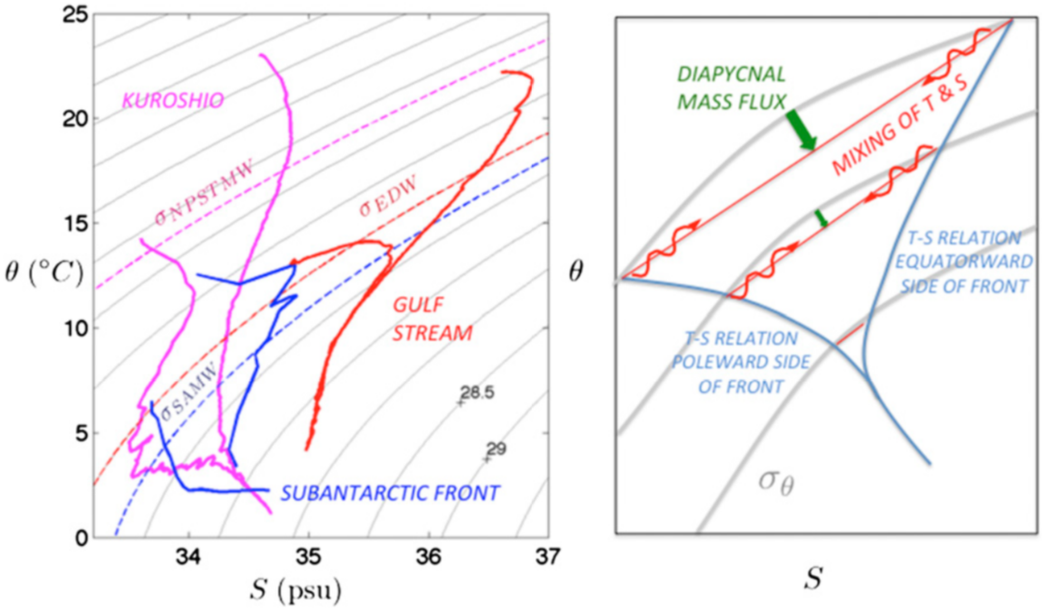

Figure 1.22: (left) θ–S diagrams from CTD casts straddling the Kuroshio (magenta), Gulf Stream (red), and Subantarctic (blue) Fronts. The isopycnal layers where the North Pacific Subtropical Mode Water σ_{NPSTMW} (dashed magenta), Eighteen Degree Water σ_{EDW} (dashed red), and Subantarctic Mode Water σ_{SAMW} (dashed blue) reside are indicated. Around these layers, the temperature and salinity contrast across the fronts decreases with density. As schematized to the right, mixing of these water masses and cabbeling would result in a convergent diapycnal mass flux that would increase the volume of mode water. (Source: [Thomas, 2015]).

In specific, cabbeling has been invoked to explain the formation of intermediate waters in the North Pacific [Talley, 2001] and deep and bottom waters in the Southern Ocean [Klocker, 2010]. Recent mesoscale-resolving simulations of the Southern Ocean suggest that the process could contribute significantly to the transformation of surface water masses throughout the water column into SAMW [Urakawa, 2012]. It has been shown that frontogenesis is essential in facilitating cabbeling at fronts [Thomas, 2015]. Figure 1.23 illustrates that cabbeling is especially important for the formation of Antarctic Intermediate Water (AAIW)and Lower Circumpolar Deep Water (LCDW), while the thermobaric effects lead to spatial variations of formation and destruction for these two water masses.

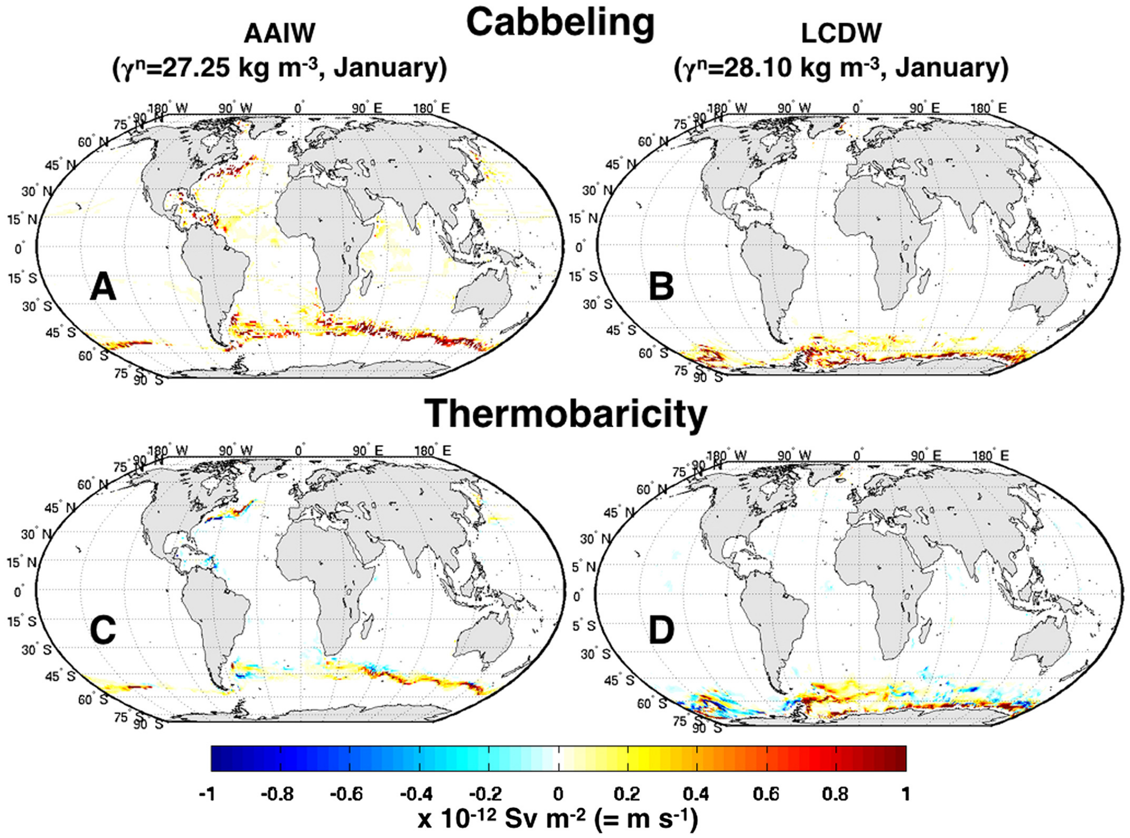

Figure 1.23: Geographical distribution of water mass transformation in January by (top) cabbeling (top) and (bottom) thermobaricity, for (left column) AAIW and (right) LCDW. (Source: [Groeskamp, 2016]).

3.3 Frontogenesis and ventilation at ocean fronts

Several studies have shown that frontogenesis plays an important role in water mass transformation and subduction at the submesoscale. To briefly describe oceanic frontogensis, it is mainly related to a constant or enhanced geostrophic strain that can drive ageostrophic motions. For example, as sketched in Figure 1.24, the most effective way for a strain to strengthen a geostrophic front and stimulate ageostrophic perturbations is to stretch in the along-front direction and compress in the cross-front direction. During this process, the background strain field continuously enhances the cross-front density/buoyancy gradient. As the cross-front density gradient strengthens and the cross-front scale shrinks, frontal instabilities develop through the release of the available potential energy of the front. The frontal instabilities generate an ageostrophic secondary circulation that has an upwelling/downwelling along the light/dense side of the front and a cross-front surface ageostrophic velocity from light side to dense side. This cross-front secondary circulation is well documented by frontal instability theories [Fox-Kemper, 2008], diagnostic vertical velocity estimations [Klein, 2009], and high-resolution numerical simulations [Freilich, 2021].

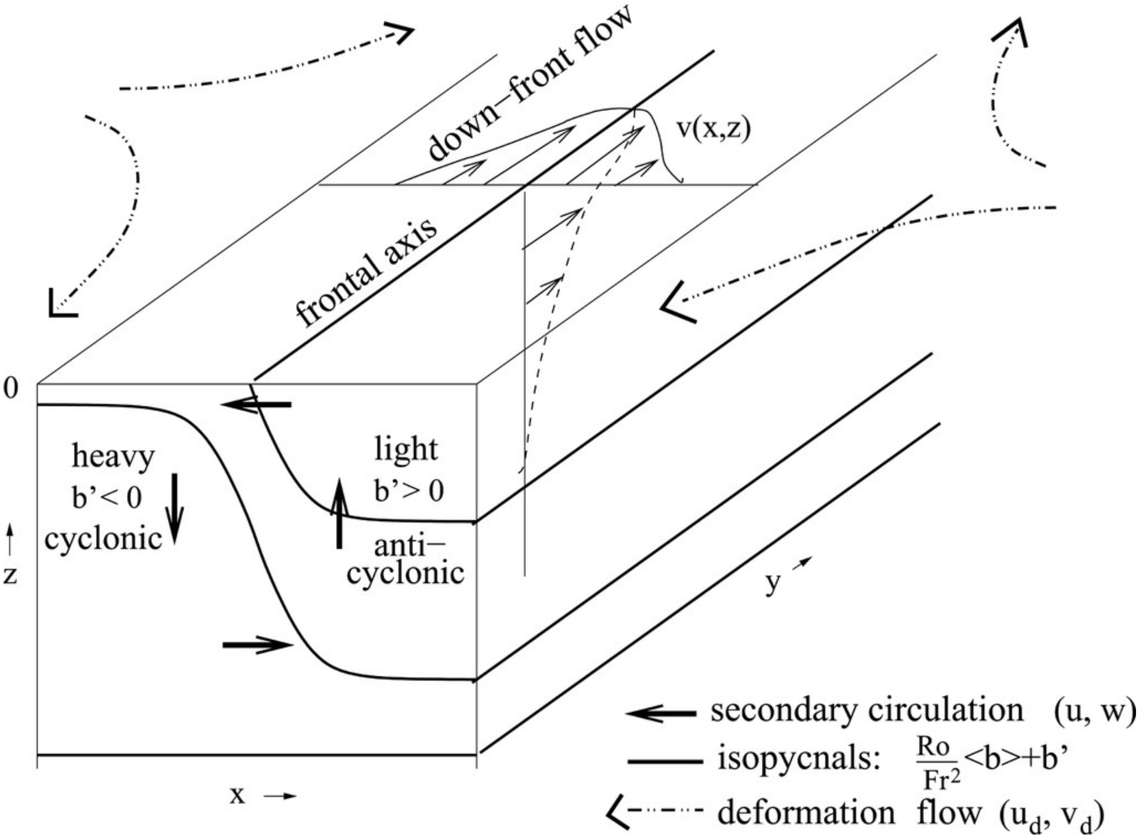

Figure 1.24: Strain-induced frontal processes. A mesoscale front exists along the y-direction with light (dense) water present in positive (negative) x-direction. Due to the background geostrophic strain field stretching along the front and compressing across the front, the cross-front density gradient is enhanced by the strain field. As the cross-front density gradient enhances, frontal instabilities develop causing release of available potential energy of the front and restratification. The resulting net effect sustains a cross-front ageostrophic secondary circulation in the x–z plane. The secondary circulation causes upwelling/downwelling along the light/dense side of the front. (Source: [McWilliams, 2016]).

In addition, QG theory also predicts that subduction occurs due to geostrophic frontogenesis, which generates ageostrophic horizontal and vertical velocities. In terms of the ventilation theory, as low PV water from the surface mixed layer crosses the front, it subducts along an isopycnal surface while conserving PV. Here, the development of an intrapycnocline eddy is shown as an example to illustrate the combination between frontogenesis and subduction. If the mixed layer is thicker than isopycnal layers in the thermocline, the subducted water mass from the surface becomes an anticyclonic intrapycnocline eddy as it is compressed during subduction. The length scale of the intrapycnocline eddy is expected to be the internal deformation radius at the submesoscale [Freilich, 2021].

An intrapycnocline eddy can be identified in a cross section as a low PV anomaly, which in Figure 1.25 (f) is shown bounded by the orange triangles and has a radius slightly smaller than the deformation radius. The formation of a low PV intrapycnocline eddy on the $\sigma = 27.8$ isopycnal surface is highlighted in the brown box in Figure 1.25 (b). The water parcels that become this intrapycnocline eddy are subducted from a region of large cyclonic vorticity (Figure 1.25 (a) and (b): orange box) due to frontogenesis. The water parcels subduct on a dense (cyclonic) filament that outcrops at the center of the front. The intrapycnocline eddy that forms during subduction moves toward the dense side of the front and is elongated as it subducts into a region where the vertical branch of the ageostrophic circulation is frontolytic. The water parcels, which initially have large values of cyclonic vorticity, develop weakly anticyclonic vorticity within one day (vorticity is in colors on the water parcels in Figure 1.25 (b)). The intrapycnocline eddy has a cyclonic surface expression (Figure 1.25 (a)).

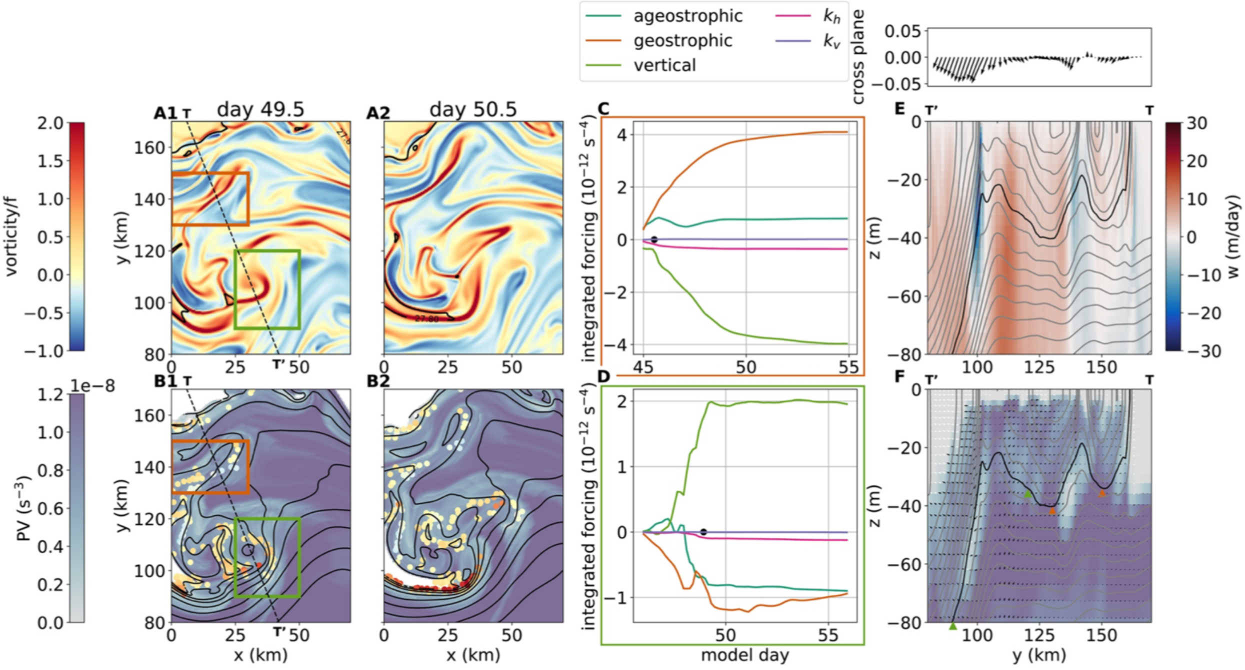

Figure 1.25: Two specific pathways for subduction from the mixed layer form an intrapycnocline eddy (orange box) and cut-off cyclone (green box). The cut-off cyclone is not discussed in the thesis and could refer to [Freilich, 2021] for more details. (a) Surface relative vorticity normalized by the Coriolis parameter on days 49.5 (1) and 50.5 (2). (b) PV on the $\sigma = 27.8$ surface. The particles are colored with their relative vorticity. (c), (d) Contributions to frontogenesis split into geostrophic and ageostrophic components (omitting such discussion in this thesis). (c) Mean time-integrated frontogenetic forcing on the particles within the orange box in panels a and b. (d) Mean time-integrated frontogenetic forcing on the particles within the green box in panels a and b. Positive slopes are frontogenetic and negative slopes are frontolytic. (e), (f) Cross sections on day 49.5 at the black dashed line on panels a and b. Contours are isopycnals. The black contour is $\sigma = 27.8$. (e) Upper panel: Surface horizontal velocity in the along plane direction (x-axis) and cross plane direction. Lower panel: Vertical velocity in meters per day. (f) PV with velocity vectors. The low PV anomaly between the orange markers is an intrapycnocline eddy formed by subduction. The green and orange triangles show the y locations of the green and orange boxes in panels a1 and b1.

Summary and thesis objectives

This chapter of introduction briefly discusses several processes related to ocean circulation and ventilation from the large scale to the submesoscale, with an emphasis on how theories were developed in terms of the ventilated thermocline and several concepts which will be used for following chapters that are the main themes of this PhD thesis. Ventilation of the ocean is presumably the most fundamental question in ocean physics and its high correlation with air-sea interactions (i.e., wind and buoyancy fluxes across the sea surface) might make it one of the key mechanisms waiting for more investigations facing the climate community.

Though the large-scale mechanisms of ocean circulation and ventilation were already extensively studied, its mesoscale and submesoscale contribution is not yet fully discovered. Thus in the following text of this thesis, mesoscale eddies — oceanic equivalent of atmospheric storms — will be treated as the main focus of the ventilation story. However, such definition of eddies is different from chapter to chapter. For example, Chapter 2 defines the eddy component of total volume subduction as the residual of an Eulerian-mean. This definition stems from a perspective of turbulence, which is often interpreted as a nonlinearity of two or more time- or space-dependent components in multiplication that results in an extra amount of product, compared with a simple multiplication of these long-term means. Chapters 3 and 4, on the other hand, define the eddies from a sea surface perspective that takes the mesoscale eddies to be nearly geostrophic. The scientific questions that are especially of interest include:

⇒ How are water masses subducted across the base of the mixed layer and how can we make such estimate more accurate? (Chapter 2)

In this chapter, we revisit the physical basis of subduction at the base of the mixed layer, from a simple perspective of continuity to a switch of coordinate to moving isopycnals. Each component contributing to subduction will be evaluated and compared, i.e., the lateral induction from neighboring columns of water that was considered as a main contributor to subduction in the Southern Ocean; the temporal variation of mixed layer depth which was omitted in the theory of Stommel's demon; and the vertical pumping velocity that was assumed to follow Ekman dynamics. These three components constitute the classic subduction theory of Cushman-Roisin [Cushman-Roisin, 1987]. Following Marshall [Marshall, 1997], we further consider the horizontal migration of isopycnals and the modification of outcropping areas from season to season. Different from Marshall's suggestions for 1) using a so-called bolus velocity to evaluate the eddy component of subduction and 2) following a Lagrangian framework, our method is based on an Eularian perspective while the quantification of this eddy contribution is still available.

Summary and thesis objectives

⇒ How is it possible to precisely detect mode waters and what is the role of mesoscale eddies in the formation, ventilation and dissipation of mode waters? (Chapter 3)

Following the discussions on subduction that termed as a process associated with a "permanent" transfer of fluid from the sea surface to the main thermocline, mode waters appear as an important phenomenon that commonly reside between the seasonal and main thermoclines. Accordingly, mode waters are usually interpreted as a memory of previous atmospheric forcing and can potentially modify the stratification of the ocean interior once subducted. In Chapter 3, we have first developed an algorithm to detect the surface mixed layer depth and mode water beneath. This algorithm was built up from an idea of calculus that the turning points of gradients are marked by second derivatives. By applying such idea to the global Argo profiling array, we are able to evaluate upper-ocean water masses of about 2 decades. With the newly-developed TOEddies algorithm [Laxenaire, 2019] that identifies mesoscale eddies and their merging/splitting events from satellite absolute dynamic topography, it further allows us to quantify the correlation between mode waters and mesoscale eddies. In specific, we will quantify the mode-water heat content anomalies that are transported by mesoscale eddies. Contrary to the theory of Stommel's demon, which is by definition the mode waters themselves, we find that they are able of being subducted and this subduction is highly associated with anticyclonic eddies.

⇒ Where do mode waters form in the South Atlantic subtropics in specific and how are they transported by mesoscale eddies? (Chapter 4)

The last chapter of South Atlantic Subtropical Mode Water is actually the first piece of work for this PhD study, with an aim to validate the algorithm of MLD and mode water detection in the South Atlantic specifically. Similar to Chapter 3, the scientific question here is also associated with the relationship between mode waters and mesoscale eddies. A cluster analysis was applied to separate all mode waters in the South Atlantic basin into 3 varieties. Such separation was performed owing to an intention of tracking the origins of mode waters in the South Atlantic. For example, different from the well-known Eighteen Degree Water in the North Atlantic, mode waters in the South Atlantic not only contain this typical type of formation at the western boundary, but also include a large amount of impact through the interbasin water exchange with the Indian Ocean. Another profile-only eddy detection method will also be discussed, which is based on the calculation of water property anomalies compared with the environment (i.e., the steric height anomaly).

Chapter 2

Subduction of surface water masses

Objectives

This chapter digs into the questions related to water mass subduction at the base of the mixed layer. Such process is crucial since it determines the relatively long memory of the ocean interior in response to surface mechanical and buoyancy forcing. This chapter follows a structure from the derivation of classic perspective to a more contemporary picture. The simplest way to think of a water parcel flowing out/into the mixed layer is based on continuity. Starting from there, this chapter then makes a revisit to the theory of Stommel's demon, which connects the long-term permanent subduction to winter-only processes. A special extension of theories in this chapter is related to the seasonal migration of isopycnals (together with the shrinking and enlargement of outcropping areas) and how it influences the mean and eddy-induced subduction rates.

Contents

1 Introduction

Ocean subduction has long been considered as the transfer of fluid from the surface mixed layer into the stratified permanent thermocline (Figure 2.1). Such name of “water subduction” makes an oceanic analogy to a geological concept that indicates a rigid plate of the Earth’s lithosphere sliding beneath a more buoyant plate and into the warmer part of the mantle. Similarly, water masses formed at the sea surface acquire their properties through the exchanges of gases, heat and moisture with the atmosphere. When the water masses are transferred beneath the mixed layer, they are shielded from the atmosphere and subsequently modify their properties only by mixing in the ocean interior, with the largest proportion of mixing being isopycnic (a recent review on isopycnal mixing is given in Abernathey et al. [Abernathey, 2022]). Hence, the subduction process helps to determine the relatively long memory of the ocean interior, compared with the surface mixed layer that is varying with higher frequencies. The subducted upper-ocean water masses spread along isopycnals zonally and meridionally, transporting heat, freshwater, nutrients, and dissolved gases from the sea surface to the ocean interior [Sarmiento, 2004; Bopp, 2015].

A reverse process of subduction leads to the transfer of fluid from the main thermocline into the seasonal boundary layer, which in turn affects the properties of the mixed layer and air-sea interactions. In another interpretation, atmospheric forcing anomalies carried by the subducted water masses in the ocean interior might impact the atmosphere in remote regions where the flow returns to the surface. Within this chapter, the consideration of both downward water mass transport and the net value (i.e., the concept itself) is termed as subduction, while the pure upward transfer of fluid is defined as obduction. A similar notation is also applied to the vertical Ekman velocity, that is, pumping indicates both the concept and downwelling, while suction is used only for upwelling. In terms of horizontal scales, subduction can occur throughout the wind-driven gyres within ocean basins spanning over several thousand kilometers [Luyten, 1983; Sallée, 2010], or across frontal zones and overturning chimneys at the scales of several hundred to tens of kilometers [Spall, 1995; Thomas, 2010; Freilich, 2021].

Traditionally, Ekman pumping has been viewed to set the rate at which surface waters are transferred into the thermocline. However, although fluid is pumped down from the surface Ekman layer into the mixed layer beneath, it is the flow through the spatially and temporally varying base of the mixed layer that ventilates the thermocline, as indicated schematically in Figure 2.1. In other words, Ekman pumping only accounts for some proportion of the total amount of subduction. For example, Ekman pumping velocities cancel those of eddy-induced subduction rates in the Southern Ocean, leaving the net subduction rate determined by the difference of mixed layer depth (MLD) between two neighboring water columns (i.e., lateral advection) [Sallée, 2010].

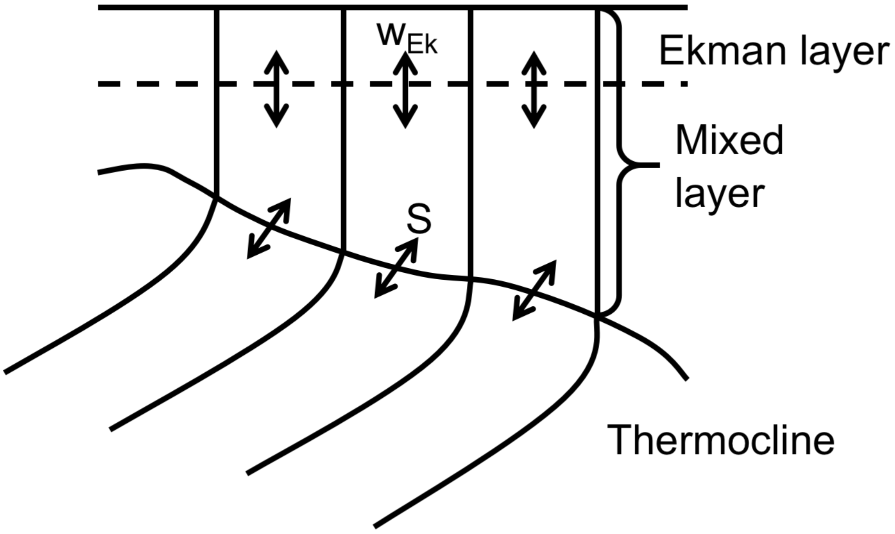

Figure 2.1: A simplified schematic showing isopycnal surfaces in the thermocline, outcropping into the mixed layer. The water masses in the mixed layer slide to and from the thermocline through the sloping base of the mixed layer. The mass flux per unit surface area through the mixed layer base is the subduction rate S that indicates the thermocline ventilation. The Ekman layer is usually thinner than the mixed layer, with the vertical pumping component w_{Ek} not enough for evaluating the total subduction.

The mixed layer is vertically homogeneous after the action of convective overturning and mixing, implying that the subduction process involves a seasonal variability associated with the seasonality of the mixed layer properties (see Figure 2.2). At the end of winter (Year 1), the mixed layer is at its maximum density and thickness and overlies the permanent thermocline, while during spring and summer (Year 2), the surface warming forms a seasonal thermocline, which is capped by a very thin wind-stirred mixed layer. During autumn and winter (Year 2), the cooling at the surface leads to a buoyancy loss and convective overturning again. The mixed layer thereby entrains fluid from the underlying thermocline until the cooling phase ceases at the end of winter. That is to say, fluid is subducted from the mixed layer into the thermocline during the warming in spring and summer, and entrained into the mixed layer from the thermocline during the cooling in autumn and winter. Whether there is annual/net subduction of fluid into the thermocline thus depends on the buoyancy input into a water column. If there is a buoyancy input over an annual cycle (as depicted in Figure 2.2), the mixed layer at the end of winter becomes lighter and thinner than at the end of the previous winter. In this case, fluid is subducted into the main or permanent thermocline over an annual cycle. Conversely, obduction may occur if a net buoyancy loss exists over an annual cycle, which results in a denser and thicker mixed layer than the previous winter.

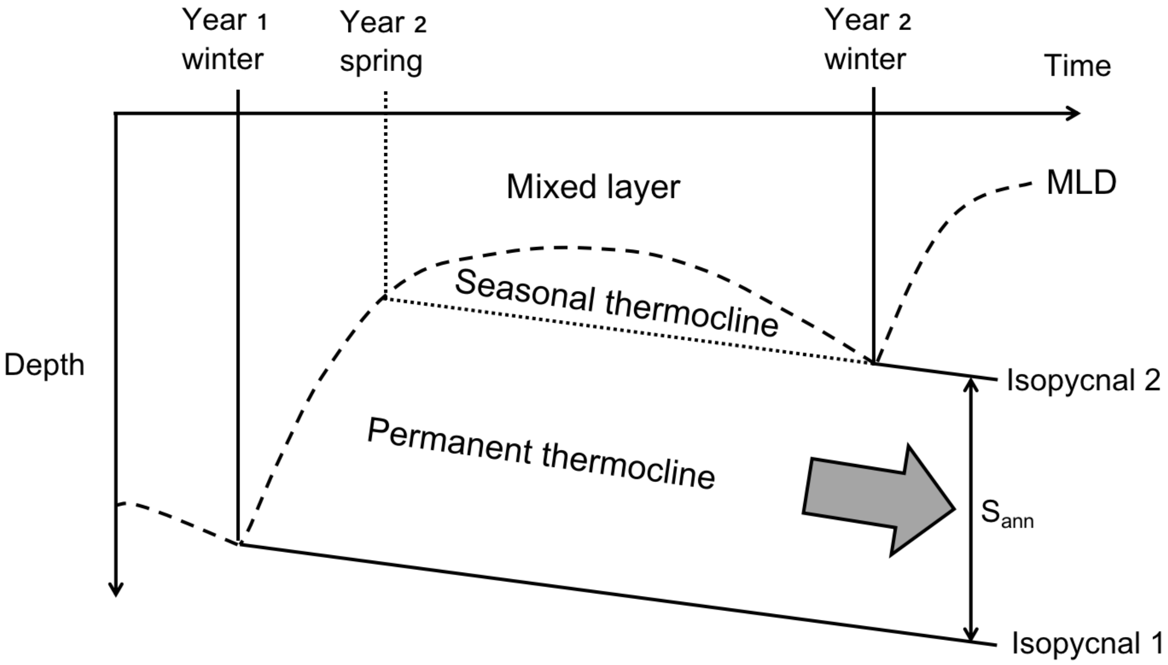

Figure 2.2: A schematic illustrating the seasonal cycle (of the Northern Hemisphere) of the mixed layer following the movement of a water column. The mixed layer thins in spring and summer, and thickens again in autumn and winter. If there is an overall buoyancy input, winter mixed layer at Year 2 becomes lighter and thinner compared with the previous Year 1. Consequently, fluid is subducted irreversibly from the mixed layer into the main or permanent thermocline. The mixed layer thickness is marked by the thick dashed line, isopycnals outcropping at the end of winter into the mixed layer by the full lines, and the isopycnal identifying the base of the seasonal thermocline by the dotted line. The annual subduction rate, S_{ann}, determines the vertical spacing between the isopycnals subducted from the mixed layer in winter for consecutive Years 1 and 2.

The properties of the main thermocline are thus controlled by the annual subduction rate S_{ann} since it is this flux that ventilates the permanent thermocline. In other words, it is only fluid leaving the mixed layer when it is deep during winter and spring that irreversibly enters the permanent thermocline; fluid subducted from the summer mixed layer is generally re-entrained when the mixed layer deepens in the following winter, which is referred to as Stommel's demon [Stommel, 1979; Williams, 1995]. Compared with a more classic perspective [Iselin, 1939], allowing for this "demon" suggests that the temperature-salinity properties of the main thermocline are adjusted according to those of the deepest mixed layers. Modeling studies that deploy Lagrangian particles in the mixed layer indeed show that subduction occurs preferentially from the late winter to early spring when the deep mixed layer shoals rapidly because of buoyancy forcing change [Woods, 1985]. However, such effects of the Stommel's demon are questioned in this chapter. There is no doubt that this theory provides a simple concept of estimating the yearly subduction of surface water masses. Mode waters, by definition, fall into the scope of Stommel's demon, however, they are observed to reside within the thermocline for more than one year and might eventually subduct into the permanent thermocline. On account of such long residence time of mode waters, the theory of Stommel's demon might underestimate the subduction rate. In addition, as shown in Figure 2.2, if such interannual variability of buoyancy forcing persists (i.e., the permanent thermocline relocates from year to year), the date at which the deepest mixed layer is found for each year is thus the critical factor of the subduction rate estimate.

The arguments above are associated with the time dependency of surface mixed layer for any specific water column, however, another component that greatly contributes to the volume of subduction is linked with the spatial difference of mixed layer depths that is sometimes defined as lateral induction (Figure 2.3 and more details in the theory section). This contribution results from the potential of water parcel at this specific column to transport into the neighboring columns. Apart from the time dependency of mixed layer depth and lateral induction, a third component in the classic perspective of water mass subduction includes the vertical velocity at the base of the mixed layer [Cushman-Roisin, 1987]. The combination between the time-varying mixed layer depth and vertical velocity at its base can be understood as the relative movement of a parcel at the base of the mixed layer. Similar to this vertical relativity, the horizontal isopycnal boundary of any moving parcel can migrate from season to season. Therefore, the calculation of lateral induction should also take into account the relativity between the speed of a parcel and the movement of its isopycnal. This consideration of isopycnal migration is the same as to track water parcels in a Lagrangian frame that resolves instantaneous outcropping area of the parcel. In the theory section, a derivation that considers isopycnal movement is provided, and it shows that such effect cancels out due to an offset between the time-dependent mixed layer depth and lateral induction. However, it is still helpful to transform from the Eulerian coordinate to the coordinate associated with migrating isopycnals so that an analysis of water masses with the same density is available.

Convincing observational and theoretical evidence proves that the mesoscale contribution to subduction is comparable with large-scale climatology [Marshall, 1997]. For example, prevalent studies of water masses at the ACC show i) a sandwich structure of ventilation (subduction of the AAIW and AABW, and obduction of Circumpolar Deep Water in between) that is at odds with the Eulerian-mean meridional circulation dominated by the wind-driven Deacon Cell; ii) an ageostrophic circulation induced by baroclinic instability that results in a subduction of the temperature minimum layer northward along its isopycnal [Garabato, 2001]; and iii) the dominance of eddy-induced subduction over the vertical mean component associated with the Pacific Antarctic Intermediate Water at the western side of the Drake Passage [Hiraike, 2016]. Meanwhile, current climate models suffer large biases in representing mesoscale subduction. In this chapter, a calculation of eddy-induced subudction rate is provided for the global ocean, incorporating an instantaneous migration of isopycnals and the varying outcropping areas of isopycnal surfaces.

Another important phenomenon associated with mesoscale subduction is mode water since they have comparable length scales from observations. As discussed, mode waters are one type of the Stommel's demon by definition, but their formation commonly results from local maxima in the ventilation processes (i.e., presumably due to winter deep convection). And the name of "mode water" was given in that they appear to be a volumetric census of the temperature and salinity characteristics of the upper ocean. These mode waters consist of large volumes of weakly stratified fluid with nearly vertically homogeneous properties. For example, strong buoyancy loss to the atmosphere over the Gulf Stream leads to the formation of 18 °C Water within the mixed layer, which is subducted following a buoyancy input along the anticyclonic circulation south of the Gulf Stream. Signals of mode water formation over the global ocean are revealed in diagnostics of water mass formation from surface buoyancy fluxes, which are shown later in the next section. Therefore, they appear as a potential state of permanent subduction that might be largely influenced by activities of mesoscale eddies.

As briefly discussed in Chapter 1, there are two commonly used approaches to estimate the rate of ventilation: 1) calculation of subduction at the base of the mixed layer that is the focus of this chapter (the kinematic approach); and 2) the concept of water mass formation [Walin, 1982] that makes a direct connection between surface buoyancy forcing and transformation rate (the thermodynamic method). The second approach has been widely used in analyzing hydrographic data to diagnose the corresponding water mass formation rate [Speer, 1992; Marshall, 1999; Nurser, 1999]. Within the thermodynamic framework, in general, the base of the mixed layer is not treated as a special interface. In this regard, the disadvantage of this approach is that a water mass formed in the near-surface layer does not necessarily enter the interior ocean below the mixed layer. For example, Brambilla et al. [Brambilla, 2008a; Brambilla, 2008b] pointed out that the core of minimum potential vorticity of SPMW in the North Atlantic is above the annual maximal mixed layer base, and thus the formation of this mode water is largely due to lateral mixing within the mixed layer (i.e, the divergence or convergence of diapycnal fluxes). This brings to mind that such mode water type might be a perfect example of Stommel's demon that does not contribute to the subduction rate. In addition to lateral mixing within the mixed layer, water masses are also formed and reshaped due to isopycnal or diapycnal mixing below the mixed layer [Speer, 1997].

Characteristic signals of subduction can also be provided by distributions of transient tracers, such as tritium and CFCs (chlorofluorocarbons), over the ocean interior [Doney, 1998; Fine, 2017]. Quantitative information on the ventilation process is provided if the transient tracers have a known source function and lifetime. The invasion of transient tracers into the main thermocline provides an integrated measure of ventilation including both contributions from the mean circulation and eddies. For example, the rate of ventilation inferred from the tracer age distribution is two to three times greater than the rate of Ekman pumping. However, the rate of ventilation inferred from influx of tracers also includes a diffusive contribution, making the exact subduction rate difficult to achieve [Hall, 2007].

In this chapter, water mass subduction is specifically regarded from the kinematic approach and in an Eulerian sense, which relies on dynamical information of mixed layer properties, including the density and depth of the mixed layer base, plus the velocity field over the mixed layer. An alternative Lagrangian perspective has been widely applied to calculate subduction [Qiu, 1995; Blanke, 2002; MacGilchrist, 2020], however, we do not make comparisons with it at the moment. The next chapter associated with mode waters and their connection to trajectories of mesoscale eddies might shed some light on such Lagrangian perspective.

2 Revisit to the physical basis

2.1 Perspective of the mixed-layer mass conservation

The classic way to calculate water mass subduction is to first look at the mass conservation of the surface layer. That is, the continuity of an impermeable ocean surface layer can be considered as

$$\frac{\mathrm{d}h}{\mathrm{d}t} + h\nabla_h \cdot \boldsymbol{u} = 0, \tag{2.1}$$

which can be reshaped as

$$\frac{\partial h}{\partial t} + \nabla_h \cdot (h\boldsymbol{u}) = 0. \tag{2.2}$$

Here, h represents the thickness of mixed layer and $\boldsymbol{u}$ denotes horizontal velocity of the mixed layer. ∇_h is the horizontal divergence. From this perspective, subduction is considered as the residual (divergent) component that leaves this surface layer, for example,

$$S = \frac{\partial h}{\partial t} + \nabla_h \cdot (h\boldsymbol{u}) \neq 0. \tag{2.3}$$

If interannual variability is ignored (i.e., the temporal term $\partial h/\partial t$ vanishes over each annual cycle), the total subduction rate is simply calculated as a time average of $\nabla_h \cdot (h\boldsymbol{u})$, leaving the subduction rate at the global scale easy to visualize.

2.2 Eulerian perspective of a water parcel at the mixed layer base

The instantaneous subduction rate S in an absolute sense has been precisely defined as the downward movement (negative values herein) of a parcel of fluid relative to the base of the mixed layer [Cushman-Roisin, 1987; Marshall, 1993] (see Figure 2.3 as the schematic),

$$S = \frac{\partial h}{\partial t} + \boldsymbol{u_b} \cdot \nabla h + w_b, \tag{2.4}$$

where $\boldsymbol{u_b}$ is the horizontal velocity of the parcel at the base of the mixed layer, and w_b is its vertical velocity. In the Eulerian sense, the mixed layer thickness h is thus a function of geographic location and time. This expression of S can thus be interpreted as the unit volume flux across the moving mixed layer base. It comprises the temporal movement of the mixed layer depth $\partial h/\partial t$, a term representing lateral induction of fluid through the sloping mixed layer $\boldsymbol{u_b} \cdot \nabla h$, and the vertical velocity w_b at the base of the mixed layer. This approach based on the instantaneous subduction rate allows us to estimate the volume of water transferred across the base of the mixed layer per unit area per unit time. A spatially integrated instantaneous subduction rate gives the volume of water that is exchanged between the mixed layer and the underlying pycnocline per unit time.

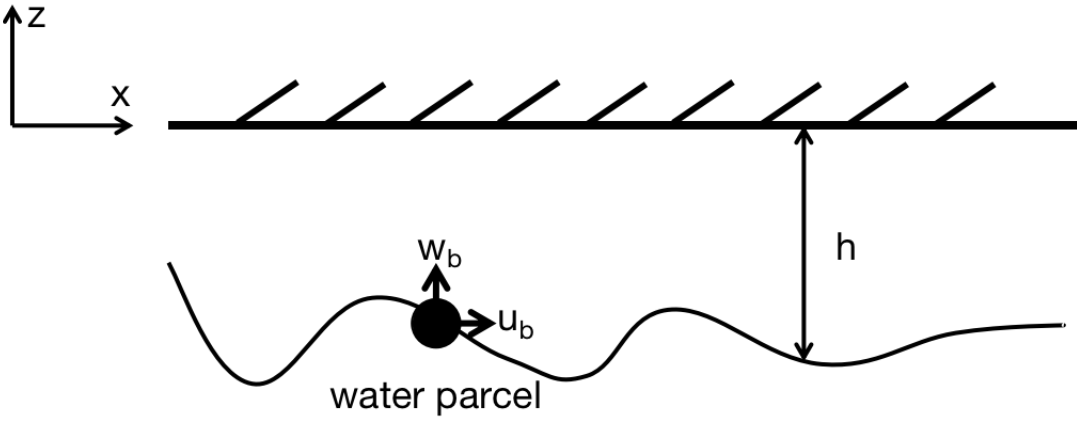

Figure 2.3: A schematic of a water parcel at the base of the mixed layer. In the classic theory, three components determine whether this water parcel is subducted downward into the thermocline or entrained into the mixed layer: 1) w_b as the parcel's vertical velocity, 2) the difference of mixed layer depth between the column of this water parcel and its neighbors (lateral induction); and 3) the shoaling or deepening of the mixed layer itself.

In reality, the seasonal cycle of warming and cooling leads to the deepest mixed layer in late winter, particularly over the subpolar gyres and the northern flank of the subtropical gyres. The instantaneous S defined as Eqn 2.4 is thus dominated by the temporal change of the mixed layer depth $\partial h/\partial t$ within such seasonal cycle. But over the course of a year, the temporal term could vanish if there is no systematic long-term change in the mixed layer properties, e.g., no interannual variability (in fact this assumption is not true according to the current warming climate). In contrast, the vertical velocity and lateral induction terms, although an order of magnitude smaller, result in a systematic transfer of fluid particles between the mixed layer and the permanent thermocline. It is this annual subduction rate across the base of the winter mixed layer that is the focus of attention in previous studies of subduction. Outside the winter season, fluid is temporarily subducted into the seasonal thermocline and is partly reentrained by the mixed layer deepening in the following winter (i.e., in a narrow sense, such temporally subducted thick layers with homogeneous properties lying between the seasonal and main thermoclines are identified as mode waters). This process of temporary subduction and reentrainment can be interpreted alternatively as the mechanism of Stommel's demon that argues only water masses leaving the deep mixed layer in winter and early spring can permanently subduct into the ocean interior.

The annual subduction S_{ann} into the permanent thermocline is thus identified as the annual volume flux across the interface of the time-invariant maximum mixed layer depth $z = -H$, assuming that the temporal term is identically zero over an annual cycle:

$$S_{ann} = \overline{\boldsymbol{u}_H} \cdot \nabla H + \overline{w_H}. \tag{2.5}$$

Here, the overbar denotes an annual average at a fixed geographic location. An integral of Eqn 2.5 over a time-invariant winter outcrop area gives the net volume exchange rate of waters across the base of the winter mixed layer. However, modeling studies that employed both approaches of Eqn 2.4 and Eqn 2.5 found substantial differences in the two estimates [Hazeleger, 2000; Costa, 2005]. A comparison is also provided here in Figures 2.9 and 2.11. Considering that the vertical velocity at the maximum MLD $z = -H$ may be related to the Ekman pumping using the linear vorticity balance, $w_H = w_{Ek} - (\beta/f)\int_{-H}^{0} v\,dz$, where f is the planetary vorticity and β is its gradient, we can accordingly decompose w_H of Eqn 2.5, and the annual subduction can be rephrased as

$$S_{ann} = \overline{\boldsymbol{u}_H} \cdot \nabla H + \overline{w_{Ek}} - \frac{\beta}{f}\int_{-H}^{0} \overline{v}\,dz. \tag{2.6}$$

Here, $\overline{v}$ denotes the meridional velocity inside the mixed layer, approximately referred to as the Ekman layer velocity. In a word, S_{ann} shown in Eqn 2.6 can be enhanced by the lateral transfer of fluid out of the winter mixed layer or Ekman pumping, and reduced by the meridional transport within the mixed layer. Note that downward transfer of fluid (subduction) is considered to be a negative value of S_{ann} resulted from Eqn 2.6.

Studies have shown that lateral advection dominates over the Ekman pumping in magnitude especially in the vicinity of western boundary currents and along the ACC. For example, Figure 8 in Sallée et al. [Sallée, 2010] compared four components (Ekman, lateral induction, β-advection and eddy-induced) that contribute to the total subduction rate along the ACC. The Ekman component and eddy-induced subduction rate compensate each other, with the total subduction rate determined by the lateral induction. Notice that the β-advection in their equation is associated with the geostrophic flow field, rather than the Ekman field. Nonetheless, it remains small compared with other contributions.

It is of interest to discuss their decomposition of the total subduction rate into these terms [Sallée, 2010], since it brings a separation between the instantaneous mixed layer and seasonal thermocline (see Figure 2.4), which are commonly treated together in the classic Cushman-Roisin [Cushman-Roisin, 1987] definition of subduction. For example, Eqn 2.3 from the continuity perspective can be rephrased as a decomposition into an instantaneous mixed layer and a seasonal thermocline,

$$S = \frac{\partial h}{\partial t} + \nabla \cdot (\int_0^{h(t)} \boldsymbol{u}\, dz) + \nabla \cdot (\int_{h(t)}^{H} \boldsymbol{u}\, dz). \tag{2.7}$$

Here, H denotes the time-invariant maximum mixed layer depth, regarded as a threshold of vertical integration (i.e., consider that the permanent subduction rate is related to the water mass leaving the maximum mixed layer depth). Now we need to think of different components of velocity (or transport) within the mixed layer and seasonal thermocline. Consider the simplest form of Ekman velocity which is purely wind-driven and still decompose the residue velocity into two components,

$$S(t) = \frac{\partial h}{\partial t} + \nabla \cdot (\boldsymbol{U}_{Ek}) + \nabla \cdot [\boldsymbol{u}_{ml}(t)h(t)] + \nabla \cdot [\boldsymbol{u}_{sth}(t)(H - h(t))]. \tag{2.8}$$

Notice that in this step the vertical shear of velocity in both the instantaneous mixed layer and seasonal thermocline has been neglected. Thus, $\boldsymbol{u}_{ml}$ and $\boldsymbol{u}_{sth}$ are the averaged velocities over the mixed layer and the seasonal thermocline respectively. Eqn 2.8 can thus be integrated or averaged over time,

$$\overline{S} = \nabla \cdot (\overline{\boldsymbol{U}_{ek}}) + \nabla \cdot (\overline{\boldsymbol{u}_{ml}}\overline{h}) + \nabla \cdot [\overline{\boldsymbol{u}_{sth}}(\overline{H - h})] + \nabla \cdot (\boldsymbol{u}^*_{ml}\overline{h}) + \nabla \cdot [\boldsymbol{u}^*_{sth}(\overline{H - h})]. \tag{2.9}$$

Here, the velocity with a superscript of star denotes an eddy-induced bolus velocity, which will be introduced shortly.

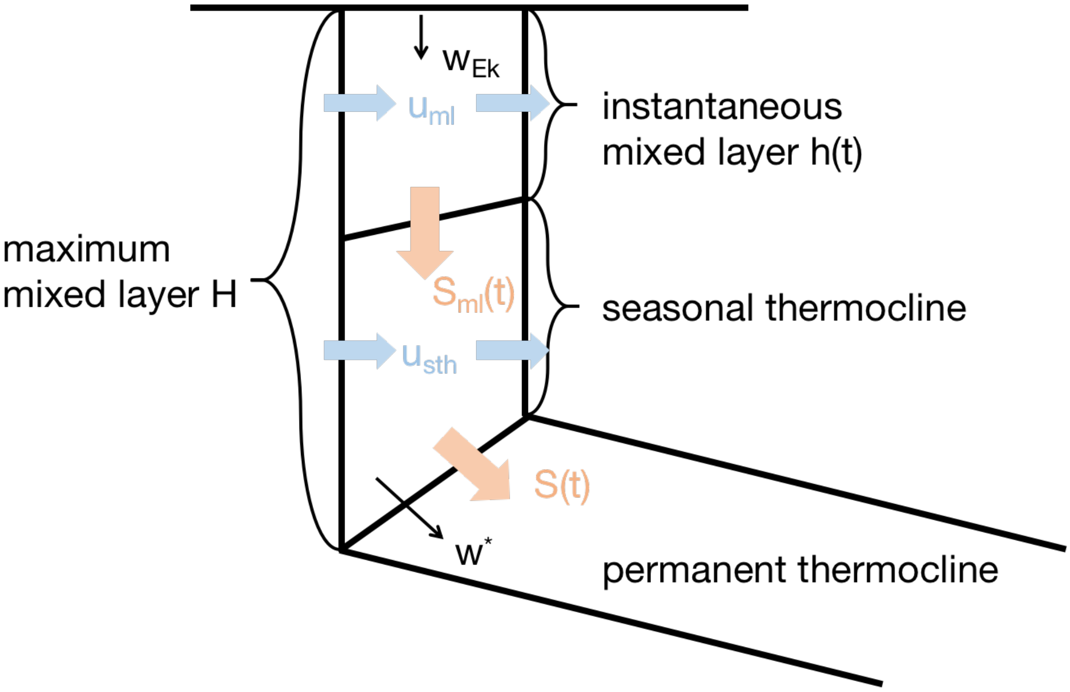

Figure 2.4: A schematic of the decomposition of subduction rate into several components. The mixed layer depth $h(t)$ seasonally varies to reach its maximum, H, in winter. The water leaving the instantaneous mixed layer enters the seasonal thermocline (this layer can be considered to have been in recent contact with the atmosphere). The subduction of interest is the water permanently leaving the seasonal thermocline, i.e., the water crossing the surface $z = -H$. Velocities u_{ml} and u_{sth} are the horizontal geostrophic velocities in the mixed layer and in the seasonal thermocline respectively; $S_{ml}(t)$ and $S(t)$ are the rate at which the water crosses the base of the mixed layer and the base of the winter mixed layer respectively; w_{Ek} is the Ekman pumping and w^* is the vertical velocity induced by eddies.

Finally the subduction rate is divided into three components

$$\overline{S} = \overline{S_{Ek}} + \overline{S_{geo}} + \overline{S_{eddy}}, \tag{2.10}$$

where

$$\begin{aligned} \overline{S_{Ek}} &= \overline{w_{Ek}}, \\ \overline{S_{geo}} &= \overline{\boldsymbol{u}_{ml}} \cdot \nabla \overline{h} + \overline{\boldsymbol{u}_{sth}} \cdot \nabla(\overline{H - h}) + \beta \text{ advection}, \\ \overline{S_{eddy}} &= \nabla \cdot (\boldsymbol{u}^*_{ml} \overline{h}) + \nabla \cdot [\boldsymbol{u}^*_{sth}(\overline{H - h})]. \end{aligned} \tag{2.11}$$

Such decomposition into several terms is important in evaluating contributions from different scales of the flow. The Ekman component approximated in this way displays a large-scale pattern, while the geostrophic component controls the in-situ subduction rate. The third eddy-induced component depends on how the eddies are parameterized and will be discussed in details shortly.

2.3 Perspective of a water parcel within a moving isopycnal layer

We show that the subduction rate of one water parcel at a fixed location (i.e., the Eulerian framework) is in part associated with its instantaneous vertical velocity relative to the movement of the mixed layer depth, i.e., $\frac{\partial h}{\partial t} + w_b$. Here, we further take into account the horizontal movement of density isolines that hold this water parcel, which is analogous to the vertical relativity. In other words, the mixed layer base moves up and down within each seasonal cycle, while the horizontal isopycnals at the same time migrate towards the equator or pole. A schematic is shown in Figure 2.5 that mimics a poleward migration of isopycnal when the mixed layer depth shoals during the winter to summer transition. This is also evident in Figure 2.6 that shows the spatial patterns of mixed layer depth for four seasons. The surface isopyncals in the North Atlantic, for example, migrate towards the equator in boreal winter while shrink towards the northeast in summer. Such migration of isopycnals are also evident in the North Pacific and along the fronts of ACC.

Now we consider the modification of $\frac{\partial h}{\partial t}$ term in Eqn 2.4, which refers to the MLD movement at a fixed location in space (i.e., in fact this term should be marked as $\left.\frac{\partial h}{\partial t}\right|_r$ with r representing a horizontal location invariant with time). Here, we are instead interested in the calculation of $\left.\frac{\partial h}{\partial t}\right|_\sigma$ that is the vertical movement of MLD in the same isopycnal, labeled with a question mark in Figure 2.5. The total subduction at a constant isopycnal over a given time period Δt can be calculated as

$$\left.\frac{\partial h}{\partial t}\right|_\sigma \Delta t = h(r_0 + \Delta r, t_0 + \Delta t) - h(r_0, t_0) = \left.\frac{\partial h}{\partial t}\right|_r \Delta t + (\boldsymbol{c}\Delta t) \cdot \nabla h, \tag{2.12}$$

with $\boldsymbol{c}$ indicating the horizontal velocity of isopycnal migration. The full subduction rate relative to the movement of isopycnal is thus rewritten as

$$S = \left.\frac{\partial h}{\partial t}\right|_\sigma + \left.\boldsymbol{u}_b\right|_\sigma \cdot \nabla h + w_b. \tag{2.13}$$

Here, $\left.\frac{\partial h}{\partial t}\right|_\sigma = \left.\frac{\partial h}{\partial t}\right|_r + \boldsymbol{c} \cdot \nabla h$, while the water parcel velocity relative to the movement of isopycnal ($\left.\boldsymbol{u}_b\right|_\sigma$) is simply $\boldsymbol{u}_b - \boldsymbol{c}$. To summarize, the expressions of subduction rate relative to moving isopycnals as shown in Eqn 2.13 and the Eulerian calculation as displayed by

Eqn 2.4 should be equal, that is,

$$S = \left.\frac{\partial h}{\partial t}\right|_{\sigma} + \left.\boldsymbol{u}_b\right|_{\sigma} \cdot \nabla h + w_b = \left.\frac{\partial h}{\partial t}\right|_{r} + \boldsymbol{c} \cdot \nabla h + (\boldsymbol{u}_b - \boldsymbol{c}) \cdot \nabla h + w_b = \left.\frac{\partial h}{\partial t}\right|_{r} + \boldsymbol{u}_b \cdot \nabla h + w_b. \tag{2.14}$$

This equation indicates that the extra term of isopycnal movement $\boldsymbol{c} \cdot \nabla h$ is added to the original time-dependent vertical movement of the mixed layer depth, but also subtracted from the lateral induction.

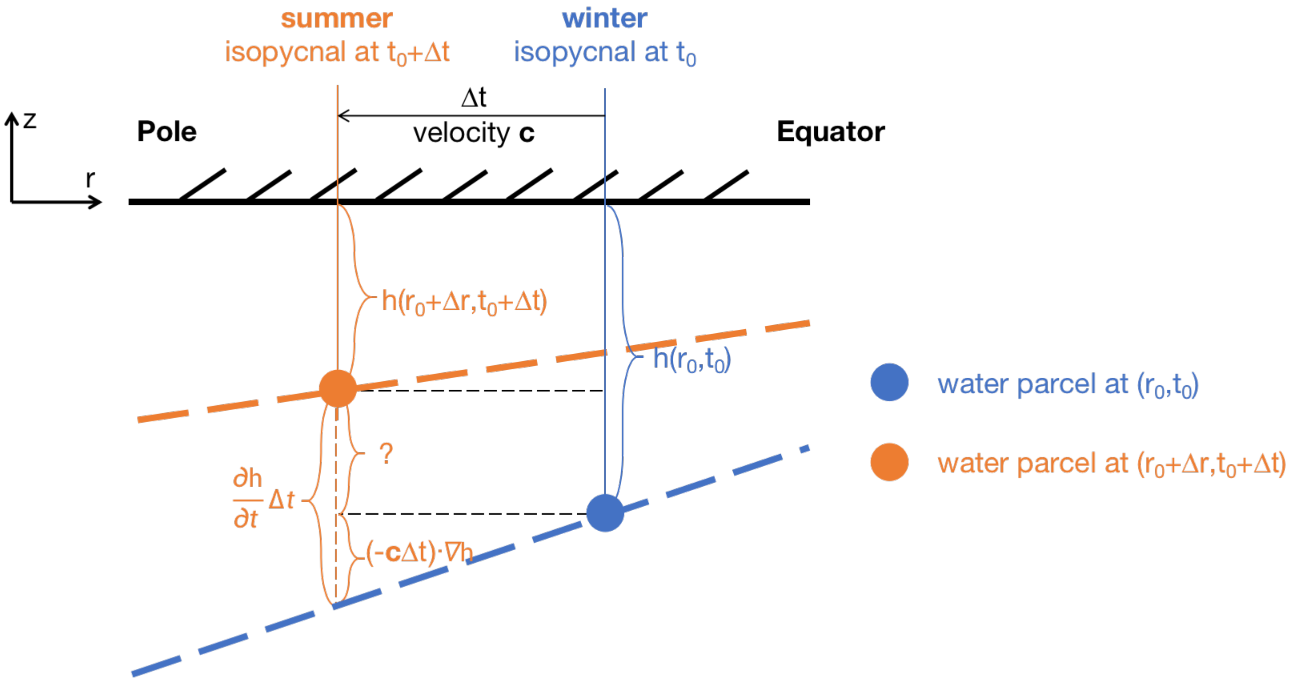

Figure 2.5: A schematic of a water parcel at the base of the mixed layer following a migrating density outcrop position. The original location of this water parcel is at (r_0, t_0) in winter. While it moves from the blue dot to the final position of the orange dot at $(r_0 + \Delta r, t_0 + \Delta t)$, the isopycnal also moves at velocity $\boldsymbol{c}$ from the equator towards the pole.

Therefore, it is necessary to diagnose the value of $\boldsymbol{c}$ if to switch from the Eulerian frame to the coordinate of moving isopycnals. Considering the continuity again for the potential density, e.g., $\frac{\partial \sigma}{\partial t} + \boldsymbol{c} \cdot \nabla \sigma = 0$, the velocity of $\boldsymbol{c}$ can be assumed as $\boldsymbol{c} = -\frac{\partial \sigma}{\partial t} / \nabla \sigma$. However, this function is difficult to solve at locations where the divisor $\nabla \sigma$ is approximately zero. Alternatively, this advection of isopycnal $\boldsymbol{c} \cdot \nabla h$ is calculated as the difference between $\left.\frac{\partial h}{\partial t}\right|_{\sigma}$ and $\left.\frac{\partial h}{\partial t}\right|_{r}$. We then need to approximate the time-dependent term $\left.\frac{\partial h}{\partial t}\right|_{\sigma}$ for each isopycnal interval ($\sigma_1 \leqslant \sigma < \sigma_2$) as

$$\left.\frac{\partial h}{\partial t}\right|_{\sigma} = \frac{\partial \langle h(\sigma_1 \leqslant \sigma < \sigma_2)\rangle}{\partial t}. \tag{2.15}$$

Here, $\langle\rangle$ is an area-weighted mixed layer depth averaged over the density interval at time t. To be more specific, for any density class and at any given time, $\left.\frac{\partial h}{\partial t}\right|_{\sigma}$ is simply calculated as an average of all the mixed layers falling in this isopycnal scope.

It is further possible to decompose Eqn 2.13 into

$$\begin{aligned} S_t &= \left.\frac{\partial h}{\partial t}\right|_{\sigma}, \\ S_h &= S_{h1} + S_{h2} = -\boldsymbol{c}\cdot\nabla h + \boldsymbol{u}_b\cdot\nabla h, \\ S_v &= w_b. \end{aligned} \tag{2.16}$$

Here, S_t is the new time-dependent term relative to the movement of isopycnals, with an approximation described in Eqn 2.15. The lateral components S_h is further divided into S_{h1} and S_{h2} since it is of interest to have a broad view of how much the velocity $\boldsymbol{c}$ of isopycnal migration takes the role in modifying the entire picture. The vertical component S_v is the same as that of Eqn 2.4.

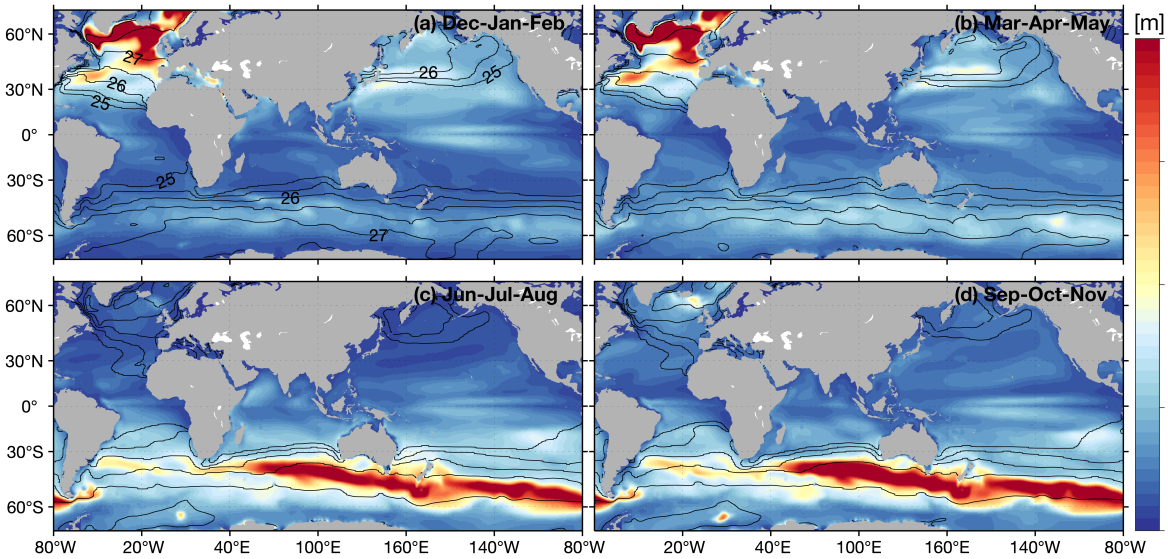

Figure 2.6: The mixed layer depth averaged over a span of 3 months (over years 1992 to 2017). Black solid contours are the isolines of potential density at the surface (assumed to be the same as the value obtained at the base of the mixed layer). The contour ranges as $25 \leqslant \sigma \leqslant 27.5$ with interval $\Delta\sigma = 0.5$. The calculations are based on the ECCO dataset [Consortium, 2021].

2.4 Eddy component of subduction relative to a long-term average

Over much of the ocean, such as the subtropical gyres of the North Atlantic and North Pacific, the basin-scale subduction of water masses is dominated by the Eulerian-mean advection as discussed above, and the climatological subduction rates can be estimated by substituting Eulerian-mean velocities into Eqn 2.4 directly. However, in regions of intense baroclinic instability (e.g., along the ACC), the contribution of an ensemble of eddies to the large-scale, time-mean subduction rate is potentially of the same order and cannot be neglected. The effectiveness of mesoscale eddies (baroclinity) in water mass subduction arises from their ability of stirring water mass properties along isopycnals, so that the subducted homogeneous mode waters are constantly erased away from their original location. This is also in part proved by a similarity between downstream water mass properties and the upstream characteristics of deepest mixed layer along eddy trajectories, which will be shown in Chapters 3 and 4. An up-gradient advection of water masses by mesoscale eddies was also investigated in numerical studies, which contradicts the typical role of diffusion by eddies [Lee, 1997].

Since the surface area over which the water mass is outcropped is evolving over time, a simple Eulerian time average of Eqn 2.4 is not appropriate. Instead we must evaluate the time mean subduction rate: i) in a Lagrangian frame of reference which follows the meandering surface density outcrops, or ii) taking account of the area over which the water mass is outcropped. In the classic theory without consideration of isopycnal migration [Marshall, 1993], and for any given period of time, the long term averaged subduction rate is simply calculated as $\overline{S} = \frac{1}{T}\int_0^T S\,dt$. Thus, the Eqn 2.5 represents a simplification of such annual integration, in terms of i) a standpoint at the maximum MLD, ii) a yearly averaged velocity field, and iii) the drop of the temporal term (an assumption that there is no interannual variability of the MLD).

In this study, the migration of isopycnals enables a calculation of outcropping surfaces of any water masses given their densities. Following Marshall [Marshall, 1997], the net subduction of a water mass, defined to lie within a density range $\sigma_1 \leqslant \sigma < \sigma_2$, is given by the local subduction rate, $S(t)$, multiplied by outcropping area, $\Delta a(t)$, between the two bounding isopycnals, σ_1 and σ_2. Separating the fluid variables into mean and eddy components, e.g., $\boldsymbol{u} = \overline{\boldsymbol{u}} + \boldsymbol{u'}$, $h = \overline{h} + h'$, etc, where the mean represents a low-pass filtering operation over several baroclinic eddy life cycles, one can find the long-time averaged volume flux as

$$\overline{S(t)\Delta a(t)} = \left(\frac{\partial \overline{h}}{\partial t} + \overline{\boldsymbol{u_b}} \cdot \nabla \overline{h} + \overline{w_b}\right)\overline{\Delta a} + \overline{\left(\frac{\partial h}{\partial t} + \boldsymbol{u_b} \cdot \nabla h + w_b\right)'\Delta a'} + \overline{\boldsymbol{u'_b} \cdot \nabla h'\Delta a}. \tag{2.17}$$

Dividing by the mean outcrop spacing gives an expression for the water mass subduction rate per unit surface area,

$$\begin{aligned}\overline{S} &= \frac{\overline{S\Delta a}}{\overline{\Delta a}} = S_{Euler} + S_{eddy},\\ S_{Euler} &= \frac{\partial \overline{h}}{\partial t} + \overline{\boldsymbol{u_b}} \cdot \nabla \overline{h} + \overline{w_b},\\ S_{eddy} &= \frac{1}{\overline{\Delta a}}\overline{(\frac{\partial h}{\partial t} + \boldsymbol{u_b} \cdot \nabla h + w_b)'\Delta a'} + \overline{\boldsymbol{u_b'} \cdot \nabla h'}.\end{aligned} \tag{2.18}$$

Here, S_{Euler} is the subduction rate evaluated using Eulerian-mean velocities, and S_{eddy} is the additional subduction resulting from eddies. Ideally, the averaging of Eqn 2.18 should be performed in a Lagrangian frame which both follows the meandering water mass outcrops, and is also weighted by the surface outcrop area. It is noteworthy that the eddy component of subduction S_{eddy} mainly includes two parts: one is resulted from the nonlinearity between the velocity field and lateral gradients of MLD (i.e., an eddy lateral induction that is the second term on the right hand side of S_{eddy}), and the other comes from a Lagrangian integration over migrating outcrops since the outcropping area of a given water parcel (at a given density class) is also time-dependent (i.e., the first term on the right hand side of S_{eddy}). In general, from the perspective of turbulence, the eddy component of subduction rate matters if there is a multiplication of two (or three) variables that are both highly-dependent on time.

If we consider a more general form of subduction rate calculated over some domain (for specific isopycnal surfaces) and over a long period of time, take Eqn 2.13 as the integrand we can have

$$\overline{S} = \frac{1}{T}\int_0^T (\frac{1}{A}\int_0^A S\,dA)\,dt. \tag{2.19}$$

Instead of a simplification shown in Eqn 2.5, the annual subduction rate in a more complex form depends on how to express the instantaneous S and its temporal or spatial integration. For an integral over any specific isopycnal outcrop $A(\sigma_1 \leqslant \sigma < \sigma_2)$,

$$\overline{S} = \frac{1}{T}\int_0^T (\frac{1}{A}\int_{A(\sigma_1 \leqslant \sigma < \sigma_2)} S\,dA)\,dt = \frac{1}{T}\int_0^T [\frac{1}{A}\int_{A(\sigma_1 \leqslant \sigma < \sigma_2)} (\frac{\partial h}{\partial t}\Big|_\sigma + \boldsymbol{u}_b\Big|_\sigma \cdot \nabla h + w_b)\,dA]\,dt. \tag{2.20}$$

In this case, the eddy component of subduction rate averaged over one year for a specific density outcrop is determined by i) the resolution in time (e.g., monthly, daily or hourly integration); ii) the nonlinearity between each term of instantaneous S and area change.

Following Marshall [Marshall, 1997], a rephrased decomposition of Eqn 2.18 into an Eulerian and eddy subduction rates that uses a bolus velocity $\boldsymbol{u}^\star$ [Gent, 1990] instead of the eddy velocity $\boldsymbol{u'}$ is written as

$$\begin{aligned} S_{Euler} &= \frac{\partial \overline{h}}{\partial t} + \overline{\boldsymbol{u_b}} \cdot \nabla \overline{h} + \overline{w_b}, \\ S_{eddy} &= \boldsymbol{u_b^\star} \cdot \nabla \overline{h} + w_b^\star. \end{aligned} \tag{2.21}$$

Since the bolus velocity is defined from water mass transport, the physical interpretation of Eqn 2.21 is that the transport velocities advecting temperature, salinity and other tracers across the base of the mixed layer lead to subduction of water masses (i.e., a perspective of continuity). The bolus velocity is generally largest in regions of intense baroclinic instability, and thus it is in such regions that we expect eddies contribute most significantly to subduction rates [Thomas, 2010; Sallée, 2011; Xu, 2014].

Following Walin [Walin, 1982], consider a column of mixed layer fluid, exposed to a surface buoyancy flux, B_{surf}, and smoothly overlying an adiabatic thermocline. The column is bounded by two time-mean isopycnals, $\overline{\sigma_1}$ and $\overline{\sigma_2}$; the lateral spacing between the outcropping density surfaces is $\overline{\Delta A}$ and within the thermocline the vertical spacing between the same isopycnals is $\overline{\Delta z}$. The ocean is assumed in a statistically-steady state. In the following, both a volume budget and a buoyancy budget are considered (see Figure 2.7 for a simplified schematic which is a 3D reproduction of Figure 4 in Marshall [Marshall, 1997]). Considering that the total transport velocity satisfies continuity $[\nabla_h \cdot (\overline{\boldsymbol{u}} + \boldsymbol{u}^\star) + \frac{\partial}{\partial z}(\overline{w_b} + w_b^\star) = 0]$, one can integrate over the mixed layer column to obtain a volume budget

$$\frac{\partial}{\partial A} \int_{-h}^{0} (\overline{\boldsymbol{u_{in}}} + \boldsymbol{u_{in}^\star})\, dz \overline{\Delta A} + (\overline{\boldsymbol{u_b}} + \boldsymbol{u_b^\star})\overline{\Delta z} = 0. \tag{2.22}$$

Here, $\overline{\boldsymbol{u_{in}}}$ and $\boldsymbol{u_{in}^\star}$ are the horizontal components of the Eulerian-mean, and eddy-induced velocities within the mixed layer, and $\overline{\boldsymbol{u_b}}$ and $\boldsymbol{u_b^\star}$ are the same velocity components at the base of mixed layer. The physical interpretation of this volume budget is that the divergence/convergence of volume flux within the mixed layer (diapycnal mixing) will be balanced by the volume into/out of the bottom of the mixed layer.

Likewise, consider the time-mean buoyancy budget for the same fluid column, which is the perspective from water mass (trans)formation. The buoyancy can be modified either by a surface buoyancy flux, Eulerian-mean advection, or eddy buoyancy fluxes,

$$\frac{\partial}{\partial A} \int_{-h}^{0} g(\overline{\boldsymbol{u_{in}}}\overline{\sigma_{in}} + \overline{\boldsymbol{u'_{in}}\sigma'_{in}})\, dz \overline{\Delta A} + g(\overline{\boldsymbol{u_b}}\overline{\sigma_{in}} + \overline{\boldsymbol{u'_b}\sigma'_b})\overline{\Delta z} + \overline{B_{surf}\Delta A} = 0. \tag{2.23}$$

Here, $\overline{\boldsymbol{u'_b}\sigma'_b}$ is the lateral eddy buoyancy flux at the base of the mixed layer and is purely advective (i.e., $\overline{\boldsymbol{u'_b}\sigma'_b} = \boldsymbol{u_b^\star}\overline{\sigma_{in}}$), since the diffusive flux of density along an isopycnal surface is zero by definition. However, the eddy buoyancy flux within the mixed layer, $\overline{\boldsymbol{u'_{in}}\sigma'_{in}}$, includes both advective and diffusive components due to diabatic mixing along the sea surface (i.e., $\overline{\boldsymbol{u'_{in}}\sigma'_{in}} = \boldsymbol{u^{\star}_{in}}\overline{\sigma_{in}} - \gamma\frac{\partial\sigma_{in}}{\partial A}$, where γ is the diapycnal mixing coefficient within the mixed layer) [Marshall, 1997]. Combining Eqns 2.22 and 2.23 and eliminating $(\overline{\boldsymbol{u_{in}}} + \boldsymbol{u^{\star}_{in}})$ result in a mixed-layer buoyancy equation,

$$(\overline{\boldsymbol{u_b}} + \boldsymbol{u^{\star}_b})\overline{\Delta z} = \frac{\partial}{\partial A}\frac{\overline{B_{surf}} + B_{eddy}}{g\partial\overline{\sigma_{in}}/\partial x}\overline{\Delta A}, \tag{2.24}$$

where $B_{eddy} = g\frac{\partial}{\partial A}(\gamma h\frac{\partial\overline{\sigma_{in}}}{\partial x})$ is the buoyancy forcing associated with the diabatic mixing of adjacent mixed-layer fluid columns. Note that the replacement of $\overline{\boldsymbol{u_{in}}} + \boldsymbol{u^{\star}_{in}}$ by $\overline{\boldsymbol{u_b}} + \boldsymbol{u^{\star}_b}$ from Eqn 2.22 only cancels one component of the first term in Eqn 2.23 (refer to Marshall [Marshall, 1997] for a more detailed derivation).

Since the motion is statistically steady, $(\overline{\boldsymbol{u_b}} + \boldsymbol{u^{\star}_b})\overline{\Delta z}$ is equivalent to the net subduction rate $\overline{S\Delta A}$. Thus,

$$\overline{S} = \frac{\partial}{\partial A}(\frac{\overline{B_{surf}} + B_{eddy}}{g\partial\overline{\sigma_{in}}/\partial x}). \tag{2.25}$$

The rate at which a water mass is subducted from the surface mixed layer into the thermocline beneath is related simply to the air-sea buoyancy flux and the buoyancy forcing associated with diapycnal mixing within the surface mixed layer. This result can be extended to a time-dependent ocean, provided that we integrate over a self-repeating cycle such as a closed seasonal cycle. Note that the eddy buoyancy flux entrained through the base of the mixed layer makes no contribution to the right hand side of Eqn 2.25. Physically, the eddies transport fluid adiabatically along density surfaces, but lead to no transformation of water masses between adjacent density classes.

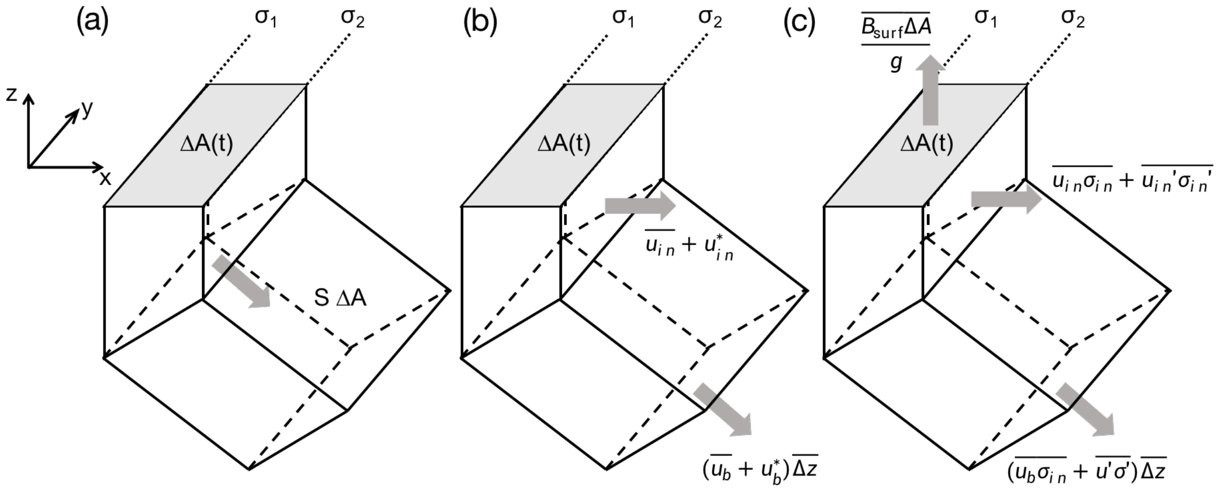

Figure 2.7: (a) Instantaneous subduction rate indicated by S and the volume subduction can be calculated as $S\Delta A$, with ΔA denoting the isopycnal area between boundaries σ_1 and σ_2. (b) The volume budget that the convergence of the transport inside mixed layer must be balanced by a velocity at the base of the mixed layer into the thermocline. (c) The buoyancy budget that the density can be modified through a surface flux, a convergence of lateral buoyancy fluxes within the mixed layer, or a buoyancy transport into the thermocline along the isopycnal.

2.5 Perspective from potential vorticity conservation

After accounting of kinematic and thermodynamic budgets of water mass subduction in previous sections, here, we further consider subduction/formation of water masses from the PV conservation. Consider the full Ertel potential vorticity as

$$q = \omega_a \cdot \nabla b, \tag{2.26}$$

where $\omega_a = f\hat{k} + \nabla \times \boldsymbol{u}$ is the absolute vorticity, and $b = -g\rho/\rho_0$ is the buoyancy, resulting from convergence/divergence of the PV flux, i.e.,

$$\frac{\partial q}{\partial t} = -\nabla \cdot \boldsymbol{J}, \tag{2.27}$$

where the PV flux

$$\boldsymbol{J} = q\boldsymbol{u} + \nabla b \times \boldsymbol{F} - D\omega_a \tag{2.28}$$

has an advective constituent $q\boldsymbol{u}$ and nonadvective constituents that arise from diabatic processes D:

$$D \equiv \frac{\partial b}{\partial t} + \boldsymbol{u} \cdot \nabla b \tag{2.29}$$

and from frictional forces $\boldsymbol{F}$. Calculating the divergence of the PV flux in Eqn 2.27, the PV equation becomes

$$\frac{\partial q}{\partial t} + \boldsymbol{u} \cdot \nabla q = \nabla \times \boldsymbol{F} \cdot \nabla b + \omega_a \cdot \nabla D, \tag{2.30}$$

showing how frictional torques on isopycnal surfaces or gradients of diapycnal mixing in the direction of absolute vorticity change the PV [Marshall, 1992].

3 Results

In this study, we aim for 3 analyses: i) the comparison between instantaneous subduction rate calculations either across the maximum mixed layer depth (usually in winter or early spring) or summing over the entire year, that is to say, the theory of Stommel's demon is revisited and compared with a calculation rather integrated over the annual cycle; ii) decomposition and quantification of the subduction rate into several components by taking into account the migration of isopycnals, though the derivation has shown that the migration of isopycnals does not influence the instantaneous subduction rate; iii) comparison between calculations based on daily and monthly data, in order to provide some insights into the eddy-induced contribution to subduction.

In achieving these goals, the Estimating the Circulation and Climate of the Ocean (ECCO) dataset has been applied for the calculation of subduction rates [Consortium, 2021]. This global ocean state estimate covers the period from 1992 to 2017, and it synthesizes nearly all modern observations with an ocean circulation model (MITgcm) into coherent, physically consistent descriptions of the ocean's time-evolving state covering the era of satellite altimetry.

Animation: four surface variables from ECCO v4r4

Also available by clicking here.

Figure 2.6 displays spatial distribution of mixed layer depths for four seasons. While panel (a) represents an average over December to February as the boreal winter, panel (c) shows June to August as the austral winter. Accordingly, the deepest mixed layers in these two panels are separately located at the polar North Atlantic region and along the ACC limited within the Indian and Pacific sectors, consistent with several observational climatologies [de Boyer Montégut, 2004; Holte, 2017]. In the Southern Ocean, mode and intermediate waters are formed within and north of the ACC, where deep winter convection drives a development of the mixed layer to reach over 500 m. As the seasonal buoyancy forcing restratifies the upper ocean, the mixed layer shoals to 50 m in summer, and at the same time, the density outcrop migrates toward the South Pole. In general, the outcropping areas expand toward the equator during cooling period and contracts toward the South Pole during heating period in the Southern Hemisphere, while an opposite direction of isopycnal movement can be found in the Northern Hemisphere. As will be shown in this study, it is the subannual correlations between the outcrop area and the rate of shoaling/deepening of the mixed layer that give rise to the time-mean net volume subduction of mode waters out of the mixed layer.

Figure 2.8 shows several surface variables for the boreal (left panels) and austral (right panels) winters from the ECCO data [Consortium, 2021]. Both the heat flux and freshwater flux are season-dependent, while the wind stress is intensified during the winter season for the frontal systems in subpolar regions, e.g., the zonal wind stress over ACC is magnified in the Indian sector in winter.

3.1 Comparison between two definitions of annual subduction rate

Figures 2.9 and 2.11 compare the difference between the Eulerian subduction rates by either taking an average over the entire year, or calculating only at the base of deepest mixed layer [Marshall, 1993]. Both cases neglect the contribution from temporal change $\partial h/\partial t$. Figure 2.9 takes the form of Eqn 2.3 (continuity perspective) and decomposes the total rate into zonal and meridional components (respectively shown in (b) and (c) panels), while Figure 2.11 displays spatial distributions of Eqn 2.4 (single parcel perspective at the mixed layer base) with separate contributions from the zonal, meridional and vertical components (as displayed in (b), (c) and (d) panels). Since the vertical velocity is resolved in the ECCO model, we do not need a further diagnosis of w_b at the base of the mixed layer from any approximation in the context of Ekman dynamics. However, such calculation of Ekman pumping could be of interest to compare with the solution of vertical velocities in the model. By doing this, it is possible to quantify how much of the subduction rate is generated due to the frictional wind forcing. The difference between the actual vertical velocity and Ekman pumping velocity might be due to smaller-scale processes, such as the mechanism of nonlinear Ekman theory, which proposes a dependence of the Ekman pumping on the background geostrophic field, high-frequency internal waves and self-advection [Chen, 2021].

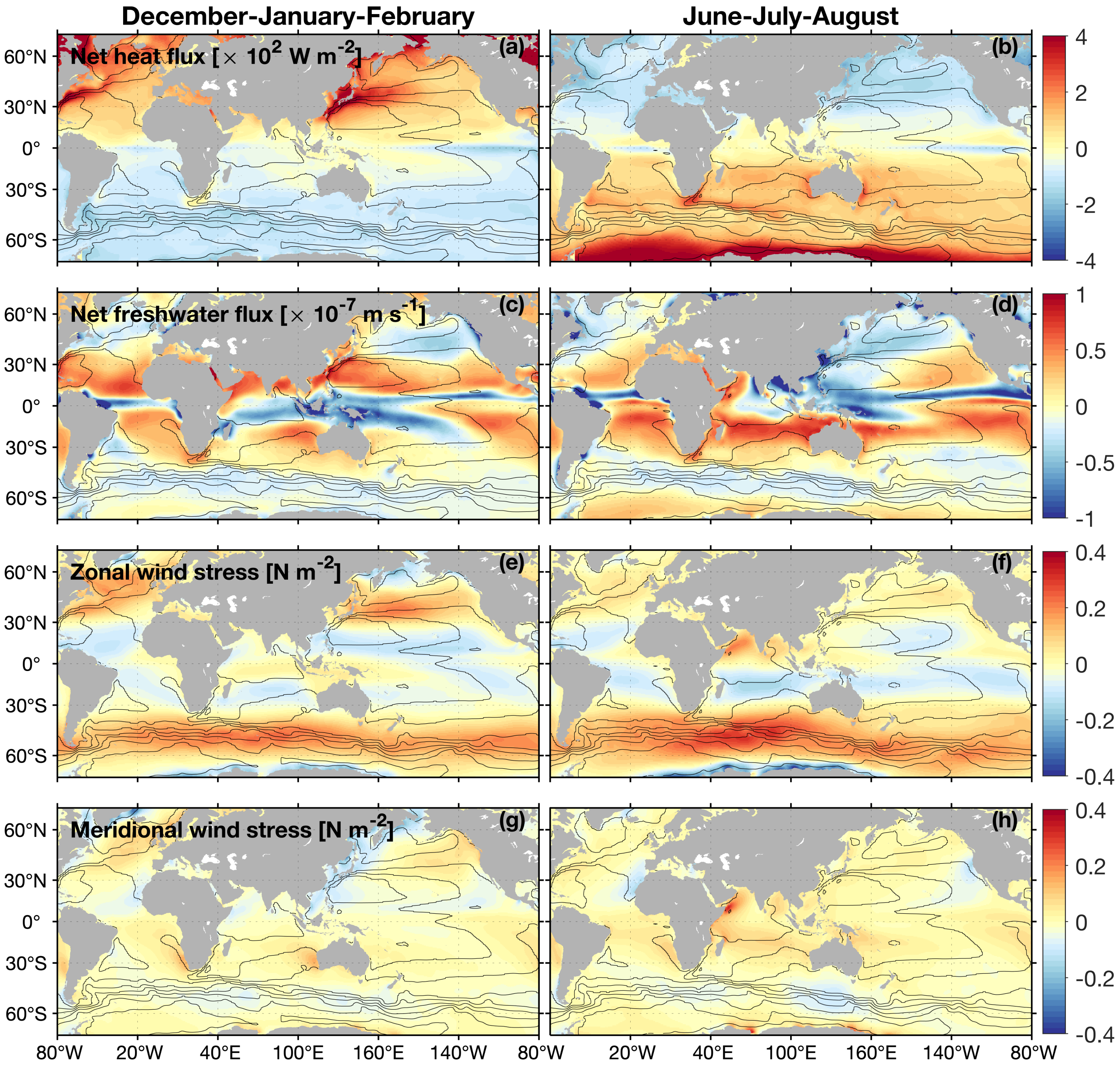

Figure 2.8: Surface variables for two seasons: December-to-February and June-to-August. (a) and (b) net heat fluxes; (c) and (d) net freshwater fluxes; (e) and (f) zonal wind stress; (g) and (h) meridional wind stress. For the two fluxes, positive values are associated with an upward direction from the ocean into the atmosphere.

The continuity solution shown in Figure 2.9 provides a comprehensive picture of the spatial distribution of subduction. The mild pattern of the total $\nabla_h \cdot (h\boldsymbol{u})$ averaged over one year shown in (a1) is due to a compensation between its zonal and meridional components, both of which display a larger magnitude and spatial variability of subduction/obduction. In general, the first-order spatial pattern of the total subduction rate shown in (a1) and (d1) follows an Ekman pumping (contained in the meridional component $\partial(vh)/\partial y$ term in (c1) and (f1)), with upwelling in the polar region and downwelling in the tropics and subtropics. Along the turbulent ACC, downwelling (blue-colored) reaches it maximum within the Malvinas Current system and at the eastern side of the New Zealand, while obduction (red-colored) can be found at the southern tip of Africa and in the tropics.

The second column of Figure 2.9 indicates a (normalized) subduction rate as a function of latitude. Such normalization is applied here in that it is of interest to compare not only the exact values of subduction, but also the difference among latitudes. The zonal component of $\nabla_h \cdot (h\boldsymbol{u})$ shown in (b2) implies an obduction in the polar North Atlantic, while the meridional component displayed in (c2) indicates a peak obduction at the equator. Subduction is found at the subtropics of both hemispheres, and at the northern boundary of the Pacific and Atlantic.

In addition, the third column of Figure 2.9 displays a cumulative subduction rate starting from 70 °S northward. In this regard, it implies that the total amount of subduction integrated until the northern boundary should be approximately equal to zero due to the balance of water masses for the entire ocean surface. However, the total integrated subduction in (a3) leads to a positive value (obduction), which further indicates that the $\partial h/\partial t$ term might result in a subduction during this one-year integration. That is to say, neglecting the temporal term in the subduction rate calculation is inappropriate, since the mixed layer depth can have interannual variability presumably due to changes of the surface buoyancy forcing.

Panels (d–f) in Figure 2.9 illustrate the same calculation of subduction rate instead obtained at the base of the thickest mixed layer. Such approximation (i.e., the theory of Stommel's demon) leads to a larger magnitude of instantaneous subduction in general. The spatial pattern (d1), however, resembles the calculation from monthly averages (a1), even for the locations of hotspot regions of subduction/obduction. The calculation as a function of latitude shown in (d2) also looks similar to the monthly mean calculation (a2), though some differences are also obvious, e.g., the relative magnitude of subduction/obduction at the same latitudinal band. The upwelling at the equator is greatly reduced for the calculation at maximum mixed layer depth. The third column of latitudinally integrated subduction rate in (d3) results in a total obduction, similar to the monthly integration of (a3). However, the magnitude at the northern boundary of this integration remains larger than that of (a3), which means that there is a larger bias in the Stommel's theory of subduction rate calculation that in the meanwhile does not consider the time-dependent MLD.

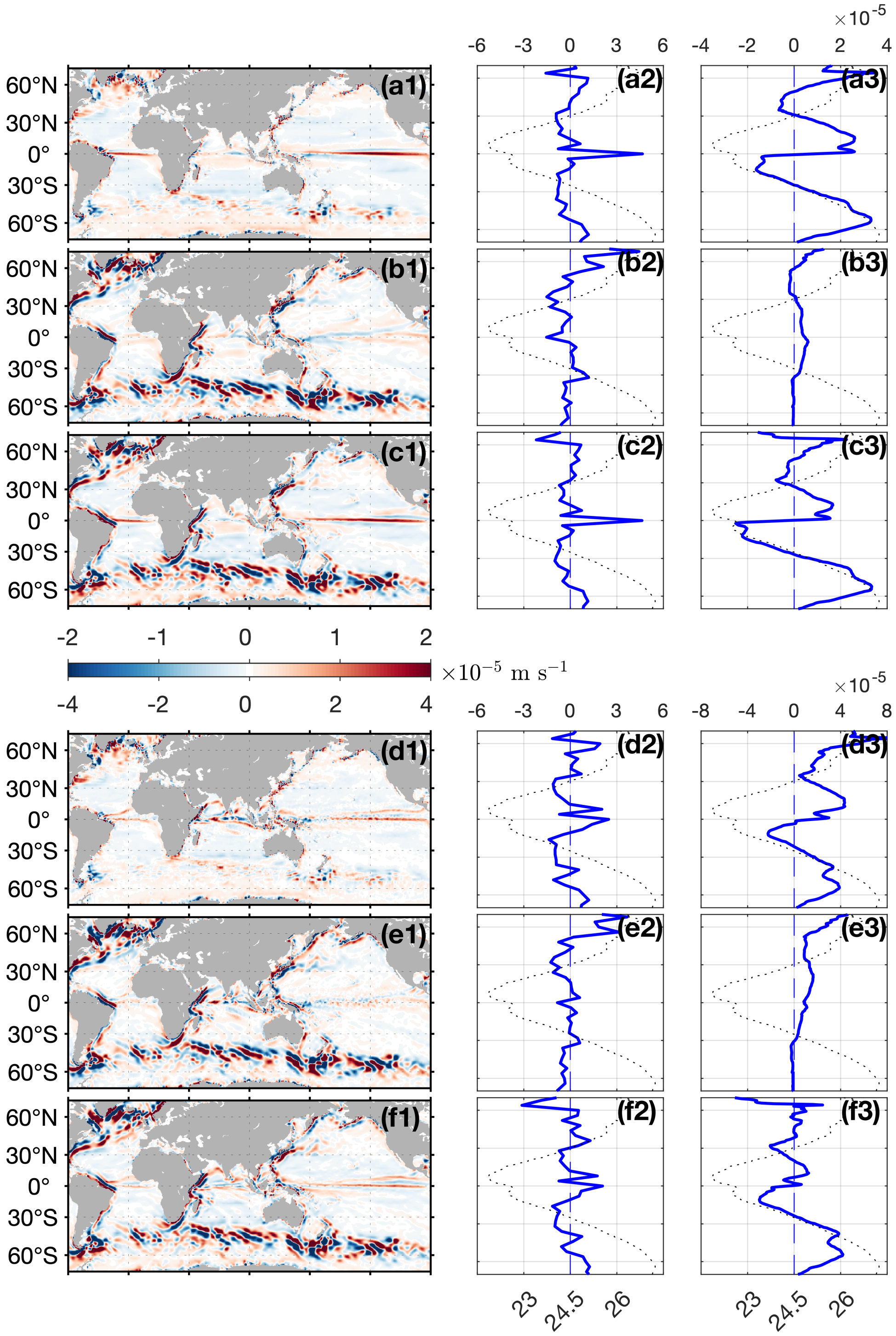

Figure 2.9: Subduction rates calculated using Eqn 2.3 (blue for subduction and red for obduction). Rows (a–c) correspond to the calculation of monthly mean MLD and (d–f) are associated with the maximum MLD for each year. Panels (b) and (c) are the zonal and meridional components of (a), while (e) and (f) are the two components for (d). The second column shows a normalized version of subduction rates that aims to provide a clean pattern of latitude bands corresponding to either subduction or obduction (note that they are not the exact values). The third column displays a northward integration of subduction rates starting from 70 °S in the ACC. The dotted black curves overlapped in the second and third columns show the surface density as a function of latitude.

Figure 2.10 further displays the spatial difference between the instantaneous subduction rate at the base of the maximum mixed layer and that of the monthly-mean mixed layer (i.e., to subtract Figure 2.9 (a1) from (d1)). It is noteworthy that the instantaneous downwelling at the subtropical gyres resulted from calculation at the maximum mixed layer depth is enhanced by a factor of two, compared with the monthly integration. Note that the subtraction was made from instantaneous fields of subduction in terms of both methods, rather than a comparison between calculations at the maximum MLD and a yearly accumulative rate from each month. Such comparison will be provided shortly in the context of isopycnal migration, since it contains both the modification of outcropping areas and the temporal change of MLD.

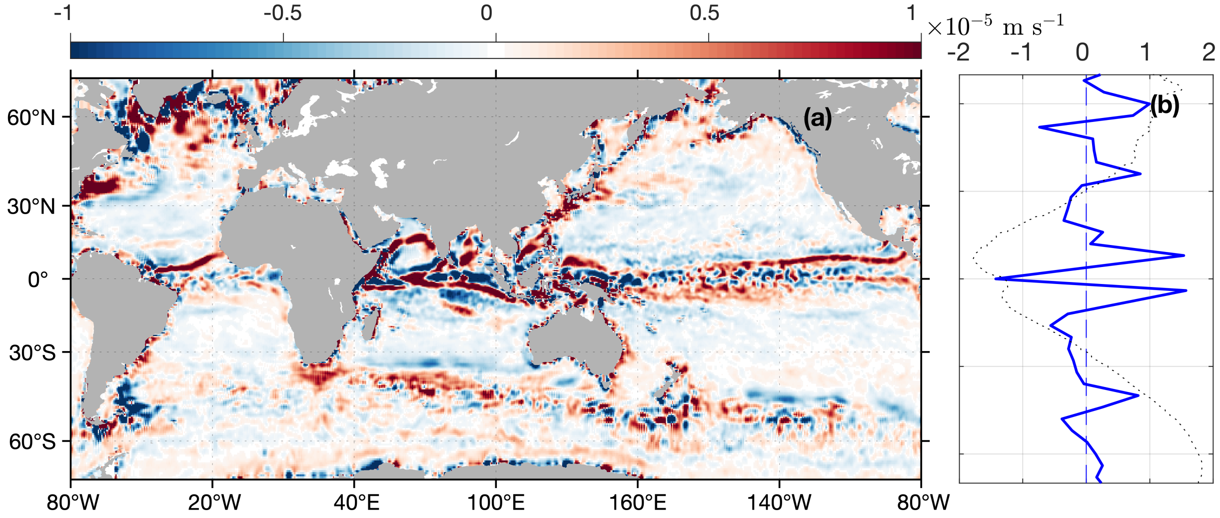

Figure 2.10: Difference of instantaneous subduction rate between the calculation at the base of the mixed layer and that of the monthly average. (a) The difference of spatial pattern between Figure 2.9 (d1) and (a1). (b) The value of subduction rate difference as a function of latitude.

Figure 2.11 shows the subduction rate using Eqn 2.4, neglecting the time-dependent term as well. Panel (a1) is thus a sum of its zonal advection (b1), meridional advection (c1) and vertical velocity at the base of the mixed layer (d1). As discussed in Figure 2.9, the spatial pattern of the total subduction rate (a1) in its first order resembles the vertical component (d1). This implies that for a crude approximation without strong currents and eddies, Ekman dynamics can be applied to calculate the subduction rate. These two advection terms (b1) and (c1) cancel the effects of each other at the ACC front and along the Gulf Stream. Subduction computed at the base of the maximum mixed layer depth (e1–h1) does not differ much from the calculation (a1–d1) averaged over one year.

From the second and third columns of Figure 2.11 that show the subduction as a function of latitude, the advection terms (b2) and (c2) compensate their impacts at the polar North

Atlantic. Compared with the similarity between spatial patterns of (a1) and (d1), the normalized version of subduction rate also displays correspondence between the total (a2) and vertical (d2) components. This confirms the conclusion in Figure 2.9 that the pattern of subduction rate is dominated by vertical pumping at the base of the mixed layer. The only discrepancy is located at the polar regions of the Northern Hemisphere, where the two horizontal advection terms generate a downward (subduction) rate, so that the total amount of subduction is dominated by advection rather than the vertical pumping.

The third column in Figure 2.11 illustrates that the globally integrated rate refers to a total subduction, in comparison with obduction shown in Figure 2.9. The zonal and meridional components shown in (b3) and (c3) respectively display an obduction and subduction, which compensate each other at the leading order, leaving the total pattern of (a3) dominated by the vertical pumping (d3). Similar to the argument about Figure 2.9, the comparison between (e3) and (a3) implies that the calculation that only considers the maximum MLD leads to an exaggerated subduction rate over the entire region.

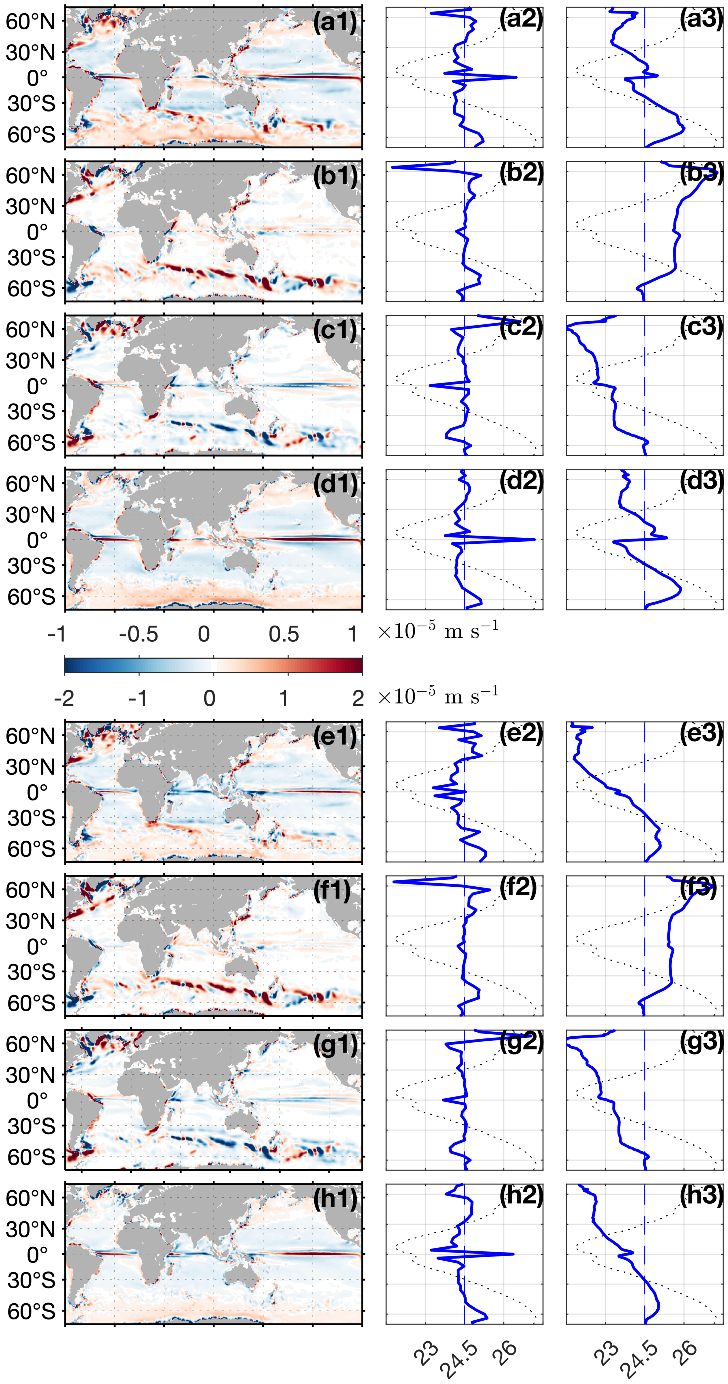

Figure 2.11: Subduction rates calculated using Eqn 2.4 (blue for subduction and red for obduction). Rows (a–d) correspond to calculation based on the monthly mean MLD and (e–h) are associated with the maximum MLD of each year. Rows (a) and (e) show the total rates. Panels (b) and (c) are the zonal and meridional components of advection in (a), while (f) and (g) are the two components of advection in (e). Panels (d) and (h) are vertical velocity fields at the base of the mixed layer. The second column shows a normalized version of subduction rates that aims to provide a clean pattern of latitude bands corresponding to either subduction or obduction (note that they are not the exact values). The third column displays a northward integration of rates starting from 70°S in the ACC. The dotted black curves overlapped in the second and third columns show the surface density as a function of latitude.

3.2 Consideration of isopycnal migration

In this section, solutions to Eqn 2.16 are considered, which takes into account the migration of isopycnals. To clarify, Table 2.1 lists these different terms and their descriptions.

Table 2.1: Four terms of instantaneous subduction rate that takes into account the migration of isopycnals.

Symbols	*Descriptions*	*Expressions*
S_t	Time-dependent MLD following isopycnal outcrops	$\left.\frac{\partial h}{\partial t}\right\vert_{\sigma}$
S_{h1}	Lateral movement of the isopycnals	$-\boldsymbol{c} \cdot \nabla h$
S_{h2}	Lateral induction at the base of the mixed layer	$\boldsymbol{u}_b \cdot \nabla h$
S_v	Vertical velocity at the base of the mixed layer	w_b

* S_{h1} was not calculated by the expression in the table (i.e. from the velocity of isopycnal movement), but rather computed as the difference between $\left.\frac{\partial h}{\partial t}\right|_{\sigma}$ and $\left.\frac{\partial h}{\partial t}\right|_{r}$.

First of all, the time-dependent subduction rate at constant isopycnal $\left.\frac{\partial h}{\partial t}\right|_{\sigma}$ is illustrated in Figure 2.12. Panels (a) and (b) respectively show the timeseries of subduction rate anomaly (in blue) and outcropping area anomaly (in red) for two density classes $\sigma = 26.8$ kg m^{-3} for (a) and $\sigma = 27.4$ for (b). Those density classes are respectively associated with the densest subtropical and subpolar mode waters. It is apparent that for $\sigma = 26.8$, the outcrop area reaches its maximum in February and October, corresponding to the late winter for Northern and Southern Hemispheres respectively. For the month of February, the subduction rate anomaly is approximately zero which means that in the Northern Hemisphere even the outcrop area is enlarging, the total subduction rate is not influenced much. However, such is not the case for the Southern Hemispheric winter in October, where both effects of the large instantaneous subduction rate and the expansion of outcrop areas lead to a maximum of subduction. From June to August, the volume transport forms an obduction in a similar manner. However during this period, the outcropping area of this density class 26.8 shrinks to a yearly minimum, results in a smaller volume obduction compared with subduction during winter. Such idea of this dual-effect is also shown in panel (c) of Figure 2.12. Though the instantaneous rates of subduction and obduction can cancel out the effect of each other, the shrinking and enlargement of outcropping area can lead to a volume subduction over an annual cycle.

For the density class at $\sigma = 27.4$, it is sill the case that the oscillations of the subduction rate and outcropping area are not in the same pace. In April, these two lines cross each other. From March to July, subduction is downward with an increasing trend of the outcropping area, which means that the total volume subduction increases during that period. From July to December, though the outcrop area remains as a positive anomaly, the subduction rate is approximately zero. It is also interesting to note that from January to March, a larger obduction rate persists. However, since the outcropping area shrinks to its minimum of the entire year, the total volume transport due to obduction is reduced.

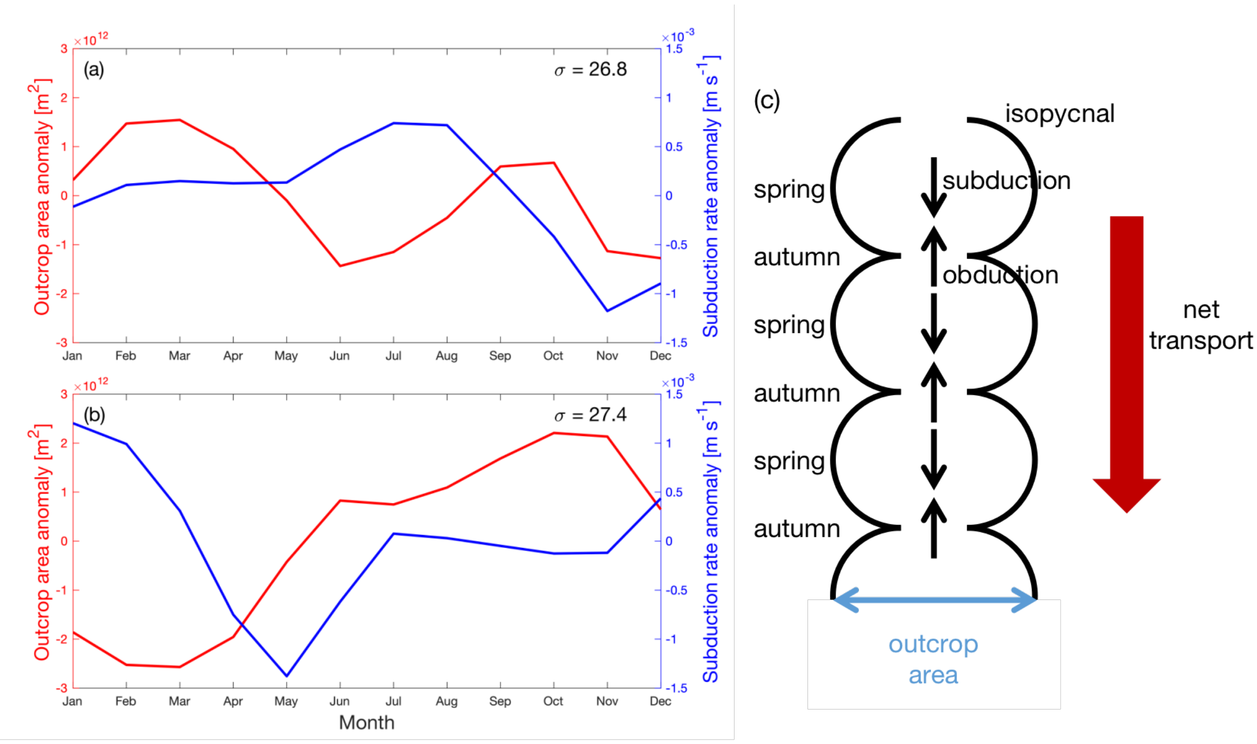

Figure 2.12: (a) Monthly variations of the temporal change in the mixed layer thickness evaluated following the outcrop $\left.\frac{\partial h}{\partial t}\right|_{\sigma}$ and the outcrop area anomaly, averaged over a density bin of $\sigma = 26.8$ kg m^{-3}. The anomaly is defined as a deviation from the annual mean. Positive rate represents obduction and negative represents subduction. (b) Same as (a) but for the density bin of $\sigma = 27.4$. (c) A cartoon illustrating the seasonal subduction resulting from the subannual correlations between the subduction/obduction rate and outcrop area. Both the rate and area are functions of density and time. Subduction occurs in early spring when the mixed layer shallows and obduction occurs in autumn when the mixed layer deepens. The outcrop area is relatively larger during the subduction period than during the obduction period, leading to net downward volume transport.

Figure 2.13 displays the decomposition of Eqn 2.16 and different terms are also described in Table 2.1. It is evident that the migration of isopycnals as shown in (b) produces high-frequency and small-scale upwelling or downwelling in terms of an annual average. Surprisingly, the movement of isopycnals is most important in the tropical and subtropical regions, leading to subduction in the western North and South Pacific, as well as the Indian Ocean. Obduction occurs at the eastern tropical Pacific and in the Mediterranean

Sea. This migration of isopycnals reflects in the time-dependent term (a) as well, with a smaller magnitude in comparison. However, the dominance of S_v term shown in the previous section that does not consider the isopycnal movement is no longer valid here. The component that dominates the subduction rate over each year is the time-dependent term that accommodates the migration of isopycnals. In the Southern Ocean, our results are consistent with Sallée et al. [Sallée, 2010] that the lateral advection determines both the magnitude and spatial pattern of subduction and obduction.

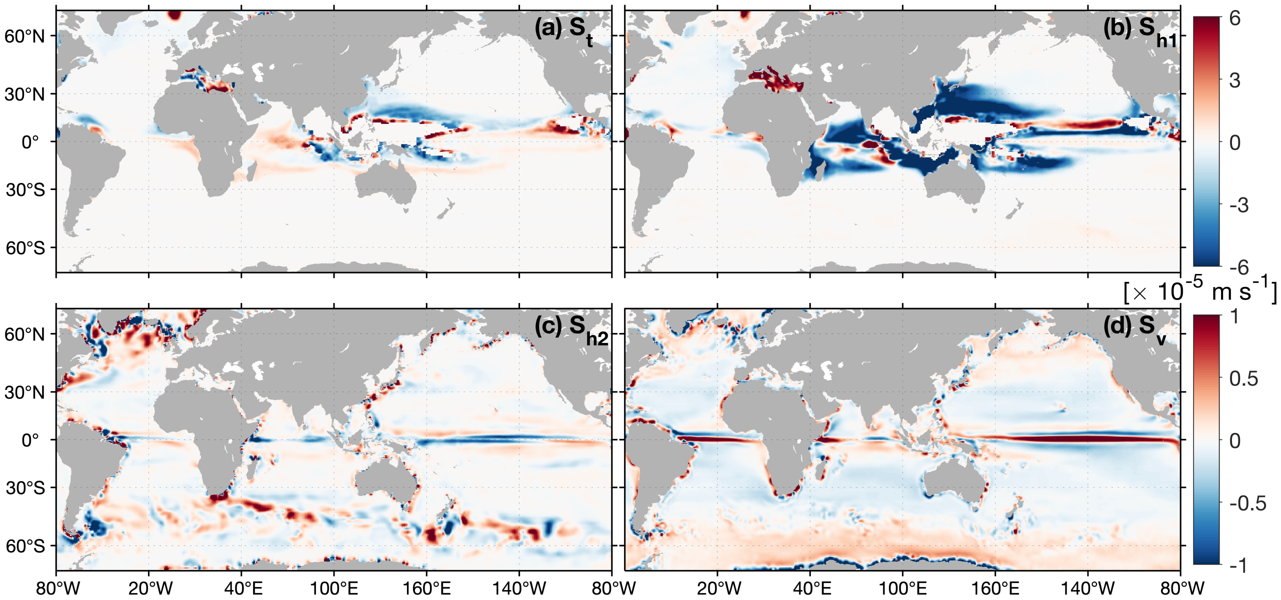

Figure 2.13: Four terms in Eqn 2.16. (a) S_t term which is the time-dependent component at a constant isopycnal. (b) S_{h1} term that indicates the movement of isopycnals. (c) S_{h2} term which is the lateral induction. (d) Vertical pumping at the base of the mixed layer S_v.

Figure 2.14 displays the outcropping area in (a), each term of Eqn 2.16 in (c–f) and the net subduction rate in (b), as a function of time and density class. The outcropping area of small σ is more season-dependent (in the range of 25–26.5), while the density class of 26.5–27.2 occupies a large area over the entire year. Such information is also obvious in Figure 2.15 where several σ classes are separated. Instead of plotting the total outcropping area for each density level, timeseries in Figure 2.15 display the area anomaly for each month compared with an annual mean. At the density class of 24.3, corresponding to a latitudinal band around 30 ° in both hemispheres, the area anomaly is determined by an expansion from January to May and a subsequent contraction for the following months. This interprets that the change of outcrop area at density level 24.3 is dominated by water masses in the Northern Hemisphere, presumably the light components of North Pacific Subtropical Mode Water (NPSTMW). The timeseries of outcropping area at densest classes of 26.7 and 27.3 shown in Figure 2.15, on the other hand, are associated with the Subtropical Mode Water (STMW) and Subantarctic Mode Water (SAMW) in the Southern Ocean.

Table 2.2 shows several water mass density properties from both the ECCO estimate and the Argo profiling data, of which the latter will be the focus of the next chapter. Compared with Figure 2.14 (a), the density range of 25–26.5 falls in the scope of STMW, while the range of 26.5–27.2 contains SAMW for the largest proportion. Intermediate waters are represented by a even higher density in the ECCO estimate, such as AAIW with the range of 27.1–27.6.

Table 2.2: Density thresholds of water masses.

Acronyms	*Full name*	*Density range (ECCO)*	*Density range (Argo)*
NPSTMW	North Pacific Subtropical Mode Water	$25.2 \leq \sigma < 26.4$	$25.1 \leq \sigma < 25.5$
NASTMW	North Atlantic Subtropical Mode Water	$25.2 \leq \sigma < 26.4$	$26.4 \leq \sigma < 26.6$
SHSTMW	Southern Hemisphere Subtropical Mode Water	$25.2 \leq \sigma < 26.4$	$26.3 \leq \sigma < 26.8$
SAMW	Subantarctic Mode Water	$26.4 \leq \sigma < 27.1$	$26.8 \leq \sigma < 27.2$
AAIW	Antarctic Intermediate Water	$27.1 \leq \sigma < 27.6$	$26.8 \leq \sigma < 27.4$

[*] For ECCO, the density class of each water mass is estimated from a previous ECCO version [Kwon, 2013] that does not separate precisely of each STMW.

[*] For Argo, the density class for each water mass will be detailed in the next chapter (Table 3.2).

[*] The AAIW was not detected from the algorithm that will be described in the next chapter, and thus the density range of it comes from other observations.

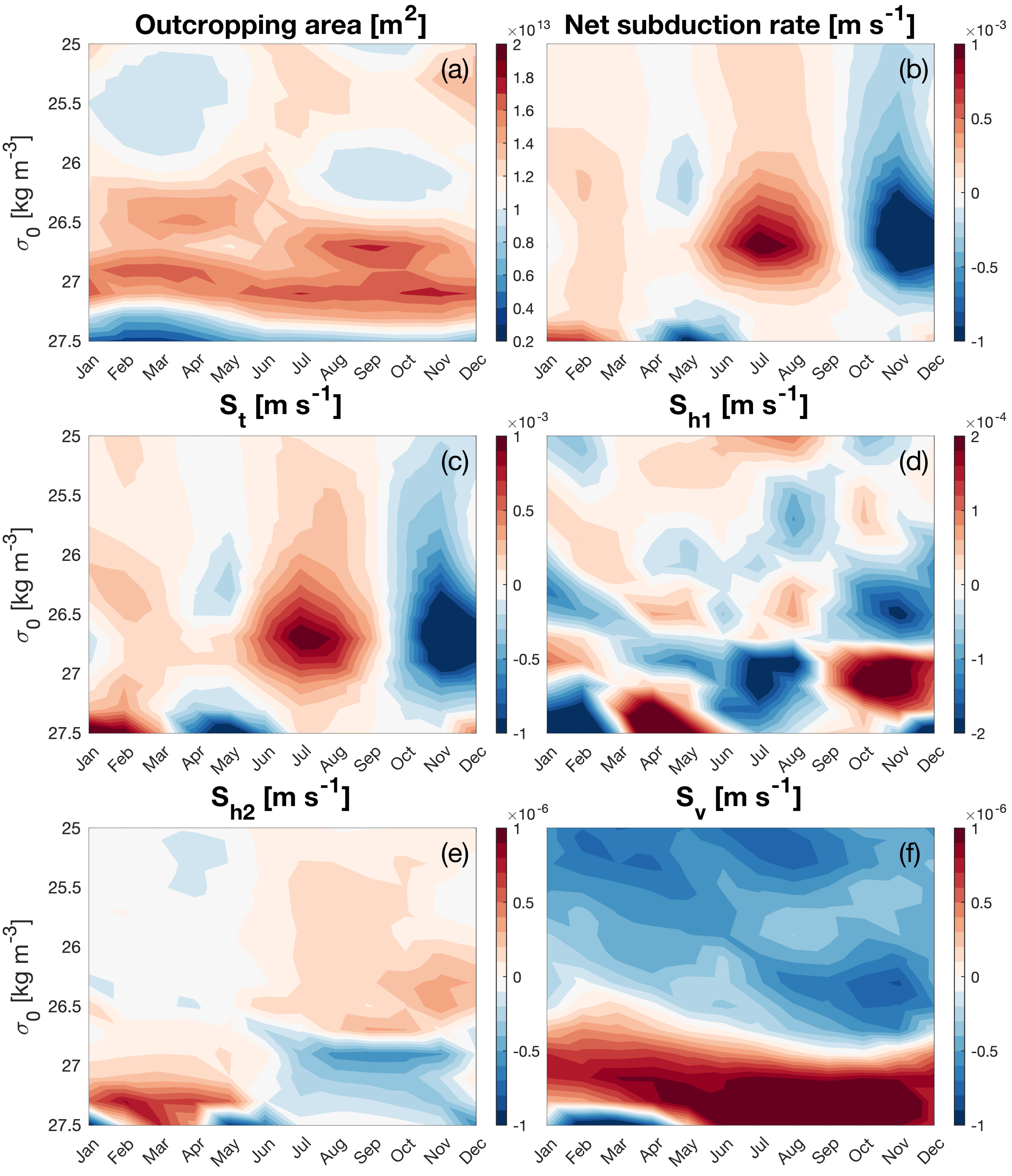

Figure 2.14: (a) Outcropping area; (b) net subduction rate; (c) temporal term S_t; (d) migration of isopycnals S_{h1}; (e) lateral induction S_{h2}; and (f) vertical velocity S_v as a function of time and density.

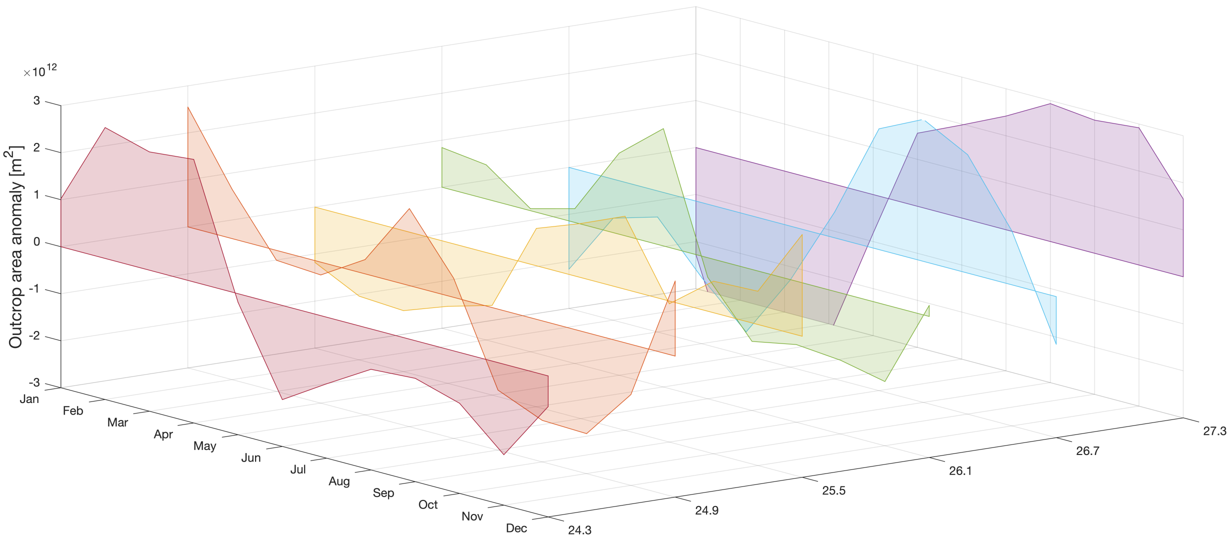

Figure 2.15: Variations of the outcropping area anomaly in terms of 6 density classes, from light to dense: 24.3, 24.9, 25.5, 26.1, 26.7, 27.3 kg m^{-3}.

The net subduction rate in Figure 2.14 (b) displays a very similar pattern to the time-dependent term (c), as is also evident in the spatial distribution discussed above. Both maxima of subduction (October to December) and obduction (June to September) occur at the density class of 26.5–27, however, they can offset each other over one year period. To be more specific, the instantaneous subduction (blue in panel (c)) is slightly larger than the obduction (red). The total volume subduction can thus be inferred from a combination between (a) and (b). Figure 2.15 shows that for the density range of 26.5–27 (i.e., the last two timeseries in blue and purple), the outcropping area starts to increase from May, associated with the maximum obduction pattern in Figure 2.14 (b). Since the outcropping area at this specific density range remains large until December, subduction is the leading pattern in a volume integration.

In Figure 2.14, the S_{h1} that quantifies the isopycnal migration shows higher-frequency components (more turbulent) compared with other terms, especially that the time variation is subseasonal. Obduction is obvious at the density centered around 27 from September to December, with another denser water mass (over 27.2) upwelling from March to June. S_{h2} also displays seasonality for all density classes. A combination between (a) and (e) reveals that obduction might be the prevailing signal for 25–26.5 density classes. Water masses denser than 26.5, on the other hand, are dominated by subduction, with the dual-effect that the outcropping area also reaches its maximum. S_v in (f), which is in large part wind-driven, does not contain as much seasonal variation as the other terms and thus the volume subduction depends upon the outcropping area.

3.3 Eddy component of the subduction rate

In this section, an eddy component of the subduction rate is considered. Note that the eddy calculation here refers to a perspective from turbulence, that is, the multiplication of two time-variant components and its average over time. In specific, the eddy subduction calculation is dependent on the shrinking or expanding of outcrop area over time, and both temporal and spatial resolutions of instantaneous subduction rates.

Figure 2.16 is an equivalent of Figure 2.14, obtained instead from a daily calculation rather than monthly. The left six panels (a1–f1) display an average over all years that resembles patterns shown in Figure 2.14, while the right six panels (a2–f2) illustrate these subduction rates for the year 2016 as an example. A low-filtered version of time-dependent term in (c2), lateral induction term in (e2) and vertical pumping in (f2) is similar to an average calculation in (c1), (e1) and (f1). The migration of isopycnals in (d2), however, contains higher-frequency components compared with (d1), which can lead to offset or enhancement to the total volume subduction rate.

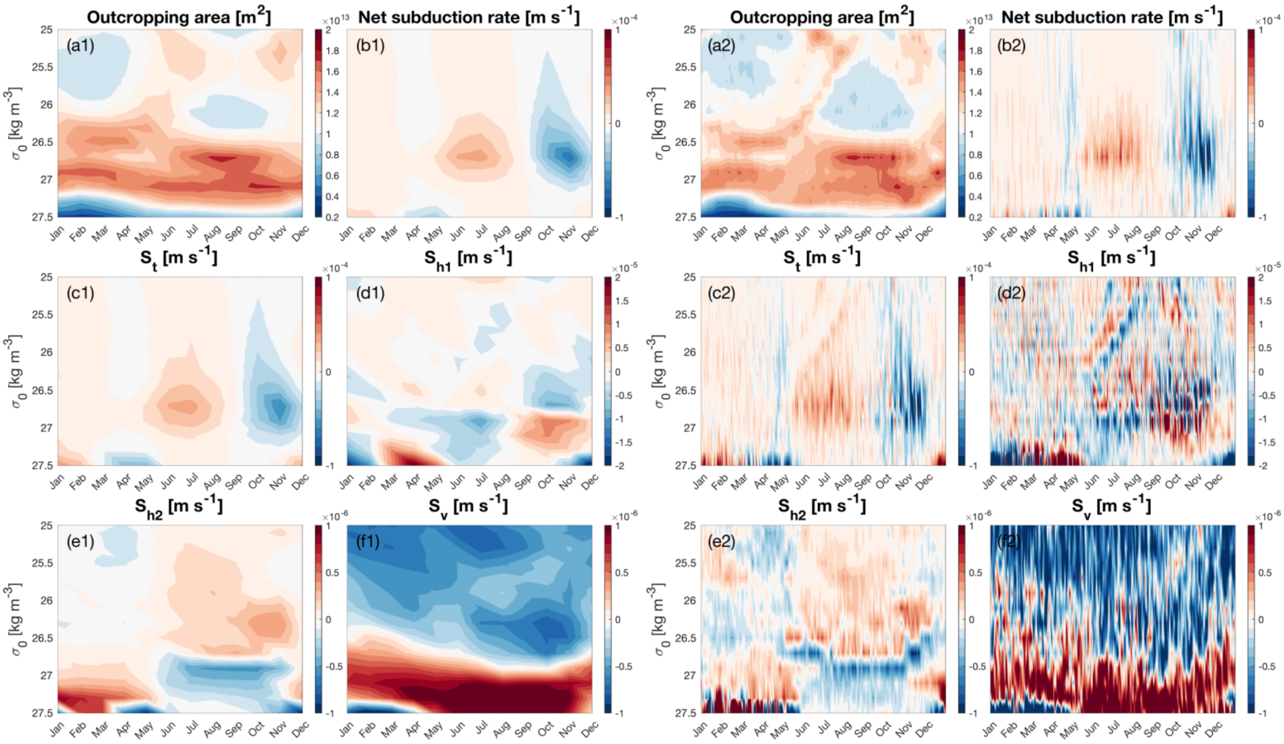

Figure 2.16: (a1) Outcropping area; (b1) net subduction rate; (c1) temporal term S_t; (d1) migration of isopycnals S_{h1}; (e1) lateral induction S_{h2}; and (f1) vertical velocity S_v as a function of time and density. Panels (a2–f2) show patterns for the specific year of 2016 as an example.

Here, we go further to consider the nonlinearity between the time variations of both the outcropping area and the instantaneous subduction rates. To interpret alternatively,

Figure 2.16 shows that both the outcropping areas and instantaneous subduction rates at each density class are dependent on time. For example, if we define daily residual subduction rates as an eddy component apart from their monthly mean, and according to Eqn 2.19, two versions of calculation can be considered in comparison: one with time-dependent outcrop area and the other without. In other words, it is of interest to integrate the total subduction from (a2) and (b), and compare this total volume subduction with the multiplication between their long-term means (a1) and (b1).

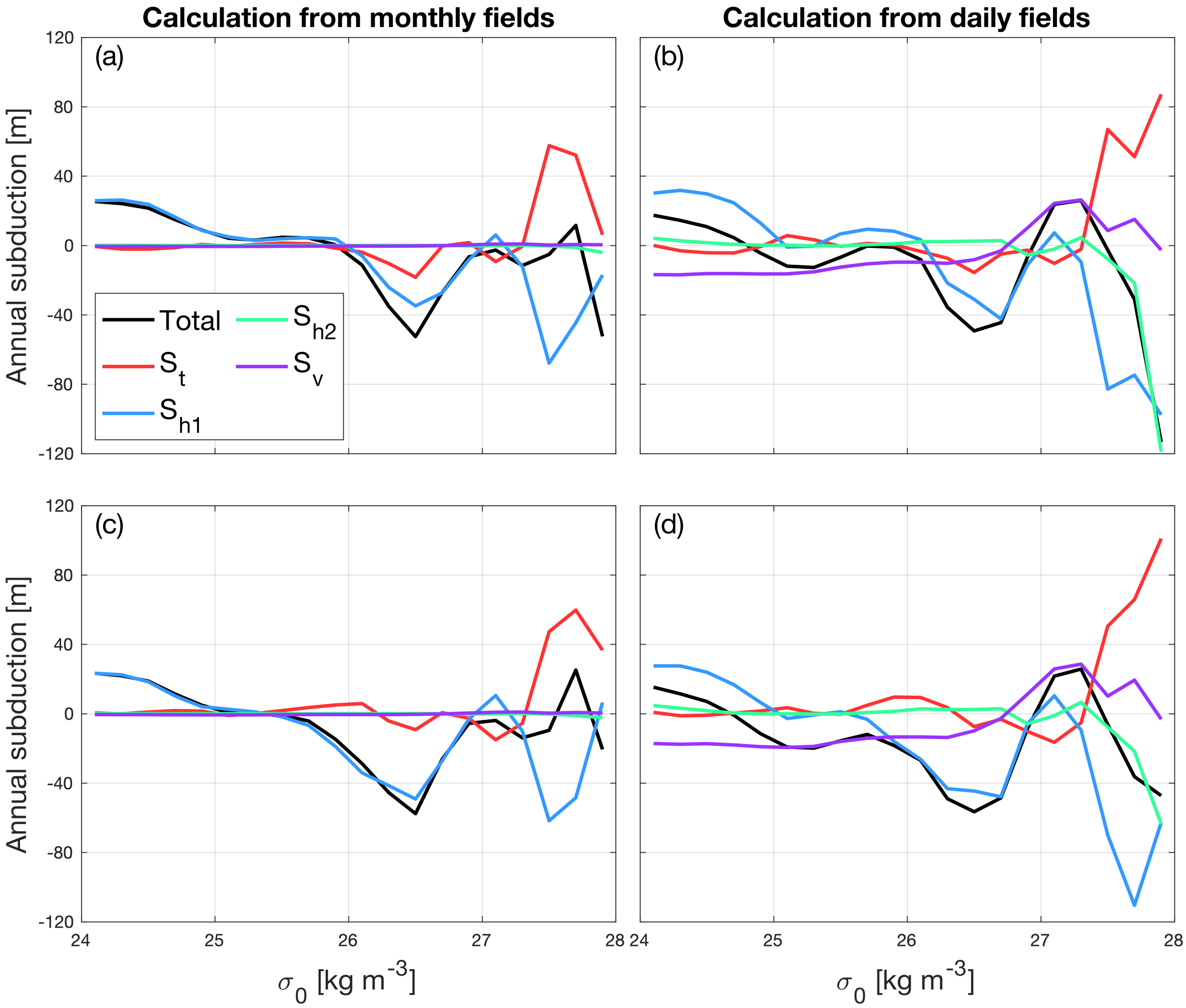

Figure 2.17: The total and separate component of subduction rates. (a) Subduction rate calculated from monthly averaged data over each year. (b) Subduction rate calculated from daily data over each year. (c) and (d) are the counterparts of (a) and (b), further allowing for the variation of outcropping area according to different latitudes.

Figure 2.17 displays such difference in four calculations. Panel (a) shows a monthly-integrated annual subduction of different terms in Eqn 2.16, while panel (b) is an equivalent of (a) but instead integrated over daily outputs. The two terms in the classic theory, vertical velocity S_v and lateral induction S_{h2}, are influenced by this incorporation of time-varying outcrops: both the downwelling at low densities and upwelling at high density levels are enhanced for S_v while the subduction at the highest level of density is increased for S_{h2}. Consistent with spatial patterns of Figure 2.13, the total subduction is determined by the temporal term S_t and a contribution from migration of isopycnals S_{h1} such that at density range 26–27, the total subduction can reach 50 m per year. At higher density classes, i.e., 27.2–28, these two terms counterbalance each other in both (a) and (b). The integration over daily maps leads to an obduction ∼25 m per year for densities 26.8–27.4.

The lower panels of (c) and (d) in Figure 2.17 further account for the variation of areas as a function of latitude. For example, grid boxes at the equator are commonly larger than those near the poles. However, such incorporation does not influence the results much as shown by the similarity between (a) and (c), or between (b) and (d).

4 Discussions and conclusions

The role of the temporal variation in the subduction rates of upper water masses has previously been discussed in modeling studies based on Lagrangian diagnostics (e.g., Woods [Woods, 1985] and Williams et al. [Williams, 1995]) and in theoretical studies based on thermodynamic approaches (e.g., Marshall et al. [Marshall, 1993]). Our study, based on the kinematic approach, agrees with previous studies in suggesting that the main mechanism driving the subduction of mode waters is rapid shoaling of the deep winter mixed layer and the subsequent detrainment of mixed layer waters into the stratified pycnocline in early spring.

It shows that the diagnosed subduction rates of upper–ocean waters differ depending on our choices of the definitions (i.e., across the temporally varying mixed layer base versus across the winter maximum mixed layer base), and choices of temporal resolutions of model solutions (i.e., whether we include the effect of mesoscale eddies). They all contribute to the subduction rate estimates of upper–ocean waters. In particular, we find that the estimates of the subduction rate based on two different definitions [i.e., the Cushman-Roisin [Cushman-Roisin, 1987]'s definition based on the varying mixed layer base versus the Marshall et al. [Marshall, 1993]'s definition based on the time-invariant winter mixed layer base] also divert over mode water density classes. But overall, these two methods correspond well with each other, though the latter usually leads to a larger magnitude of subduction/obduction rate. To understand it from the theory of Stommel's demon, our results suggest that the water masses situated between the seasonal and main thermoclines are capable of subducting permanently.

Our study also shows that the seasonal/subseasonal correlations between the temporal change in the mixed layer thickness and the seasonal/subseasonal expansion/contraction of outcrop areas lead to the net annual transport of mixed-layer waters into the underlying pycnocline: that is, newly formed mixed-layer waters are injected into the pynocline while the winter mixed layer shoals over an expanded outcrop area. This seasonal subduction owing to dual-effect, along with subduction driven by mesoscale eddies [Marshall, 1997], constitutes the dominant mechanism by which global mode waters are formed and transferred to the pycnocline. The seasonal eddy subduction process is most pronounced in SAMW density classes (i.e., 26.4–27.1 in the ECCO estimate) whose winter outcrop positions coincide with the northern flank of the ACC where the mixed layer depths undergo the largest seasonal cycle. The seasonal eddy subduction also plays an important role in determining the net subduction rates of STMW density classes with another important contribution of downward fluid transfer made by Ekman dynamics.

Compared with previous studies, especially Marshall [Marshall, 1997] and its applications to different domains of interest, our study was performed in an Eulerian framework instead of tracking each water mass from a Lagrangian method, eliminating heavy computations and uncertainties of the trajectories of water masses. However, such seasonal and subseasonal variation of outcropping areas is still available by switching to the coordinate of migrating isopycnals. This further allows for an evaluation of subduction rate at the global scale, which was previously achieved mostly by Lagrangian methods [Blanke, 2002; Liu, 2012]. Apart from the ECCO outputs, we can also apply this new version of subduction rate calculation to models with higher resolutions so as to better approximate the contributions from mesoscale eddies or even smaller-scale features. Furthermore, it will be also of interest to quantify the contributions from Ekman dynamics, which was not examined in this chapter since the vertical velocity at the base of the mixed layer was resolved. For example, we can quantify the nonlinear Ekman pumping, as described in Chapter 1, and compare this higher-order effect to the total subduction as shown in this chapter, to visualize the places where this nonlinear pumping prevails for surface water subduction.

Summary

In a nutshell, this chapter of surface water mass subduction compares several mechanisms and assumptions of subduction: 1) the Stommel's demon that only takes into account the surface water mass pumped from the winter mixed layer into the thermocline; 2) contribution from the time-variant mixed layer depth to the annual subduction and its temporal resolution; 3) subduction rate following the migration of isopycnals; and 4) variations of the outcropping area and their combination with instantaneous subduction rates.

Quantification of water masses transmitting from the surface layer into the thermocline is an important scientific question in terms of the current warming climate, since over 90% of the anthropogenic heat released in the entire climate system is taken up by the ocean due to its large thermal inertia. However, the physical mechanisms that absorb, transport, and subduct heat from the surface into the ocean interior need more investigations, especially at the mesoscale and smaller. Specifically in the ventilation theory, temperature can be regarded as a natural tracer, so that once the dynamics and thermodynamics of ventilation is known, the knowledge of ocean heat content uptake is extended.

In this study, we have shown that the variations of outcropping areas at each density class play an important role in controlling the annual accumulative subduction. For example, when this contribution from area expansion or contraction is considered, a net obduction of ∼25 m per year results in at the density range of 27–27.5 kg m^{-3}, which is absent from the calculation without considering the area change. This density class is associated with the densest Subantarctic Mode Water (SAMW), implying that the previous estimates of subduction rates in the Southern Ocean might underestimate the process of obduction.

In the next chapter, we will focus on the phenomenon of mode waters — a specific water mass in the upper ocean — which play an important role in capturing and transporting heat in the ocean interior. Moreover, preliminary studies suggest that mesoscale eddies are key in the formation and transport of mode waters. We will assess these processes from observations.

Chapter 3

Global mode waters at the mesoscale

Objectives

Following the calculation of surface water mass subduction, this chapter provides a revisit to the global mode water detection and its connection with mesoscale eddies. As defined in Chapter 1, mode water acts as a mediator between the mixed layer and permanent pycnocline, carrying a memory of previous atmospheric forcing, and redistributing property anomalies in the ocean interior. This chapter will specially focus on the role that mesoscale eddies play in mode water formation at the surface and subduction along the eddy trajectories.

Contents

1 Introduction

As the largest heat reservoir in the Earth system, the ocean mediates climate variations by directly sequestering CO_2 [Sabine, 2004; DeVries, 2014; Friedlingstein, 2020] and taking up about 90% of the radiative imbalance due to this anthropogenic interference [Levitus, 2012; Cheng, 2017; Schuckmann, 2020]. The spatio-temporal variability of such heat and CO_2 uptake and storage is dependent on various physical mechanisms from both ocean surface and subsurface perspectives. Intuitively, air-sea heat and momentum fluxes generate and modulate sea surface temperature (SST) anomalies, which in turn, provide feedback to these fluxes [Park, 2005]. In addition, studies have also observed and examined a reemergence mechanism of SST anomalies from one winter to another, without maintaining through the summer in between [Alexander, 1995; Deser, 2003; Hanawa, 2004; Liu, 2012]. Such reemergence has been linked to the presence of mode waters capped underneath the seasonal thermocline and characterized by a substantial volume of thermostad or pycnostad (a layer with low temperature or density gradients) distributed broadly in the ocean interior [Hanawa, 2001; Speer, 2013].

Commonly formed due to wintertime convection and buoyancy loss, this homogeneous water mass — mode water — can be thought of as an intermediate state of fluid in the ocean interior that connects, via subduction and mixing, the surface boundary layer with the permanent thermocline [Stommel, 1979; Walin, 1982; Qiu, 1995; Marshall, 1997]. Alternatively interpreted as a transient mediator in ventilation, mode water carries a memory of previous atmospheric forcing acting over the mixed layer deepening [Yasuda, 1997; Bates, 2002; Davis, 2011], as well as a potential ability of reshaping the interior ocean stratification. A reverse process such as obduction can also occur and lead to an upward transfer of fluid from the main thermocline into the surface boundary layer, which provides feedback to the atmosphere via air-sea interactions. In the last chapter, the definition of subduction is mainly associated with the transfer of surface water masses into the permanent thermocline. In this chapter, such definition is relaxed and the development of mode waters from thick mixed layers are sometimes referred to as subduction, since the vertical position of mode waters moves down from the surface, though not beneath the main thermocline.

Mode water is firstly introduced to describe the phenomenon of 18 °C Water in the North Atlantic that repeatedly appears as a thick near-surface isothermal layer in winter [Worthington, 1958]. Extended to define water masses with nearly uniform properties (temperature, salinity, and density etc) over large volumes, mode waters are subsequently recognized and described in every ocean basin, mainly situated on the equatorward side of major mid-latitude ocean fronts [Hanawa, 2001]. Confronting the evidence that over 90% of the buildup of additional heat in the Earth system caused by human activities over recent decades is contained in the ocean [Schuckmann, 2020], and the large thermal inertia of mode waters which are closely linked to air-sea heat exchanges, it also requires attention to the role that these water masses play in regional and global heat budgets of the upper ocean. Understanding the underlying dynamics and thermodynamics of mode water formation, ventilation and dissipation, and quantifying the rates associated with these processes, are therefore one of the key scientific challenges for the climate community.

Since the formation and transport of mode water are highly dependent on the seasonal variability of MLD while the transfer of mass, momentum, and energy across the mixed layer provides the source of almost all motions in the ocean, it is crucial to properly identify MLD and to accurately detect mode water at depth from observations. The most widely employed methods of MLD detection rely on a predefined threshold of temperature or density changes between a reference depth at the surface and the bottom of the mixed layer [Kara, 2000; de Boyer Montégut, 2004], or a critical gradient threshold that the base of mixed layer might satisfy [Dong, 2008]. Simple to apply, nonetheless, these methods are limited in that it is difficult to decide on a single criterion for all profiles in the world ocean. Based on these methods, Holte et al. [Holte, 2009] developed a hybrid algorithm to select the best MLD estimates and the greatest utility of their algorithm lies in its ability to work with temperature-only profiles. This hybrid MLD selection was employed by Schmidtko et al. [Schmidtko, 2013] to construct a global isopycnal upper-ocean climatology, applied by Gaube et al. [Gaube, 2019] in examining the effect of mesoscale eddies on the modulation of MLD, and commonly used to compare with numerical results [Bachman, 2017]. Here, considering the homogeneity of both surface mixed layers and mode waters, we propose a new algorithm that uses the conditions of both the gradients and second derivatives to diagnose vertical features. Low gradients reveal segments of water mass homogeneity, while extreme values of second derivatives indicate the precise depths at which the gradients sharply change. A similar detection applied to historical hydrographic profiling data was developed by Lorbacher et al. [Lorbacher, 2006] that sought for the shallowest extreme curvature as the MLD. Details of this new algorithm and its application to the Argo profiles will be described in this chapter.

Due to the temporal and spatial scarcity of observations in the past, our knowledge of the long-term and basin-scale variability of mode waters remains limited. Early studies discussed characteristics (mainly temperatures) of mode waters along specific ship-based hydrographic sections, e.g., the 18 °C Subtropical Mode Water (STMW) in the North Atlantic [Worthington, 1958] and its equivalent in the North Pacific with slightly cooler temperatures [Masuzawa, 1969], as well as the Subantarctic Mode Water (SAMW) longitudinally varying from 14.5 °C in the western Atlantic to 5.5 °C in the southeast Pacific [McCartney, 1977]. With the increasing coverage of Argo profiles [Argo, 2020], large-scale examinations of mode water properties are able to perform, in addition to a similar feasibility in the visualization of their temporal variability [Hanawa, 2001; Speer, 2013; Tsubouchi, 2016; Feucher, 2019].

Concerning the formation and propagation mechanisms of mode waters, compelling theoretical and observational evidences suggest a considerable contribution of meso- and smaller-scale dynamics. In terms of the mesoscale:

1. Mesoscale eddies have been shown to influence the surface mixed layer depth [Gaube, 2019] and the deepening/uplifting of thermocline [Cessi, 2004].
2. A similar interpretation has that the eddy diffusion plays a substantial role in modifying the winter mixed layer heat budget of the Southern Ocean, by enhancing or offsetting the cooling due to air-sea fluxes and Ekman advection [Sallée, 2008].
3. The contribution of eddies to the subduction rate can cancel that of the Eularian-mean component at leading order, or even substantially dominates the total downward transfer in certain circumstances when baroclinic eddies disperse the convective products away from their formation sites [Marshall, 1997; Xu, 2016].
4. Counter-intuitively, the decadal variability of STMW properties depends more sensitively on the stability of the recirculation gyre (i.e., eddy activities), instead of variations in air-sea fluxes [Qiu, 2007].

The presence of submesoscale processes alters the mode water (trans)formation and subduction in a more complex way, e.g., by producing a potential vorticity source that counter-balances the larger-scale wintertime buoyancy loss [Wenegrat, 2018], enhancing buoyancy gradients due to continuous frontogenesis that subducts surface water masses into the permanent pycnocline [Freilich, 2021], and mixing different water masses along isopycnals yet producing a denser water mass due to nonlinearities in the equation of state [Groeskamp, 2016; Shakespeare, 2017]. These studies provoke us to consider the implications that the ocean small-scale features carry to mediate the nature of mode water ventilation and the incorporated heat budget.

The primary focus of this study is to revisit the detection and separation of mode waters in each ocean basin, and to redefine the windows of their properties. This will be in part achieved by applying the recently developed mixed layer depth (MLD) and mode water detection algorithm [Chen, 2022], in which the searching of these homogeneous layers is determined by positioning gradient and second derivative extremes of temperature and density profiles. The separation of different mode water types in each basin, on the other hand, relies on a statistical method of cluster analysis that binds mode waters with similar properties together [Lloyd, 1982]. Lastly, the co-location between mode waters and satellite-deduced mesoscale eddy positions [Laxenaire, 2018; Laxenaire, 2019; Laxenaire, 2020] further allows for an evaluation of the role that eddies undertake in mode water ventilation and the associated heat content uptake.

This chapter is organized as follows: in the next section, the mixed layer depth and mode water detection algorithm will be introduced, followed by a brief description of the mesoscale eddy detecting algorithm TOEddies in the section 3. The section of results will emphasize 1) the properties of each mode water detected by the new algorithm, 2) the percentage of mode waters co-located with mesoscale eddies, and 3) heat content anomalies residing in mode waters that are transported by mesoscale eddies.

2 Mixed layer depth and mode water detection algorithm

Here, an algorithm of mixed layer depth (MLD) and mode water detection is developed that is applicable to any data suite of vertical profiles, such as the global array of Argo profiles, shipborne conductivity-temperature-depth (CTD) collections and profiling bathythermographs (XBTs) etc. For the global mode water detection, we have applied the algorithm to Argo data since these autonomous floats can provide a vast array of CTD vertical profiles from the ocean surface down to 2000 m [Argo, 2020]. Thus, the contributions of Argo array to the ocean observing system, particularly with regard to the availability of subsurface quantities and extensive coverage of remote ocean areas, are a profound progress to characterize water masses and large-scale motions. Furthermore, these data have been widely used to make accurate estimates of heat and freshwater storage and their transport by ocean currents.

In this study, these profiling data were retrieved from the global TOEddies atlas [Laxenaire, 2019] that not only contains the detection of mesoscale eddies from closed absolute dynamic topography (ADT) contours, but also includes co-location of these detected eddies with Argo profiles. In the original TOEddies atlas, some selections were made to use the delayed-mode Argo data available at the Coriolis Global Data Center (Coriolis GDAC) with quality control flags equal to 1 and 2, which refer to “good observation” and “probably good observation”. These selections then involved a preference of minimum vertical resolution for several depth ranges, and enough observations at the surface and deeper than 1200 m (more details in Laxenaire et al. [Laxenaire, 2020]). The data of profiles satisfying all these criteria are interpolated vertically at a 10-m interval eventually.

In brief, this algorithm firstly interpolates each profile’s properties at equal pressure intervals $\Delta p = 2$ dbar using the Akima spline [Akima, 1970]. Subsequently, it estimates a first guess for the MLD by searching for the extreme curvature[1] of density profile that is located above the extreme gradient. This first estimate is then validated by the density threshold of difference as applied in previous studies of the mixed layer detection. Instead of a derivation from density as the MLD, the identification of mode water is based on temperature profiles. Here, we consider two vertical configurations of mode water, counting both i) outcropping mode waters that capture the processes of formation or renewal close to the western boundary currents and adjacent areas, as well as the influence of inter-basin water exchanges; and ii) subsurface mode waters identified as thick thermostads underneath the seasonal thermocline, implying possible histories of subduction. The detailed description of our approach is provided below accompanied by a flowchart of processes (Figure 3.1) and several detections of surface MLD shown in Figure 3.2.

The detecting algorithm starts with calculations of gradient and curvature profiles. We denote $i = 1$ as the level closest to the surface, then the gradient of the vertical profile at level i is defined by central difference

$$g_{\sigma_0}(i) = \frac{\sigma_0(i+1) - \sigma_0(i-1)}{2\Delta p}, \tag{3.1}$$

where the indication σ_0 as potential density (1000 kg m^{-3} was subtracted from the potential density to produce sigma units) could be switched to θ as potential temperature. Accordingly, the algorithm works for both temperature and density profiles. Also note that the subscript i varies between 2 and $n-1$ with n indicating the length of the profile. This method computes values along the edges of the profile with single-sided differences, $g_{\sigma_0}(1) = [\sigma_0(2) - \sigma_0(1)]/\Delta p$ and $g_{\sigma_0}(n) = [\sigma_0(n) - \sigma_0(n-1)]/\Delta p$, where g_{σ_0} is positive since potential density commonly increases with pressure while g_θ is conversely negative. Then the curvature is given by

$$c_{\sigma_0}(i) = \frac{g_{\sigma_0}(i+1) - g_{\sigma_0}(i-1)}{2\Delta p}, \tag{3.2}$$

where the values at edges also follow single-sided calculations.

---

[1] Lorbacher et al. [Lorbacher, 2006] used the word "curvature" to relate to the second derivative in calculus. In this article, we follow this diction.

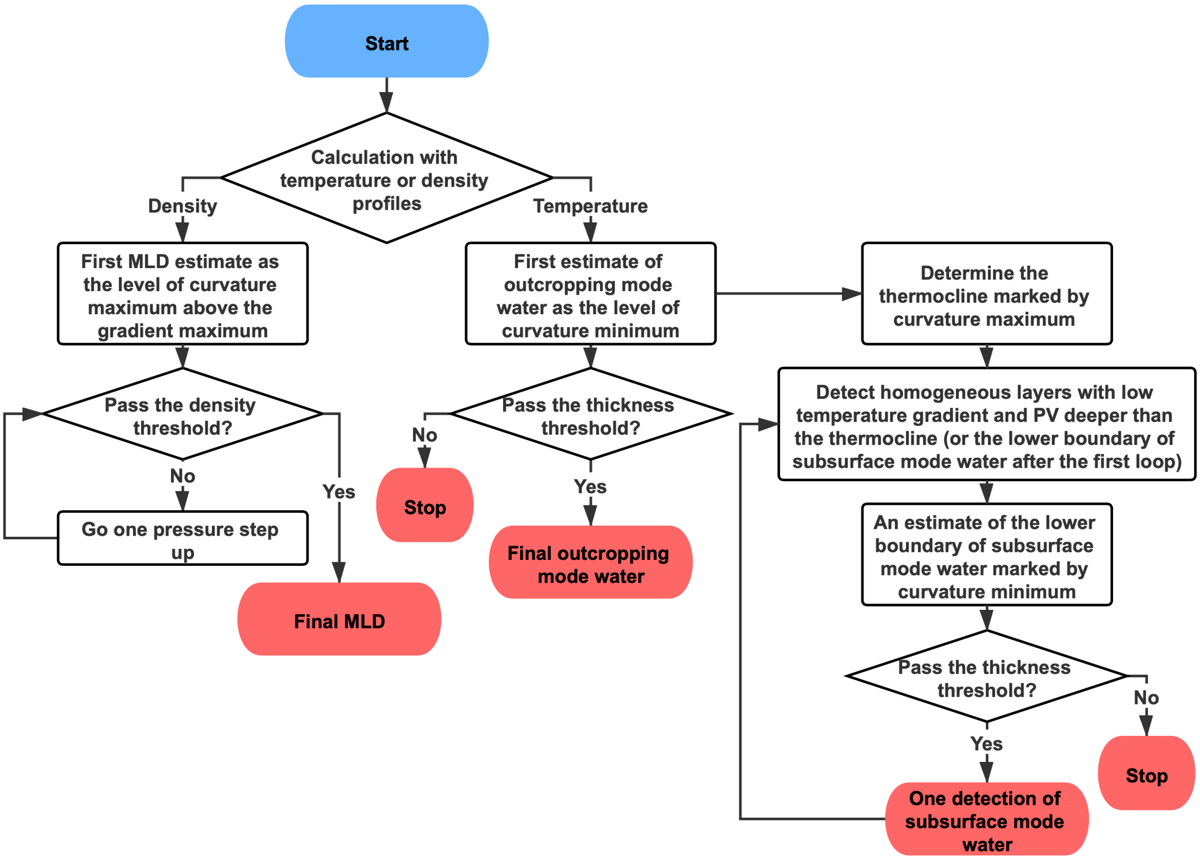

Figure 3.1: Flowchart of the mixed layer depth (MLD) and mode water detecting algorithm to precisely capture the depths and thicknesses associated with these homogeneous layers. While the MLD calculation is based on density, mode waters are identified as thick thermostads. For the detection of mode waters, it goes through temperature as shown here because the searching of extreme values of the second derivatives are based on the temperature profiles. However, potential temperature (similar to density gradient) is also applied as a threshold to find the homogeneous mode waters.

In this study, while the detection of mode water is based on temperature, the MLD is alternatively estimated from density profiles. One of the reasons comes to the phenomena of barrier layers that are typically found in tropical regions or near river mouths [Sprintall, 1992; Sato, 2006]. These barrier layers are named given the conditions of a thick thermostad layer that coexists with a shallower stratification in salinity, and thus are defined by the discrepancy between a deeper temperature-based mixed layer and a thinner density-based mixed layer. It has been shown that the barrier layers exist between the two 20 ° latitudes and the occurrence rates of barrier layer development increase in winter (see Figure 1 in Sato et al. [Sato, 2006]). The thickest barrier layers can be found in the tropical Pacific, along the Antilles Current in the North Atlantic, and in the Bay of Bengal for boreal winters, while some relatively weak ones are observed in the eastern

South Pacific for austral winters. With a focus on well-mixed properties of the surface, density profiles are accordingly used to detect the MLD.

To find the pressure level closest to the bottom of the mixed layer, our next step is to select a good representative of pycnocline (or thermocline in θ profiles) that is indicated by the extreme local values of gradients. Since any pycnocline is a spanning over a depth range rather than a specific level, this detection therefore does not point to a precise diagnosis but rather a lower boundary condition for the MLD. That is, the first estimate of MLD is proposed to be the extreme local maximum of curvature above this approximate pycnocline, given that extreme values of density curvature indicate the depths at which the gradients sharply change.

To validate the MLD detection, a predefined threshold of density is introduced to check whether the density difference between the first detected MLD level and the surface reference depth is lower than this threshold value. That is to say, the density threshold works as a constraint to approve the detection of mixed layer that is homogeneous enough. The surface reference depth is chosen to be the very first one in the profile rather than 10 dbar that is more widely used in the literature, since the profiles have been interpolated in a way that already remove outliers at the very surface. In other words, this validation translates the previous threshold methods in the literature to a new application that verifies the algorithm result. Hence, we follow to set the same values of thresholds as $\sigma_{0th} = 0.03$ kg m^{-3} for density profiles and $\theta_{th} = 0.2$ °C for temperature profiles summarized in de Boyer Montégut et al. [de Boyer Montégut, 2004] and Holte et al. [Holte, 2009]. If the first approximate MLD does not satisfy the validation test against the density threshold, a loop subsequently follows starting with the closest pressure level on top. The bottom boundary of pycnocline (or in some literature the pycnocline itself) can also be marked by the local minimum of curvature below the level of the extreme density gradient.

Some examples are given in Figure 3.2, and in each panel of (a–l), the horizontal blue dash-dot lines indicate the density threshold-determined MLD while the red dash-dot lines represent the density gradient-determined MLD. The black lines indicate the resulting MLD detected by the new algorithm. The geographical locations of these example profiles are also marked by stars in the bottom panel of Figure 3.2. These example profiles were chosen to represent winter MLD in the subpolar region of the North Atlantic (a–d) and along the ACC in the Southern Ocean (e–l), where the deepest convection can occur. In most cases, the algorithm leads to a MLD that is approximately identical to the threshold-based detection, which means the chosen 0.03 kg m^{-3} difference as the “gatekeeper” in this algorithm is indispensable. In addition, as shown in panels (b), (j) and (l), MLD that develops due to deep convection is difficult to capture and thus induces uncertainties in the polar regions.

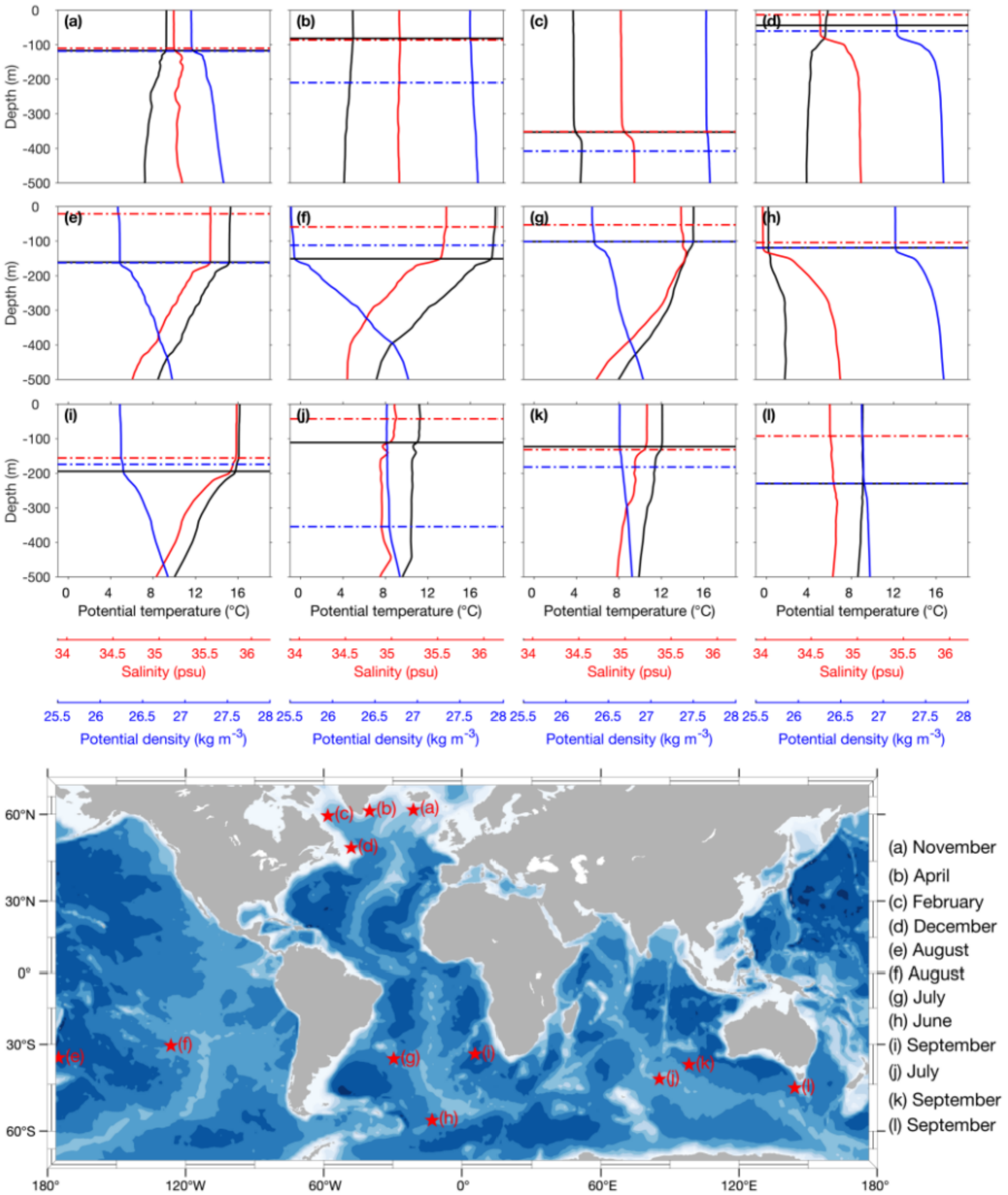

Figure 3.2: Winter MLD examples in the North Atlantic and along the ACC in the Southern Ocean. Panels (a–d) display four examples in the polar North Atlantic, while panels (e–l) are associated with the Southern Ocean. The horizontal black lines indicate the MLD resulting from the new algorithm. Blue and red lines respectively represent the density threshold and gradient methods of MLD detection. The bottom panel locates these profiles and indicates the month of occurrence.

In theory, this gradient- and curvature-dependent algorithm improves the precision of detection compared with previous MLD detecting methods based on threshold criteria. Figure 3.2 features the complexity of the upper ocean vertical structures, indicating that stratification depends strongly on the dynamical regions and seasons. Many other examples are also shown in other domains of the global ocean, e.g., Figure 2 in Lorbacher et al. [Lorbacher, 2006]. This complexity implies that a value of threshold chosen subjectively for one region or season might not be applicable to another condition. At the same time, Lorbacher et al. [Lorbacher, 2006] recognized four systematic biases of the resulting MLD when a threshold is applied to idealized temperature profiles: the uncertainties of the threshold itself; the choices of surface reference value; vertical resolution and lastly the vertical gradient at the base of the mixed layer. Another popular MLD definition takes a prescribed gradient threshold (either temperature or density) as the criterion. The fact that this gradient threshold is usually kept constant for all domains and time, likewise, makes it less robust. The method in this study, on the contrary, allows for each profile to decide on its own MLD by pinpointing the local extreme curvature (with the same set of thresholds functioning as to validate the estimates). Presumably, the first MLD detection marks a distinguished feature of the depth to which the most recent mixing process penetrates.

As summarized in the flowchart of Figure 3.1, the algorithm next detects mode water layers from temperature profiles. This dependence of mode water detection on temperature takes into account a unique vertical structure of undifferentiated density that results from the offset between temperature and salinity stratification. With this regard, mode waters with different origins can thus be separated when the detection is applied to temperature profiles instead of density. Firstly, a similar process to the density-derived MLD detection is implemented in order to identify the outcropping mode water. Such definition can also be found in studies aimed to infer the renewal of mode waters at the sea surface with intense convection [Oka, 2011; Sato, 2014]. Here, we define surface layers thicker than 100 dbar as potential candidates for outcropping mode waters due to their deeply-homogenized thermal characteristics. Similar to the setting of density threshold for MLD validation, $\theta_{th} = 0.2$ °C is applied to validate the homogeneity of outcropping mode water layers from temperature profiles.

To further detect the potential presence of subsurface mode water layers, a limitation on temperature gradients is applied in addition to a typical constraint of potential vorticity (i.e., the subsurface mode water detection requires both homogeneity in temperature and density). The potential vorticity q, when relative vorticity is ignored, is estimated as $q = (f/\rho) \cdot (\partial\rho/\partial z)$, where f is the Coriolis parameter and ρ is the potential density. Any portion of the profile where $|q| <= 1.50 \times 10^{-10}$ m^{-1} s^{-1} is indicated as a candidate for mode water, while the criterion of potential temperature gradient is set to be $|g_\theta| <=$

0.015 °C m^{-1}. These two critical values are applicable to all domains of interest as universal criteria to detect mode waters, whilst other parameters were evaluated, for example in Provost et al. [Provost, 1999] and Sato et al. [Sato, 2014] for the detection of South Atlantic STMW, restrictions on geographical location, temperature, salinity and density ranges were added to facilitate the detection in the specific domain. Accordingly, the selection determined by low potential vorticity and temperature gradient searches for consecutive vertical layers exceeding 100 dbar as the total thickness that contains mode waters in between, and afterwards a similar calculation to that of the mixed layer follows. That is, it then seeks the level of extreme curvature of the temperature profile and specifies this level as the lower boundary of mode water. In some special cases, two or more subsurface mode water cores are obtained using this algorithm, e.g., two mode water cores are discovered to be co-located with each other that are associated with a subsurface-intensified anticyclonic Agulhas Ring (which will be shown in Chapter 4).

This algorithm for MLD and mode water detection has also been tested with other databases, e.g., temperature profiles of expendable bathythermographs (XBTs), hydrographic CTD profiles and gridded climatologies. And to generally compare the new algorithm's applicability with mode water detecting methods for other subtropical basins, Table 3.1 displays a collection of methods developed in the literature. In an attempt to search for layers of weak stratification, methods based on density profiles tend to look for density gradient minimum that is approximately equivalent to searching for the lowest potential vorticity [Provost, 1999; Sato, 2014; Feucher, 2016; Xu, 2017], whilst methods in terms of temperature accordingly seek for a thermostad [Roemmich, 1992; Kwon, 2004; Tsubouchi, 2007; Tsubouchi, 2010; Wu, 2020]. For the latter, the layer with minimal temperature gradients is also referred to as the core layer of mode water and has been used to determine the upper and lower boundaries of mode water. For example, Tsubouchi et al. [Tsubouchi, 2016] made a comparison of mode waters in five subtropical basins by computing the core layer temperature (CLT) that is the temperature found at the depth of gradient minimum. In each subtropical gyre, CLTs of all profiles are averaged and mode water in each profile is then defined as a window spanning over the averaged CLT ±1°C with the layer thickness greater than 100 m. In other studies, the specific thresholds of temperature or density gradient (or PV) that have been applied to define the boundaries of mode waters in certain domains remain empirical.

Figure 3.3 shows a schematic of co-location between mode waters and mesoscale eddies. Panel (a) displays a typical difference between surface anticyclones and cyclones, with vertical structures characteristic of the first baroclinic mode that tend to lower and raise the main thermocline respectively. This difference implies that anticyclones at the surface are associated with lighter water masses and warm sea surface temperature (SST) anomalies, while cyclones are instead detected as cold-core anomalies with higher density.

Therefore, near-surface mode waters with homogeneous properties are closely linked with anticyclonic eddies.

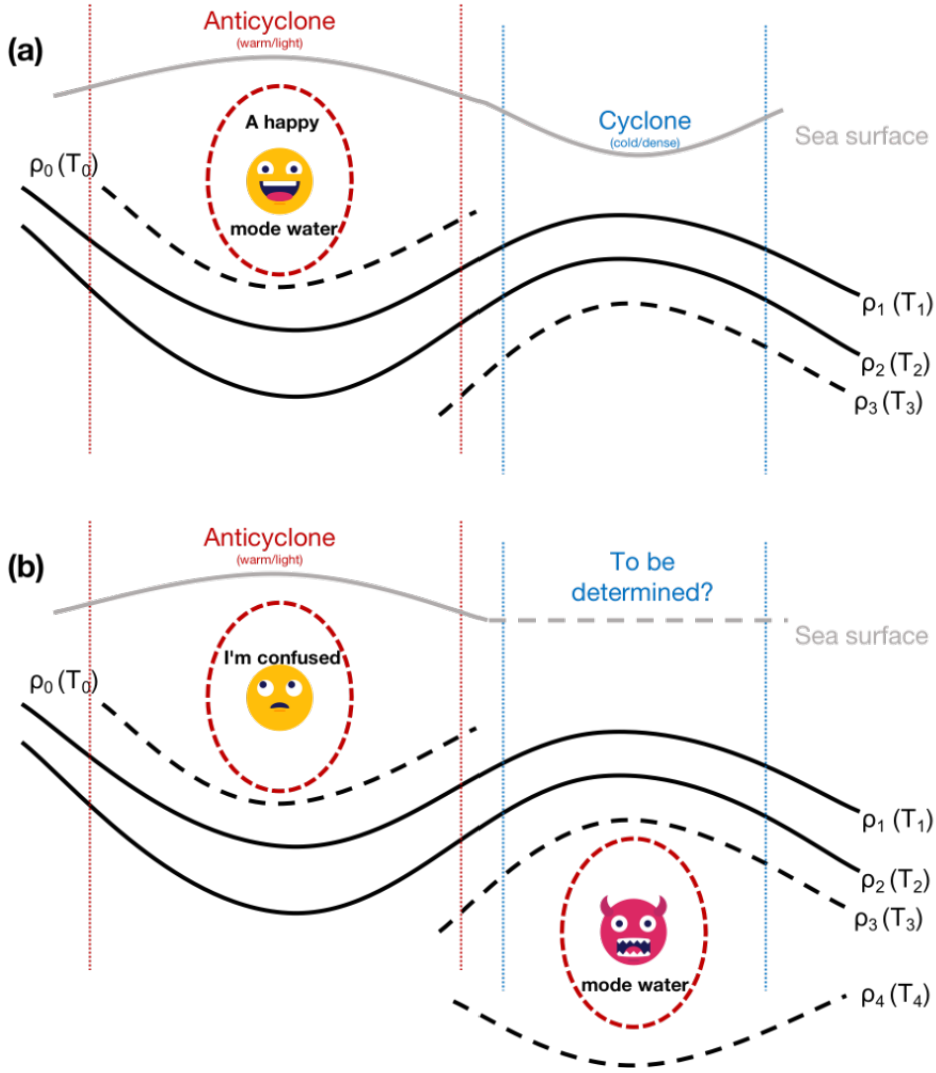

Figure 3.3: Schematics of (a) a typical difference between anticyclonic and cyclonic eddies, with near-surface mode waters co-located with anticyclones; (b) an appearance of subsurface mode waters within the seasonal and permanent thermoclines, which complicates the sea surface height anomaly. If dominated by the structure of permanent thermocline, this mode water still imprints as positive sea surface height anomaly at the surface, detected as an anticyclone.

However, more complex vertical structures are not uncommon. Specifically, as shown in (b), if any mode water subducts between the seasonal and main thermoclines, this bolus of fluid tends to depress the main thermocline and raise the seasonal thermocline. Displacement of the main thermocline in common cases dominates both geostrophic velocity and sea level perturbations, such that these mode waters are detectable as positive sea level anomalies in satellite altimetry (i.e., anticyclonic rotation). This phenomenon is sometimes referred to as intrathermocline eddy or submesoscale coherent vortex, depending upon the depth of its eddy core [Gordon, 2017; Barceló-Llull, 2017; Meunier, 2018]. Their velocity field is characterized by a deep maximum of azimuthal velocity presenting an azimuthal symmetry [Thomas, 2008a], and thus, these eddies are particularly abundant in the vicinity of major intermediate water outflows linked to baroclinity. An analogous second baroclinic mode structure in the cyclonic case is upward displacement of the main thermocline and downward displacement of the seasonal thermocline (not shown), resulting in a thinner cyclonic eddy compared with the normal case shown in (a).

These mode-water eddies contained between the seasonal and permanent thermoclines have origins that could be traced back considerable distances from where they were sampled, as revealed by water mass analysis, transient tracer distributions, and backtracking of their trajectories via satellite altimetry (e.g. in McGillicuddy et al. [McGillicuddy, 2007]). As such, their complex vertical structure is attributable at least in part to their nonlocal origins: a bolus of mode water formed south of the Gulf Stream could have been subducted, subsequently penetrating into the Sargasso Sea as a mesoscale eddy [Ebbesmeyer, 1986].

Figure 3.4 displays an example of mode water detection by the new algorithm applied to a hydrographic CTD section [Stevens, 2021]. This section is co-located with an anticyclonic eddy detected from the altimetric absolute dynamic topography (ADT). A mode water with the thickness of $\sim$ 400 m has been identified underneath, appearing as an oxygen pool just below the seasonal thermocline.

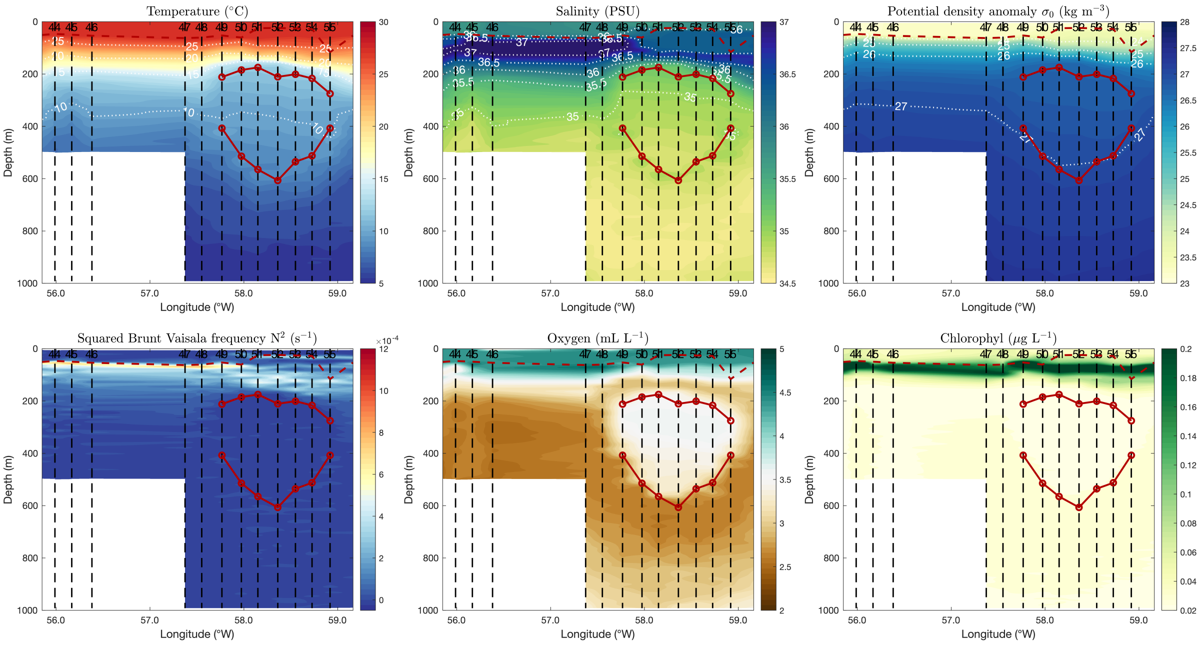

Figure 3.4: One example of mode water detection from a hydrographic section during the EUREC^{4}A campaign [Stevens, 2021]. The mode water underneath surface detection of anticyclonic eddy is delimited by the red lines with circles.

Animation: an example of mode water detection from Argo profiles (NASTMW)

Also available by clicking here.

Table 3.1: Methods of subtropical mode water detection in the global ocean.

Subtropical domains	Data in use	Methods	References
North Atlantic	Climatology (WOD2001) and profiling data (both from WOCE floats and Argo)*	To look for temperature gradients less than 0.006 °C m^{-1}	Kwon et al. [Kwon, 2004]
	Argo	To seek stratification minimum (N^2) and also to refer to the maximum as pycnocline	Feucher et al. [Feucher, 2016]
South Atlantic	Hydrographic CTDs and XBTs	To look for potential vorticity minimums (and then determine the thresholds of temperature gradient adapted to different mode water types)	Provost et al. [Provost, 1999]
	Argo	To search for potential vorticity less than 1.50 × 10^{-10} m^{-1} s^{-1}	Sato et al. [Sato, 2014]
North Pacific	Argo	To look for potential vorticity less than 2.0 × 10^{-10} m^{-1} s^{-1}	Xu et al. [Xu, 2017]
	Climatology (Ishii, EN4 and IAP data)*	To seek temperature gradients less than 0.015 °C m^{-1}	Wu et al. [Wu, 2020]
South Pacific	XBTs	To look for temperature gradients less than 0.02 °C m^{-1}	Roemmich et al. [Roemmich, 1992]
	Climatology (WOD2001) and two HRX lines*	To seek temperature gradient minimum	Tsubouchi et al. [Tsubouchi, 2007]
Indian Ocean	Climatology (IOHB)*	To seek temperature gradient minimum	Tsubouchi et al. [Tsubouchi, 2010]

[*] The WOD2001 represents the World Ocean Database 2001 that is a collection of objectively analyzed climatological data, and the WOCE stands for the World Ocean Circulation Experiment of which some temperature profiling data were used in this study.

[*] These three datasets provide three-dimensional monthly grid temperature and salinity data [more details in Wu et al. [Wu, 2020]].

[*] The HRX denotes the high-resolution XBT that was used to collect temperature profiles along a number of shipping transects by the Scripps Institution of Oceanography.

[*] The IOHB represents the Indian Ocean HydroBase climatology.

3 Cluster analysis

Here, mode waters detected in each basin are classified by a statistical method of cluster analysis into several groups. This is accomplished by a non-hierarchical clustering method known as the k-means [Lloyd, 1982]. Since the k-means method requires a predetermined number k of clusters, an evaluation follows to assess the performance of the previous clustering. For each domain of interest, we have applied several choices of this predetermined number k and at the end selected the best option.

The basic concept of the cluster analysis is that all mode water profiles are partitioned into k mutually exclusive clusters, such that mode waters within each cluster are as close to each other as possible, and as far from mode waters in other clusters as possible. Each cluster is characterized by its centroid and mode waters are sorted relative to the distance to this centroid with the condition that the sum of the squared Euclidean distances within each cluster is minimized.

The vertically-averaged potential temperature, salinity, potential density and potential vorticity inside each mode water layer are used. These four parameters accompanied by the latitude, longitude and depth compose the seven variables that are treated equally for the classification of mode waters in the Northern Hemisphere (i.e., separate cluster analyses in the North Atlantic and North Pacific), whereas for the Southern Hemisphere only latitude is added as the fifth parameter. We have tested several choices of k as shown in Figures 3.13, 3.14 and 3.17. In the North Atlantic, it is evident that the EDW is clearly separated out no matter how many clusters we have chosen at the beginning. In terms of a relatively small number of mode waters detected in the North Pacific, the result in Figure 3.14 displays that $k = 2$ divided the mode waters precisely into a subtropical variety and another type slightly colder and fresher.

4 Mesoscale eddy detection: TOEddies

In this thesis, MLDs and mode waters detected from Argo profiles have been co-located with mesoscale eddies derived from the TOEddies algorithm [Laxenaire, 2018; Laxenaire, 2019; Laxenaire, 2020]. Such eddy detection algorithm follows the evolution of several eddy detecting methods, based on the primary assumption that for geostrophic eddies, the streamlines correspond to the closed contours of sea surface height. This algorithm is a two-step process: it identifies the occurrence of eddies before deriving their trajectories.

At the beginning of eddy detection, this algorithm first identifies the local extrema of ADT fields as possible eddy centers. Then, it looks for the outermost closed ADT contours around each extremum center containing at least 4 grid points. An eddy amplitude is thus defined by the ADT difference between the center extremum and the outermost contour, which is then bounded by a minimum constraint that determines whether this ADT center can be considered as an eddy. This parameter (the eddy amplitude threshold) can be interpreted as eddy persistence that has been widely used, for example, to eliminate any artificial separation of a large eddy into two or more smaller elements. In the TOEddies algorithm, this parameter is set to be 1 mm.

The detected ADT extrema that pass the persistence threshold are each identified as the center of an eddy. The size of each eddy is then characterized by two distinct radii. The equivalent outermost radius, R_{out}, which corresponds to the radius of a disk having the same area (A_{out}) as that delimited by the outermost closed ADT contour. Its value is given by $R_{out} = \sqrt{A_{out}/\pi}$. However, the outermost closed contour is often strongly distorted by the surrounding flow and interactions with others mesoscale structures. For this reason, the TOEddies algorithm also derives a radius that corresponds to the ADT contour along which the mean azimuthal geostrophic velocity is maximum, defined as R_{Vmax}. Figure 3.5 displays one example of eddy detection near the Agulhas Current, with two cyclones on either side of an anticyclone. It is evident that R_{Vmax} is always smaller or equal to R_{out}.

For the second step, a complete and continuous set of eddy trajectories is recovered by following the paths of the eddies between successive ADT maps. Since mesoscale eddies move slowly (displacements of less than 10 km/day) compared with their radii of $\sim$ 100 km, the areas covered by the same eddy for two consecutive days overlap. In this second step, the outermost eddy contour has been used to track the overlapping area. Another threshold is introduced here that is to compare with the ratio of the overlapping area to the area of the smaller eddy. This threshold thus enables a more robust tracking of the same eddy in its history of trajectory.

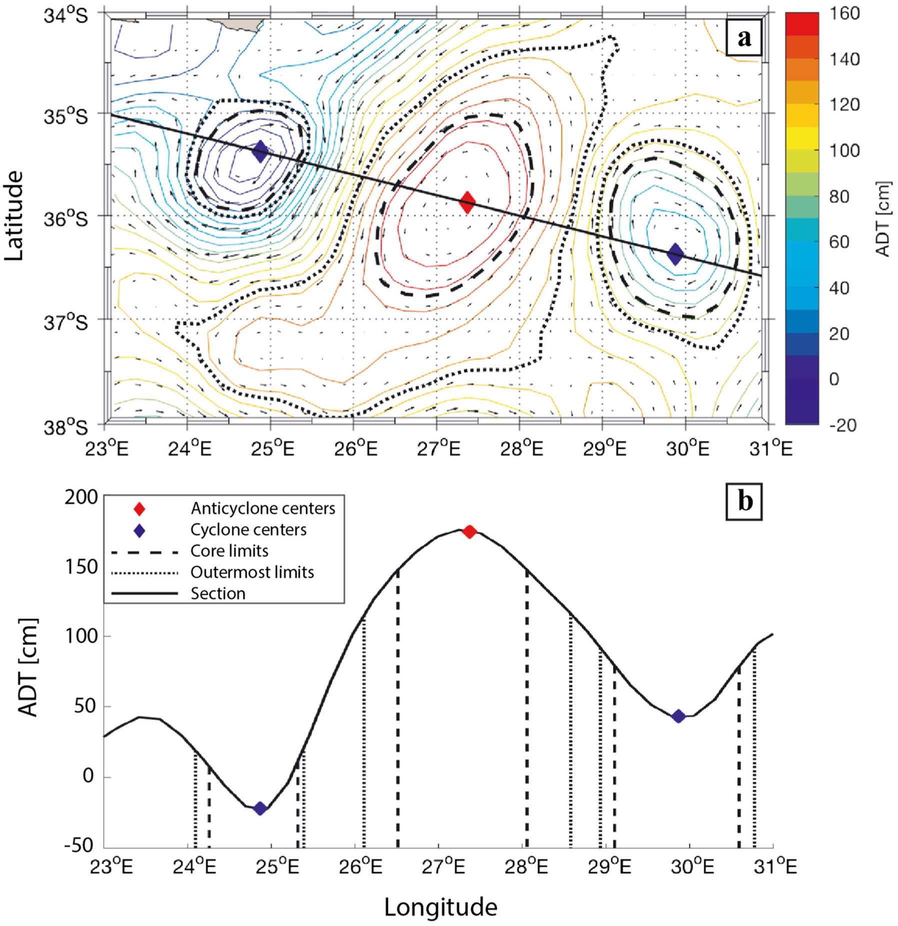

Figure 3.5: Example of eddies detected near the Agulhas Current on 23 March 2000. Two cyclones and one anticyclone are shown in (a) an absolute dynamic topography (ADT) map and (b) in terms of ADT amplitude along a section crossing the extrema of the eddies detected in (a). For each eddy, the ADT contours where the azimuthal speed is maximum (eddy core limit definition: dashed lines) and the outermost closed contour (eddy outer limit definition: dotted line) are shown. ADT isolines with 10-cm intervals and the geostrophic velocity vectors distributed by AVISO are superimposed in (a). (Source: [Laxenaire, 2018]).

Nonlinear interactions between distinct eddies or between eddies and topography are some of the processes that can induce the splitting or merging of eddies. The TOEddies algorithm belongs to the very few eddy detection and tracking algorithms that consider both processes. It combines the separation of a large eddy with two or more smaller eddies in the case of splitting and relates the coalescence of two or more small eddies into a larger eddy in the case of merging. To take these processes into account, a relationship tree is created to associate each eddy with its potential parents and children. Independent eddy trajectory segments are constructed by scanning this tree. These segments are trajectories that link the eddy positions between the merging and splitting events. Therefore, each segment begins either after the detection of a new eddy, or after the merging/splitting of eddies, and makes an end at the time step before a new eddy-eddy interaction or when the eddy disappears from the altimetry maps.

After constructing segments of eddy merging and splitting events, the next step is to combine these segments to reconstruct the main eddy trajectories. Here, a cost function has been applied, which takes into account the distance between the successive eddies and the change of surface properties near the eddy core. Independent segments that minimize the cost function are linked together. The resulting long series of segments is identified as the main eddy trajectory. The remaining trajectories are classified as the result of an eddy splitting from the main trajectory or an eddy merging with the main trajectory. Figure 3.6 shows one eddy trajectory that consists of several segments assigning to an order. In this formalism, the order 0 of the trajectory network is the main trajectory identified by applying the cost function for each occurrence of merging and splitting. With order 1, segments are linked to the main trajectory either by an eddy splitting or an eddy merging. Similarly, the order 2 refers to segments that are associated with eddy merging or splitting with order 1 trajectories, etc. This recursive classification in ordered trajectories continues until no new orders are detected. Each network is therefore associated with an order n of trajectories. The order 0 of each network of trajectories is defined according to the target of the study as, for example, the assessment of the origin and fate of a mesoscale eddy identified by in-situ observations or a global view of mesoscale eddies formed in a particular region of the ocean, such as the Agulhas Rings in the study of Laxenaire et al. [Laxenaire, 2018].

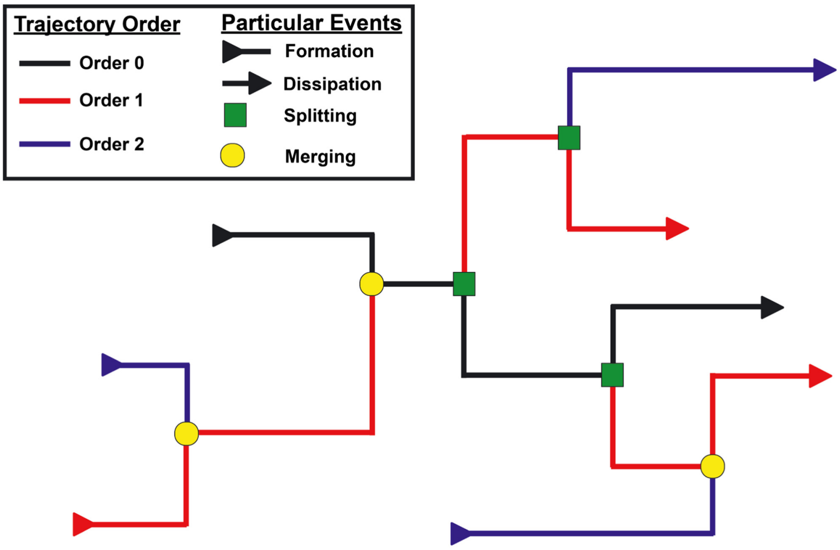

Figure 3.6: A schematic of a simple network of trajectories up to order 2. This network is characterized by four formations, four disappearances, and three merging and splitting events. With each merging and splitting, the cost function is applied to follow the main trajectory by associating a segment with a higher order. (Source: [Laxenaire, 2018]).

Figure 3.7 provides two examples of order 0 eddy trajectories associated with Agulhas Rings that originate from the southern tip of Madagascar and end at the far western boundary of the South Atlantic. The eddy shown in (a) forms near Madagascar and remains very coherent until it reaches the Cape Basin, while the eddy trajectory in (b) indicates a more complicated evolution of eddies in terms of the resizing and merging/splitting of Agulhas Rings.

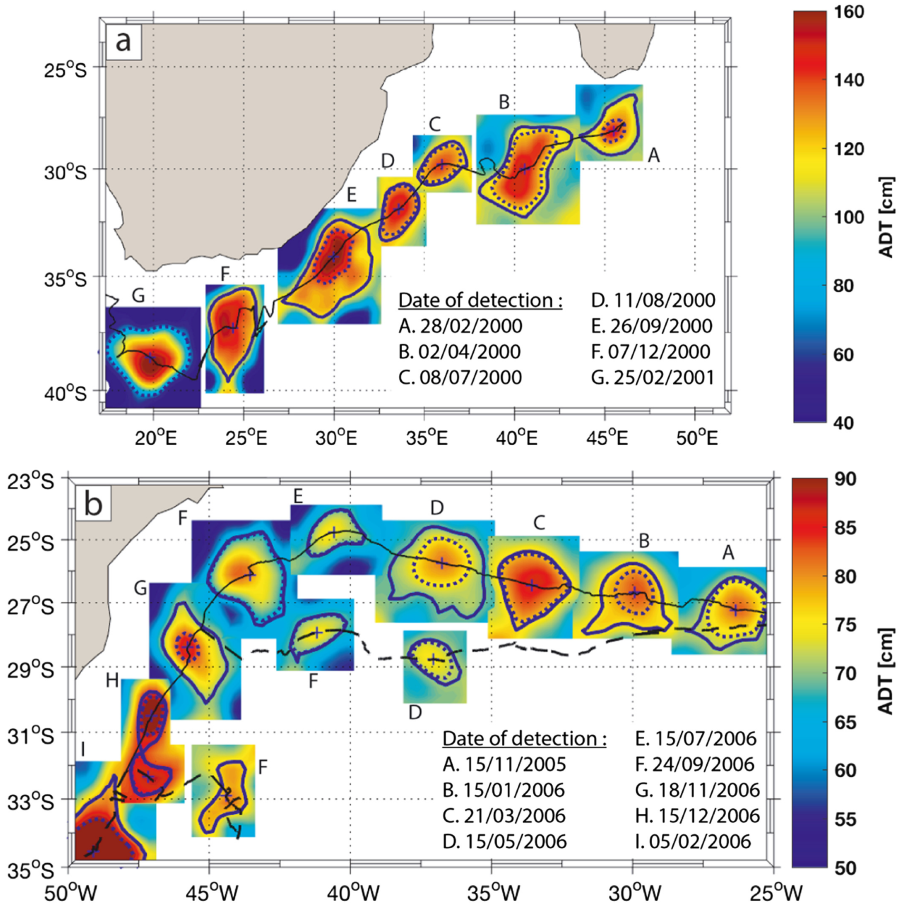

Figure 3.7: A composite figure of the order 0 Agulhas Ring Eddy Network (a) starting from the eastern boundary and (b) ending by the western boundary. Snapshots on selected dates are given, in blue the eddy centroid (cross symbol), the absolute dynamic topography (ADT) contour associated with the maximum speed (dotted), and the outermost ADT (solid line) contours. The trajectory of panel (b) interacts with two order 1 trajectories whose paths are drawn in dashed lines. (Source: [Laxenaire, 2018]).

Figure 3.8 (a) and (b) display a whole set of Agulhas Ring trajectories (from order 0 to order 29) and the percentage of time during which each 1° × 1° grid cell is inside an anticyclonic eddy. It is evident that TOEddies provides a very different overview of the origins, pathways, and fate of Agulhas Rings. Compared with previous eddy tracking methods, TOEddies is able to construct long trajectories of Agulhas Rings that travel across the entire basin to reach the southern end of the South Brazil Current. Panel

(a) also indicates that the eddies contributing to the formation of Agulhas Rings may originate from the southwestern tropical Indian Ocean, further upstream than the Agulhas Retroflection. Figure 3.8 (c) and (d) show that the fastest westward propagating eddies correspond to the western boundary currents of the Indian Ocean and South Atlantic.

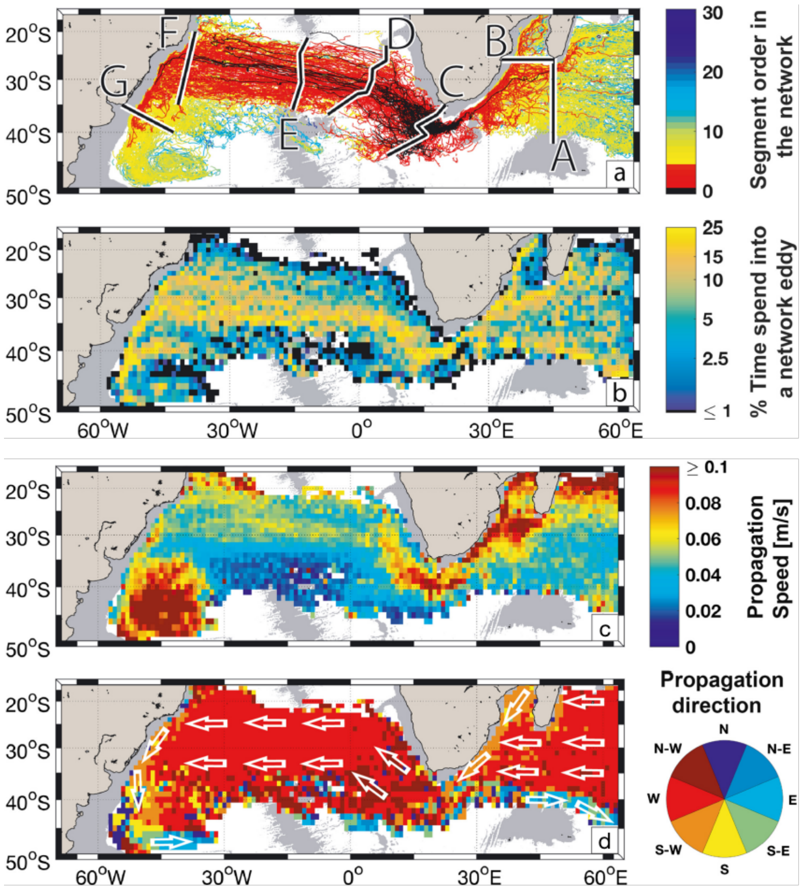

Figure 3.8: (a) Whole set of Agulhas Ring Eddy Network trajectories (from order 0 to maximum order 29). (b) Percentage of time each 1° × 1° grid cell is within an Agulhas Ring Eddy Network trajectory. (c) Median of the propagation velocity of the Agulhas Ring Eddy Network (m/s) and (d) associated main propagation direction. These properties are calculated on a 1° × 1° grid, and the propagation direction is computed from the eddy positions 1 week apart. Schematic white arrows have been added in the bottom panel to highlight the main propagation direction. (Source: [Laxenaire, 2018]).

5 Results

This section of results will first consider the global distribution of mixed layer depths and its connection with eddies, followed by a revisit to each mode water type in the global ocean that is newly detected and redefined from the algorithm.

5.1 Global mixed layer depth and its connection with mesoscale eddies

The MLDs produced by four different methods are considered here so as to evaluate the new algorithm's ability of detection. The four MLD estimates for each Argo profile are 1) the algorithm's calculation that pinpoints extreme values of the density second derivative, 2) the density threshold estimate (threshold of 0.03 kg m^{-3} from de Boyer Montégut et al. [de Boyer Montégut, 2004]), 3) a density gradient estimate (criterion of 0.0005 kg m^{-4} from Dong et al. [Dong, 2008]), and 4) a hybrid method that assembles a suite of all possible MLD values and then selects a final estimate [Holte, 2009].

Figure 3.9 displays such comparison of these four methods by showing the winter-averaged MLDs over years 2000–2018. As expected, the thickest mixed layers calculated from the new algorithm are located in the (sub)polar region of the North Atlantic and the subpolar portion of the meandering ACC bounded within the Pacific and Indian Oceans. These thick layers might indicate and presuppose hotspots of mode water formation and subduction [Marshall, 1993; Liu, 2012; Sallée, 2010], particularly associated with the North Atlantic Subpolar Mode Water (NASPMW) and Subantarctic Mode Water (SAMW). Relatively thick mixed layers are also found in the vicinity of western boundary currents of subtropical gyres.

In the South Atlantic subtropics, a discussion on the striking consistency between the new algorithm's resulting MLD and that of the density threshold method indicates that such predefined density difference between the mixed layer bottom and surface is necessary, though it is applied in the former method as a gatekeeper to approve or refuse the resulting MLD estimated at the second derivative maximum [Chen, 2022]. However, this is not true when it comes to high latitudes. As shown in Figure 3.9 (b), both the subpolar North Atlantic and ACC fronts delimited within the South Pacific and Indian Oceans imply a more conservative MLD estimate of the algorithm, compared with the threshold method. While the density gradient method results in thinner MLDs almost everywhere in the ocean (except in the polar regions with higher uncertainties), the difference between the new algorithm and the hybrid method [Holte, 2009] leads to opposite trends in low and high latitudes (see Figure 3.9 (c) and (d)).

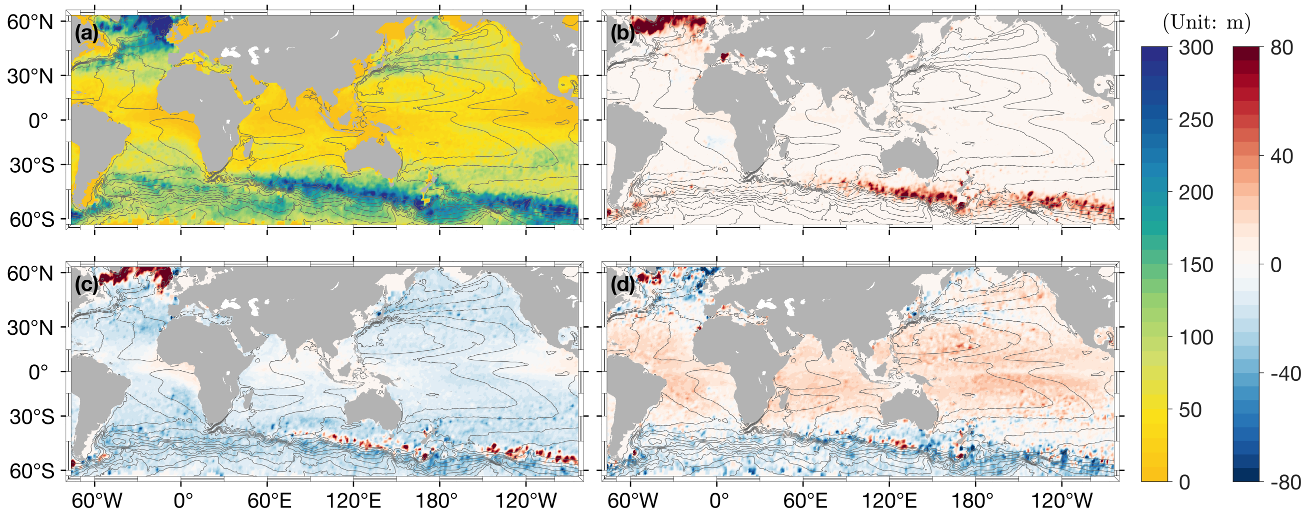

Figure 3.9: Winter-mean mixed layer depths (MLDs) detected by the newly-developed algorithm [Chen, 2022] and three other classic methods. The boreal or austral winters are defined as December to March or June to September. Panel (a) displays the general distribution of MLDs calculated from the algorithm, while other panels show the differences between the algorithm and other detecting methods, namely, (b) the density threshold method, (c) the density gradient method, and (d) a hybrid method developed by Holte et al. [Holte, 2009]. The overlapping grey contours indicate the mean dynamic topography (MDT) as an estimate of the mean sea surface height above geoid over the 1993–2012 period [Mulet, 2021]. These MDT contours are used to provide the structure of the upper-ocean circulation.

This uncertainty among different methods at high latitudes of the Northern and Southern Hemispheres might be in part due to deficient data coverage. For example, in the North Atlantic the yearly-averaged number of profiles captured within $50 - 65$ °N for the boreal winter is 880. In comparison, the subtropics are sampled on average by 3000 profiles per year for the same latitudinal span (15 °). Another contributing factor might be associated with vertical profiles that do not vary greatly with depth. In other words, the upper-layer superimposition (memory) of the imprint of consecutive intense events such as mixing, advection, and entrainment generates a weak layering of the upper ocean (see Figure 3.2 for the complexity of profiles in the subpolar North Atlantic and Subantarctic region). In addition, different performances of these four MLD detection methods within regions of high eddy kinetic energy (EKE) such as the Southern Ocean might arise from the rapidly changing (sub)mesoscale eddies and filaments that constantly modulate the spatial evolution of the mixed layer [Gaube, 2019]. Several systematic biases were also proposed for the density threshold and gradient methods, with the largest concern arising from the uniform criterion itself [Lorbacher, 2006].

Figure 3.10 (a) of annual accumulative heat flux indicates locations of possible mode water formation sites (in blue), encompassing the western boundary of each basin and the

ACC. These regions are also characterized by high level of EKE shown in (b). Since mode waters are found beyond their outcropping area as a result of advection both by the main currents and eddies, our focus here is to assess the possible impact of the latter on mode water formation and propagation in the ocean subsurface. The presence of anticyclonic and cyclonic eddies shown in (c) and (d) coincides with the high EKE hotspots of the global ocean outside the near-equatorial regions. Trajectories of long-lived anticyclonic eddies in (e) depict westward and equatorward inter-basin connections, e.g., Agulhas Rings spawned from the Agulhas Current into the South Atlantic, and eddies in the South Indian Ocean that are leaked from the Eastern Australia and Tasman Sea. A similar cross-basin connectivity of eddies is also observed in the North Atlantic and Pacific. Pathways of cyclones, on the other hand, display a more zonal pattern if not slightly poleward with the longest-lived bunch of eddies propagating in the Indian Ocean that are injected along the west coast of Australia.

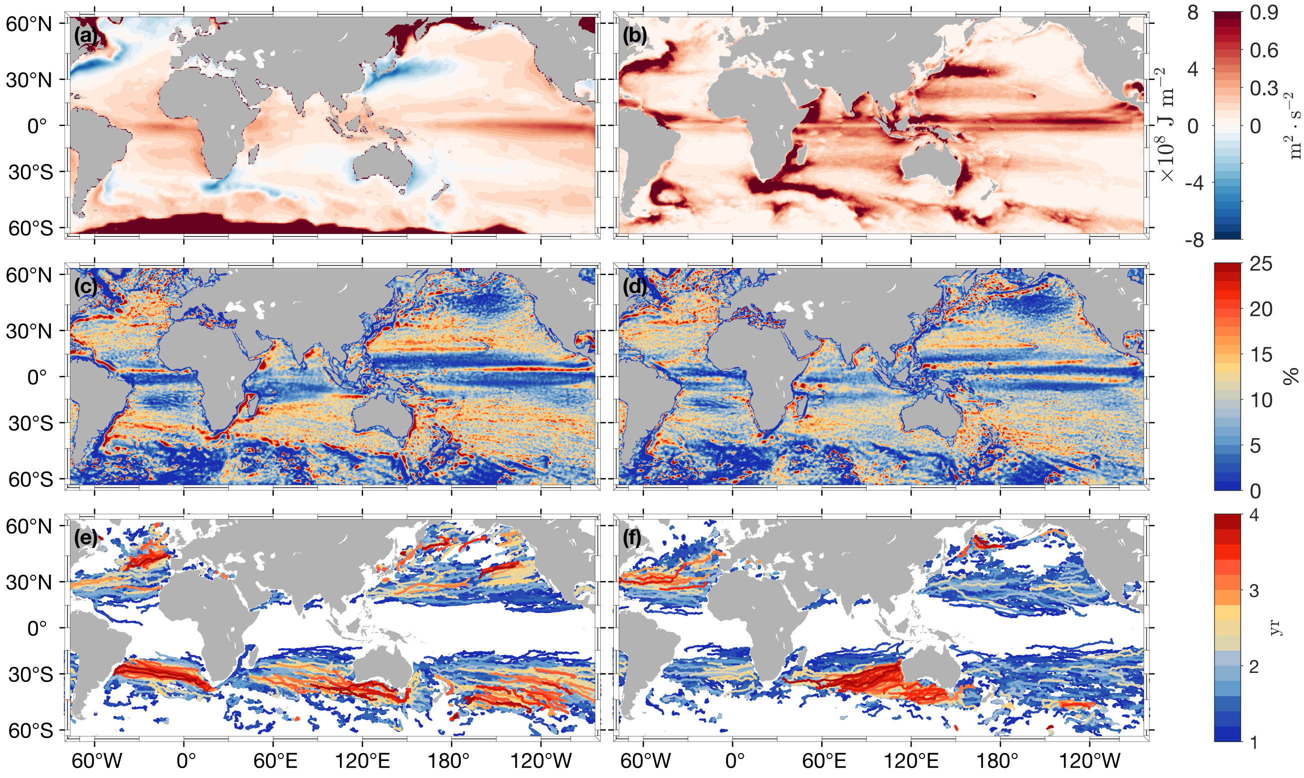

Figure 3.10: Spatial patterns of (a) the cumulative heat flux (positive downward) calculated by adding the daily maps between 2002 and 2009 from the WHOI OAFlux Project [Yu, 2008], and (b) cumulative eddy kinetic energy (EKE) derived from the sea level anomaly (SLA) field and based on the geostrophic relationship [Pujol, 2016]. Panels (c-f) provide characteristics of mesoscale eddies detected by the TOEddies algorithm from the satellite ADT maps [Laxenaire, 2019]. They include (c) the presence of anticyclonic eddies indicated by percentage and (e) trajectories of anticyclonic eddies along their lifetimes. Panels (d) and (f) show the same information for cyclones.

Figure 3.11 displays the mixed layer depths co-located with mesoscale eddies. This co-location reveals rich geographic and seasonal variability in the influence of eddies on MLD. In general, anticyclones deepen the mixed layer depth, whereas cyclones thin it, with the magnitude of these eddy-induced MLD anomalies being largest in winter, as shown in the middle column of Figure 3.11. Moreover, large eddy-mediated mixed layer depth anomalies are more common in anticyclones when compared to cyclones, i.e., the mixed layer deepened by anticyclones is more intensified compared with the mixed layer shoaled by cyclones. The last column in Figure 3.11 display the summer MLD co-located with eddies. It is evident that cyclonic eddies lead to shallower mixed layers in summer, albeit a smaller reduction compared with that in winter.

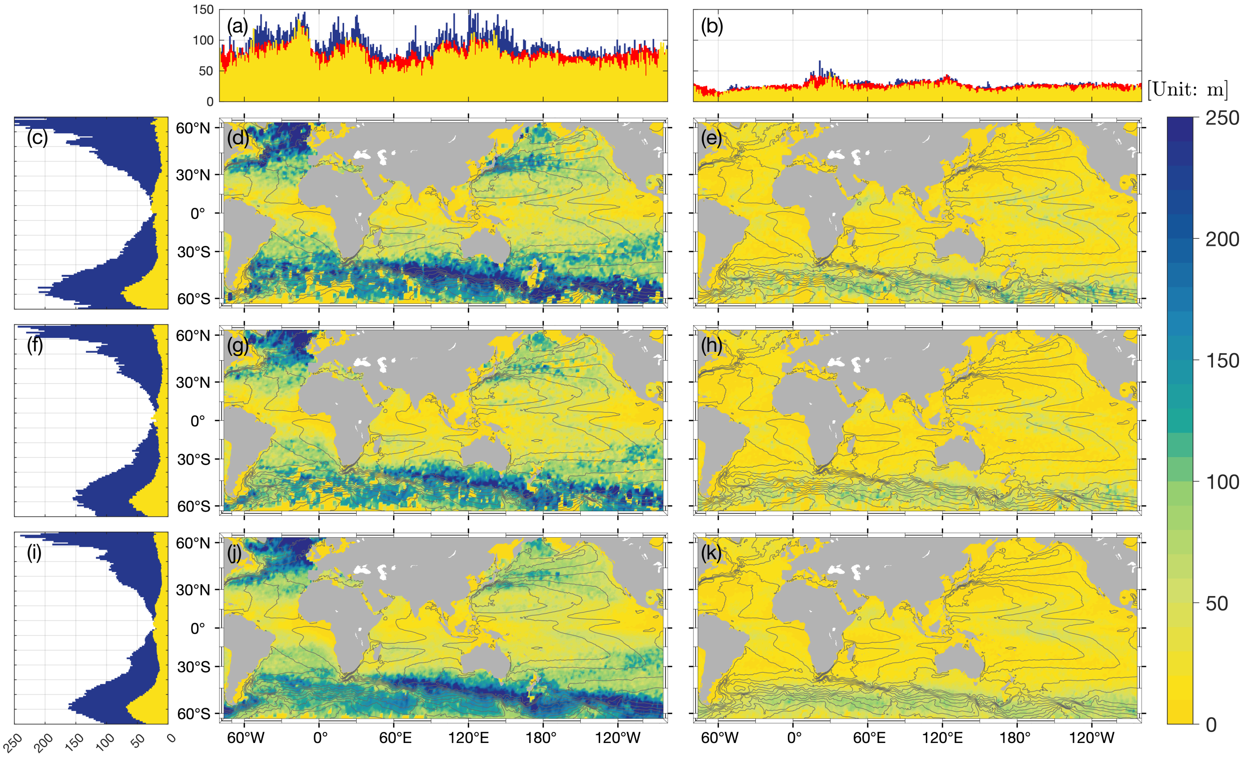

Figure 3.11: Seasonal mean MLD associated with anticyclones, cyclones or outside of either type. (c), (d) and (e) are related to anticyclones, with (d) showing the winter-averaged MLD and (e) displaying the summer-averaged MLD. (c) is then a comparison between winter (in blue) and summer (in yellow) MLDs as a function of latitude. The row of (f), (g) and (h) shows the same information instead for cyclones, while the row of (i), (j) and (k) illustrates MLD outside eddies. The top panels (a) and (b) show the comparison of MLD in anticyclones (blue), cyclones (yellow) and outside eddies (red) as a function of longitude.

5.2 Mode waters in the Northern Hemisphere

Outcropping and subsurface mode waters detected by the new algorithm are displayed in Figure 3.12 in a volumetric census in that water masses could be defined and separated by their potential temperature-salinity (θ-S) properties. Three main elevated ridges or branches are evident in (a) that represent water masses (from left to right, or from fresh to salty) of the North Pacific, Southern Hemisphere and North Atlantic [Speer, 2013]. These branches are not as apparent in (b), since firstly, not all thick mixed layers transform into subsurface mode waters thicker than 100 m, and secondly, different types of subsurface mode waters overlap in properties.

Nevertheless, STMWs in the North Pacific (17 °C, 35 psu) and North Atlantic (18 °C, 36.7 psu) stand out as isolated peaks, implying that these water masses are both vertically and horizontally homogeneous in properties. In contrast, the middle branch of the Southern Hemisphere persists in the subsurface θ-S plot but narrows down in width, which is often interpreted as a ridge consisting of central mode waters (defined as a group of vertically homogeneous water masses displaying relatively large differences in space). However, the averaged east-west temperature gradient of mode waters in the Southern Ocean reaches 1 °C/3000 km that is the same order of magnitude as NASTMW and NPSTMW [McCartney, 1977]. This further indicates a comparable longitudinal variation for these water masses, and that the discernible homogeneity of NASTMW and NPSTMW results from the relatively small area of formation and circulation. In other words, the length of such ridge signifies different formation and mixing mechanisms at play, giving rise to the question of properly separating STMW from SAMW in the Southern Hemisphere.

Speer et al. [Speer, 2013] depicted a similar ridge and defined SAMW ranging from 14 °C, 35.4 psu north of the Subantarctic Front to cooler and fresher values near 5 °C, 34.4 psu in the South Pacific. Their range accommodates all the central mode waters shown in (b), however in this study, we distinguish STMW from SAMW based on both the formation regions of these water masses and a cluster analysis. Speer et al. [Speer, 2013] also described a less conventional peak near 19 °C and 35.6 psu, associated with the South Pacific Subtropical Mode Water (SPSTMW). This peak, however, only appears in the surface diagram of (a) here. Besides different detection methods, this inconsistency might also stem from the relatively large thickness control in this study. In addition to the aforementioned three ridges, a short wing near 11 °C and saltier than the North Atlantic branch appears in the subsurface, yet absent in the outcropping θ-S plot. This wing is associated with the outflow of Mediterranean Sea that originates in the Gulf of Cadiz and is constantly transformed by dragging and entraining subsurface and intermediate waters of the northeast Atlantic [Carracedo, 2016].

Figure 3.13 and Figure 3.14 respectively show results of separate cluster analysis for the

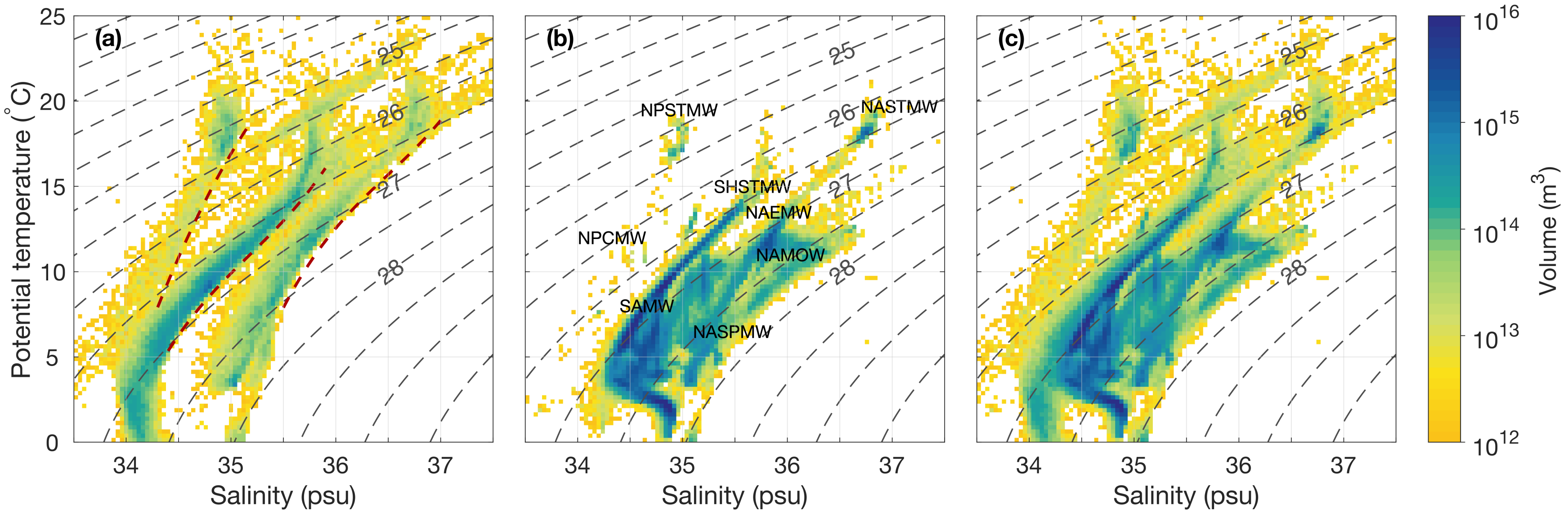

Figure 3.12: Potential temperature-salinity (θ-S) diagrams superimposed by potential density contours of (a) outcropping mode waters, (b) subsurface mode waters, and (c) total volume of the two. Notice that two or more subsurface mode waters might be detected in one single Argo profile, given that water masses with difference sources can be transported and gather in the same location but at different depths [Chen, 2022]. The volume of each mode water is calculated as to multiply the thickness by the area of 1° × 1° grid box that holds this mode water profile. The total θ-S field is divided into 100 × 100 bins, with θ ranging from 0 to 25 °C and the salinity scope of 33.5–37.5 psu. The volume of all mode waters in each bin is added together to obtain the final volumetric estimate (in the logarithmic scale). Three red curves in (a) indicate main branches of mode waters that are associated with the fresher North Pacific, the Southern Hemisphere encompassing all basins, and the saltier North Atlantic. Mode waters identified in this study are marked with acronyms in (b), including the North Pacific Subtropical Mode Water (NPSTMW), North Pacific Central Mode Water (NPCMW), Southern Hemisphere Subtropical Mode Water (SHSTMW), Subantarctic Mode Water (SAMW), North Atlantic Subtropical Mode Water (NASTMW), North Atlantic Eastern Mode Water (NAEMW), North Atlantic Mediterranean Outflow Water (NAMOW), and North Atlantic Subpolar Mode Water (NASPMW).

North Atlantic and North Pacific. In order to generate an optimized solution, we prescribe the number of cluster groups as 2–5. For the North Atlantic, it shows panel (c) that divides all mode waters into 4 varieties is the best option compared with the other three, and these four mode water types are (from salty to fresh) Subtropical Mode Water, two types of Eastern Mode Water and Subpolar Mode Water. Due to a relatively small amount of mode waters detected in the North Pacific, Figure 3.14 displays the final cluster choice of two varieties that represent the Subtropical and Central Mode Water.

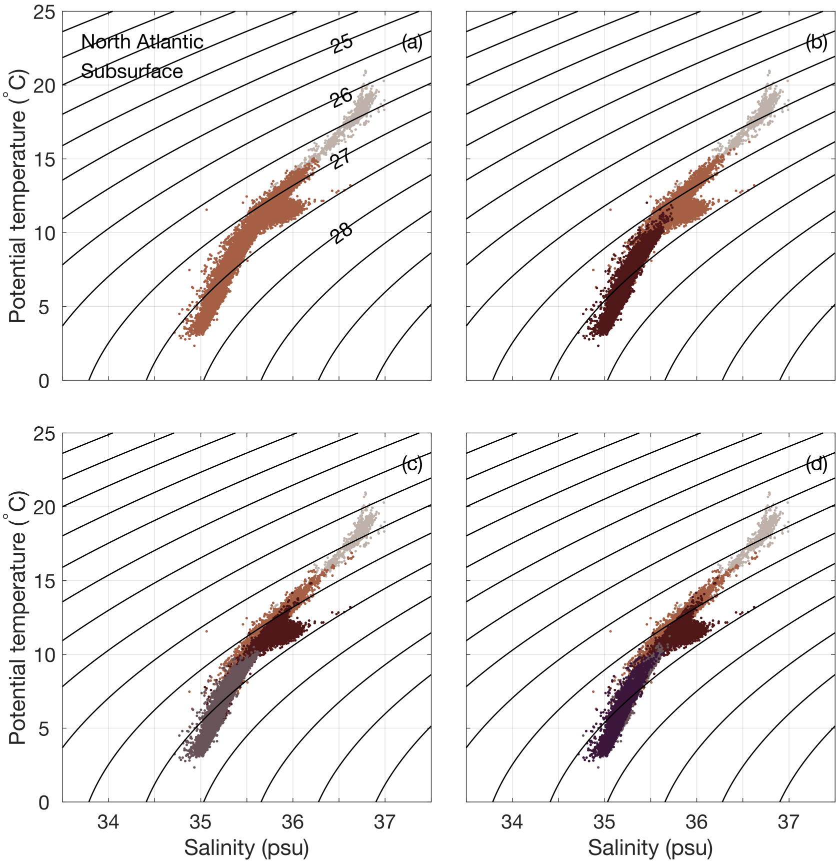

Figure 3.13: Cluster analysis for the North Atlantic, divided into 2–5 clusters respectively shown in panels (a–d).

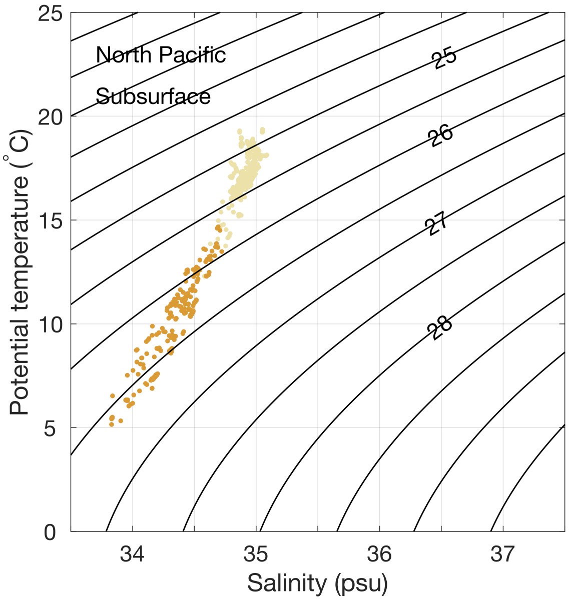

Figure 3.14: Cluster analysis for the North Pacific, divided into Subtropical and Central Mode Waters.

The cluster analysis leads to four and two mode water varieties in the North Atlantic and North Pacific respectively, as summarized in Table 3.2 with their main properties. Rows 2 and 5 in Figure 3.15 display the spatial distribution of mode water thickness in terms of the vertical configuration, i.e., the subsurface mode waters and their surface counterparts. These outcropping/surface mode waters have been retrieved to be in the same range of properties as the subsurface ones so that two types of surface mode waters might overlap in both properties and spatial distribution. The NASTMW (or Eighteen Degree Water, EDW) is most distinctive in properties compared with the other three types in the North Atlantic basin. Surface EDWs are located along the Gulf Stream Extension while their subsurface expression occupies the entire subtropical gyre as defined by the steric height referenced to 1200 dbar and integrated upward to 400 dbar shown in (a1). Compared with a narrower definition of EDW uniform in temperature and occupying 250 m in thickness [Worthington, 1958], EDW identified here has a slightly wider range of properties.

There are two types of mode waters located in the eastern basin of the North Atlantic, as shown in their spatial difference in Figure 3.15 (b) and (c). The lighter variety (NAEMW-l) is conspicuous in the subsurface θ-S diagram, with a slightly larger range of temperatures than EDW. Most components of this mode water type are formed on the southeastern side of the North Atlantic Current, encompassing the entire eastern basin. The denser variety (NAEMW-d) lies at deeper depths compared with the NAEMW-l (see Figure 3.16) and it has a tendency to be detected as thick lenses downstream (northward) of the Mediterranean Outflow through the Strait of Gibraltar [Price, 1993]. Though such influence from

Table 3.2: The classification of all subsurface mode water types detected from the algorithm.

	Potential temperature (°C)	Salinity (psu)	Potential density (kg m^{-3})	Thickness (m)	Depth (m)	Potential vorticity ($\times10^{-10}$ m^{-1} s^{-1})
NASTMW	18.0 ± 0.5	36.71 ± 0.07	26.46 ± 0.07	173 ± 67	316 ± 64	0.58±0.12
NAEMW-l	11.7 ± 1.2	35.77 ± 0.17	27.10 ± 0.11	320 ± 160	327 ± 79	0.51±0.12
NAEMW-d	10.8 ± 1.8	35.73 ± 0.22	27.23 ± 0.15	346 ± 248	521 ± 79	0.70±0.09
NASPMW	5.6 ± 1.7	35.16 ± 0.14	27.58 ± 0.12	273 ± 175	378 ± 133	0.38±0.16
NPSTMW	17.1 ± 0.6	34.93 ± 0.06	25.30 ± 0.13	179 ± 59	271 ± 50	0.57±0.13
NPCMW	9.6 ± 2.3	34.31 ± 0.21	26.32 ± 0.23	161 ± 49	216 ± 67	0.42±0.21
SASTMW	14.3 ± 1.5	35.61 ± 0.24	26.46 ± 0.17	148 ± 43	226 ± 61	0.45±0.15
SASAMW	4.5 ± 1.3	34.36 ± 0.13	27.09 ± 0.09	187 ± 96	434 ± 147	0.54±0.11
SISTMW	12.6 ± 1.1	35.34 ± 0.16	26.60 ± 0.10	261 ± 105	349 ± 86	0.44±0.13
SISAMW	9.3 ± 1.4	34.85 ± 0.15	26.82 ± 0.09	308 ± 131	464 ± 96	0.35±0.13
SPSTMW	12.7 ± 1.4	35.33 ± 0.22	26.57 ± 0.18	154 ± 49	216 ± 67	0.43±0.17
SPSAMW	7.1 ± 1.4	34.57 ± 0.16	26.93 ± 0.08	310 ± 149	497 ± 132	0.43±0.13

[*] Absolute values are shown for the potential vorticity.

[*] This table only displays statistics for the subsurface mode waters, because the surface ones associated with each type are retrieved from the total surface mode water pool by searching for the same properties as subsurface mode waters.

the Mediterranean Outflow was ignored in climatology [Feucher, 2019], it further recalls the formation and spreading of Mediterranean eddies (meddies) off the Atlantic coast, which are generated from instabilities of the Mediterranean Undercurrent and might play a critical role in the transport of the NAEMW-d [Bashmachnikov, 2015].

The North Atlantic Subpolar Mode Water (NASPMW) is the coldest, freshest and densest variety in the basin. Notice that the same name might be given to different water masses in other studies, e.g., NASPMW in Hanawa et al. [Hanawa, 2001] with the lowest temperature of 8 °C refers more to the Eastern Mode Water here. Given that formations commonly occur in conjunction with permanent fronts, and on the low-density (warm) side of the front where the isopycnal slopes precondition the mechanism of subduction, this does not seem to apply to NASPMW. Indeed, NASPMW formation areas in Figure 3.15 (d4) are located in the North Atlantic northern subpolar gyre, in the Iceland, Irminger, and Labrador Seas. McCartney et al. [McCartney, 1982] draw a thorough pic-

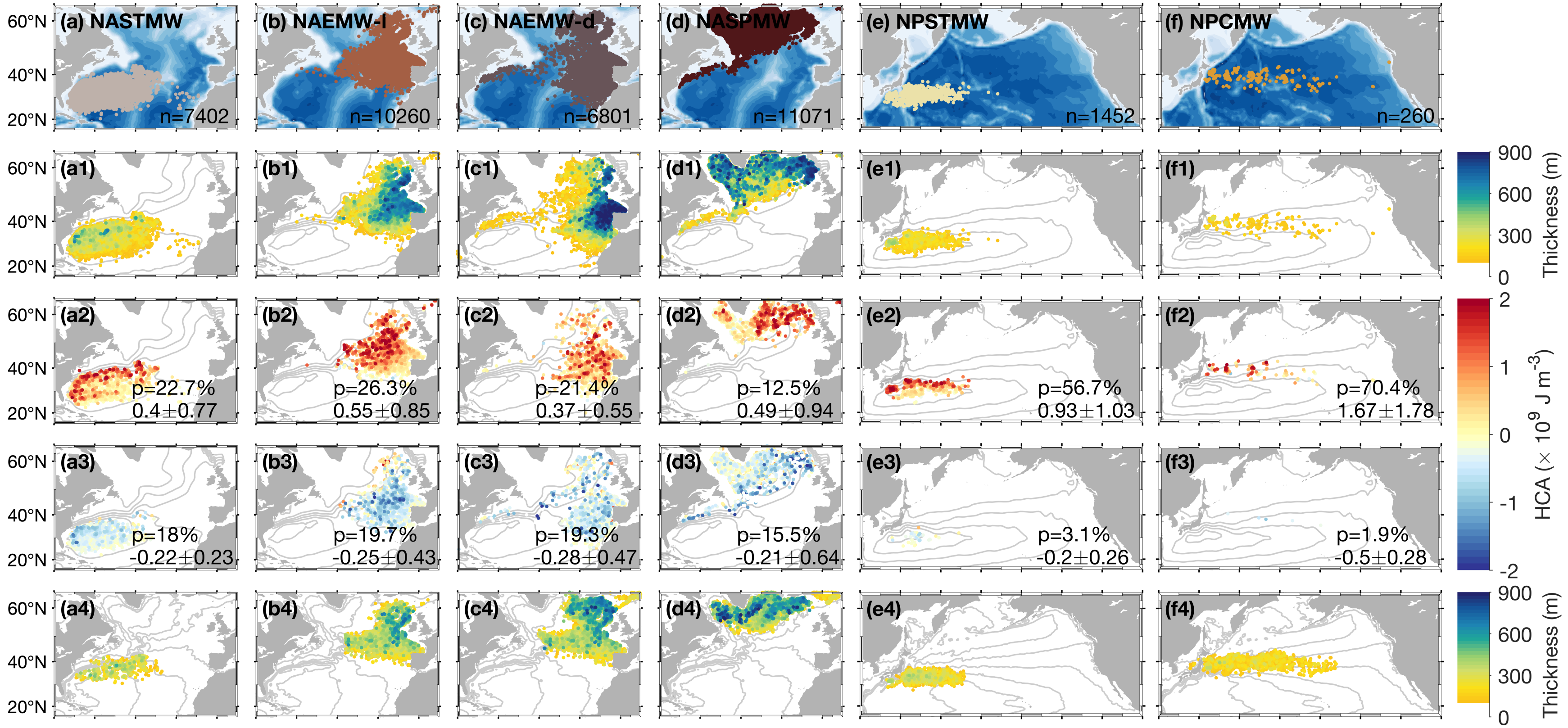

Figure 3.15: Spatial distribution of mode waters in the Northern Hemisphere. The first row (a-f) provides the locations of each mode water type (both outcropping and subsurface), with n at the corner indicating the number of detected waters. The second row (a1-f1) displays the thickness of subsurface mode waters, while the last row (a4-f4) shows outcropping mode waters. The third and fourth rows (a2-f2) and (a3-f3) display the heat content anomaly (HCA) integrated over the subsurface mode water layer that is co-located with anticyclonic and cyclonic mesoscale eddies respectively. Panels of surface mode waters are overlapped by the mean dynamic topography (MDT) as contours in light grey [Mulet, 2021] and panels of subsurface mode waters are superimposed by the steric height (anomaly) contours at 400 dbar integrated from 1200 dbar. The bottom right corners of the third and fourth rows provide information of the percentage of co-location and the mean value ± standard deviation of HCA.

ture of mode water distribution in the northern and eastern regions of the Atlantic that confirms a development of density increase and temperature drop from the Norwegian coast to the Labrador Sea. Our result displays a similar spatial pattern of properties, but the underlying mechanisms associated with NASPMW formation and subduction need further analysis.

In the Pacific Ocean (see Figure 3.15 (e–f)), the Central Mode Water (NPCMW) generally differs from the Subtropical Mode Water (NPSTMW) by temperature and latitudinal occupation. Similar to STMWs in the North Atlantic, outcropping NPSTMWs are positioned along the Kuroshio Extension whereas subsurface ones are identified within the recirculation gyre defined by the steric height contours shown in (e1). The NPCMW is identified in the transition domain between the Kuroshio and Oyashio Fronts, with surface waters accounting for a larger proportion compared with the subsurface ones. Unlike NASTMW, both the properties and spatial distributions of NPSTMW and NPCMW are less spread in comparison to previous studies [Oka, 2009] owing to stricter thresholds of detection in the algorithm. Mode waters located in the eastern basin with higher temperature around 20 °C [Hautala, 1998] are neglected since they only show surface signatures in Figure 3.12 (a).

5.3 Mode waters in the Southern Hemisphere

Figure 3.17 (a1–d1) displays several choices of groups for the cluster analysis. Firstly, we notice that such results from cluster analysis are a linear function of potential temperature, or salinity. Hanawa et al. [Hanawa, 2001] mentioned in their definition of the circumpolar SAMW that it is actually one type of subtropical waters. This denotation is reasonable given that SAMW forms at the northern boundary of ACC and propagates along isopycnal layers in the subtropical gyres [Jones, 2016]. This means mode waters in the Southern Ocean can be regarded as one group that varies according to their geographical locations.

Here, we divide mode waters in the entire Southern Hemisphere into two varieties, and define the warmer one as the STMW and the colder one as the SAMW, as shown in Figure 3.17 (a2–d2). Considering that properties of each mode water type vary across and even within basin, the basin-averaged properties of the same type are therefore different. Though this division into two mode water varieties here results from a cluster analysis, it is still plausible to do so since the spatial distribution shown in Figure 3.18 suggests different formation and spreading areas of these two types. The largest pool of STMW is located in the Indian Ocean, while SAMW is generally formed in the eastern Pacific and propagates either towards the northwest inside the basin, or across the Drake Passage and enters the western Atlantic. Consistent with Hanawa et al. [Hanawa, 2001], SAMW in this study is approximately identical to the STMW Type 3 in their summary, and STMW

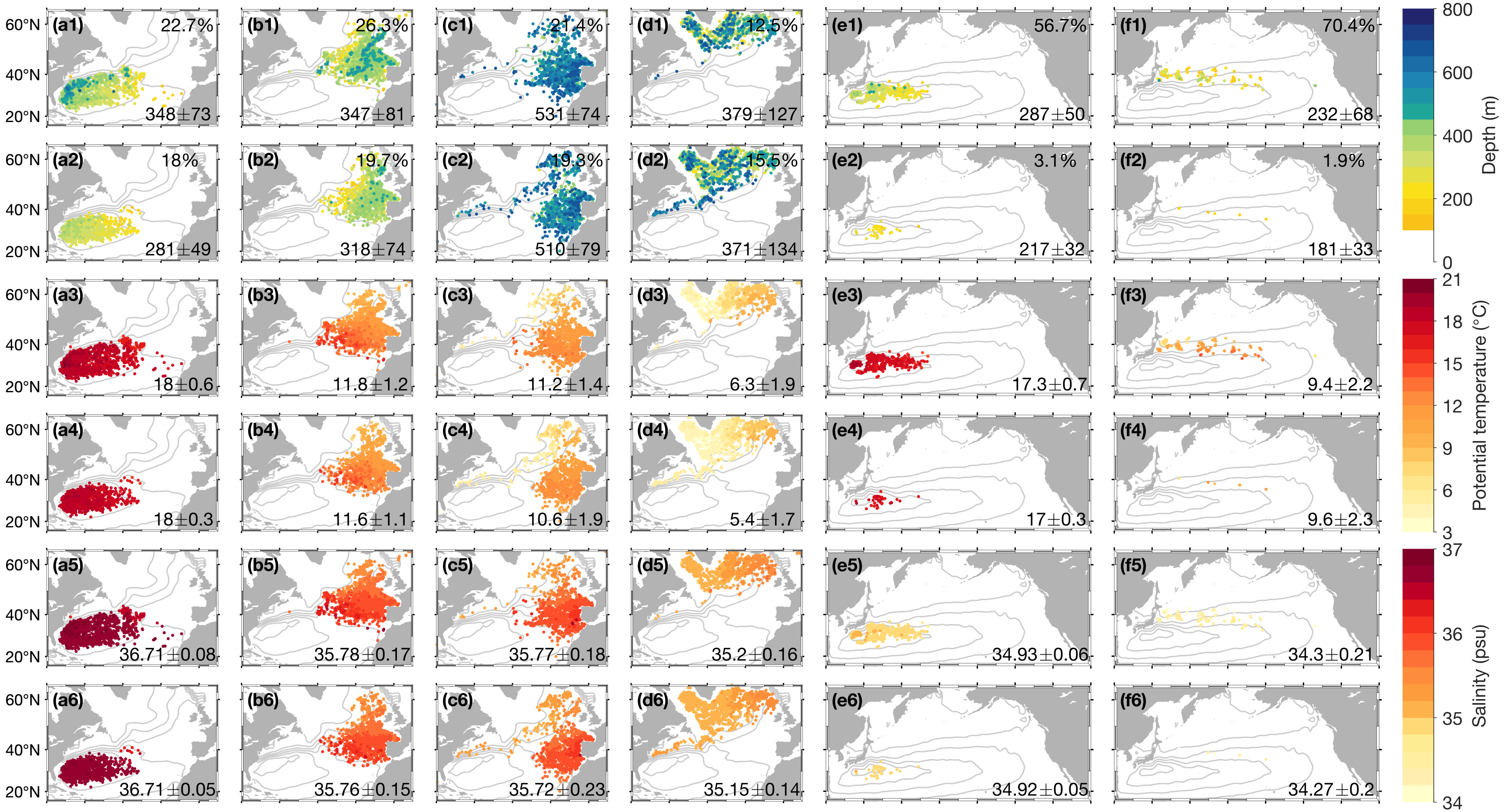

Figure 3.16: Spatial distribution of subsurface mode waters in the Northern Hemisphere. The first two rows (a1–f2) provide the depths of each mode water type respectively co-located with anticyclonic and cyclonic eddies. The middle two rows (a3–f4) show the potential temperature, while the last two rows (a5–f6) display the salinity. Panels are superimposed by the steric height (anomaly) contours at 400 dbar integrated from 1200 dbar.

here refers to Types 1 and 2. As mentioned earlier, since water masses in the Southern Hemisphere shape like a narrow branch in their θ-S combination, a simple cut at around 12 °C might also lead to a similar separation.

Given that there are two circumpolar fronts associated with mode water formation (i.e., the Subtropical and Subantarctic Fronts [Orsi, 1995] displayed in the uppermost panels of Figure 3.18), we also relate the formation of STMW to the equatorward region of the Subtropical Front and SAMW to the Subantarctic Zone between these two fronts. Consistent with previous studies, the density of SAMW reduces when it enters the Indian basin from the Pacific, and slightly increases when it spreads eastward to the South Atlantic [Koch-Larrouy, 2010; Sallée, 2010]. Despite of these consistencies, we recognize some discrepancies associated with STMWs in particular. For example, the properties of SASTMW are more restricted whereas their spatial distribution remains comparable to previous studies [Sato, 2014; Chen, 2022]. This results from stricter PV and gradient thresholds of mode water detection in the algorithm and the application of cluster analysis to the subsurface mode water pool only. Ascribed to the same reasons, STMWs in the Indian and Pacific basins indicate more confined ranges of properties and slightly lowered temperatures compared with Tsubouchi et al. [Tsubouchi, 2010] and Roemmich et al. [Roemmich, 1992] in which the temperature of STMWs can reach 16 °C.

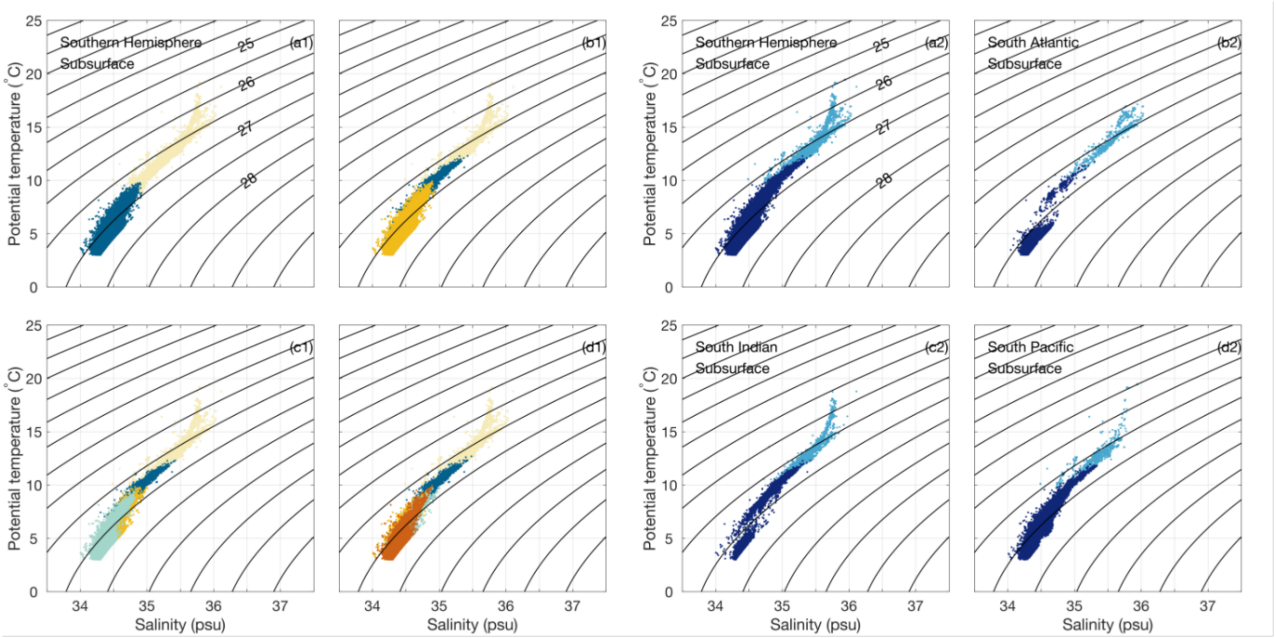

Figure 3.17: Cluster analysis for the Southern Hemisphere: (a1–d1) four tests on the number of clusters; (a2–d2) final clustering results for each basin.

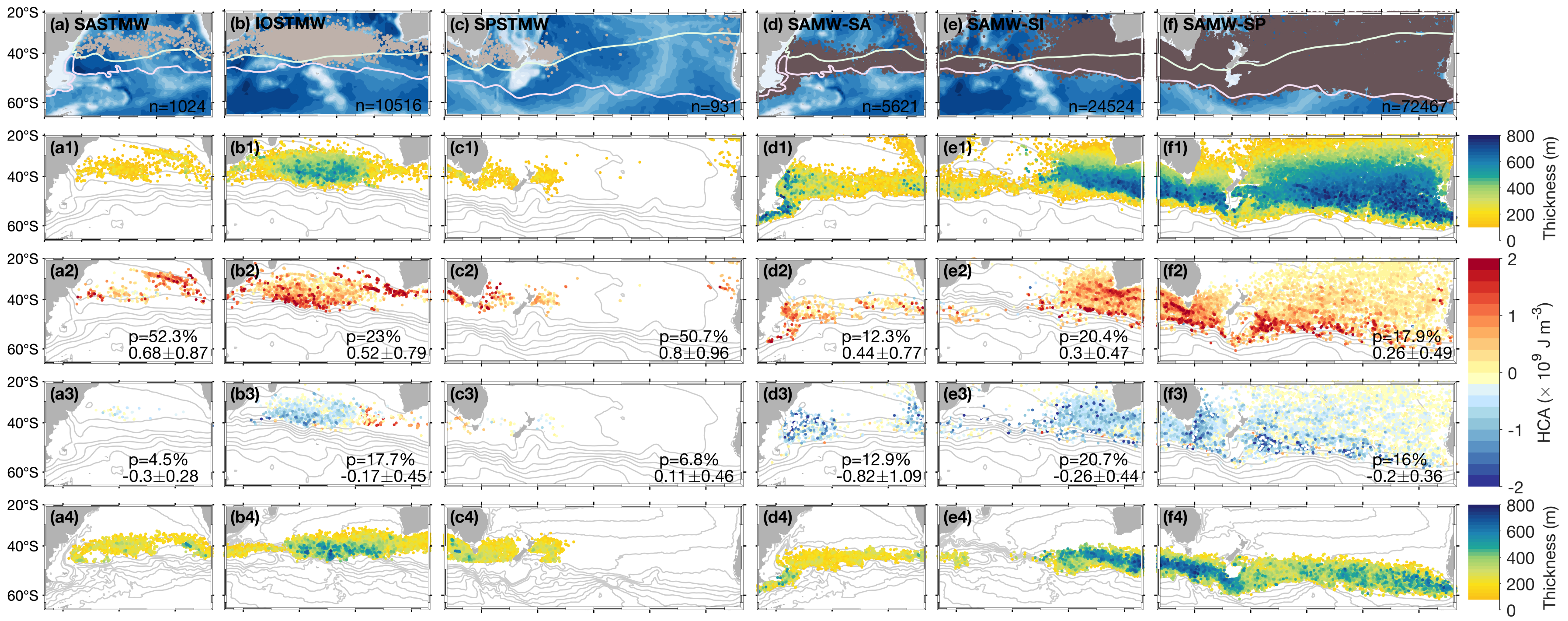

Figure 3.18: Spatial distribution of mode waters in the Southern Hemisphere. The first row (a-f) provides the locations of each mode water type, with n at the corner indicating the number of detected waters. The second row (a1-f1) displays the thickness of subsurface mode waters, while the last row (a4-f4) shows outcropping mode waters in the same range of properties. The third and fourth rows (a2-f2) and (a3-f3) display the heat content anomaly (HCA) integrated over the subsurface mode water layer that is co-located with anticyclonic and cyclonic mesoscale eddies respectively. Panels of surface mode waters are overlapped by the mean dynamic topography (MDT) as contours in light grey [Mulet, 2021] and panels of subsurface mode waters are superimposed by the steric height (anomaly) contours at 400 dbar integrated from 1200 dbar. The bottom right corners of the two rows co-located with mesoscale eddies provide information of the percentage of co-location and the mean value ± standard deviation of HCA. The light green and purple contours in the first row provide the location of the Subtropical Front (STF) and Subantarctic Front (SAF) from Orsi et al. [Orsi, 1995].

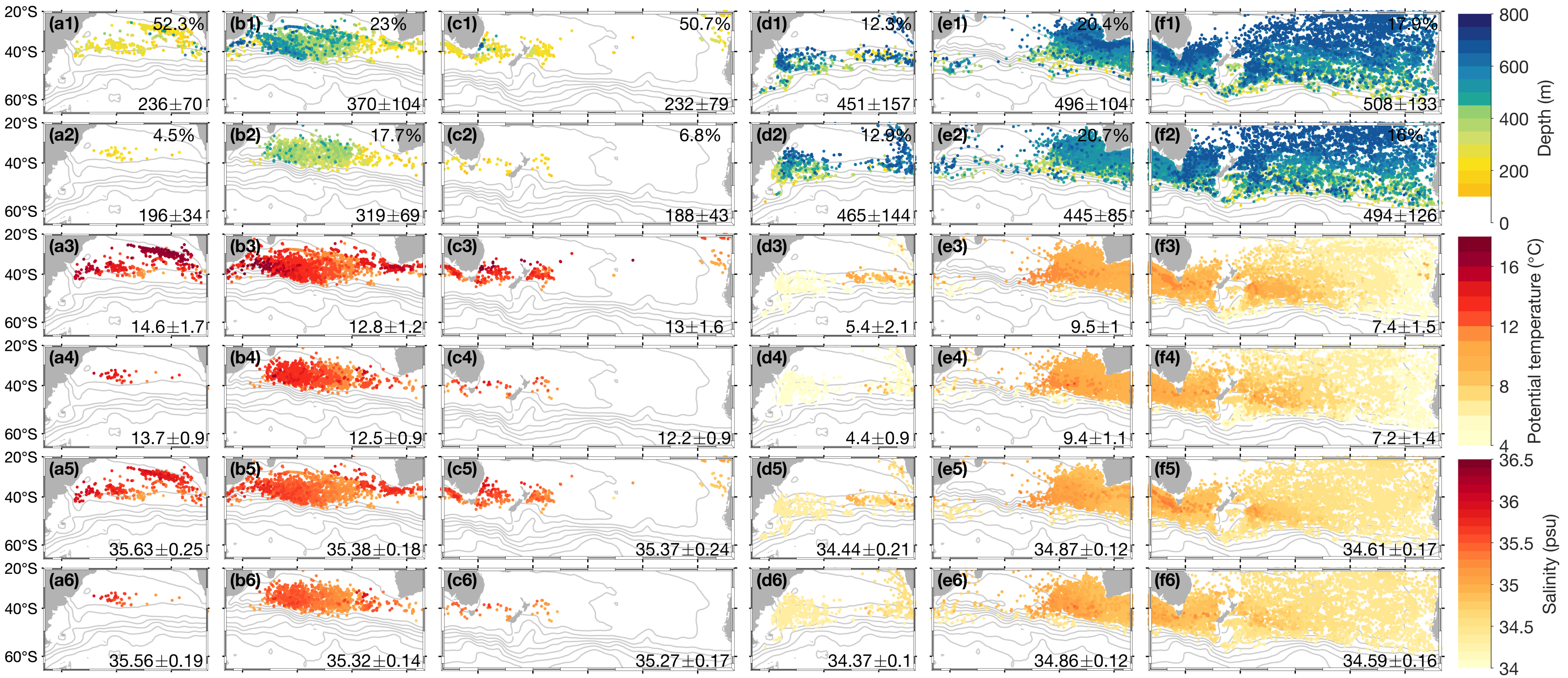

Figure 3.19: Spatial distribution of subsurface mode waters in the Southern Hemisphere. The first two rows (a1–f2) provide the depths of each mode water type respectively co-located with anticyclonic and cyclonic eddies. The middle two rows (a3–f4) show the potential temperature, while the last two rows (a5–f6) display the salinity. Panels are superimposed by the steric height (anomaly) contours at 400 dbar integrated from 1200 dbar.

5.4 Mode-water heat anomalies carried by eddies

Dependent on different clustering strategies for these three domains (North Atlantic, North Pacific and the Southern Ocean), several assessments are available, such as depictions of mode water property (anomaly) and hypotheses of underlying mechanisms either consistent with or presupposing the large-scale thermohaline circulation. We then specifically focus on the heat content anomaly inside mode waters, computed as follows:

$$HCA = \int_{d1}^{d2} (\rho C_p T - \rho_r C_{pr} T_r) dz, \tag{3.3}$$

where ρ is the potential density, C_p is the thermal capacity of seawater, and T is the conservative temperature. The subscript r of the subtrahend is associated with a referenced climatology, while the integration is calculated over $d1$ (the lower) and $d2$ (the upper) boundaries of any mode water layer. For each mode water, its climatological profile that represents the local environment is computed as an average over all possible profiles satisfying both spatial and temporal criteria. Spatially, these component profiles are supposed to be positioned within a rectangular box of $2.5° \times 2.5°$ centered by the mode water profile, while the selection based on time applies a window spanning of 30 days (i.e., independent of year) over the date of this mode water at center. These criteria ensure that any calculation of anomalies is restricted to local variations.

Figure 3.10 (a) of annual accumulative heat flux indicates locations of possible mode water formation sites (in blue), encompassing the western boundary of each basin and the ACC. These regions are also characterized by high level of EKE shown in (b). Since mode waters are found beyond their outcropping area as a result of advection both by the main currents and eddies, the focus here is to assess the possible impact of the latter on mode water formation and propagation in the ocean subsurface. The presence of anticyclonic and cyclonic eddies shown in (c) and (d) coincides with the high EKE hotspots of the global ocean outside the near-equatorial regions. Trajectories of long-lived anticyclonic eddies in (e) depict westward and equatorward inter-basin connections, e.g., Agulhas Rings spawned from the Agulhas Current into the South Atlantic, and eddies in the South Indian Ocean that are leaked from the Eastern Australia and Tasman Sea. A similar cross-basin connectivity of eddies is also observed in the North Atlantic and Pacific. Pathways of cyclones, on the other hand, display a more zonal pattern if not slightly poleward with the longest-lived bunch of eddies propagating in the Indian Ocean that are injected along the west coast of Australia.

The third and fourth rows in Figure 3.15 (or Figure 3.18) respectively show the heat content anomaly (HCA) of subsurface mode waters co-located with anticyclonic and cyclonic eddies for the Northern (or Southern) Hemisphere. In terms of mode water-eddy co-location (see Table 3.3 for statistics in detail), anticyclones dominate cyclones in holding and transporting STMWs. A similar conclusion could be inferred from SAMWs in the Southern Ocean albeit the largest amount remaining outside the eddy contours. Besides SAMWs, a large proportion of NAEMWs (both light and dense types) and NASPMWs are not captured inside eddies. These three types are deep mode waters, whereas other types that show high correlation with eddies (e.g., the NPSTMW, NPCMW, SASTMW and SPSTMW) are much shallower (see Figures 3.16 and 3.19 for the spatial distribution of depth for different water masses). This dependence of mode water-eddy co-location on depth refers to possible presence of subsurface-intensified eddies that do not engender any imprint on the surface dynamic height field, which in other words, suggests that to detect eddies merely from their signatures on satellite altimetry maps is not sufficient. With regard to the heat anomaly, mode waters inside anticyclones account for a positive HCA compared with their surroundings, while the opposite is observed for cyclonic eddies. The averaged values of mode water HCA inside anticyclones are in accordance with the percentage of co-location. For example, both mode water types in the North Pacific (Figure 3.15 (e2) and (f2)) retain higher values of HCA compared with water masses in the North Atlantic. This is also the case for the Southern Ocean where, overall, STMWs inside anticyclones hold higher HCA than SAMWs.

The combination of eddy trajectories in Figure 3.10 and the third and fourth rows in Figure 3.18 suggests that a considerable number of mode waters in the Southern Ocean are generally carried westward by anticyclonic eddies following the central and northern branches of the subtropical gyres (depicted by the steric height contours in Figures 3.15 and Figure 3.18). Such transport of STMWs, in specific, is connected with the supergyre system [Speich, 2002; Speich, 2007; Ridgway, 2007], of which eddies associated with the East Australian Current are shed westward around Tasmania and leaked into the Indian Ocean. The properties (temperature and salinity in specific) of anticyclone-trapped STMWs that display connections at the basin boundaries support this inference, though the deepest and largest pool of STMWs is found in the Indian basin. A similar gyre connection between the Indian and Atlantic systems south of Africa is also observed with squeezed steric height contours at the Agulhas Leakage. Here, Agulhas Rings act as coherent subsurface eddies and advect STMWs northwestward up to the Mid-Atlantic Ridge [Chen, 2022]. SAMWs that form at the northern periphery of the Subantarctic Front nearby the South American continent, on the other hand, interplay with the supergyre system only within the branch that connects the Pacific and Indian Oceans. The warmest and saltiest SAMW variety is located south of Australia and in the Indian Ocean, following a northwestward route of propagation after undergoing subduction near their area of formation (see Figure 3.19 and Cerovečki et al. [Cerovečki, 2013]). A small portion of SAMWs circulating the Zapiola gyre are carried by anticyclonic eddies that are shed eastward from the Drake Passage.

6 Discussions and conclusions

By combining the newly developed MLD and mode water detection algorithm [Chen, 2022] with cluster analysis [Lloyd, 1982], this study, for the first times, attempts to assess the global mode water distribution independently from any prescribed specifications of mode waters with respect to temperature, salinity and density. Results of mode water separation are different from previous studies, in terms of 1) a more restricted threshold set of PV, gradients and thickness that removes less homogeneous mode waters in several places (the subtropics in specific), 2) a retrieval of surface/outcropping mode waters with the same properties as the clustered subsurface mode waters that does not take into account surface-only water masses unable to subduct. This also allows us to investigate more precisely the possible link between mode water formation regions and their spreading into the subsurface. Respectively, 4, 2, and 2 mode water varieties are identified in the North Atlantic, North Pacific and Southern Oceans. The prominent mode water types in volume are NASTMW, NPSTMW and SAMW, with the former two concentrating within isolated peaks in the θ-s diagram, whereas the last one stretches out as a narrow ridge.

Table 3.3: The co-location between mesoscale eddies and subsurface mode waters.

	Number	Anticyclones	Cyclones	Outside
NASTMW	7402	22.7%	18%	59.3%
NAEMW-l	10260	26.3%	19.7%	54%
NAEMW-d	6801	21.4%	19.3%	59.3%
NASPMW	11071	12.5%	15.5%	71.9%
NPSTMW	1452	56.7%	3.1%	40.2%
NPCMW	260	70.4%	1.9%	27.7%
SASTMW	1024	52.3%	4.5%	43.2%
SASAMW	5621	12.3%	12.9%	74.8%
SISTMW	10516	23%	17.7%	59.3%
SISAMW	24524	20.4%	20.7%	58.9%
SPSTMW	931	50.7%	6.8%	42.5%
SPSAMW	72467	17.9%	16%	66.1%

We also provide indications on how mesoscale eddies, anticyclones in particular, are involved in mode water subduction, spreading and heat uptake. By calculating the heat content anomaly associated with mode waters and relating it to the co-located eddies detected from satellites, we show that anticyclonic (cyclonic) eddies are related to positive (negative) heat anomalies. The magnitude of positive HCA is closely related to the percentage of mode water-anticyclone co-location (see Table 3.3 for the statistics), suggesting that mode waters formed within anticyclonic eddies (such as Agulhas Rings) might play an important role in the oceanic heat uptake. However in this study, the number of mode waters that lie outside satellite-deduced eddies remains large, especially for SAMWs, NAEMWs and NASPMWs. These are relatively deep mode waters that might be co-located with subsurface eddies which produce little (if any) imprint on the surface dynamic height field and therefore are not detected by the TOEddies algorithm. In the Southern Hemisphere, the combination of eddy trajectories and mode water properties highlights inter-basin connections for STMWs and partially for SAMWs via the subtropical supergyre system across the Tasman and Agulhas Leakages as suggested by Speich et al. [Speich, 2007].

Table 3.4: Potential temperature and salinity anomalies of mode waters and their co-location with mesoscale eddies.

	Temp–anti	Temp–cyc	Temp–out	Sal–anti	Sal–cyc	Sal–out
NASTMW	0.4±0.7	-0.3±0.3	0.1±0.6	0.09±0.12	-0.02±0.04	0.03±0.09
NAEMW-l	0.4±0.6	-0.2±0.4	0.1±0.5	0.07±0.1	-0.03±0.07	0.01±0.08
NAEMW-d	0.3±0.5	-0.3±0.6	0±0.5	0.04±0.07	-0.02±0.06	0±0.06
NASPMW	0.3±0.7	-0.3±0.7	0±0.6	0.03±0.07	-0.01±0.06	0±0.06
NPSTMW	1.1±1.1	-0.3±0.4	0.3±0.7	0.1±0.09	0.01±0.04	0.05±0.06
NPCMW	2.1±1.9	-0.9±0.5	-0.1±1.3	0.18±0.17	-0.08±0.07	0±0.13
SASTMW	1±1.2	-0.6±0.6	0.2±0.8	0.17±0.2	-0.07±0.08	0.05±0.14
SASAMW	0.5±0.7	-1.1±1.3	-0.1±0.8	0±0.1	-0.1±0.15	-0.03±0.08
SISTMW	0.6±0.9	-0.2±0.6	0.1±0.5	0.1±0.14	-0.02±0.11	0.02±0.09
SISAMW	0.2±0.4	-0.3±0.6	0±0.5	0.03±0.06	-0.03±0.07	-0.01±0.06
SPSTMW	1.1±1.1	0.1±0.8	0.2±0.7	0.2±0.16	0.04±0.12	0.06±0.12
SPSAMW	0.2±0.4	-0.2±0.4	0±0.3	0.02±0.05	-0.02±0.04	0±0.04

[*] In addition to co-location between mode waters and mesoscale eddies, extra columns (Temp–out and Sal–out) also show mode waters outside eddies.
[*] Units: °C for temperature and psu for salinity.

The characteristics (property values and standard deviations) of global mode waters and their distribution presented herein are intended to guide water mass analysis of hydrographic data and expected to provide a basis for other applications (Table 3.4 further provides temperature and salt anomalies inside each mode water and their co-location with mesoscale eddies). In particular, our study reveals some processes linked with the formation, subduction, and subsurface propagation of mode waters. These are important elements in understanding and monitoring the ocean heat uptake and transport, which might provide useful information to stimulate improvements in Earth system models that do not resolve such processes explicitly.

Summary

In this chapter, we described the newly-developed algorithm for detecting surface mixed layer depth and mode water, based on their features in the temperature and density profiles. That is to say, the upper and lower boundaries of these homogeneous layers (characterized by low gradients) can be marked by the second derivative extreme values. By applying such algorithm to Argo profiles, an estimate of subsurface mode waters is available, as well as their property anomalies compared with the environment.

Applying separate cluster analyses to the North Atlantic, North Pacific and Southern Hemisphere leads to 4, 2, and 2 mode water types in these domains. Such separation is different from previous studies in that the mode water types with centralized properties (e.g., the Eighteen Degree Water) remain as an individual variety, whereas other mode waters that spread both in their θ-S properties and the spatial distribution, such as both types of the NAEMW, are also identified as mode waters owing to their vertical homogeneity. It is also plausible to divide mode waters in the Southern Hemisphere into 2 varieties, though they were both regarded as SAMWs in other studies of water masses in the Southern Ocean. In the North Pacific, our result also corresponds well with previous studies, in terms of the detection of NPSTMW and NPCMW. However, due to both the small amount and their distribution only at the surface, mode waters detected previously as the eastern mode waters are ignored in this study.

Combined with the TOEddies algorithm of eddy identification and tracking, it further allows for an evaluation of mode water transport by mesoscale eddies. In the next chapter, we will be specifically focused on the subtropical region in the South Atlantic for such connection between mode waters and mesoscale eddies. We confirm with the theory that anticyclonic eddies play an important role in transporting mode waters and their property anomalies.

As discussed in this chapter, high percentage of mode water-eddy co-location and large values of heat anomalies carried by eddies are all associated with shallow eddies. In the next chapter, we also propose another method to detect subsurface-intensified eddies that might imprint little or none signatures on sea surface, invisible from the satellite.

Chapter 4

South Atlantic Subtropical Mode Water

Objectives

After the general description of global mode waters and their property anomalies associated with mesoscale eddies in the previous chapter, this chapter then focuses on the South Atlantic Subtropical Mode Water in specific, since the mode waters in the South Atlantic not only contain the typically formed types in the vicinity of western boundary current system (the Brazil Current and its interaction with the Malvinas Current), but also include influence of water mass intrusion from the Indian Ocean that engenders anticyclonic Agulhas Rings at the Leakage Zone where the Agulhas Current retroflects. It is thus of interest to quantify the different origins of subtropical mode waters in the South Atlantic.

Contents

1 Introduction and motivation

Despite the large area occupied by mode waters, their formation is much more bounded to specific locations. In particular, the STMW has been documented to originate, in common cases, in the vicinity of western boundary currents, where surface waters lose buoyancy in winter and deep mixed layer develops due to convection. Part of this winter mixed layer is later capped by heating and isolated from the surface while circulating in the subtropical gyres, and might eventually subduct [Marshall, 1997]. Of all the five subtropical gyres, STMW is thus commonly divided into three varieties in terms of formation zones and thermodynamic characteristics: the one that has a western-boundary origin of formation, e.g., [Suga, 1990; Roemmich, 1992; Kwon, 2004; Tsubouchi, 2016], the one linked to the downstream transport and subduction along the poleward boundary of the subtropical gyre [Nakamura, 1996; Oka, 2011], and a third variety that appears in the eastern extremity of gyres, which is sometimes influenced by inter-basin exchanges of water masses [Hautala, 1998; Wong, 2003; Souza, 2018].

With the progress in eddy detecting and tracking from satellite altimetry, several methods have been developed to objectively reconstruct the evolution of mesoscale eddies over time [Chaigneau, 2011; Chelton, 2011; Pegliasco, 2015; Laxenaire, 2018; Vu, 2018]. Combining the results of eddy-permitting models with observed diagnoses, it is widely accepted that mesoscale eddies make a substantial contribution to mode water dynamics, including the formation of deep winter mixed layer that is closely associated with anticyclonic eddies [Uehara, 2003; Kouketsu, 2012; Dufois, 2016], the enhancement of mode water subduction by eddy-driven ageostrophic motions [Spall, 1995; Marshall, 1997; Qu, 2002; Nishikawa, 2010; Xu, 2016], and the dependence of STMW decadal variability on stability of the recirculation gyre rather than variations in air-sea fluxes [Qiu, 2006]. Though some eddies evolve in the ocean interior along their trajectories, very often signatures are generated at the surface that can still be detected by satellites [Bashmachnikov, 2012; Laxenaire, 2019]. In particular, Laxenaire et al. [Laxenaire, 2018] showed that a significant fraction of eddies can be followed from the Indian Ocean to the South Brazil Current with around 3.5 years to cross the entire South Atlantic. Other observations also suggest that long-lived and far-traveled subsurface eddies exhibit a preference for rapid anticyclonic rotation that leads to the isolation of core water masses [Schütte, 2016].

To distinguish subsurface-intensified eddies from surface ones, a recent study [Assassi, 2016] has proposed a simple index of distinction based on the ratio of SST anomalies and sea level anomalies (SLAs). However, this separation encounters errors when strong currents exist close to eddies, implying that the method is not feasible to identify the mode water trapping eddies that just detach from the main currents. Here in this study, we instead make use of the calculation of steric height anomaly (SHA) to separate subsurface eddies from surface ones [Gill, 1973]. This method was also applied to identify pathways of eddies propagating westward in the South Indian Ocean in Dilmahamod et al. [Dilmahamod, 2018], where several generation mechanisms of subsurface eddies were also reviewed. A recent study [McCoy, 2020] further draws a global distribution of subsurface eddies detected from a more complex algorithm that is dependent on three criteria: spiciness as a measure of thermohaline variability, buoyancy frequency as an estimate of stratification, and lastly the dynamic height anomaly indicative of the horizontal gradient force. It is noteworthy that the dynamic height anomaly is calculated for the detection of subsurface eddies in this study, while the other two criteria are more or less equivalent to our mode water detecting algorithm.

Here, we specifically validate the algorithm of MLD and mode water detection through the South Atlantic Subtropical Mode Water (SASTMW), which has received much less attention compared with the northern hemisphere oceans [Provost, 1999; Sato, 2014; Souza, 2018; Bernardo, 2020]. It is of interest to study the South Atlantic subtropics primarily for the reason that the SASTMW not only contains a typical variety that develops from the western boundary (i.e., the Brazil-Malvinas Confluence), but also includes other types that interconnect with another basin (i.e., the water mass intrusion through the Agulhas Ring Corridor from the Indian Ocean). In a nutshell, the objectives of this study are to:

1. clarify the new algorithm applied to Argo profiles to detect surface mixed layers and mode waters;
2. briefly summarize the distribution and characteristics of SASTMW detected by the algorithm, and mainly compare with Sato et al. [Sato, 2014], the most recent study of SASTMW;
3. co-locate eddy positions extracted by the satellite-deduced TOEddies algorithm [Laxenaire, 2018] with the Argo profiles, in an attempt to evaluate the effect of mesoscale eddies on mode water formation and transport in this region;
4. follow the steric height anomaly method that separates subsurface eddies from surface ones, and apply this separation to TOEddies algorithm to further draw possible patterns of subduction associated with mode waters.

This chapter is organized as follows. In the next section, the data we have used are described and the methods we have developed are introduced. Validation of the new algorithm to calculate MLD and mode water thickness is also presented. For the results, we firstly compare our MLD detection in the South Atlantic with other simple threshold methods and the hybrid method developed by Holte et al. [Holte, 2009], and we subsequently present a reconstruction of the SASTMW field and a reclassification into three mode water types; the reclassification allows for a closer inspection of the spatial distribution, vertical configuration and thermodynamic features of each type, providing a more quantifiable correlation with mesoscale eddies. A discussion and conclusion are followed in the last section.

Our publication: Formation and Transport of the South Atlantic Subtropical Mode Water in Eddy-Permitting Observations

Also available by clicking here.

2 Detection of the South Atlantic Subtropical Mode Water

The South Atlantic region of interest is bounded from the equator to 60 °S in the latitude direction, and assumed to extend from the entire subtropical gyre system to the formation area of Agulhas Rings longitudinally (70 °W–30 °E), including 122202 profiles in total between years 2000 and 2018, as shown in Figure 4.1. The number of profiles has greatly increased since 2004, due to additional deployments of floats, e.g., the histogram from Figure 1 in Sato et al. [Sato, 2014]. Since the actual float trajectories are affected by currents and smaller-scale motions, the spatial distribution of profiles as counted in each $1^\circ \times 1^\circ$ grid shown in Figure 4.1 (b) remains subject to the dynamical patterns, with a hotspot area in the turbulent Cape Basin where the Agulhas Rings are formed.

In the last Chapter, the newly-developed algorithm for MLD and mode water detection has been introduced. To recap, the key points of this algorithm include:

1. The main idea of this algorithm is based on the gradients and their derivatives of density and temperature profiles, for the searching of precise depths that bound homogeneous layers.

2. The detection of surface MLD is dependent on density profiles, with the classic threshold of $\sigma_{0th} = 0.03$ kg m^{-3} included as a gatekeeper.

3. The outcropping mode water is detected in the same way as the mixed layer, but by looking for gradient changes in temperature profiles.

4. The detection of subsurface mode waters is more complicated. Though these extreme values of gradient and second derivative are pointed from temperature, a

typical constraint on temperature gradient and potential vorticity (i.e., density gradient) is applied, in order to find water masses that are homogeneous enough.

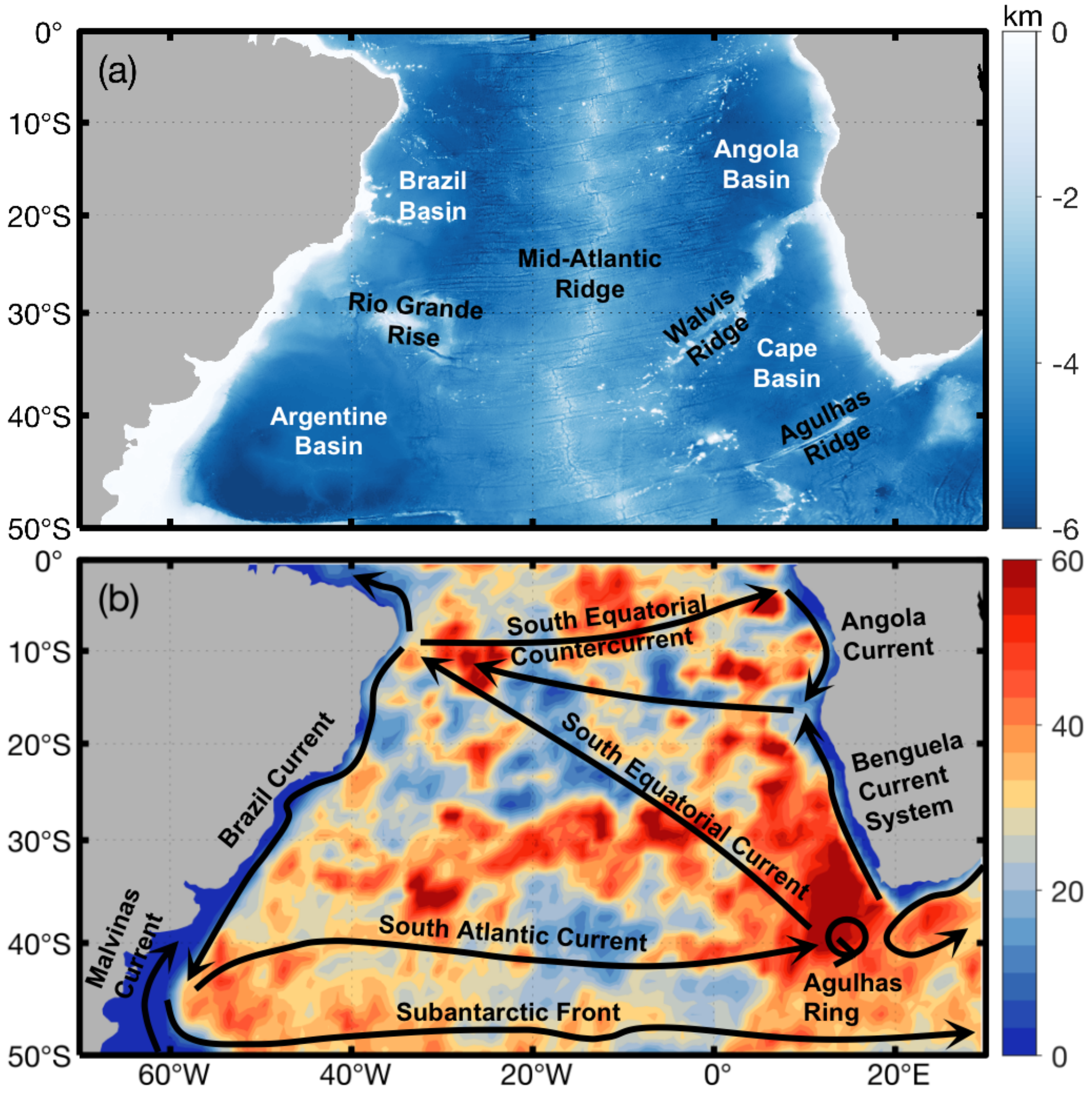

Figure 4.1: The area of study including (a) bathymetry from the ETOPO2 dataset [Smith, 1997] and (b) spatial distribution of Argo profiles in the South Atlantic between years 2000 and 2018, superposed by the main surface circulation structures (the South Atlantic subtropical gyre, limited by the South Equatorial Current at its equatorward limit, the Benguela Current system at its eastern limit, the Agulhas Current Retroflection and Agulhas Rings at its southeastern end, the Circumpolar Current at its southern frontiers, the Brazil-Malvinas Confluence at its southwestern end and the South Brazil Current materializing its western boundary). The schematic of surface circulation is manually drawn in accordance with the overview of the South Atlantic circulation pattern in Talley et al. [Talley, 2011]. The number of profiles is counted in each 1° × 1° grid and then smoothed by a Gaussian filter of 3° in space.

Specifically in the South Atlantic, other parameters were evaluated in Provost et al. [Provost, 1999] and Sato et al. [Sato, 2014], such as restrictions on geographical location, temperature, salinity and density ranges in order to facilitate the detection of subtropical mode waters in the South Atlantic. To select only the SASTMW, a similar set of categories is also applied in this study, e.g., a potential temperature range $11-20$ °C, a salinity range $34.5-36.5$ psu and a potential density range $25.5-26.8$ kg m^{-3}. These values were chosen from the temperature-salinity relation of the subtropical mode waters that also conform to the selection in Sato et al. [Sato, 2014]. Accordingly, the selection determined by low potential vorticity and temperature gradient searches for consecutive vertical layers exceeding 100 dbar as the total thickness that contains mode waters in between. In some special cases, two or more subsurface mode water cores are obtained using this algorithm, e.g., the (c/d) profile in Figure 4.2 that is co-located with a subsurface-intensified anticyclonic Agulhas Ring.

In previous studies, mode waters identified in the subtropical South Atlantic have been divided into three varieties. This division can be attributed to Provost et al. [Provost, 1999] whose definition was based on the potential vorticity minimums found from four hydrographic CTD sections and the World Ocean Circulation Experiment (WOCE) XBT dataset. This systematic study for the first time described three mode water varieties and their thermodynamic characteristics as well as thicknesses. Sato et al. [Sato, 2014] subsequently applied a k-means clustering method [Lloyd, 1982] to the more broadly-distributed Argo profiles, which aimed to partition all mode water observations into a predefined number k of clusters ($k = 3$ in their study). This clustering analysis led to the typical classification scheme of subtropical mode waters: the one linked to the Brazil Current and its recirculation gyre (SASTMW1), the most saline variety that is directly related to the intrusion of the Indian Ocean water masses (SASTMW2), and lastly the densest one associated with the Subtropical Front (SASTMW3). Dependent on this well-established division into three mode water types, several studies [Souza, 2018; Bernardo, 2020] accordingly depicted the volumetric influence of mode waters on the South Atlantic subtropical gyre circulation.

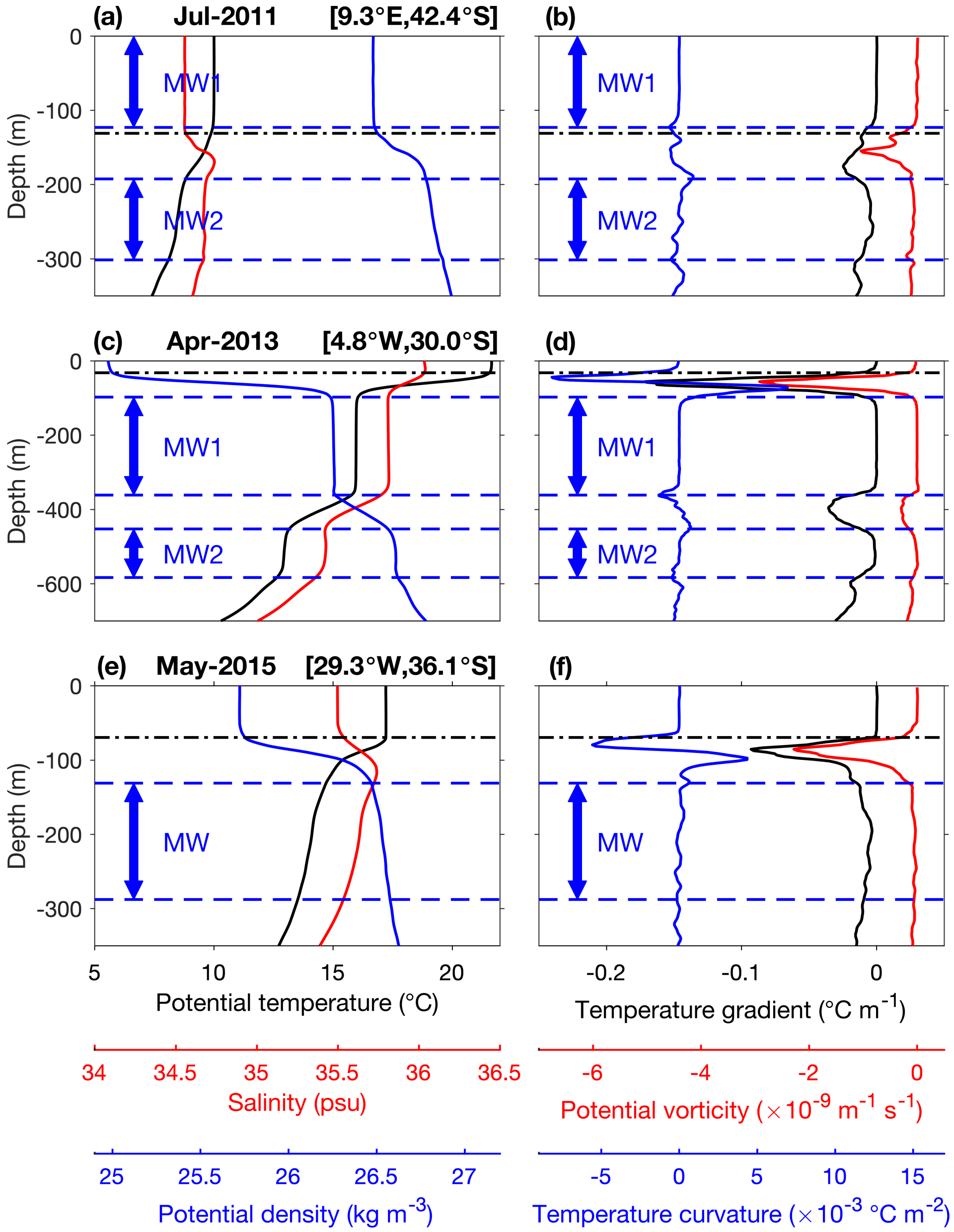

Figure 4.2: Three Argo profile examples of the mixed layer depth (MLD) and mode water detection. The left panels show profiles of potential temperature, salinity and potential density. The right panels show profiles of temperature gradient, potential vorticity and temperature curvature. The black dash-dot lines indicate the final estimates of MLD and the extent between the two blue dashed lines in each panel is a potential presence of mode water. The profile (c/d) is co-located with an anticyclonic Agulhas Ring detected from TOEddies algorithm [Laxenaire, 2019], and has been identified as a subsurface eddy from the calculation of steric height anomaly (SHA). Profiles (a/b) and (e/f) are not detected as eddies from the altimetry, but these two profiles display a maximum SHA in the subsurface and at the surface respectively (The possibility of eddy detection by the calculation of steric height anomaly alone is discussed in the result section).

Here, following Sato et al. [Sato, 2014], a k-means clustering is applied to classify profiles that have been detected with mode waters by the new detecting algorithm into groups. Since the k-means method requires a predetermined number k of clusters, an evaluation follows to assess the performance of the previous clustering. All mode water profiles have been partitioned into k mutually exclusive clusters, such that mode waters within each cluster are as close to each other as possible, and as far from mode waters in other clusters as possible. Each cluster is characterized by its centroid and mode waters are sorted relative to the distance to this centroid with the condition that the sum of the squared Euclidean distances within each cluster is minimized. The potential temperature, salinity and potential density at the depth of median potential vorticity inside each mode water are used for each profile. These three parameters accompanied by the latitude, longitude and season compose the six variables that are treated equally for the classification. The variable of season corresponds to a three-month period of time (i.e., June-August is the austral winter, and so on). In addition to the division into three clusters, we also tested other possibilities, e.g., $k = 2$ and 4. The $k = 2$ choice mainly separates light mode waters from dense ones, according to their potential temperature and density properties. While on the other hand, the division into four clusters further splits the SASTMW1 that originates from the western boundary into a warm variety that is presumably linked to the formation process, and a cold variety, most of which are found in the subsurface.

3 Detection of surface and subsurface eddies in the South Atlantic

Satellite altimetry data provide the ideal complement to the sparse distribution of Argo profiles, which facilitate to address the issues of ocean heat and fresh water storage, transport and variability associated with mesoscale dynamics. In the current study, we apply the eddy detection algorithm TOEddies [Laxenaire, 2018] that is mainly a two-step process: it first identifies eddy structures from altimetry ADT maps and then derives their trajectories together with eddy splitting and merging events. The TOEddies method also makes it possible to co-locate the detected eddies with Argo profiles that possibly capture deep mixed layers and thick mode waters. There are two types of eddy contours in the eddy detection algorithm: one is associated with the outermost closed ADT contour to define each eddy, and the other is related to the maximum azimuthal velocity of the vortex. In this study, the radius of the outer contour R_{out} is used to determine whether the location of an Argo profile falls in the scope of an eddy in that the trapped water in an eddy is not expected to stay exactly within the maximum velocity contour R_{Vmax} [Laxenaire, 2019]. The co-location of Argo profiles and altimeter-detected eddies results in the separation of these vertical profiles into three groups: those sampling a cyclonic eddy, those sampling an anticyclonic eddy, and those falling outside of either type.

Sometimes these eddies evolve in the ocean interior along their trajectories, but their signatures often remain measurable at the surface so that they can still be detected by satellites. Next, a method that separates subsurface-intensified eddies from surface ones is introduced to partition these altimeter-detected eddies and associate the eddy vertical locations with mode water detection. This separation is accomplished by taking into account the pressure-dependent steric height anomaly, h', following the definition by Gill et al. [Gill, 1973]:

$$h'(p) = \frac{1}{\rho_0} \int_{1500}^{p} {\sigma_0}' dp, \tag{4.1}$$

where ρ_0 is the reference seawater density and ${\sigma_0}'$ is the anomaly of potential density, relative to a climatological profile that represents the local environment. The pressure of 1500 dbar is regarded as the no-motion reference level. For each profile detected with an eddy from the TOEddies algorithm, its related climatological profile is calculated as an average over all profiles that satisfy both criteria of locations and time. Spatially, these profiles are supposed to be positioned within a rectangular box of 2.5° × 2.5° centering on the eddy profile, while the selection based on time applies a window spanning over 30 calendar days (i.e., independent of the year) from the date of the eddy. These criteria ensure that the anomaly profile ${\sigma_0}'$ is restricted to local variations.

For each eddy, the h' displays a different shape of profile (see Figure 4.3). Those with larger h' values in the subsurface compared to the surface could be representatives of subsurface-intensified eddies. Alternatively, h' maximum is usually found within surface layers for profiles presumably representing surface-intensified eddies. In this study, the previously detected MLD is used as the depth criterion for classifying an eddy as surface or subsurface. That is, subsurface eddies are defined by h' profiles with maximum values below the MLD. The sign of h' also determines the polarity of an eddy: cyclonic eddies are correlated with negative h', while the profiles displaying positive values of h' are associated with anticyclonic eddies.

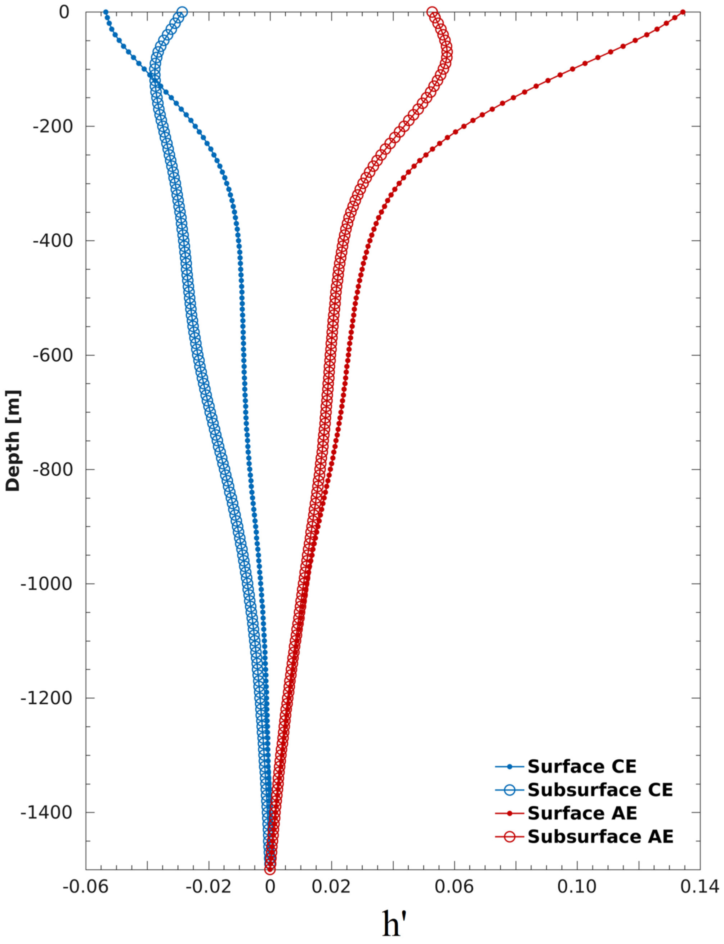

Figure 4.3: Steric Dynamic Height anomaly, h', for surface (small dots) and subsurface (large dots) intensified cyclonic (blue) and anticyclonic (red) eddies. (Source: [Dilmahamod, 2018]).

It is also of interest to test whether this SHA separation of surface and subsurface eddies could be applied alone as eddy detecting method (i.e., without any detection derived from altimetry maps at the beginning). Though sometimes subsurface eddies are observed to exert sea surface signatures and thus can be detected from satellites, the proportion remains unclear. However, an obvious issue with the SHA method is that almost every SHA profile predetermines an eddy since the profile typically holds an h' maximum no matter at what depth it is located. Thus, some discussions regarding the possibility of eddy detection by SHA are provided in the last part of results.

4 Results

4.1 Spatial distribution of SASTMW

Before the general description of SASTMW, Figure 4.4 shows the patterns of (SST), sea surface salinity (SSS), heat flux and eddy kinetic energy (EKE) in the South Atlantic Ocean over months from July to October (austral winter). The SST and SSS patterns are displayed to provide the location of the Subtropical Front along 40 °S that separates the subtropical domain from the subantarctic region, which is indicative of the boundary of SASTMW. These maps are also overlapped with the season-averaged ADT contours in dark grey and bottom topography in light brown, respectively showing the upper-ocean general circulation and providing positions where mode waters might be formed and transported.

Figure 4.4 (c) then displays the pattern of winter cumulative heat flux to estimate the strength of winter cooling. Regions of heat loss excess would be regarded as favourable areas of mode water formation or renewal due to the commonly observed co-occurrence with convective mixing maximum. In the subtropical South Atlantic, it seems obvious that two regions dominate as venues of intense heat loss to the atmosphere. The western region is located at the confluence zone where the Brazil Current meets the Malvinas Current [Gordon, 1989], while the eastern region corresponds to the dynamics of Agulhas Rings in the southeastern Cape Basin, stimulated by the intrusion and retroflection of the Agulhas Current that brings warm and salty waters from the Indian Ocean [Gordon, 1992; Speich, 2007; Capuano, 2018]. Those regions with intense cooling are also consistent with the EKE pattern shown in (d), suggesting a possible role of mesoscale dynamics in buoyancy loss, mode water formation and transport.

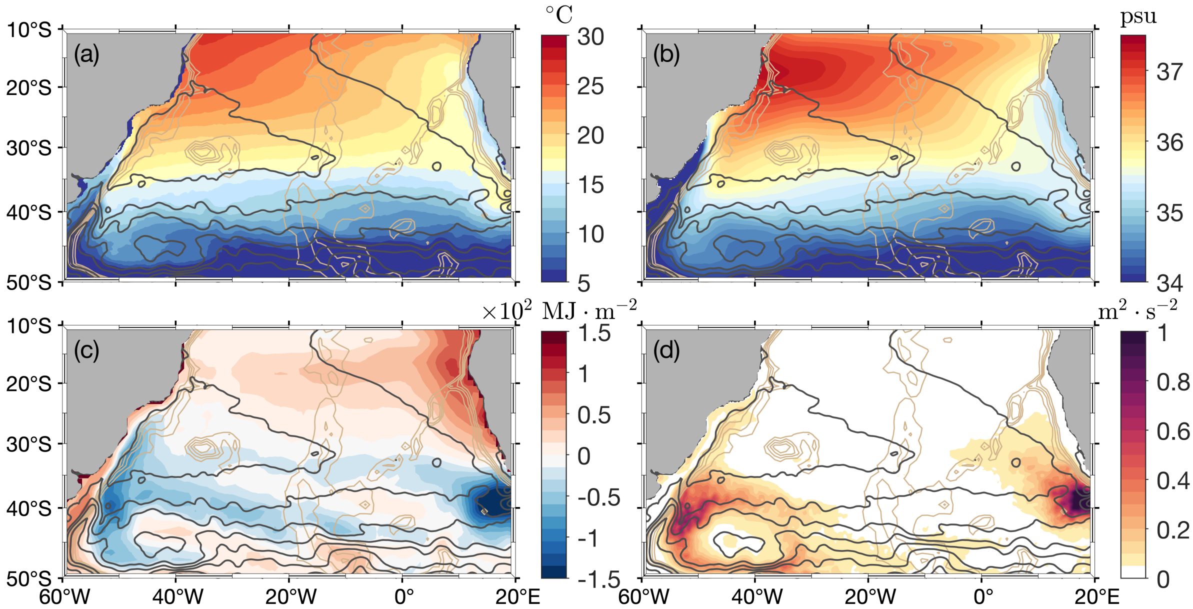

Figure 4.4: Spatial patterns of austral winter-time (a) mean sea surface temperature (SST) calculated over daily maps of the period 2000-2016 from the European Space Agency (ESA) Climate Change Initiative (CCI) database [Merchant, 2019], (b) mean sea surface salinity (SSS) averaged over the monthly database from 2000 to 2018 archived in the Copernicus Marine Service [Droghei, 2018], (c) cumulative heat flux (positive downward) calculated by adding the daily maps between 2002 and 2009 from the WHOI OAFlux Project [Yu, 2008], and (d) cumulative eddy kinetic energy (EKE) in the South Atlantic region, derived from the SLA field and based on the geostrophic relationship [Pujol, 2016]. The austral winter in these maps is defined from July to October. The overlapping dark grey lines indicate the season-averaged ADT contours [provided by SSALTO/Data Unification and Altimeter Combination System (DUACS)] and the light brown lines show contours of bathymetry over −3600 to −1800 m.

Counting both outcropping and subsurface components in the subtropical South Atlantic, in total we detected SASTMWs in 10472 profiles (with 7375 outcropping mode waters, and 3097 subsurface mode waters that also involve 50 profiles with double cores at depth). When limited to the south of 15 °S and north of 45 °S, some profiles are intentionally excluded. That is, the total number of 10472 profiles was confined to this latitudinal band, while other mode waters exist outside this domain yet still fill in the ranges of temperature, salinity and density of subtropical mode waters in the South Atlantic. This process of exclusion is added because the temperature and salinity of mode waters in the South Atlantic show a wider spectrum especially compared with, for example, the Eighteen Degree Water as one type of the North Atlantic subtropical mode waters. A specific constraint of latitudes and longitudes is thus required to separate the subtropical mode waters from subantarctic ones in the South Atlantic. For example, outcropping mode waters located within the Zapiola basin might be one type of the Subantarctic

Mode Water (SAMW) formed on the northern flank of the ACC [Herraiz-Borreguero, 2011]. From this perspective, we set the southern boundary of 45°S to exclude other water masses.

Figure 4.5 illustrates the maximal values of mode water thickness calculated by the new algorithm and displays two configurations in terms of the vertical. In order to spatially interpolate the scatter pattern of mode waters to show a more general distribution, the maximal values of mode water thickness were selected in each 1° × 1° grid and those isolated mode water dots that are not connected to other profiles were removed. For this reason, the spatial patterns of both (a) outcropping and (b) subsurface mode waters display thoroughly connected belts. The upper panel shows a thick outcropping mode water layer developed in the southwestern part of the subtropical gyre where warmer water carried by the southward Brazil Current is subject to severe winter cooling by the polar air outbreaks from the continents, and as it encounters the Malvinas Current that brings cold water northward. The thickest outcropping SASTMWs are found at the eastern boundary of the Brazil Current recirculation gyre nearby 30 °W. More generally, thick layers of outcropping mode waters extend along the South Atlantic Current from the Brazil-Malvinas Confluence region as well as along the path of Agulhas Rings in the Cape Basin, at the eastern end of the subtropical gyre.

The distribution of subsurface SASTMW thickness is displayed in Figure 4.5 (b). Superimposed are the steric height contours at 400 dbar that result from an integration over all climatological profiles starting from 1200 dbar. Such contours illustrate the subsurface structure of the ocean circulation and, in particular, that of the subtropical gyre which shifts poleward at depth. The figure shows that the subsurface SASTMW is confined within and spans across the entire subtropical gyre. Analogous to the pattern of outcropping mode water thickness, the thickest layers are also located along the South Atlantic Current with maximums situated on top of the Mid-Atlantic Ridge and nearby 40 °W. Other regions of relatively thick subsurface mode waters are observed along the routes of Agulhas Rings in the eastern and northern areas of the subtropical gyre. Agulhas Rings carry transformed Indian warm and saline waters northwestward, following the subsurface Benguela Current system [Guerra, 2018; Laxenaire, 2019], with the thickest subsurface mode waters situated between the Walvis and Mid-Atlantic Ridges.

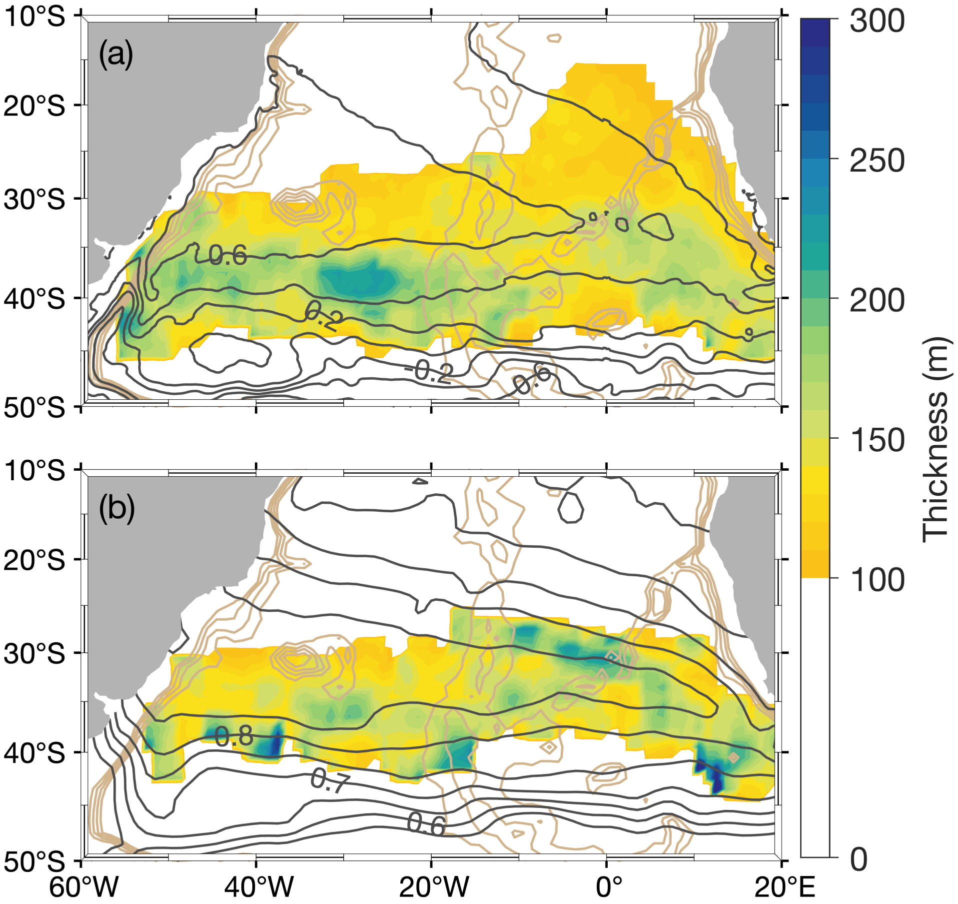

Figure 4.5: Maximal mode water thicknesses for (a) outcropping mode waters overlapped by the mean dynamic topography (MDT) as contours in dark grey [Mulet, 2021]; and (b) subsurface mode waters instead superimposed by the steric height (anomaly) contours at 400 dbar integrated from 1200 dbar and averaged in each 1° × 1° grid [Boyer, 2019]. If more than one subsurface mode water is detected for a profile, the thickness is the sum of the two subsurface mode waters. The light brown contours draw the mean pattern of bottom topography over -3600 to -1800 m.

A cluster analysis is applied to separate the SASTMW profiles based on six parameters that bind similar members together. The difference between our analysis and that of Sato et al. [Sato, 2014] is that in our method the parameters were picked at the depth where the median potential vorticity was found within the detected mode water layers while their target depth of the median potential vorticity was spotted from the entire profile. At first sight of Figure 4.6 (a), (b) and (c), the separation leads to three clusters with their centroids respectively located in the west (SASTMW1), northeast (SASTMW2) and southeast poleward edge of the subtropical gyre (SASTMW3). Generally, mode waters in the SASTMW1 cluster are concentrated around the Brazil Current extension and its recirculation area, situated in the western side of the basin. Figure 4.6 (d) and (e) show that SASTMW1 is characterized by intermediate values of properties between SASTMW2 (the warmest, saltiest and lightest variety) and SASTMW3 (the coldest, freshest and densest of the three). In favor of comparison, the colors of these three varieties were intentionally chosen to match the separation in Figure 4 of Sato et al. [Sato, 2014]. Consistent with the general separation patterns of both Sato et al. [Sato, 2014] and Provost et al. [Provost, 1999], Figure 4.6 also brings several detailed differences. Concerning the separation between SASTMW1 and SASTMW2, it is evident from (d) the T-S diagram that SASTMW2 contains mode waters with more saline properties than SASTMW1. However, such is not the case in the study of Sato et al. [Sato, 2014], of which the two varieties of mode waters share the same salinity range. The overlapped area of any pairwise combination remains large, while these three varieties are more separable in Sato et al. [Sato, 2014].

Besides the general division of SASTMW into three clusters, Figure 4.6 also displays a separation of mode waters by configuration. The lower five panels (f–j) provide another cluster analysis limited to only subsurface mode waters. In comparison to a broader range of the potential density of total mode waters, the three varieties of subsurface mode waters are characterized by densities above 26 kg m^{-3}, with shrinking density range in each cluster. Noticeably, both subsurface SASTMW2 and SASTMW3 shift northward in contrast to the total SASTMW2 and SASTMW3 patterns (see the comparison of histograms (b) and (h)). The spatial distribution of subsurface SASTMW2 in (i) approximately follows the route of subduction along the deep Benguela Current. This shift also implies that the SASTMW3 stems more likely from the water supply shedding from the Agulhas Current into the Cape Basin that contains Indian warm and saline properties. Sato et al. [Sato, 2014], on the contrary, attributes the origin of SASTMW3 derived from their calculation to the western boundary that can be transported by the South Atlantic Current along the southernmost boundary of the subtropical gyre towards the east. In other words, they suggested the same formation region for SASTMW1 and SASTMW3 in that both have footprints west of 45 °W and south of 40 °S. However, it is thus difficult to explain the mechanisms that separate these two mode water types holding similar density ranges.

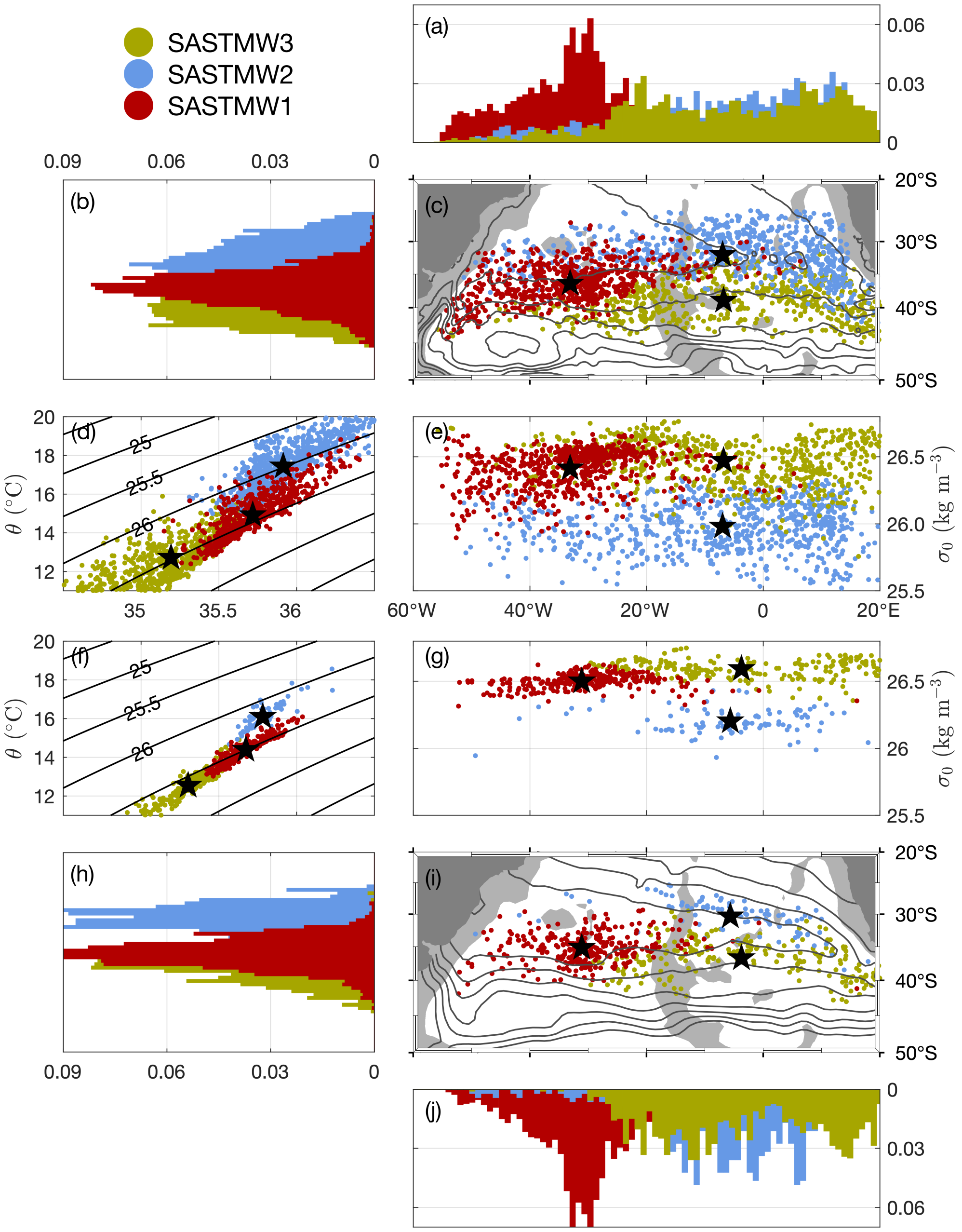

Figure 4.6: Three types of SASTMW selected by the cluster analysis based on parameters measured at the depth of median potential vorticity of each mode water layer: SASTMW1 (red), SASTMW2 (blue), and SASTMW3 (green). The upper five panels (a-e) provide an analysis of the total number of mode water layers and the lower five panels (f-j) comparatively show another analysis only for subsurface mode waters. These panels contain (a/j) histograms as a function of longitude; (b/h) histograms as a function of latitude; (c/i) the spatial distributions; (d/f) temperature-salinity diagrams with potential density contours; and (e/g) the potential density as a function of longitude. The location of centroids determined by the cluster analysis is identified as black stars. For the two patterns of spatial distribution, (c) is overlapped with the mean dynamic topography (MDT) as contours [Mulet, 2021], while (i) is superimposed by the steric height (anomaly) contours at 400 dbar integrated from 1200 dbar.

With the aim to specify the genesis and evolution of individual mode water types, Figure 4.7 then highlights the information of layer thicknesses divided into outcropping and subsurface ones. The outcropping SASTMW1 variety (Figure 4.7 (a), holding 1782 profiles and taking up 17.0% of the total number) concentrates in the south-westernmost part of the subtropical gyre between the Confluence region and the Subtropical Front mostly west of the Mid-Atlantic Ridge. The subsurface SASTMW1 (Figure 4.7 (b), counted in 1712 profiles in total (16.3%)) is extensively distributed across the inner core of the deep subtropical gyre. While the averaged thickness of outcropping SASTMW1 reaches 164 m, the mean thickness of subsurface SASTMW1 is slightly lower (142 m). Composed of 3378 profiles in total (32.3%), the outcropping SASTMW2 (Figure 4.7 (c)) spans over the north-eastern portion of the subtropical gyre and reaches the far west coast. The SASTMW2 in the subsurface (Figure 4.7 (d), with 395 profiles (3.8%)) outspreads the northeastern part of the basin, displaying an explicit path of thick mode water layer along the deep Benguela Current. The spatial distribution of total SASTMW2 and its length of spreading thus imply that the Benguela Current and potential paths of Agulhas Rings play a crucial role in advecting mode waters zonally to the west [Stramma, 1999]. The mean thicknesses of outcropping and subsurface SASTMW2 reach 133 m and 147 m respectively, and this is the only type of the three featured by a much thicker subsurface mode water layer than the outcropping one. The SASTMW3 that outcrops (Figure 4.7 (e), displaying 2215 profiles (21.2%)) lies in the south-easternmost part of the gyre, with the thickest water layers clustering along the South Atlantic Current above the Mid-Atlantic Ridge as well as aligned along the routes for Agulhas Rings. Although the thickest layers of outcropping SASTMW2 and SASTMW3 approximately overlap at the intrusion of Agulhas Rings, it is plausible to associate the SASTMW2, the lighter SASTMW variety, with the northern and central routes of Agulhas Rings and to relate the SASTMW3, the denser variety, to the southern route as described in Dencausse et al. [Dencausse, 2010]. It is also the case for the comparison between these two varieties in the subsurface that SASTMW3 (Figure 4.7 (f), with 990 profiles (9.5%)) penetrates in the subtropical gyre from the Cape Basin and extends until the Mid-Atlantic Ridge, following a route more southern and deeper than that of the subsurface SASTMW2. The averaged thickness of outcropping SASTMW3 is 150 m, and this value is similar to the subsurface SASTMW3 thickness, which reaches 151 m. In general, our calculation results in thinner mode waters compared with Sato et al. [Sato, 2014], however, both studies suggest that SASTMW2 is characterized as the thinnest type of the three.

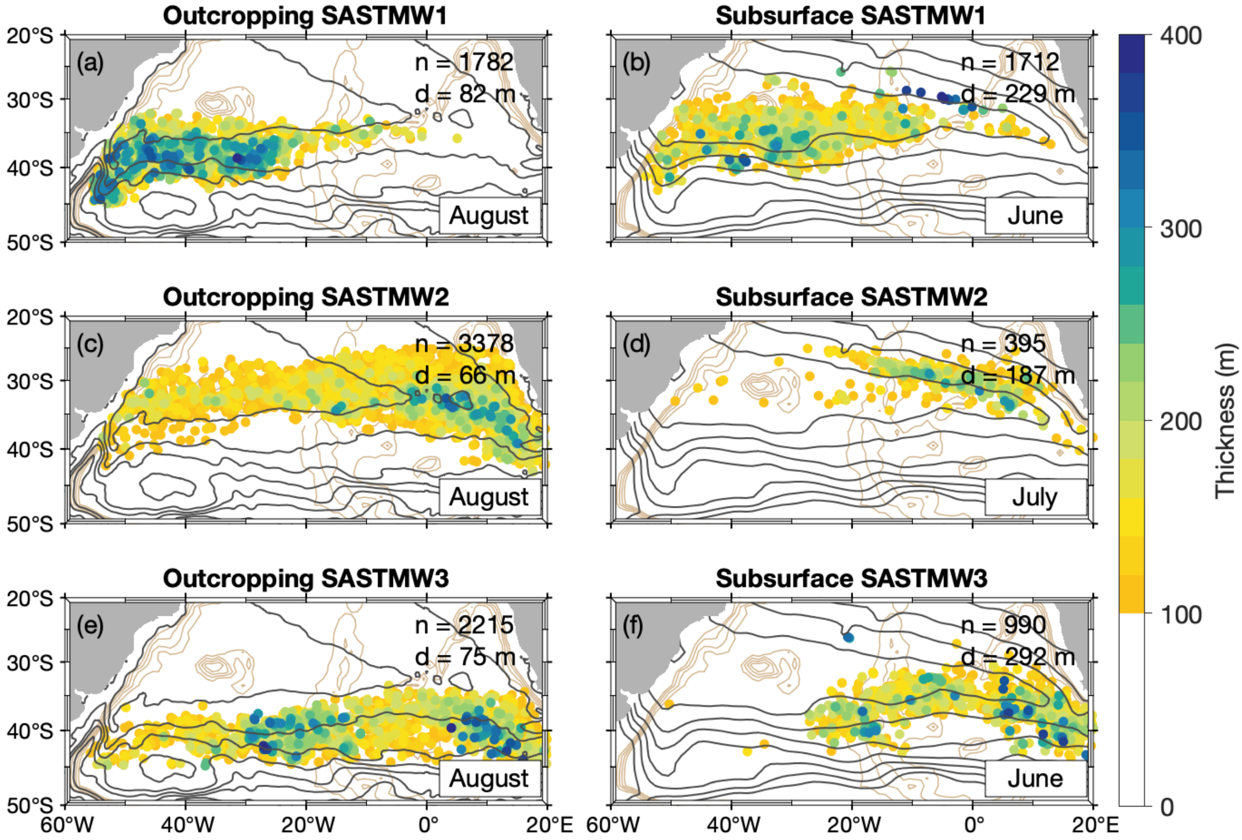

Figure 4.7: The thicknesses of outcropping and subsurface mode waters. The number n on the top right corner of each panel indicates the number of profiles detected as mode waters for each specific type. The number d is indicative of the mean depth of mode waters. Panels of outcropping mode waters (a), (c) and (e) are overlapped by the mean dynamic topography (MDT) as contours in dark grey [Mulet, 2021] and panels of subsurface mode waters (b), (d) and (f) are superimposed by the steric height (anomaly) contours at 400 dbar integrated from 1200 dbar. The light brown contours draw the mean pattern of bottom topography over -3600 to -1800 m. At the bottom right corner in each panel, the averaged month of occurrence for mode waters is added.

As expected, the outcropping SASTMW layers are found mostly in winter and early spring months in coherence with the formation processes whereas the subsurface varieties are identified at any time, suggesting that these waters move in the ocean interior and are disconnected from any interaction with the atmosphere. This is true in Figure 4.7 that the averaged month of occurrence for outcropping mode water detection is concentrated on July and August (austral winter), while the subsurface mode waters could be found at any season of the year (not shown). This seasonal variation together with their spatial distribution suggests that SASTMW1 is formed at the southwestern edge of the subtropical gyre. Once subducted, these mode waters move in the gyre interior following the recirculation flow. By contrast, the SASTMW2 and SASTMW3 both take their origins mostly in the eastern corner of the subtropical gyre in the Cape Basin and extend towards the western boundary.

As mentioned earlier, a similar cluster analysis by Sato et al. [Sato, 2014] assigned the formation and transport of SASTMW3 to the Subtropical Front of the South Atlantic Current, suggesting that any potential subduction processes of mode waters are linked to the eastward transport. Other differences between our cluster analysis and theirs are also observed. For example, we have detected more subtropical mode water layers compared with them (also taking into account 5 more years of profiles). A more recent revisit to the cluster analysis of SASTMW [Bernardo, 2020] confirms that even using a more restricted temperature range to select subtropical mode waters, it still yields a division into three clusters that highly matches the results of Sato et al. [Sato, 2014]. In both studies, the spatial distribution of each mode water type is almost entirely separated from others, while in our study different varieties overlap in their properties (compare Figure 4.7 with the Figure 5 in Sato et al. [Sato, 2014]). Another evident difference between our results and those of Sato et al. [Sato, 2014] is related to the thickness pattern. Both studies display similar hotspot areas of thickest mode waters, but Figure 4.7 provides a more obvious route of mode water transport along the paths of Agulhas Rings.

Laxenaire et al. [Laxenaire, 2019] suggested that heat content anomalies transported by Agulhas Rings were concentrated in mode water cores. Here, we quantify the potential temperature anomalies calculated within each mode water layer, which helps to understand the amount of heat anomalies carried by mode waters. Figure 4.8 displays the anomaly for the three types of SASTMW and further shows a division of subsurface mode waters into upper (middle panels) and lower cores if present (right panels). The anomaly is computed as the subtraction of the climatological temperature from each Argo profile and averaged over isopycnals of mode water layer to obtain a single value for each detection. The pressure coordinate is commonly used to calculate the anomaly within mode water layers (e.g., to integrate anomalies over pressure or depth); nonetheless, the computation in Figure 4.8 is based on the density coordinate and this choice more correctly captures the anomaly values, which highlights the different abilities of mode waters and the environment in trapping heat. It is also interesting to note the existence of lower subsurface mode water cores in some profiles (albeit much fewer in number than the upper subsurface and outcropping ones, only counted in 50 profiles). In other words, the double-core profiles that are more or less indicative of co-location between water masses with different origins, are sparse and mostly limited to the Brazil Current recirculation gyre or narrowed within the routes of Agulhas Rings.

The regions of Brazil-Malvinas Confluence and paths of Agulhas Rings constitute the two main areas of heat release to the atmosphere, and hence favourable for convective mixing and water mass formation. Counter-intuitively, all panels in Figure 4.8 display warm temperature anomalies inside mode water layers as compared to the monthly averaged environment. The maximal warm anomalies of outcropping SASTMW1 shown in Figure 4.8 (a) are situated exactly at the the Brazil-Malvinas Confluence zone and extend along the Subtropical Front. This mode water type originates from the southward Brazil Current that carries tropical warm and saline waters. It is also evident in Figure 4.4 (a) and (b) that local hotspots of SST and SSS exhibit at the western boundary with centers at 15 °S and 18 °S respectively. The other two types of mode waters, SASTMW2 and SASTMW3, initiate from the Agulhas Leakage where Indian warm and saline waters overshoot via anticyclonic Agulhas Rings. Interestingly, the spatial pattern of temperature anomalies inside SASTMW2 and SASTMW3 is also consistent with studies of individual Agulhas Ring tracking that correspond the salt and temperature fluxes over the Agulhas Leakage to these rings more than their surroundings [Laxenaire, 2019]. These facts recall a possible link between mode water transport and mesoscale eddies, with an emphasis on the anticyclonic ones that can trap such anomalies inside isopycnal layers. In the next section, we specifically focus on such analysis.

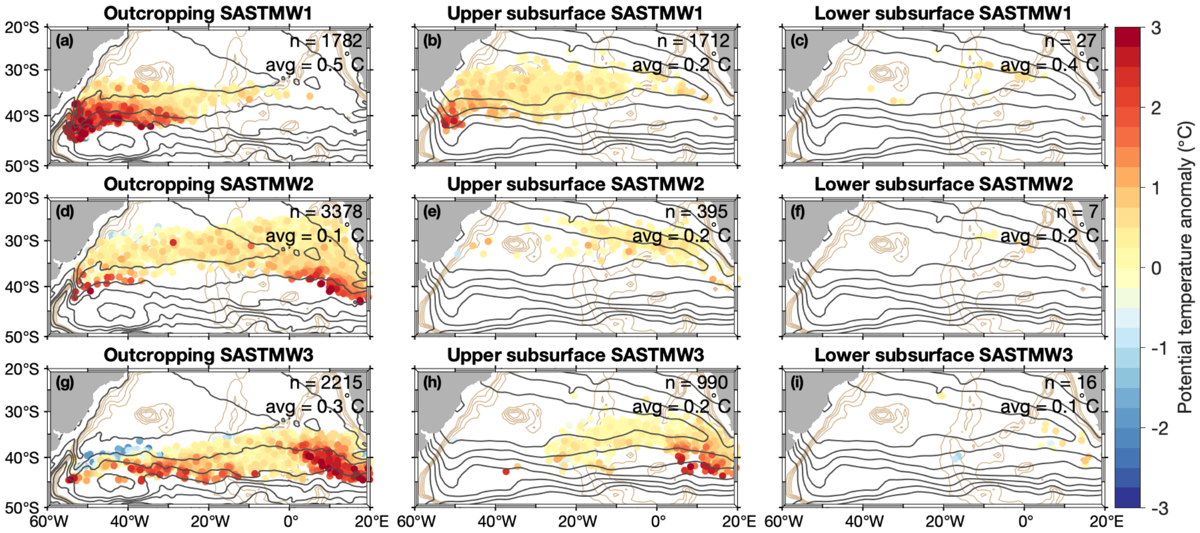

Figure 4.8: The potential temperature anomaly of outcropping and subsurface mode waters. These values of anomaly were calculated as the difference between the original Argo profiles and climatological profiles associated with each individual Argo profile [Laxenaire, 2019]. The number n on the top right corner of each panel indicates the number of profiles detected as mode waters, and the value marked by avg is the mean value of potential temperature anomalies averaged over all mode waters. Panels of outcropping mode waters are overlapped by the mean dynamic topography (MDT) as contours in dark grey [Mulet, 2021] and panels of subsurface mode waters are superimposed by the steric height (anomaly) contours at 400 dbar integrated from 1200 dbar.

4.2 Co-location between mesoscale eddies and SASTMW

Here, a specific focus on the connection between mesoscale eddies and mode waters is studied. Mesoscale eddies are detected by the TOEddies algorithm from altimetry ADT maps [Laxenaire, 2018]. Figure 4.9 displays (a/d) the presence of anticyclones/cyclones in percentage of time at each altimetric grid point, (b/e) their maximum radii in each 1° × 1° grid cell and (c/f) trajectories of anticyclonic/cyclonic eddies living more than 1 year in the South Atlantic. These maps show that eddies are particularly present near the basin boundaries, but also located across the South Atlantic where they cluster along quasi-zonal paths, with the longer-lived eddies propagating from the eastern boundary westward. The adjacent area of the Brazil Current and its interaction with the Malvinas and South Atlantic Currents are occupied by both cyclonic and anticyclonic eddies, with more intense presence and larger size of anticyclones. The Zapiola gyre appears as a very active region for both eddy polarities. The presence of cyclonic eddies specifically follows the Benguela Current along the eastern coast while the anticyclonic eddies are largely linked to the formation of Agulhas Rings and their transport westward in a zonal band centered at around 35 °S. It is more apparent from the trajectories of anticyclonic eddies that under certain circumstances these eddies can live for more than 3 years and travel across the entire basin [Laxenaire, 2018].

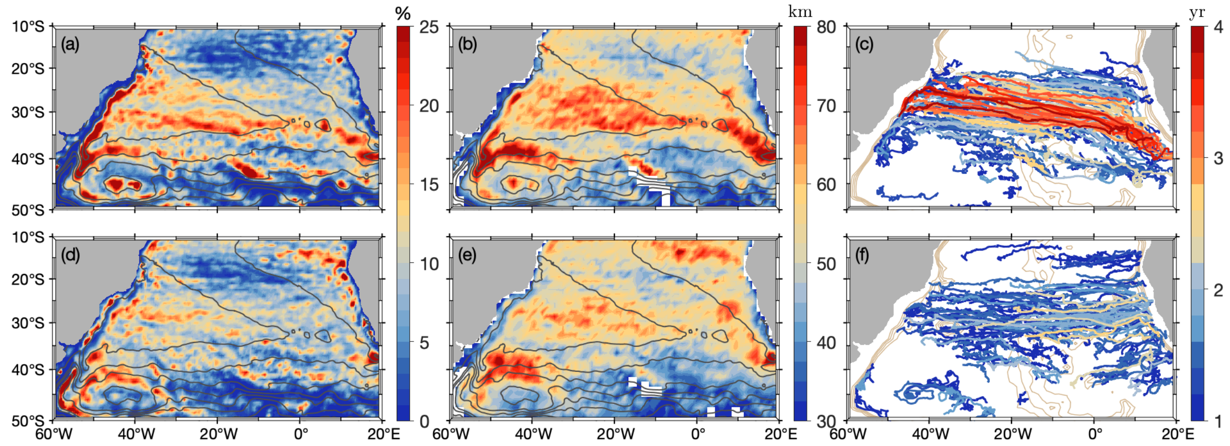

Figure 4.9: The characteristics of mesoscale eddies in the South Atlantic detected from the TOEddies algorithm [Laxenaire, 2018]. The panels show (a/d) the presence indicated by percentage, (b/e) radii, and (c/f) trajectories along with their lifetimes of anticyclonic eddies (in the upper panels) and cyclonic eddies (in the lower panels). The grey contours indicate the mean dynamic topography (MDT) as an estimate of the mean sea surface height above geoid over the 1993–2012 period [Mulet, 2021]. The light brown lines at the background in (c) and (f) show contours of bathymetry over -3600 to -1800 m.

Of the total number of Argo profiles (122202) in the South Atlantic as shown in Figure 4.1, 15093 (12.4%) and 15945 (13.0%) profiles are respectively co-located with TOEddies cyclonic and anticyclonic eddies. This result is consistent with a statement in Sato et al. [Sato, 2014] that Argo profilers indicate indifference to the presence of mesoscale eddies. In their study, 19.6% of Argo profiles were observed inside eddies identified and cataloged by Chelton et al. [Chelton, 2011]. Here, mode waters are more likely to be found in an eddy (41.6% out of the total mode water number of 10472). This fraction is largely enhanced compared with the proportion of profiles that generally sample eddies. However, Sato et al. [Sato, 2014] showed that mesoscale eddies co-located with mode waters display a similar percentage (22.4%) to that of the general co-location between eddies and all profiles.

A more detailed co-location between mesoscale eddies and mode waters is shown in Figure 4.10. The left panels (a), (c) and (e) compare the presence of outcropping SASTMWs falling within anticyclones, cyclones and outside of eddies, while the right panels (b), (d) and (f) show the relationship between subsurface mode waters and eddies. In general, mode water layers co-located with anticyclonic eddies are thicker and more expansive than those inside cyclones. This difference is particularly evident for the subsurface SASTMW, for which the co-located anticyclones outnumber cyclones by 4 to 1. It is also of interest to compare the region of maximum thickness in Figure 4.10 (a) with the left panels in Figure 4.8 of temperature anomalies. This comparison strongly supports that positive temperature anomalies are associated with anticyclones. The presence of subsurface SASTMWs inside anticyclones shown in Figure 4.10 (b) also suggests a route of water subduction following the paths of westward Agulhas Rings, with the thickest mode water layers lying between the Malvis Ridge and Mid-Atlantic Ridge. Though the number of mode waters trapped inside eddies remains smaller than those falling outside, it is still obvious that the thickest mode waters are commonly inside anticyclones. Additionally, both out-of-eddy outcropping and subsurface mode waters (see Figure 4.10 (e) and (f)) show similar patterns to co-location between mode waters and anticyclones (see Figure 4.10 (a) and (b)), but with relatively smaller thicknesses. It is worthwhile recalling that in the TOEddies algorithm, only those subsurface-intensified eddies that still maintain a surface signature are detected. In this regard, it is very likely that some subsurface eddies are not strong or stable enough to be detected by altimetry maps, but they are still efficient in transporting mode waters. Next, we further discuss this perspective in details of whether the steric height anomaly (HCA) can be regarded as an alternative to the TOEddies or other altimetry-derived eddy detecting methods, in order to detect eddies simply from Argo profiles.

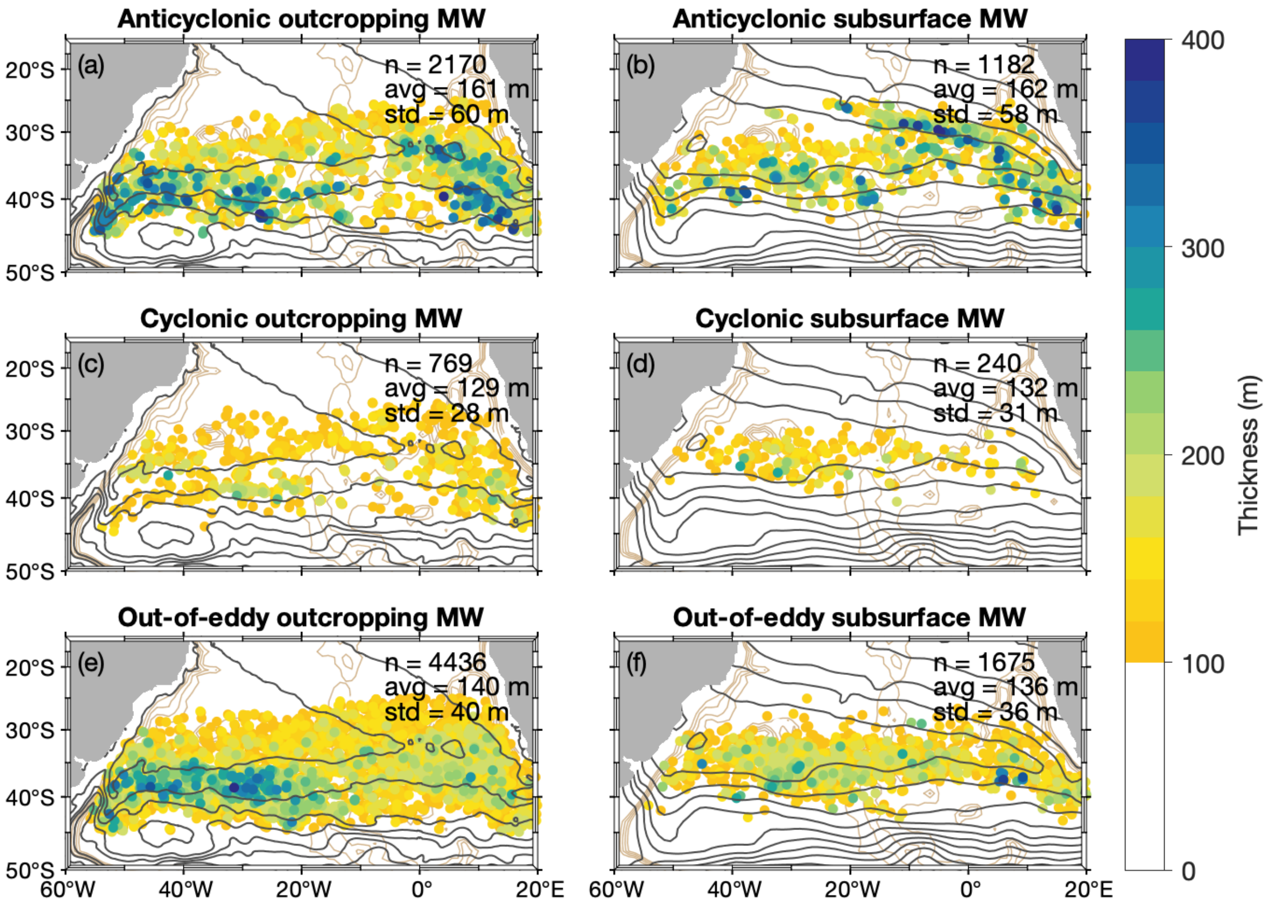

Figure 4.10: The co-location between mode waters and mesoscale eddies detected by TOEddies algorithm. Left panels show outcropping mode waters associated with (a) anticyclones, (c) cyclones, and (e) neither type. Right panels (b), (d) and (f) display the co-location between subsurface mode waters and eddies. The numbers marked by n, avg and std are respectively indicative of the total number, mean value and standard deviation of mode water thicknesses. The grey contours in the left panels indicate the mean dynamic topography (MDT) as an estimate of the mean sea surface height above geoid over the 1993–2012 period [Mulet, 2021], whereas in the right panels they represent the steric height (anomaly) contours at 400 dbar integrated from 1200 dbar and averaged in each 1° × 1° grid. The light brown contours show bathymetry over -3600 to -1800 m.

To complete the SASTMW-eddy analysis, we apply an eddy separation process based on the calculation of SHA for each Argo profile that is co-located with an eddy, in favor of dividing eddies into surface- and subsurface-intensified types. Table 4.1 displays such division by showing the percentage of mode waters trapped in eddies. The calculation of percentage was separated by the two mode water configurations (i.e., the sum of outcropping mode waters is 100%, and so is the sum of subsurface mode waters). It is evident for both outcropping and subsurface mode waters that anticyclonic eddies trap three and five times more of the quantity than cyclonic eddies respectively, even though the largest quantity of mode waters drop outside of either type. This is also in accordance with several previous studies that anticyclones provide favorable conditions for mode water formation and transport [Uehara, 2003; Sato, 2014]. Moreover, it is also true that the SHA method does not always provide a division into surface- and subsurface-intensified eddies. This is due to several factors such as insufficient length of profiles, unidentified peaks of the SHA profiles etc. Unsurprisingly, surface anticyclones play a crucial role in transporting outcropping mode waters while subsurface mode waters are more likely to be co-located with subsurface anticyclones. However, this is not the case for cyclonic eddies, which show preferences towards subsurface ones to trap both outcropping and subsurface mode waters. Since the separation of surface- and subsurface-intensified eddies depends on the MLD, the relatively shallow mixed layers associated with cyclonic eddies allow more eddies to be detected as subsurface eddies.

Table 4.1: The percentage of mesoscale eddies associated with mode water detection.

	Outcropping mode water		Subsurface mode water	
Anticyclonic TOEddies	29.4		38.2	
(Surface/subsurface)	21.8	4.3	11.9	23.1
Cyclonic TOEddies	10.4		7.7	
(Surface/subsurface)	2.6	6.0	1.6	4.8
Outside of TOEddies	60.2		54.1	

* The percentage was calculated relative to the numbers of outcropping and subsurface mode waters respectively.

Previously, we mainly applied the TOEddies detection algorithm to detect eddies from the sea surface absolute dynamic topography, and then co-located them with mode waters detected from Argo profiles. Subsequently, the steric height anomaly (SHA) for each Argo profile is calculated to determine whether the specific co-located eddy is surface- or subsurface-intensified; nonetheless, the vertical location of some profiles is unidentified from the SHA method. At the same time, we also acknowledge that satellite altimetry does not always provide precise detection since eddies can evolve into the subsurface when they relocate. Only when these subsurface ones still have a surface signature can they be detected from satellites. Accordingly following these analyses, we show the possibility of using SHA alone to detect eddies, without any altimetry-based detection in advance.

In general, this SHA method implies that each Argo profile makes up one eddy detection, which seems unrealistic. However, it might be appealing to apply this SHA detection method to Argo profiles that are already detected with mode waters, since the homogeneity of mode waters implies less mixing in progress at the core both horizontally and vertically, which refers to specific features like mesoscale eddies. Figure 4.11 shows patterns of eddy-mode water co-location as a comparison between TOEddies and SHA eddy detection methods. Left and middle panels display respectively TOEddies- and SHA-detected surface eddies (co-located with both outcropping and subsurface mode waters), which suggest that these two methods are comparable. It also provides some confidence for using SHA to analyze the co-location between eddies and mode waters. At the same time, TOEddies detection generally leads to a larger number of eddy-mode water co-location than that of the SHA surface eddy detection, except that outcropping mode waters inside SHA-detected surface anticyclones (Figure 4.11 (e)) outnumber those inside TOEddies-derived anticyclones (Figure 4.11 (d)) by more than 1000. The outnumbered co-location between TOEddies and mode waters confirms that detection methods based on altimeters are to some extent capable of identifying subsurface-intensified eddies. From another point of view, the difference between the TOEddies and SHA detection methods is dependent on the depth threshold of the maximum steric height anomaly that is used in the latter to distinguish subsurface eddies from surface ones. In other words, this depth threshold determines the proportion of surface- and subsurface-intensified eddies, as the comparison between the numbers of profiles shown in the middle and right panels of Figure 4.11. Moreover, the percentage of profiles containing SASTMW yet indiscernible from the SHA surface eddy detection is very small (31.8% inside cyclones, 63.2% inside anticyclones and only 5.0% that is unknown from the calculation), in contrast with the resulting percentage of mode waters outside of TOEddies detection (58.4%).

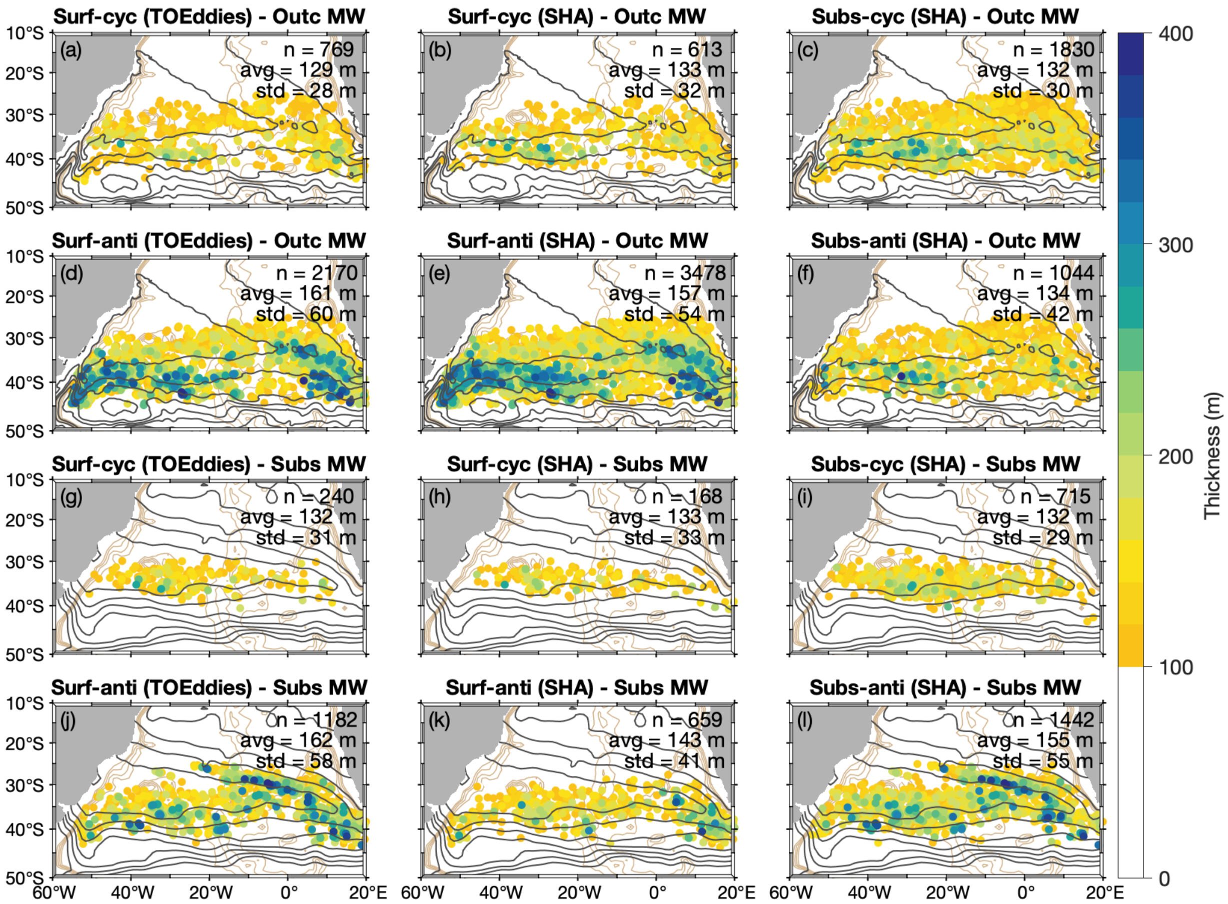

Figure 4.11: The co-location between mesoscale eddies and mode waters. Left panels (a/d/g/j) show mode waters associated with the TOEddies detection applied to absolute dynamic topography (ADT) maps; middle (b/e/h/k) and right (c/f/i/l) panels show mode waters inside eddies that are detected by the steric height anomaly. Since the calculation of steric height anomaly is mainly used to distinguish subsurface-intensified eddies from surface ones, panels (b/e/h/k) display mode waters associated with surface-intensified eddies whereas panels (c/f/i/l) show mode waters related to subsurface-intensified eddies. The numbers marked by n, avg and std are respectively indicative of the total number, mean value and standard deviation of mode water thicknesses. The grey contours in the panels of the upper two rows indicate the mean dynamic topography (MDT) as an estimate of the mean sea surface height above geoid over the 1993–2012 period [Mulet, 2021], whereas in the panels of the lower two rows they represent the steric height (anomaly) contours at 400 dbar integrated from 1200 dbar and averaged in each 1° × 1° grid. The light brown contours show bathymetry over -3600 to -1800 m.

Another climatological profiling dataset was also applied to replace the one from the TOEddies atlas that was subtracted from the original σ_0 profile to calculate SHA, i.e., the monthly mean profile (averaged over 2005–2017 years) retrieved from the 1/4° gridded World Ocean Atlas 2018 (WOA18). For the application of this climatology, the calculation of σ_0' is thus accomplished by looking for the closest WOA18 profile to each Argo profile in the geographical coordinate. However, we find the calculation of SHA highly depends on the choices of climatology. Recalling Figure 4.2 that shows three example profiles of mode water detection, we find the (c/d) profile is co-located with a TOEddies-detected anticyclonic Agulhas Ring. By calculating SHAs, the other two profiles (a/b) and (e/f) are also co-located with anticyclonic eddies, albeit they have not been identified as such from the TOEddies method. However, when the WOA18 climatology is employed instead of the TOEddies climatology, these two profiles are instead detected as surface cyclones. Though it seems plausible to assume that both (a/b) and (e/f) are co-located with anticyclonic eddies since both profiles hold thick mode water layers, the dependence of eddy detection on climatologies makes the result more ambiguous. We found this ambiguity results from the assumption that the pressure of 1500 dbar is regarded as the no-motion reference level. However, it is not the case when WOA18 climatology is applied to calculate the steric height anomaly in that at the lowest depth, a relatively large difference is observed for the comparison between the WOA18 value and the Argo profile value. This indicates that the WOA18 climatology is not the optimal choice, even though we apply the monthly mean climatology with 1/4° as resolution.

Briefly, the eddy detection with this steric height method gives an alternative definition of eddies with respect to the satellite altimetry, and its combination with mode water detection provides an opportunity to use only Argo profiles to quantify the influence of eddies on mode water formation and variability. Whichever eddy detection method is combined with mode waters, anticyclonic eddies predominantly contain more than two folds of mode waters than cyclonic eddies. However, the SHA lacks verification to be used alone to detect eddies and it is also noteworthy that steric height anomalies might also represent signatures of internal waves [Dilmahamod, 2018]. Further tests on the choices of climatological profile, the minimum magnitude of SHA to be identified as an eddy, and the threshold depth that separates subsurface eddies from surface ones are required.

4.3 Water mass subduction along Agulhas Ring trajectories

This section then considers mode water development or subduction along specific paths of mesoscale eddies in the South Atlantic. Figure 4.12 shows two trajectories of Agulhas Rings shedding from the Leakage Zone northwestward into the western boundary of the South Atlantic. The portions with red dots along the yellow-colored trajectories are mode waters detected from the new algorithm, which are co-located with eddies along their trajectories. These two trajectories are among the longest eddy trajectories identified from the TOEddies algorithm and it commonly takes more than 3 years for each Agulhas Ring to cross the entire basin, in addition to several merging or splitting events. It is evident that along both eddy trajectories, mode waters start to develop after passing by the

Walvis Ridge. While the mode water transport along the trajectory in (a2) surpasses the Mid-Atlantic Ridge, the example in (a1) only displays mode water development between the Walvis and Mid-Atlantic Ridges.

Such is not the case for cyclonic eddies as shown in Figure 4.13 as one trajectory example. Though several trajectories of cyclonic eddies are comparably long-lived in comparison with anticyclonic eddies (e.g., they can also travel across the Mid-Atlantic Ridge once generated nearby the east coast), it is often difficult to detect thick mode waters beneath them.

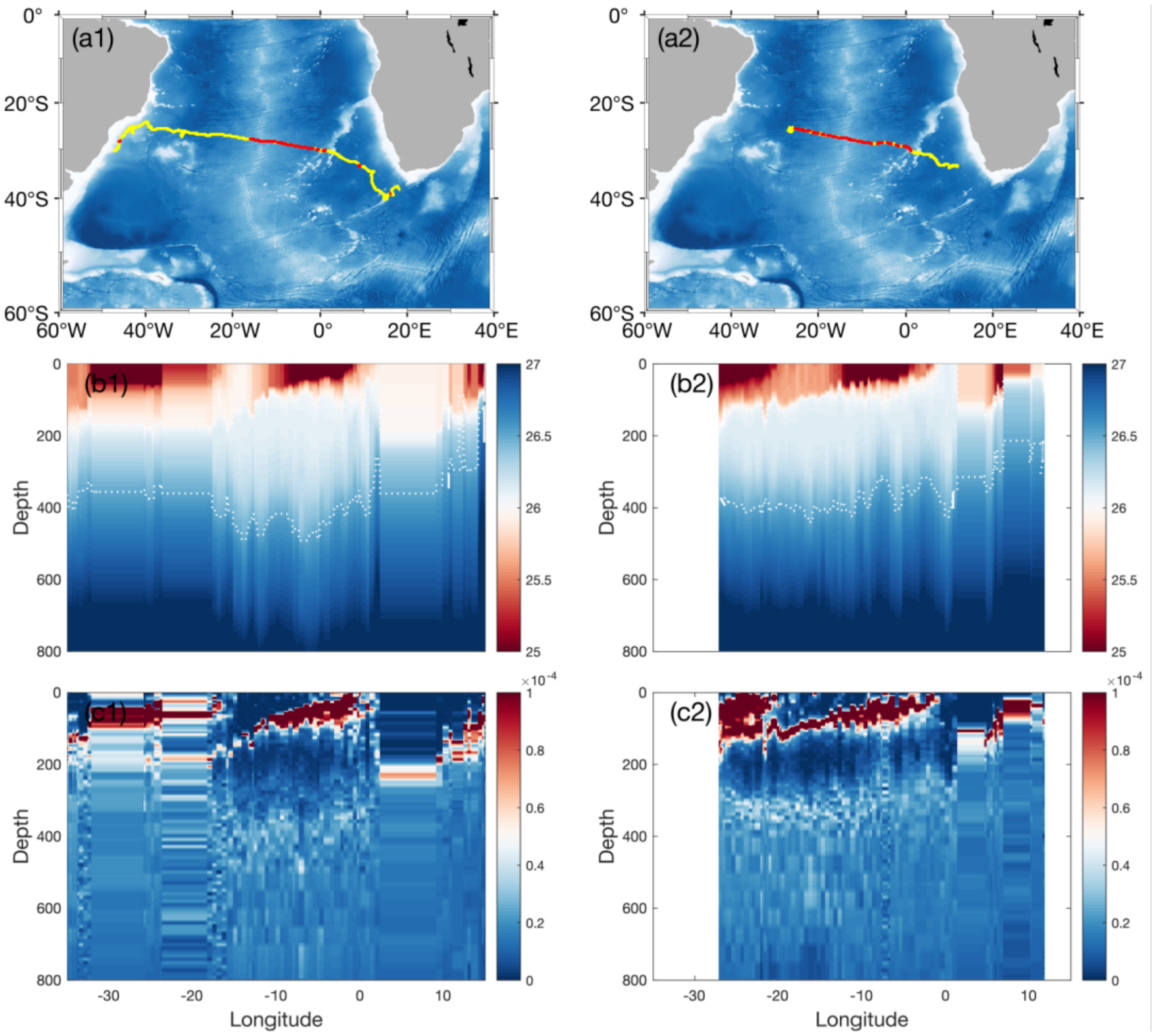

Figure 4.12: Two examples of mode water detection along anticyclonic eddy trajectories. The yellow line in (a) represents the trajectory and the red section denotes mode waters underneath. Panels (b) and (c) respectively indicate the potential density and stratification (N^2).

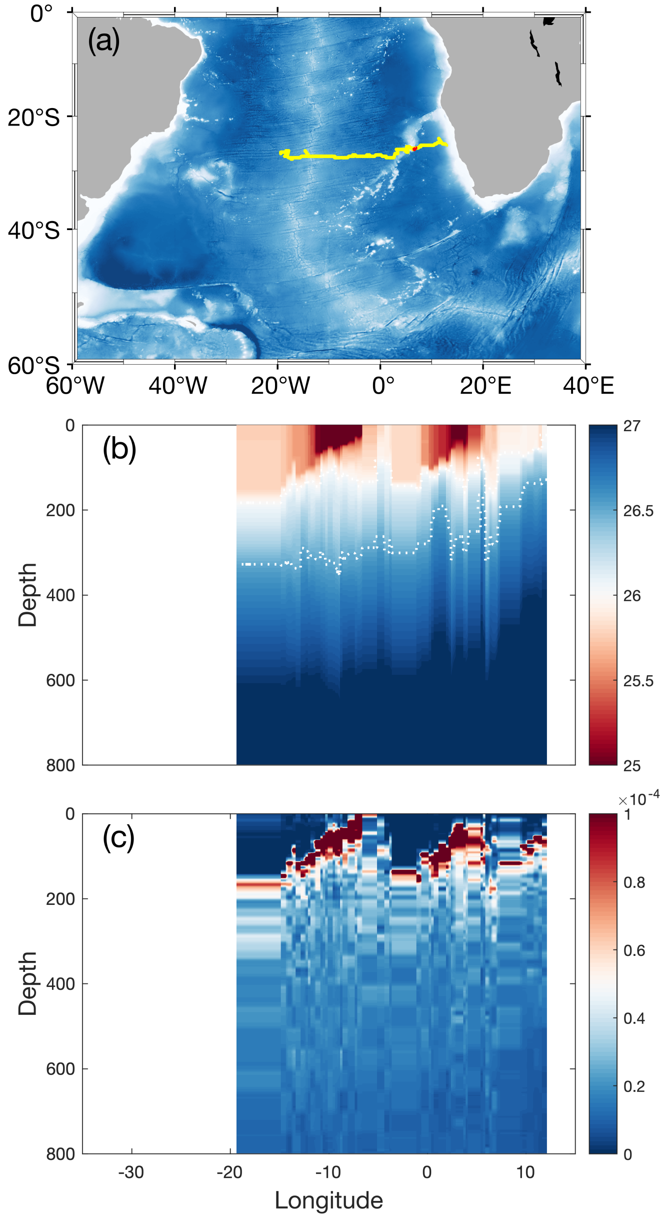

Figure 4.13: One example of mode water detection along a cyclonic eddy trajectory. The yellow line in (a) represents the trajectory and the red section (dots) denotes mode waters underneath. Panels (b) and (c) respectively indicate the potential density and stratification (N^2).

Animation: a trajectory of Agulhas Ring with detection of MLD

Also available by clicking here.

5 Discussions and conclusions

A simple algorithm to estimate the upper-ocean mixed layers and mode waters has been presented, which is dependent on the gradients and curvatures of each individual Argo profile. In comparison with previous MLD detecting methods according to (temperature or density) thresholds and gradient thresholds, this new algorithm determines the base of the mixed layer in a more explicit way that accurately locates the depth at which the gradient greatly changes. This algorithm is specifically applied to the subtropical South Atlantic and helps to gain new insights into mode water formation and transport associated with several mechanisms, e.g., air-sea heat exchanges, western boundary current system and water intrusion from another basin.

In particular, we revisit the cluster analysis of Sato et al. [Sato, 2014] to divide all SASTMWs into three varieties, yet the division leads to different results. The major difference is associated with the origin of SASTMW3, the densest variety of these three mode water types. We observe that both SASTMW2 and SASTMW3 develop essentially in the southeastern Cape Basin where the warm Agulhas Current leaks water via the Agulhas Retroflection and forms Agulhas Rings. Only a small fraction of SASTMW3 seems to originate from the South Atlantic Current before its interception by the Mid-Atlantic Ridge. Conversely, Sato et al. [Sato, 2014] attributed the formation of SASTMW3 to the Brazil Current and its interaction with the Subtropical Front. In addition, the general surface and subsurface geographical distribution of the three mode water varieties in Sato et al. [Sato, 2014] differs from the present study. Here, the surface expression of SASTMW1 occupies the entire region of the southern limit of the subtropical gyre, between the Brazil-Malvinas Confluence and the 0 ° meridian, while the subsurface SASTMW1 extends across the entire subtropical gyre. In Sato et al. [Sato, 2014], the zonal spreading of SASTMW1 is less expanded. The opposite is also observed for the densest subsurface SASTMW variety, SASTMW3, that in our study it is delimited to the eastern half of the basin and extends slightly westward of the Mid-Atlantic Ridge, whereas in Sato et al. [Sato, 2014] the subsurface SASTMW3 was found up to 40 °W as its western limit.

These discrepancies might be due to the different methods of determination used to define both, the surface mixed layers and mode waters. The SASTMW selection criteria of Sato et al. [Sato, 2014] are limitations on potential vorticity ($|q| <= 1.50 \times 10^{-10}$ m^{-1} s^{-1}), potential temperature (11.5 – 18.5 °C) and salinity (34.7 – 36.5 psu). The last two limitations also led to a density range of 25.6 – 26.8 kg m^{-3} as well as a temperature gradient less than 0.01 °C m^{-1}. After applying those strict criteria, their analysis resulted in two configurations of the vertical (surface and subsurface mode waters). The surface mode water that represents the formation process was compared to the local climatological maximum MLD [Holte, 2009] to distinguish it from a regular mixed layer. In the current study, both the surface MLD and lower boundary of mode water are detected at the depth of extreme curvatures. While MLDs are estimated from density profiles, mode water layers, on the other hand, are derived from temperature profiles in addition to a universal limitation on potential vorticity. Outcropping mode waters are simply defined as temperature-based mixed layers thicker than 100 dbar, yet still show the most frequent occurrence between winter and early spring.

Another focus in this study is on the relationship between mesoscale eddies and mode waters. Here, we apply the recently developed eddy-detection TOEddies algorithm [Laxenaire, 2018] that objectively defines eddies from satellite altimetry maps of absolute dynamic topography. The resulting eddies are then co-located with Argo profiles. Although TOEddies provides 2D daily eddy fields that enable to access the horizontal distribution of eddies and their complex trajectories, its ability to include the whole spectrum of eddies is limited. This limitation is not only due to the spatio-temporal resolution of the altimetry fields, but also to the fact that only when subsurface features have a signature in altimetry maps can they be detected. In this study we applied a second method to determine the presence of eddies and their depth extent directly from Argo data by constructing vertical profiles of steric height anomaly (SHA). We used it to separate subsurface eddies from surface ones when the profile has already been co-located with an altimeter-detected eddy. Such SHA separation provides only sparse observations of the eddy fields, which does not allow to reconstruct the 3D eddy structure alone, but it enables to better assess the presence of subsurface features. In the study, TOEddies allows us to obtain the South Atlantic eddy characteristics and main propagation pathways, while the SHA method provides supplementary information of subsurface-intensified eddies.

The Argo-TOEddies co-location provides a lower percentage of eddies sampled by Argo profilers than that of Sato et al. [Sato, 2014]. Though both studies show that Argo profilers are indifferent to the presence of mesoscale eddies, eddy-mode water co-location in the current study exhibits higher percentage (41.6% of mode waters falling in eddies in this study against 22.4% for Sato et al. [Sato, 2014] who used the Chelton et al. [Chelton, 2011] eddy climatology). The study also suggests a particularly large amount of mode water presence associated with TOEddies anticyclonic eddies and their transport as coherent structures (32.0% inside anticyclones and 9.6% inside cyclones). The study of Sato et al. [Sato, 2014] divided the total number into surface and subsurface mode waters, and in both cases, the co-located anticyclones outnumbered cyclones by nearly 4 to 1. Moreover, the SHA eddy separation method brings an additional perspective. Not all TOEddies-detected eddies are separable into surface- and subsurface-intensified eddies (93.3% of all eddies were separated), but more subsurface mode waters are captured by subsurface eddies. Hence, our results indicate a clear influence of mesoscale dynamics and, in particular, of anticyclonic eddies on the formation, transport and subduction of mode waters in the subtropical gyre interior of the South Atlantic.

Moreover, the analysis of temperature anomalies along isopycnals related to the detected subtropical mode waters shows that mode waters carry heat from the surface subtropical gyre edges into the gyre's interior. Laxenaire et al. [Laxenaire, 2020] suggested that Agulhas Rings transport heat efficiently into the South Atlantic subtropical gyre, with heat anomalies centered in the mode water layers. The present study generalizes these results to the entire scope of the SASTMW, with anticyclonic eddies playing an important role in ventilating the upper South Atlantic thermocline and advecting heat in the subtropical gyre interior.

In general, the present study offers an improved understanding of subtropical mode waters in the South Atlantic. Despite the qualitative agreement between the pattern of eddy presence and spatial distribution of mode waters, the new algorithm has a number of facts to improve. The identification of pycnocline and thermocline is interpreted as the lower boundary of mixed layer detection, and thus is a rather poor representation. In addition, there has been a dilemma when it comes to choose whether the calculation should be based on temperature or density profiles. The surface mixed layer is commonly defined by strong convection that is better detected from density, while mode water is frequently observed as a specific water mass and sometimes a remarkably uniform density profile results from a compensation between salinity and temperature. This study thus depends on both temperature and density homogeneity to identify mode waters, and refers to density to define the MLD. A similar selecting process following Holte et al. [Holte, 2009] to find the best estimate of MLDs could also be added to the current algorithm for i) comparing with other mixed layer definitions, and ii) providing an ensemble of several mode water identification methods (e.g., the temperature method based on CLT with layer thickness control, or a single application of potential vorticity threshold to define mode waters).

Studies on global mode water analysis [Tsubouchi, 2016; Feucher, 2019] usually compare spatial structures of mode waters in different basins, however, the effect of mesoscale eddies is not extensively taken into consideration, while other studies that concentrate on the dynamical explanation concerning the relationship between mode waters and eddies generally delimit to specific conditions and locations [Qiu, 2007]. Our algorithm for mode water detection and the co-location with eddies will allow an extension to other observational platforms and to other domains of interest (as shown in the previous chapter). This algorithm was also validated by applying it to several hydrographic CTD profiles in the South Atlantic region. Combined with bottle data of carbon and oxygen, we will be able to obtain the link between mode waters and several other biogeochemical properties.

With the combination of thickness and area, it is also of interest to calculate the volume distribution associated with each type of mode water. Such calculation was considered by Bernardo et al. [Bernardo, 2020] that draws a volumetric picture of the three SASTMW types clustered in Sato et al. [Sato, 2014]. Subsequently, another important characteristic associated with mode water, the volume transport starting from their original regions of formation to the areas of spreading, can be calculated and evaluated at the global scale. Regarding the important role that eddies play in mode water transport, the calculation of mode water volume transport can thus be achieved by accurately tracking coherent eddies and computing the momentum changes along the eddy tracks. This will allow us to understand to what extent eddies transport mode waters and how much of mode waters dissipate associated with these eddy trajectories. However, such estimates can be roughly approximated only by using altimetry eddy detection together with vertical profiles provided by Argo or other platforms. Indeed, for eddies detected by satellite altimetry we can gather information on the eddy size and shape whereas this information is not available from eddies that are detected by sparse vertical profiles (e.g., the SHA method we implemented here (if applied alone to detect eddies)).

In this study, the SHA method was applied to distinguish subsurface eddies from surface ones. However, the applicability of this method greatly depends on vertical scales of these eddies, and sampling rates of temperature and salinity data. This profile-only method could also be applied to detect eddies alone, yet it highly requires verification and comparison with other more traditional satellite-based eddy detection methods. Considering the large number of eddies that can be detected from the SHA method, the dependence of eddy determination on several aspects of the SHA needs to be tested further, e.g., the choice of climatological profile to deduct, the minimum magnitude of SHA to be identified as an eddy, and the threshold depth that separates subsurface eddies from surface ones. It will also be of interest to look into numerical results to visualize and analyze the relationship between mode waters and several small-scale mechanisms.

Summary

In this chapter, we zoom in the detection of mode waters in the South Atlantic subtropics and associate their relationship with mesoscale eddies identified through the TOEddies algorithm. The cluster analysis applied previously in Chapter 3 for each ocean basin (i.e., North Atlantic, North Pacific and the Southern Ocean) has been employed again to separate the total SASTMW into 3 varieties, two of which are related to the subtropical water mass intrusion from the Indian Ocean at the Agulhas Leakage.

We specifically illustrated that mode waters in the South Atlantic are warm anomalies along isopycnals, and their formation and transport have close relationship with anticyclonic eddies. By inspecting individual eddy trajectories in the South Atlantic, we also find that mode water develops between the Walvis and Mid-Atlantic Ridges as anticyclonic Agulhas Ring forms in the Cape Basin and travels towards the western boundary.

The profile-only eddy detection is also developed, which is dependent on the vertical location of the steric height anomaly calculated from profiles. However, it needs further investigation on the validity of applying it to detect eddies without surface signatures displayed from satellite images.

Conclusions and perspectives

The uptake and storage of climatically important substances, such as heat and carbon, is arguably the most important role of the ocean in the climate system. Ventilation — the subduction and spreading of water, along with its properties, from the surface mixed layer into the ocean interior — is at the heart of this process. While ocean ventilation has been observed and considered important for decades, the governing mechanisms remain poorly understood. As with many oceanic processes, understanding is inhibited by a scarcity of observations and the difficulty of representation in numerical simulations.

The aim of this thesis is to contribute understanding to some of the outstanding questions around the ventilation processes. Specifically, we address questions pertaining to mechanisms and pathways of ventilation in numerical ocean circulation models (Chapter 2), and detection of mode water subduction and transport from several observational platforms (Chapters 3 and 4). A special focus is given to mesoscale eddies — the weather system of the ocean — that play a crucial role in water mass ventilation processes.

1 Conclusions of the studies

Chapter 2 summarizes and compares several perspectives of water mass subduction, counting 1) a general form of continuity which relates the vertical velocity at the base of the mixed layer to the divergence of horizontal transport over the entire layer, 2) the calculation that only considers the winter deepest mixed layer base (Stommel's Demon), and 3) a perspective from the horizontally migrating isopycnals that further includes a shrinking or expansion of isopycnal areas. We conclude that the estimates based on the Stommel's Demon often lead to a larger value of subduction compared with its long-time averages. This implies that during the rest of the year, water masses from the ocean interior are entrained into the surface layer, and such amount of obduction is underestimated. The instantaneous subduction rate regarding the migration of isopycnals, in general, does not differ from the classic calculation provided by Cushman-Roisin [Cushman-Roisin, 1987], since the new term associated with the isopycnal migrating velocities that appears in the time-dependent component is later cancelled out in the lateral advection term. However, this is not true for a volume subduction (integration) that explicitly represents the shrinking and enlarging of outcropping areas for each isopycnal. From this perspective, water masses at different density classes do not result in a same amount of volume subduction, for which the time and spatial resolution is important that contributes to the eddy component of subduction. In specific, we found at the density class of SAMW, the expansion of isopycnal area in winter as well as the intensification of instantaneous subduction rate result in a downward transfer of water masses.

Chapter 3 describes an algorithm applied to detect surface mixed layer depth and mode water from profiling data, which pinpoints the depths of gradient and second derivative extreme values. Such algorithm is employed to all Argo profiles for the years 2000–2018 for the identification of mode waters at depth. A cluster analysis is then applied to each ocean basin (North Atlantic, North Pacific, and Southern Ocean) to divide mode waters into several varieties, which leads to 4, 2, and 2 types respectively. Later, we co-locate these water masses with mesoscale eddies derived from the TOEddies algorithm that detects the closed contours of absolute dynamic topography to locate isolated eddies and their merging/splitting events with other eddies. We found near-surface mode waters are especially associated with the movement of mesoscale eddies, for example, over 50 % of the North Pacific Subtropical Mode Water, North Pacific Central Mode Water, South Atlantic Subtropical Mode Water and South Pacific Subtropical Mode Water are co-located with anticyclonic eddies. The spatial distribution of heat content anomalies inside these mode waters also refers to the inter-basin transport of mesoscale eddies, specifically at the Agulhas Leakage and the Tasman Leakage.

Chapter 4 subsequently focuses on the South Atlantic Subtropical Mode Water that is clustered into three sub-varieties: one originating from the western boundary current (at the Brazil-Malvinas Confluence), and the other two spreading from the Indian Ocean. They are different in terms of properties: the western mode water type (SASTMW1) has a temperature in between a colder and fresher SASTMW3 and a warmer and saltier SASTMW2. Anticyclonic eddies, i.e., the Agulhas Rings, are shown to be a dominant factor in the South Atlantic for transporting and subducting mode waters along their trajectories of movement. Agulhas Rings can reach the western boundary and merge with the Brazil Current, while mode water subduction can occur between the Walvis and Mid-Atlantic Ridges.

2 Future perspectives

The results presented in this thesis have opened up many avenues for further analysis. From the calculation of subduction rate to the detection of mode waters, some topics are listed below that take into account several aspects of articulating a broader picture of ventilation:

PV fluxes across the base of the mixed layer The entry and exit of potential vorticity into ocean circulation, and the flux of potential vorticity through it, is described in the framework provided by the flux form of the potential vorticity equation (Eqn 2.27), that is $\partial q/\partial t + \nabla \cdot \boldsymbol{J} = 0$, where $\boldsymbol{J}$ is a generalized flux of potential vorticity q. This conservation of potential vorticity q has a number of notable properties: i) the mass-weighted PV can always be written as the divergence of a vector, and hence a flux-form PV equation can always be written for an appropriately defined $\boldsymbol{J}$, ii) even in the presence of sources of momentum and buoyancy, the rhs of this equation is zero, iii) the flux of $\boldsymbol{J}$ cannot pass through a σ surface. It will then be of interest to look at the PV flux at the base of the mixed layer and its time variability. Since we have already looked at how the migration of isopycnals influence the subduction rate and its implications for the mesoscale influence, it is thus interesting to quantify mesoscale and smaller-scale processes in modifying the picture of this PV fluxes at the base of the mixed layer.

Lagrangian perspective of subduction Limitations in observationally derived estimates of the meridional overturning circulation mean that we largely rely on ocean models to understand its latitude-dependent strength and temporal variability. Climate models are furthermore used to predict future changes in circulation and to guide policy. As such, a current problem in climate studies is the need to understand what leads to differences between the various model representations of the MOC, which can be large. Several studies have seeded Lagrangian particles into ocean models, which can be used to calculate the overturning streamfunction. These Lagrangian methods can also diagnose which geographical regions of mixed layer subduction source the deep flowing water. It would be of interest to compare the Eulerian calculation in the current study with other Lagrangian perspectives, especially to quantify processes of isopynal and diapycnal mixing.

Mode water properties on isopycnals Chapter 3 shows several analyses associated with the separation of mode waters and their properties. It would be of interest to further draw pictures of mode waters on the same isopycnal levels and to quantify how different they are in terms of spiciness. This analysis will be of importance to quantify other formation mechanisms of mode waters, e.g., the cabbeling effect that mixes different water masses along isopycnals yet creates a denser one. The figure below displays mode waters in each density class from 25.2 to 27.2. Compared with the cluster analysis used in Chapter 3 which separates mode waters in each basin according to their property differences, this map in the isopycnal coordinate provides information of how mode waters are linked from basin to basin.

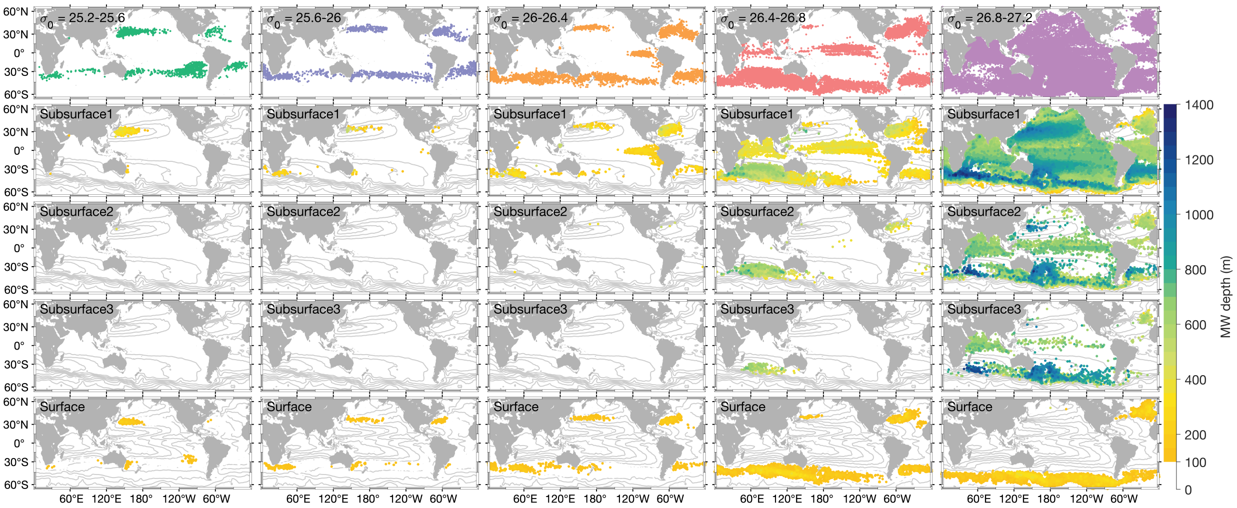

Figure 5.1: Mode water depths on five isopycnal surfaces.

Nonlinear effects in water mass transformation The nonlinear equation of state of seawater leads to some exotic forms of water mass transformation. In particular, cabbeling and thermobaricity are both a consequence of a combination of eddy mixing and nonlinearities in the equation of state. Cabbeling is the process in which the mixing of two water parcels with different temperature and salinity, but equal density, results in a water parcel denser than the two original water parcels. Thermobaricity is the process in which the mixing of two water parcels with different temperatures and pressures, but equal density, results in a water parcel which is either lighter or denser than the two original water parcels. Hence, both these processes can occur when mesoscale eddies mix temperature and salinity along isopycnal surfaces.

Subsurface eddy detection from profiling data In the schematic of Figure 3.3, we have shown that mode-water eddies tend to depress the main thermocline and raise the seasonal thermocline. In this regard, a development of subsurface eddy detection is necessary.

Subduction at the submesoscale Several studies have demonstrated the relevance of submesoscales to the production of phytoplankton and the ocean absorption of anthropogenic CO_2. However, the submesoscale-induced rates of subduction and obduction at the bottom of the mixed layer have received less attention and have not been fully quantified. Some studies [Canuto, 2018] show that at the ACC, the maximum submesoscale subduction rates are not significantly smaller than those due to mesoscales, but the submesoscale subduction rates exhibit a topology opposite to that of mesoscales: obduction is equatorward and subduction is poleward.

3 Concluding remarks

Observations in the past few decades have revealed widespread changes in the ocean content of oxygen [Stramma, 2008], carbon [Sabine, 2004] and heat [Levitus, 2012] in both the upper and deep ocean. Ventilation of water from the sea surface into its interior is implicated as an important process in all three. Understanding these changes and predicting their future evolution, therefore, depends on robust understanding of the physical processes involved in ventilation, their variability, and their tendency to change. The results of this thesis have shown that such process is complex, for both a potential extension of theories behind observations in terms of several spatial and temporal scales, and further an endeavor of representing these physical mechanisms in models.

While the discussions related to subduction rates are from an Eulerian perspective, the mode water-eddy co-location provides a pseudo-Lagrangian diagnostic of surface water subduction. Although there are substantial challenges and it is certain that such efforts into physics have no end, these results in this thesis have enabled quantitative assessment of the processes involved in ocean ventilation, offering insights into these processes at the mesoscale.

List of publications

Articles in peer-reviewed journals

Yanxu Chen, Sabrina Speich, Rémi Laxenaire. "*Formation and Transport of the South Atlantic Subtropical Mode Water in Eddy-Permitting Observations*". Journal of Geophysical Research: Oceans.
DOI: https://doi.org/10.1029/2021JC017767

Yanxu Chen, David Straub, Louis-Philippe Nadeau. "*Interaction of Nonlinear Ekman Pumping, Near-Inertial Oscillations, and Geostrophic Turbulence in an Idealized Coupled Model*". Journal of Physical Oceanography.
DOI: https://doi.org/10.1175/JPO-D-20-0268.1

Articles in preparation

Yanxu Chen, Sabrina Speich. "*Role of mesoscale eddies in global mode water distribution and heat uptake*". Geophysical Research Letters.

Yanxu Chen, Sabrina Speich. "*Revisiting subduction rates of the upper-ocean waters at the mesoscale*". Journal of Physical Oceanography.

Presentations in conferences

Yanxu Chen, Sabrina Speich. "*Global mode water detection and its representation in heat transport*". Ocean Sciences Meeting, 2022.

Yanxu Chen, Sabrina Speich, Rémi Laxenaire. "*Formation and transport of the South Atlantic subtropical mode water in eddy-permitting observations*". TRIATLAS General Assembly, 2021.

Yanxu Chen, Sabrina Speich, Rémi Laxenaire. "*Effect of mesoscale eddies on mode water formation, transport and heat uptake in the world ocean*". AGU Fall Meeting, 2020.

Yanxu Chen, Sabrina Speich, Rémi Laxenaire. "*Effect of mesoscale eddies on subtropical mode water formation and ocean heat storage*". EGU General Assembly, 2020.

Yanxu Chen, David Straub, Louis-Philippe Nadeau. "*Flow-dependent Ekman theory and its application to shallow water models*". EGU General Assembly, 2019.

Bibliography

[Abernathey, 2022] Ryan Abernathey, Anand Gnanadesikan, Marie-Aude Pradal, and Miles A. Sundermeyer. “Chapter 9 - Isopycnal mixing”. *Ocean Mixing*. Ed. by Michael Meredith and Alberto Naveira Garabato. Elsevier, 2022, pp. 215–256 (cit. on p. 53).

[Akima, 1970] Hiroshi Akima. “A New Method of Interpolation and Smooth Curve Fitting Based on Local Procedures”. *Journal of the Association for Computing Machinery* 17.4 (1970), pp. 589–602 (cit. on p. 94).

[Alexander, 1995] Michael A. Alexander and Clara Deser. “A Mechanism for the Recurrence of Wintertime Midlatitude SST Anomalies”. *Journal of Physical Oceanography* 25.1 (1995), pp. 122–137 (cit. on p. 91).

[Argo, 2020] Argo. *Argo float data and metadata from Global Data Assembly Centre (Argo GDAC)*. Dataset. 2020 (cit. on pp. 92, 94).

[Assassi, 2016] C. Assassi, Y. Morel, F. Vandermeirsch, A. Chaigneau, C. Pegliasco, R. Morrow, et al. “An Index to Distinguish Surface- and Subsurface-Intensified Vortices from Surface Observations”. *Journal of Physical Oceanography* 46.8 (2016), pp. 2529–2552 (cit. on p. 133).

[Bachman, 2017] S. D. Bachman, J. R. Taylor, K. A. Adams, and P. J. Hosegood. “Mesoscale and Submesoscale Effects on Mixed Layer Depth in the Southern Ocean”. *Journal of Physical Oceanography* 47.9 (2017), pp. 2173–2188 (cit. on p. 92).

[Barceló-Llull, 2017] Bàrbara Barceló-Llull, Pablo Sangrà, Enric Pallàs-Sanz, Eric D. Barton, Sheila N. Estrada-Allis, Antonio Martínez-Marrero, et al. “Anatomy of a subtropical intrathermocline eddy”. *Deep Sea Research Part I: Oceanographic Research Papers* 124 (2017), pp. 126–139 (cit. on p. 102).

[Bashmachnikov, 2012] I. Bashmachnikov and X. Carton. “Surface signature of Mediterranean water eddies in the Northeastern Atlantic: effect of the upper ocean stratification”. *Ocean Science* 8.6 (2012), pp. 931–943 (cit. on p. 133).

[Bashmachnikov, 2015] I. Bashmachnikov, F. Neves, T. Calheiros, and X. Carton. “Properties and pathways of Mediterranean water eddies in the Atlantic”. *Progress in Oceanography* 137 (2015), pp. 149–172 (cit. on p. 119).

[Bates, 2002] Nicholas R. Bates, A. Christine Pequignet, Rodney J. Johnson, and Nicolas Gruber. “A short-term sink for atmospheric CO2 in subtropical mode water of the North Atlantic Ocean”. *Nature* 420.6915 (2002), pp. 489–493 (cit. on p. 91).

[Bernardo, 2020] Piero S. Bernardo and Olga T. Sato. “Volumetric Characterization of the South Atlantic Subtropical Mode Water Types”. *Geophysical Research Letters* 47.8 (2020), e2019GL086653 (cit. on pp. 134, 137, 150, 164).

[Blanke, 2002] Bruno Blanke, Sabrina Speich, Gurvan Madec, and Rudy Maugé. “A global diagnostic of interior ocean ventilation”. *Geophysical Research Letters* 29.8 (2002), pp. 108-1-108–4 (cit. on pp. 58, 88).

[Bopp, 2015] L. Bopp, M. Lévy, L. Resplandy, and J. B. Sallée. “Pathways of anthropogenic carbon subduction in the global ocean”. *Geophysical Research Letters* 42.15 (2015), pp. 6416–6423 (cit. on p. 53).

[Boyer, 2019] Tim P. Boyer, Hernan E. Garcia, Ricardo A. Locarnini, Melissa M. Zweng, Alexey V. Mishonov, James R. Reagan, et al. *World Ocean Atlas 2018*. NOAA National Centers for Environmental Information, 2019 (cit. on p. 145).

[Brambilla, 2008a] Elena Brambilla and Lynne D. Talley. “Subpolar Mode Water in the northeastern Atlantic: 1. Averaged properties and mean circulation”. *Journal of Geophysical Research: Oceans* 113.C4 (2008) (cit. on p. 57).

[Brambilla, 2008b] Elena Brambilla, Lynne D. Talley, and Paul E. Robbins. “Subpolar Mode Water in the northeastern Atlantic: 2. Origin and transformation”. *Journal of Geophysical Research: Oceans* 113.C4 (2008) (cit. on p. 57).

[Canuto, 2018] V. M. Canuto, Y. Cheng, and A. M. Howard. “Subduction by Submesoscales”. *Journal of Geophysical Research: Oceans* 123.12 (2018), pp. 8688–8700 (cit. on p. 169).

[Capuano, 2018] Tonia Astrid Capuano, Sabrina Speich, Xavier Carton, and Remi Laxenaire. “Indo-Atlantic Exchange, Mesoscale Dynamics, and Antarctic Intermediate Water”. *Journal of Geophysical Research: Oceans* 123.5 (2018), pp. 3286–3306 (cit. on p. 142).

[Carracedo, 2016] L. I. Carracedo, P. C. Pardo, S. Flecha, and F. F. Pérez. “On the Mediterranean Water Composition”. *Journal of Physical Oceanography* 46.4 (2016), pp. 1339–1358 (cit. on p. 115).

[Cerovečki, 2013] Ivana Cerovečki, Lynne D. Talley, Matthew R. Mazloff, and Guillaume Maze. “Subantarctic Mode Water Formation, Destruction, and Export in the Eddy-Permitting Southern Ocean State Estimate”. *Journal of Physical Oceanography* 43.7 (2013), pp. 1485–1511 (cit. on p. 127).

[Cessi, 2004] Paola Cessi and Maurizio Fantini. “The Eddy-Driven Thermocline”. *Journal of Physical Oceanography* 34.12 (2004), pp. 2642–2658 (cit. on p. 93).

[Chaigneau, 2011] Alexis Chaigneau, Marie Le Texier, Gérard Eldin, Carmen Grados, and Oscar Pizarro. “Vertical structure of mesoscale eddies in the eastern South Pacific Ocean: A composite analysis from altimetry and Argo profiling floats”. *Journal of Geophysical Research: Oceans* 116.C11 (2011) (cit. on p. 133).

[Charney, 1947] J. G. Charney. “THE DYNAMICS OF LONG WAVES IN A BAROCLINIC WESTERLY CURRENT”. *Journal of Atmospheric Sciences* 4.5 (1947), pp. 136–162 (cit. on p. 35).

[Charney, 1950] J. G. Charney, R. FJÖRTOFT, and J. Von NEUMANN. “Numerical Integration of the Barotropic Vorticity Equation”. *Tellus* 2.4 (1950), pp. 237–254 (cit. on p. 35).

[Chelton, 2010] Dudley Chelton and Shang-Ping Xie. “Coupled Ocean-Atmosphere Interaction at Oceanic Mesoscales”. *Oceanography* 23 (2010) (cit. on p. 42).

[Chelton, 2011] Dudley B. Chelton, Michael G. Schlax, and Roger M. Samelson. “Global observations of nonlinear mesoscale eddies”. *Progress in Oceanography* 91.2 (2011), pp. 167–216 (cit. on pp. 37, 133, 153, 162).

[Chen, 2022] Yanxu Chen, Sabrina Speich, and Rémi Laxenaire. “Formation and Transport of the South Atlantic Subtropical Mode Water in Eddy-Permitting Observations”. *Journal of Geophysical Research: Oceans* 127.1 (2022), e2021JC017767 (cit. on pp. 93, 111, 112, 116, 123, 127, 128).

[Chen, 2021] Yanxu Chen, David Straub, and Louis-Philippe Nadeau. “Interaction of Nonlinear Ekman Pumping, Near-Inertial Oscillations, and Geostrophic Turbulence in an Idealized Coupled Model”. *Journal of Physical Oceanography* 51.3 (2021), pp. 975–987 (cit. on pp. 42, 72).

[Cheng, 2017] Lijing Cheng, Kevin E. Trenberth, John Fasullo, Tim Boyer, John Abraham, and Jiang Zhu. “Improved estimates of ocean heat content from 1960 to 2015”. *Science Advances* 3.3 (2017) (cit. on p. 91).

[Consortium, 2021] ECCO Consortium, Ichiro Fukumori, Ou Wang, Ian Fenty, Gael Forget, Patrick Heimbach, et al. *Synopsis of the ECCO Central Production Global Ocean and Sea-Ice State Estimate, Version 4 Release 4*. Version 4 Release 4. 2021 (cit. on pp. 65, 71, 72).

[Costa, 2005] Maria Valdivieso Da Costa, Herlé Mercier, and Anne Marie Treguier. “Effects of the Mixed Layer Time Variability on Kinematic Subduction Rate Diagnostics”. *Journal of Physical Oceanography* 35.4 (2005), pp. 427–443 (cit. on p. 60).

[Cushman-Roisin, 1987] B Cushman-Roisin. “Subduction”. *Dynamics of the oceanic surface mixed layer* (1987), pp. 181–196 (cit. on pp. 50, 56, 59, 61, 87, 166).

[Cushman-Roisin, 2011a] Benoit Cushman-Roisin and Jean-Marie Beckers. “Chapter 18 - Fronts, Jets and Vortices”. *Introduction to Geophysical Fluid Dynamics*. Ed. by Benoit Cushman-Roisin and Jean-Marie Beckers. Vol. 101. International Geophysics. Academic Press, 2011, pp. 589–623 (cit. on pp. 33, 35).

[Cushman-Roisin, 2011b] Benoit Cushman-Roisin and Jean-Marie Beckers. “Chapter 8 - The Ekman Layer”. *Introduction to Geophysical Fluid Dynamics*. Ed. by Benoit Cushman-Roisin and Jean-Marie Beckers. Vol. 101. International Geophysics. Academic Press, 2011, pp. 239–270 (cit. on p. 8).

[Davis, 2011] Xujing Jia Davis, Lewis M. Rothstein, William K. Dewar, and Dimitris Menemenlis. “Numerical Investigations of Seasonal and Interannual Variability of North Pacific Subtropical Mode Water and Its Implications for Pacific Climate Variability”. *Journal of Climate* 24.11 (2011), pp. 2648–2665 (cit. on p. 91).

[Dawe, 2006] Jordan T. Dawe and LuAnne Thompson. “Effect of Ocean Surface Currents on Wind Stress, Heat Flux, and Wind Power Input to the Ocean”. *Geophysical Research Letters* 33.9 (2006) (cit. on pp. 5, 42).

[de Boyer Montégut, 2004] Clément de Boyer Montégut, Gurvan Madec, Albert S. Fischer, Alban Lazar, and Daniele Iudicone. “Mixed layer depth over the global ocean: An examination of profile data and a profile-based climatology”. *Journal of Geophysical Research: Oceans* 109.C12 (2004) (cit. on pp. 71, 92, 97, 111).

[Dencausse, 2010] Guillaume Dencausse, Michel Arhan, and Sabrina Speich. “Routes of Agulhas rings in the southeastern Cape Basin”. *Deep Sea Research Part I: Oceanographic Research Papers* 57.11 (2010), pp. 1406–1421 (cit. on p. 148).

[Deser, 2003] Clara Deser, Michael A. Alexander, and Michael S. Timlin. “Understanding the Persistence of Sea Surface Temperature Anomalies in Midlatitudes”. *Journal of Climate* 16.1 (2003), pp. 57–72 (cit. on p. 91).

[DeVries, 2014] Tim DeVries. “The oceanic anthropogenic CO2 sink: Storage, air-sea fluxes, and transports over the industrial era”. *Global Biogeochemical Cycles* 28.7 (2014), pp. 631–647 (cit. on p. 91).

[Dilmahamod, 2018] A. F. Dilmahamod, B. Aguiar-González, P. Penven, C. J. C. Reason, W. P. M. De Ruijter, N. Malan, et al. “SIDDIES Corridor: A Major East-West Pathway of Long-Lived Surface and Subsurface Eddies Crossing the Subtropical South Indian Ocean”. *Journal of Geophysical Research: Oceans* 123.8 (2018), pp. 5406–5425 (cit. on pp. 134, 141, 158).

[Doney, 1998] Scott C. Doney, John L. Bullister, and Rik Wanninkhof. “Climatic variability in upper ocean ventilation rates diagnosed using chlorofluorocarbons”. *Geophysical Research Letters* 25.9 (1998), pp. 1399–1402 (cit. on p. 57).

[Dong, 2008] Shenfu Dong, Janet Sprintall, Sarah T. Gille, and Lynne Talley. “Southern Ocean mixed-layer depth from Argo float profiles”. *Journal of Geophysical Research: Oceans* 113.C6 (2008) (cit. on pp. 92, 111).

[Droghei, 2018] Riccardo Droghei, Bruno Buongiorno Nardelli, and Rosalia Santoleri. “A New Global Sea Surface Salinity and Density Dataset From Multivariate Observations (1993–2016)”. *Frontiers in Marine Science* 5 (2018), p. 84 (cit. on p. 143).

[Dufois, 2016] François Dufois, Nick J. Hardman-Mountford, Jim Greenwood, Anthony J. Richardson, Ming Feng, and Richard J. Matear. “Anticyclonic eddies are more productive than cyclonic eddies in subtropical gyres because of winter mixing”. *Science Advances* 2.5 (2016) (cit. on p. 133).

[Duhaut, 2006] Thomas H. A. Duhaut and David N. Straub. “Wind Stress Dependence on Ocean Surface Velocity: Implications for Mechanical Energy Input to Ocean Circulation”. *Journal of Physical Oceanography* 36.2 (2006), pp. 202–211 (cit. on pp. 5, 42).

[Eady, 1949] E. T. Eady. “Long Waves and Cyclone Waves”. *Tellus* 1.3 (1949), pp. 33–52 (cit. on p. 35).

[Ebbesmeyer, 1986] C. C. Ebbesmeyer and E. J. Lindstrom. “Structure and origin of 18C water observed during the POLYMODE local dynamics experiment”. *Journal of Physical Oceanography* 16 (1986), pp. 443–453 (cit. on p. 102).

[Ekman, 1905] V. Walfrid Ekman. “On the influence of the Earth’s rotation on ocean curents”. *Arkiv For Matematik Astronomi Och Fysik* 2.11 (1905), pp. 1–52 (cit. on pp. 4, 6).

[Feucher, 2016] Charlène Feucher, Guillaume Maze, and Herlé Mercier. “Mean Structure of the North Atlantic Subtropical Permanent Pycnocline from In Situ Observations”. *Journal of Atmospheric and Oceanic Technology* 33.6 (2016), pp. 1285–1308 (cit. on pp. 100, 104).

[Feucher, 2019] Charlène Feucher, Guillaume Maze, and Herlé Mercier. “Subtropical Mode Water and Permanent Pycnocline Properties in the World Ocean”. *Journal of Geophysical Research: Oceans* 124.2 (2019), pp. 1139–1154 (cit. on pp. 93, 119, 163).

[Fine, 2017] Rana A. Fine, Synte Peacock, Mathew E. Maltrud, and Frank O. Bryan. “A new look at ocean ventilation time scales and their uncertainties”. *Journal of Geophysical Research: Oceans* 122.5 (2017), pp. 3771–3798 (cit. on p. 58).

[Fox-Kemper, 2008] Baylor Fox-Kemper, Raffaele Ferrari, and Robert Hallberg. “Parameterization of Mixed Layer Eddies. Part I: Theory and Diagnosis”. *Journal of Physical Oceanography* 38.6 (2008), pp. 1145–1165 (cit. on p. 47).

[Freilich, 2021] Mara Freilich and Amala Mahadevan. “Coherent Pathways for Subduction From the Surface Mixed Layer at Ocean Fronts”. *Journal of Geophysical Research: Oceans* 126.5 (2021), e2020JC017042 (cit. on pp. 47–49, 53, 93).

[Friedlingstein, 2020] P. Friedlingstein, M. O’Sullivan, M. W. Jones, R. M. Andrew, J. Hauck, A. Olsen, et al. “Global Carbon Budget 2020”. *Earth System Science Data* 12.4 (2020), pp. 3269–3340 (cit. on p. 91).

[Garabato, 2001] Alberto C. Naveira Garabato, Harry Leach, John T. Allen, Raymond T. Pollard, and Volker H. Strass. “Mesoscale Subduction at the Antarctic Polar Front Driven by Baroclinic Instability”. *Journal of Physical Oceanography* 31.8 (2001), pp. 2087–2107 (cit. on p. 56).

[Gaube, 2015] Peter Gaube, Dudley B. Chelton, Roger M. Samelson, Michael G. Schlax, and Larry W. O’Neill. “Satellite Observations of Mesoscale Eddy-Induced Ekman Pumping”. *Journal of Physical Oceanography* 45.1 (2015), pp. 104–132 (cit. on p. 42).

[Gaube, 2019] Peter Gaube, Dennis J. McGillicuddy Jr., and Aurélie J. Moulin. “Mesoscale Eddies Modulate Mixed Layer Depth Globally”. *Geophysical Research Letters* 46.3 (2019), pp. 1505–1512 (cit. on pp. 92, 93, 112).

[Gent, 1990] Peter R. Gent and James C. Mcwilliams. “Isopycnal Mixing in Ocean Circulation Models”. *Journal of Physical Oceanography* 20.1 (1990), pp. 150–155 (cit. on p. 67).

[Gill, 1973] A.E. Gill and P.P. Niller. “The theory of the seasonal variability in the ocean”. *Deep Sea Research and Oceanographic Abstracts* 20.2 (1973), pp. 141–177 (cit. on pp. 134, 140).

[Gordon, 1989] Arnold L. Gordon. “Brazil-Malvinas Confluence–1984”. *Deep Sea Research Part A. Oceanographic Research Papers* 36.3 (1989), pp. 359–384 (cit. on p. 142).

[Gordon, 2017] Arnold L. Gordon, Emily Shroyer, and V. S. N. Murty. “An Intrathermocline Eddy and a tropical cyclone in the Bay of Bengal”. *Scientific Reports* 7.1 (2017), p. 46218 (cit. on p. 102).

[Gordon, 1992] Arnold L. Gordon, Ray F. Weiss, William M. Smethie Jr., and Mark J. Warner. “Thermocline and intermediate water communication between the south Atlantic and Indian oceans”. *Journal of Geophysical Research: Oceans* 97.C5 (1992), pp. 7223–7240 (cit. on p. 142).

[Gray, 2014] Alison R. Gray and Stephen C. Riser. “A Global Analysis of Sverdrup Balance Using Absolute Geostrophic Velocities from Argo”. *Journal of Physical Oceanography* 44.4 (2014), pp. 1213–1229 (cit. on p. 11).

[Groeskamp, 2016] Sjoerd Groeskamp, Ryan P. Abernathey, and Andreas Klocker. “Water mass transformation by cabbeling and thermobaricity”. *Geophysical Research Letters* 43.20 (2016), pp. 10, 835–10, 845 (cit. on pp. 46, 93).

[Groeskamp, 2019] Sjoerd Groeskamp, Stephen M. Griffies, Daniele Iudicone, Robert Marsh, A.J. George Nurser, and Jan D. Zika. “The Water Mass Transformation Framework for Ocean Physics and Biogeochemistry”. *Annual Review of Marine Science* 11.1 (2019), pp. 271–305 (cit. on pp. 22, 45).

[Grooms, 2016] Ian Grooms and Louis-Philippe Nadeau. “The Effects of Mesoscale Ocean–Atmosphere Coupling on the Quasigeostrophic Double Gyre”. *Fluids* 1.4 (2016), p. 34 (cit. on p. 42).

[Guerra, 2018] Luiz Alexandre A. Guerra, Afonso M. Paiva, and Eric P. Chassignet. “On the translation of Agulhas rings to the western South Atlantic Ocean”. *Deep Sea Research Part I: Oceanographic Research Papers* 139 (2018), pp. 104–113 (cit. on p. 144).

[Hall, 2007] Timothy M. Hall, Thomas W. N. Haine, Darryn W. Waugh, Mark Holzer, Francesca Terenzi, and Deborah A. LeBel. “Ventilation Rates Estimated from Tracers in the Presence of Mixing”. *Journal of Physical Oceanography* 37.11 (2007), pp. 2599–2611 (cit. on p. 58).

[Hanawa, 2004] Kimio Hanawa and Shusaku Sugimoto. “‘Reemergence’ areas of winter sea surface temperature anomalies in the world’s oceans”. *Geophysical Research Letters* 31.10 (2004) (cit. on p. 91).

[Hanawa, 2001] Kimio Hanawa and Lynne D. Talley. “Chapter 5.4 Mode waters”. *Ocean Circulation and Climate*. Vol. 77. International Geophysics. Academic Press, 2001, pp. 373–386 (cit. on pp. 28, 30, 91, 93, 119, 121).

[Hart, 2000] J. E. Hart. “A note on nonlinear corrections to the Ekman layer pumping velocity”. *Physics of Fluids* 12.1 (2000), pp. 131–135 (cit. on p. 42).

[Hartin, 2011] Corinne A. Hartin, Rana A. Fine, Bernadette M. Sloyan, Lynne D. Talley, Teresa K. Chereskin, and James Happell. “Formation rates of Subantarctic mode water and Antarctic intermediate water within the South Pacific”. *Deep Sea Research Part I: Oceanographic Research Papers* 58.5 (2011), pp. 524–534 (cit. on p. 29).

[Hautala, 1998] Susan L. Hautala and Dean H. Roemmich. “Subtropical mode water in the Northeast Pacific Basin”. *Journal of Geophysical Research: Oceans* 103.C6 (1998), pp. 13055–13066 (cit. on pp. 29, 121, 133).

[Haynes, 1990] P. H. Haynes and M. E. McIntyre. “On the Conservation and Impermeability Theorems for Potential Vorticity”. *Journal of Atmospheric Sciences* 47.16 (1990), pp. 2021–2031 (cit. on p. 21).

[Hazeleger, 2000] W. Hazeleger and S. S. Drijfhout. “Eddy Subduction in a Model of the Subtropical Gyre”. *Journal of Physical Oceanography* 30.4 (2000), pp. 677–695 (cit. on p. 60).

[Herraiz-Borreguero, 2011] Laura Herraiz-Borreguero and Stephen Rich Rintoul. “Subantarctic mode water: distribution and circulation”. *Ocean Dynamics* 61.1 (2011), pp. 103–126 (cit. on pp. 29, 144).

[Hieronymus, 2014] Magnus Hieronymus, Johan Nilsson, and Jonas Nycander. “Water Mass Transformation in Salinity–Temperature Space”. *Journal of Physical Oceanography* 44.9 (2014), pp. 2547–2568 (cit. on p. 22).

[Hiraike, 2016] Yuri Hiraike, Yukio Tanaka, and Hiroyasu Hasumi. “Subduction of Pacific Antarctic Intermediate Water in an eddy-resolving model”. *Journal of Geophysical Research: Oceans* 121.1 (2016), pp. 133–147 (cit. on p. 56).

[Hoffman, 2005] Ross N. Hoffman and S. Mark Leidner. “An Introduction to the Near–Real–Time QuikSCAT Data”. *Weather and Forecasting* 20.4 (2005), pp. 476–493 (cit. on pp. 5, 9).

[Holte, 2009] James Holte and Lynne Talley. “A New Algorithm for Finding Mixed Layer Depths with Applications to Argo Data and Subantarctic Mode Water Formation”. *Journal of Atmospheric and Oceanic Technology* 26.9 (2009), pp. 1920–1939 (cit. on pp. 92, 97, 111, 112, 134, 161, 163).

[Holte, 2017] James Holte, Lynne D. Talley, John Gilson, and Dean Roemmich. “An Argo mixed layer climatology and database”. *Geophysical Research Letters* 44.11 (2017), pp. 5618–5626 (cit. on p. 71).

[Huang, 1991] Rui Xin Huang. “The Three-Dimensional Structure of Wind-Driven Gyres: Ventilation and Subduction”. *Reviews of Geophysics* 29.S2 (1991), pp. 590–609 (cit. on p. 23).

[Huang, 2009] Rui Xin Huang. “Thermohaline circulation”. *Ocean Circulation: Wind-Driven and Thermohaline Processes*. Cambridge University Press, 2009, pp. 480–760 (cit. on p. 17).

[Iselin, 1939] Iselin. “The influence of vertical and lateral turbulence on the characteristics of the waters at mid-depths”. *Eos, Transactions American Geophysical Union* 20.3 (1939), pp. 414–417 (cit. on pp. 23, 28, 55).

[Jackett, 1997] David R. Jackett and Trevor J. McDougall. “A Neutral Density Variable for the World’s Oceans”. *Journal of Physical Oceanography* 27.2 (1997), pp. 237–263 (cit. on p. 19).

[Jones, 2016] Daniel C. Jones, Andrew J. S. Meijers, Emily Shuckburgh, Jean-Baptiste Sallée, Peter Haynes, Ewa K. McAufield, et al. “How does Subantarctic Mode Water ventilate the Southern Hemisphere subtropics?” *Journal of Geophysical Research: Oceans* 121.9 (2016), pp. 6558–6582 (cit. on pp. 25, 121).

[Kara, 2000] A. Birol Kara, Peter A. Rochford, and Harley E. Hurlburt. “Mixed layer depth variability and barrier layer formation over the North Pacific Ocean”. *Journal of Geophysical Research: Oceans* 105.C7 (2000), pp. 16783–16801 (cit. on p. 92).

[Klein, 2009] Patrice Klein and Guillaume Lapeyre. “The Oceanic Vertical Pump Induced by Mesoscale and Submesoscale Turbulence”. *Annual Review of Marine Science* 1.1 (2009), pp. 351–375 (cit. on p. 47).

[Klocker, 2010] Andreas Klocker and Trevor J. McDougall. “Influence of the Nonlinear Equation of State on Global Estimates of Dianeutral Advection and Diffusion”. *Journal of Physical Oceanography* 40.8 (2010), pp. 1690–1709 (cit. on p. 46).

[Koch-Larrouy, 2010] Ariane Koch-Larrouy, Rosemary Morrow, Thierry Penduff, and Mélanie Juza. “Origin and mechanism of Subantarctic Mode Water formation and transformation in the Southern Indian Ocean”. *Ocean Dynamics* 60.3 (2010), pp. 563–583 (cit. on p. 123).

[Kouketsu, 2012] Shinya Kouketsu, Hiroyuki Tomita, Eitarou Oka, Shigeki Hosoda, Taiyo Kobayashi, and Kanako Sato. “The role of meso-scale eddies in mixed layer deepening and mode water formation in the western North Pacific”. *Journal of Oceanography* 68.1 (2012), pp. 63–77 (cit. on p. 133).

[Kwon, 2013] Eun Young Kwon, Stephanie M. Downes, Jorge L. Sarmiento, Riccardo Farneti, and Curtis Deutsch. “Role of the Seasonal Cycle in the Subduction Rates of Upper–Southern Ocean Waters”. *Journal of Physical Oceanography* 43.6 (2013), pp. 1096–1113 (cit. on p. 82).

[Kwon, 2004] Young-Oh Kwon and Stephen C. Riser. “North Atlantic Subtropical Mode Water: A history of ocean-atmosphere interaction 1961–2000”. *Geophysical Research Letters* 31.19 (2004) (cit. on pp. 100, 104, 133).

[Large, 1981] W. G. Large and S. Pond. “Open Ocean Momentum Flux Measurements in Moderate to Strong Winds”. *Journal of Physical Oceanography* 11.3 (1981), pp. 324–336 (cit. on p. 5).

[Large, 2001] William G. Large and A.J. George Nurser. “Chapter 5.1 Ocean surface water mass transformation”. *Ocean Circulation and Climate*. Ed. by Gerold Siedler, John Church, and John Gould. Vol. 77. International Geophysics. Academic Press, 2001, pp. 317–336 (cit. on pp. 21, 22).

[Laxenaire, 2018] R. Laxenaire, S. Speich, B. Blanke, A. Chaigneau, C. Pegliasco, and A. Stegner. “Anticyclonic Eddies Connecting the Western Boundaries of Indian and Atlantic Oceans”. *Journal of Geophysical Research: Oceans* 123.11 (2018), pp. 7651–7677 (cit. on pp. 37, 93, 105, 107–110, 133, 134, 139, 152, 162).

[Laxenaire, 2019] R. Laxenaire, S. Speich, and A. Stegner. “Evolution of the Thermohaline Structure of One Agulhas Ring Reconstructed from Satellite Altimetry and Argo Floats”. *Journal of Geophysical Research: Oceans* 124.12 (2019), pp. 8969–9003 (cit. on pp. 51, 93, 94, 105, 113, 133, 138, 139, 144, 150, 151).

[Laxenaire, 2020] R. Laxenaire, S. Speich, and A. Stegner. “Agulhas Ring Heat Content and Transport in the South Atlantic Estimated by Combining Satellite Altimetry and Argo Profiling Floats Data”. *Journal of Geophysical Research: Oceans* 125.9 (2020), e2019JC015511 (cit. on pp. 93, 94, 105, 163).

[Le Traon, 2001] P.Y. Le Traon and R. Morrow. “Chapter 3 Ocean Currents and Eddies”. *Satellite Altimetry and Earth Sciences*. Ed. by Lee-Lueng Fu and Anny Cazenave. Vol. 69. International Geophysics. Academic Press, 2001, pp. 171–xi (cit. on p. 36).

[Lee, 1994] Dong-Kyu Lee, Peter Niiler, Alex Warn-Varnas, and Steve Piacsek. “Wind-driven secondary circulation in ocean mesoscale”. *Journal of Marine Research* 52.3 (1994), pp. 371–396 (cit. on p. 42).

[Lee, 1997] Mei-Man Lee, David P. Marshall, and Richard G. Williams. “On the eddy transfer of tracers: Advective or diffusive?” *Journal of Marine Research* 55.3 (1997), pp. 483–505 (cit. on p. 66).

[Levitus, 2012] S. Levitus, J. I. Antonov, T. P. Boyer, O. K. Baranova, H. E. Garcia, R. A. Locarnini, et al. “World ocean heat content and thermosteric sea level change (0–2000 m), 1955–2010”. *Geophysical Research Letters* 39.10 (2012) (cit. on pp. 91, 170).

[Levy, 2013] M. Levy and A. P. Martin. “The influence of mesoscale and submesoscale heterogeneity on ocean biogeochemical reactions”. *Global Biogeochemical Cycles* 27.4 (2013), pp. 1139–1150 (cit. on p. 41).

[Liu, 2017] L. Liu, D. Silver, K. Bemis, D. Kang, and E. Curchitser. “Illustrative Visualization of Mesoscale Ocean Eddies”. *Computer Graphics Forum* 36.3 (2017), pp. 447–458 (cit. on p. 39).

[Liu, 2012] Ling Ling Liu and Rui Xin Huang. “The Global Subduction/Obduction Rates: Their Interannual and Decadal Variability”. *Journal of Climate* 25.4 (2012), pp. 1096–1115 (cit. on pp. 88, 91, 111).

[Lloyd, 1982] S. Lloyd. “Least squares quantization in PCM”. *IEEE Transactions on Information Theory* 28.2 (1982), pp. 129–137 (cit. on pp. 93, 105, 128, 137).

[Lorbacher, 2006] K. Lorbacher, D. Dommenget, P. P. Niiler, and A. Köhl. “Ocean mixed layer depth: A subsurface proxy of ocean-atmosphere variability”. *Journal of Geophysical Research: Oceans* 111.C7 (2006) (cit. on pp. 92, 95, 99, 112).

[Luyten, 1983] J. R. Luyten, J. Pedlosky, and H. Stommel. “The Ventilated Thermocline”. *Journal of Physical Oceanography* 13.2 (1983), pp. 292–309 (cit. on pp. 23, 53).

[MacGilchrist, 2020] Graeme A. MacGilchrist, Helen L. Johnson, David P. Marshall, Camille Lique, Matthew Thomas, Laura C. Jackson, et al. “Locations and Mechanisms of Ocean Ventilation in the High-Latitude North Atlantic in an Eddy-Permitting Ocean Model”. *Journal of Climate* 33.23 (2020), pp. 10113–10131 (cit. on p. 58).

[Mahadevan, 2008] Amala Mahadevan, Leif N. Thomas, and Amit Tandon. “Comment on "Eddy/Wind Interactions Stimulate Extraordinary Mid-Ocean Plankton Blooms"”. *Science* 320.5875 (2008), pp. 448–448 (cit. on p. 42).

[Marshall, 1997] David Marshall. “Subduction of water masses in an eddying ocean”. *Journal of Marine Research* 55.2 (1997), pp. 201–222 (cit. on pp. 50, 56, 66–69, 88, 91, 93, 133).

[Marshall, 1999] John Marshall, Daniel Jamous, and Johan Nilsson. “Reconciling thermodynamic and dynamic methods of computation of water-mass transformation rates”. *Deep Sea Research Part I: Oceanographic Research Papers* 46.4 (1999), pp. 545–572 (cit. on pp. 21, 24, 57).

[Marshall, 1992] John C. Marshall and A. J. George Nurser. “Fluid Dynamics of Oceanic Thermocline Ventilation”. *Journal of Physical Oceanography* 22.6 (1992), pp. 583–595 (cit. on pp. 23, 71).

[Marshall, 1993] John C. Marshall, Richard G. Williams, and A. J. George Nurser. “Inferring the Subduction Rate and Period over the North Atlantic”. *Journal of Physical Oceanography* 23.7 (1993), pp. 1315–1329 (cit. on pp. 23, 59, 66, 72, 87, 111).

[Masuzawa, 1969] Jotaro Masuzawa. “Subtropical mode water”. *Deep Sea Research and Oceanographic Abstracts* 16.5 (1969), pp. 463–472 (cit. on pp. 29, 92).

[McCartney, 1977] M. S. McCartney. “Subantarctic Mode Water”. *A Voyage of Discovery: George Deacon 70th Anniversary Volume, Supplement to Deep-Sea Research* (1977), pp. 103–119 (cit. on pp. 29, 92, 115).

[McCartney, 1982] Michael S. McCartney and Lynne D. Talley. “The Subpolar Mode Water of the North Atlantic Ocean”. *Journal of Physical Oceanography* 12.11 (1982), pp. 1169–1188 (cit. on pp. 29, 119).

[McCoy, 2020] Daniel McCoy, Daniele Bianchi, and Andrew L. Stewart. “Global observations of submesoscale coherent vortices in the ocean”. *Progress in Oceanography* 189 (2020), p. 102452 (cit. on p. 134).

[McGillicuddy, 2007] Dennis J. McGillicuddy, Laurence A. Anderson, Nicholas R. Bates, Thomas Bibby, Ken O. Buesseler, Craig A. Carlson, et al. “Eddy/Wind Interactions Stimulate Extraordinary Mid-Ocean Plankton Blooms”. *Science* 316.5827 (2007), pp. 1021–1026 (cit. on pp. 42, 102).

[McGillicuddy, 2008] Dennis J. McGillicuddy, James R. Ledwell, and Laurence A. Anderson. “Response to Comment on "Eddy/Wind Interactions Stimulate Extraordinary Mid-Ocean Plankton Blooms"”. *Science* 320.5875 (2008), pp. 448–448 (cit. on p. 42).

[McWilliams, 2016] James C. McWilliams. “Submesoscale currents in the ocean”. *Proceedings of the Royal Society A: Mathematical, Physical and Engineering Sciences* 472.2189 (2016), p. 20160117 (cit. on pp. 40, 47).

[McWilliams, 2019] James C. McWilliams. “A survey of submesoscale currents”. *Geoscience Letters* 6.1 (2019), p. 3 (cit. on p. 41).

[McWilliams, 1979] James C. McWilliams and Glenn R. Flierl. “On the Evolution of Isolated, Nonlinear Vortices”. *Journal of Physical Oceanography* 9.6 (1979), pp. 1155–1182 (cit. on p. 37).

[Merchant, 2019] Christopher J. Merchant, Owen Embury, Claire E. Bulgin, Thomas Block, Gary K. Corlett, Emma Fiedler, et al. “Satellite-based time-series of sea-surface temperature since 1981 for climate applications”. *Scientific Data* 6.1 (2019), p. 223 (cit. on p. 143).

[Meunier, 2021] Thomas Meunier, Enric Pallás Sanz, Charly de Marez, Juan Pérez, Miguel Tenreiro, Angel Ruiz Angulo, et al. “The Dynamical Structure of a Warm Core Ring as Inferred from Glider Observations and Along-Track Altimetry”. *Remote Sensing* 13.13 (2021) (cit. on p. 37).

[Meunier, 2018] Thomas Meunier, M. Tenreiro, Enric Pallàs-Sanz, Jose Ochoa, Angel Ruiz-Angulo, Esther Portela, et al. “Intrathermocline Eddies Embedded Within an Anticyclonic Vortex Ring”. *Geophysical Research Letters* 45.15 (2018), pp. 7624–7633 (cit. on p. 102).

[Morrow, 2004] Rosemary Morrow, Florence Birol, David Griffin, and Joël Sudre. “Divergent pathways of cyclonic and anti-cyclonic ocean eddies”. *Geophysical Research Letters* 31.24 (2004) (cit. on p. 37).

[Morrow, 2012] Rosemary Morrow and Pierre-Yves Le Traon. “Recent advances in observing mesoscale ocean dynamics with satellite altimetry”. *Advances in Space Research* 50.8 (2012), pp. 1062–1076 (cit. on p. 36).

[Mulet, 2021] S. Mulet, M.-H. Rio, H. Etienne, C. Artana, M. Cancet, G. Dibarboure, et al. “The new CNES-CLS18 Global Mean Dynamic Topography”. *Ocean Science Discussions* 2021 (2021), pp. 1–31 (cit. on pp. 112, 120, 124, 145, 147, 149, 151, 152, 154, 157).

[Munk, 1950a] W. H. Munk and G. F. Carrier. “The Wind-driven Circulation in Ocean Basins of Various Shapes”. *Tellus* 2.3 (1950), pp. 158–167 (cit. on p. 10).

[Munk, 1998] Walter Munk and Carl Wunsch. “Abyssal recipes II: energetics of tidal and wind mixing”. *Deep Sea Research Part I: Oceanographic Research Papers* 45.12 (1998), pp. 1977–2010 (cit. on p. 16).

[Munk, 1950b] Walter H. Munk. “ON THE WIND-DRIVEN OCEAN CIRCULATION”. *Journal of Atmospheric Sciences* 7.2 (1950), pp. 80–93 (cit. on pp. 4, 10).

[Nakamura, 1996] Hirohiko Nakamura. “A pycnostad on the bottom of the ventilated portion in the central subtropical North Pacific: Its distribution and formation”. *Journal of Oceanography* 52.2 (1996), pp. 171–188 (cit. on p. 133).

[Niiler, 1969] Pearn P. Niiler. “On the Ekman Divergence in an Oceanic Jet”. *Journal of Geophysical Research (1896-1977)* 74.28 (1969), pp. 7048–7052 (cit. on p. 42).

[Nishikawa, 2010] Shiro Nishikawa, Hiroyuki Tsujino, Kei Sakamoto, and Hideyuki Nakano. “Effects of Mesoscale Eddies on Subduction and Distribution of Subtropical Mode Water in an Eddy-Resolving OGCM of the Western North Pacific”. *Journal of Physical Oceanography* 40.8 (2010), pp. 1748–1765 (cit. on p. 133).

[Nurser, 1999] A. J. G. Nurser, Robert Marsh, and Richard G. Williams. “Diagnosing Water Mass Formation from Air–Sea Fluxes and Surface Mixing”. *Journal of Physical Oceanography* 29.7 (1999), pp. 1468–1487 (cit. on p. 57).

[ONeill, 2012] Larry W. O’Neill, Dudley B. Chelton, and Steven K. Esbensen. “Covariability of Surface Wind and Stress Responses to Sea Surface Temperature Fronts”. *Journal of Climate* 25.17 (2012), pp. 5916–5942 (cit. on p. 42).

[Oka, 2009] Eitarou Oka. “Seasonal and interannual variation of North Pacific Subtropical Mode Water in 2003–2006”. *Journal of Oceanography* 65.2 (2009), pp. 151–164 (cit. on p. 121).

[Oka, 2011] Eitarou Oka, Shinya Kouketsu, Katsuya Toyama, Kazuyuki Uehara, Taiyo Kobayashi, Shigeki Hosoda, et al. “Formation and Subduction of Central Mode Water Based on Profiling Float Data, 2003–08”. *Journal of Physical Oceanography* 41.1 (2011), pp. 113–129 (cit. on pp. 99, 133).

[Omand, 2015] Melissa M. Omand, Eric A. D’Asaro, Craig M. Lee, Mary Jane Perry, Nathan Briggs, Ivona Cetinić, et al. “Eddy-driven subduction exports particulate organic carbon from the spring bloom”. *Science* 348.6231 (2015), pp. 222–225 (cit. on p. 40).

[Orsi, 1995] Alejandro H. Orsi, Thomas Whitworth, and Worth D. Nowlin. “On the meridional extent and fronts of the Antarctic Circumpolar Current”. *Deep Sea Research Part I: Oceanographic Research Papers* 42.5 (1995), pp. 641–673 (cit. on pp. 123, 124).

[Park, 2005] Sungsu Park, Clara Deser, and Michael A. Alexander. “Estimation of the Surface Heat Flux Response to Sea Surface Temperature Anomalies over the Global Oceans”. *Journal of Climate* 18.21 (2005), pp. 4582–4599 (cit. on p. 91).

[Pedlosky, 2008] Joseph Pedlosky. “On the Weakly Nonlinear Ekman Layer: Thickness and Flux”. *Journal of Physical Oceanography* 38.6 (2008), pp. 1334–1339 (cit. on p. 42).

[Pegliasco, 2015] Cori Pegliasco, Alexis Chaigneau, and Rosemary Morrow. “Main eddy vertical structures observed in the four major Eastern Boundary Upwelling Systems”. *Journal of Geophysical Research: Oceans* 120.9 (2015), pp. 6008–6033 (cit. on p. 133).

[Price, 1993] James F. Price, Molly O’Neil Baringer, Rolf G. Lueck, Gregory C. Johnson, Isabel Ambar, Gregorio Parrilla, et al. “Mediterranean Outflow Mixing and Dynamics”. *Science* 259.5099 (1993), pp. 1277–1282 (cit. on p. 118).

[Provost, 1999] Christine Provost, Christelle Escoffier, Keitapu Maamaatuaiahutapu, Annie Kartavtseff, and Véronique Garçon. “Subtropical mode waters in the South Atlantic Ocean”. *Journal of Geophysical Research: Oceans* 104.C9 (1999), pp. 21033–21049 (cit. on pp. 100, 104, 134, 137, 146).

[Pujol, 2016] M.-I. Pujol, Y. Faugère, G. Taburet, S. Dupuy, C. Pelloquin, M. Ablain, et al. “DUACS DT2014: the new multi-mission altimeter data set reprocessed over 20 years”. *Ocean Science* 12.5 (2016), pp. 1067–1090 (cit. on pp. 113, 143).

[Qiu, 2006] Bo Qiu and Shuiming Chen. “Decadal Variability in the Formation of the North Pacific Subtropical Mode Water: Oceanic versus Atmospheric Control”. *Journal of Physical Oceanography* 36.7 (2006), pp. 1365–1380 (cit. on p. 133).

[Qiu, 2007] Bo Qiu, Shuiming Chen, and Peter Hacker. “Effect of Mesoscale Eddies on Subtropical Mode Water Variability from the Kuroshio Extension System Study (KESS)”. *Journal of Physical Oceanography* 37.4 (2007), pp. 982–1000 (cit. on pp. 93, 163).

[Qiu, 1995] Bo Qiu and Rui Xin Huang. “Ventilation of the North Atlantic and North Pacific: Subduction Versus Obduction”. *Journal of Physical Oceanography* 25.10 (1995), pp. 2374–2390 (cit. on pp. 58, 91).

[Qu, 2002] Tangdong Qu, Shang-Ping Xie, Humio Mitsudera, and Akio Ishida. “Subduction of the North Pacific Mode Waters in a Global High-Resolution GCM”. *Journal of Physical Oceanography* 32.3 (2002), pp. 746–763 (cit. on p. 133).

[Ridgway, 2007] K. R. Ridgway and J. R. Dunn. “Observational evidence for a Southern Hemisphere oceanic supergyre”. *Geophysical Research Letters* 34.13 (2007) (cit. on p. 127).

[Robinson, 1984] A. R. Robinson, J. A. Carton, C. N. K. Mooers, L. J. Walstad, E. F. Carter, M. M. Rienecker, et al. “A real-time dynamical forecast of ocean synoptic/mesoscale eddies”. *Nature* 309.5971 (1984), pp. 781–783 (cit. on p. 35).

[Roemmich, 1992] Dean Roemmich and Bruce Cornuelle. “The Subtropical Mode Waters of the South Pacific Ocean”. *Journal of Physical Oceanography* 22.10 (1992), pp. 1178–1187 (cit. on pp. 100, 104, 123, 133).

[Rossby, 1939] C-G. Rossby. “Relation between variations in the intensity of the zonal circulation of the atmosphere and the displacements of the semi-permanent centers of action”. *Journal of Marine Research* 2 (1939), pp. 38–55 (cit. on p. 10).

[Sabine, 2004] Christopher L. Sabine, Richard A. Feely, Nicolas Gruber, Robert M. Key, Kitack Lee, John L. Bullister, et al. “The Oceanic Sink for Anthropogenic CO2”. *Science* 305.5682 (2004), pp. 367–371 (cit. on pp. 91, 170).

[Sallée, 2008] J.-B. Sallée, R. Morrow, and K. Speer. “Eddy heat diffusion and Subantarctic Mode Water formation”. *Geophysical Research Letters* 35.5 (2008) (cit. on p. 93).

[Sallée, 2011] Jean-Baptiste Sallée and Stephen R. Rintoul. “Parameterization of eddy-induced subduction in the Southern Ocean surface-layer”. *Ocean Modelling* 39.1 (2011), pp. 146–153 (cit. on p. 68).

[Sallée, 2010] Jean-Baptiste Sallée, Kevin Speer, Steve Rintoul, and S. Wijffels. “Southern Ocean Thermocline Ventilation”. *Journal of Physical Oceanography* 40.3 (2010), pp. 509–529 (cit. on pp. 53, 61, 81, 111, 123).

[Sarmiento, 2004] J. L. Sarmiento, N. Gruber, M. A. Brzezinski, and J. P. Dunne. “High-latitude controls of thermocline nutrients and low latitude biological productivity”. *Nature* 427 (2004), pp. 56–60 (cit. on p. 53).

[Sato, 2006] Kanako Sato, Toshio Suga, and Kimio Hanawa. “Barrier layers in the subtropical gyres of the world’s oceans”. *Geophysical Research Letters* 33.8 (2006) (cit. on p. 96).

[Sato, 2014] O. T. Sato and P. S. Polito. “Observation of South Atlantic subtropical mode waters with Argo profiling float data”. *Journal of Geophysical Research: Oceans* 119.5 (2014), pp. 2860–2881 (cit. on pp. 99, 100, 104, 123, 134, 135, 137, 139, 145, 146, 148, 150, 153, 155, 161, 162, 164).

[Schmidtko, 2013] Sunke Schmidtko, Gregory C. Johnson, and John M. Lyman. “MIMOC: A global monthly isopycnal upper-ocean climatology with mixed layers”. *Journal of Geophysical Research: Oceans* 118.4 (2013), pp. 1658–1672 (cit. on p. 92).

[Schuckmann, 2020] K. von Schuckmann, L. Cheng, M. D. Palmer, J. Hansen, C. Tassone, V. Aich, et al. “Heat stored in the Earth system: where does the energy go?” *Earth System Science Data* 12.3 (2020), pp. 2013–2041 (cit. on pp. 91, 92).

[Schütte, 2016] F. Schütte, P. Brandt, and J. Karstensen. “Occurrence and characteristics of mesoscale eddies in the tropical northeastern Atlantic Ocean”. *Ocean Science* 12.3 (2016), pp. 663–685 (cit. on p. 133).

[Shakespeare, 2017] Callum J. Shakespeare and Leif N. Thomas. “A New Mechanism for Mode Water Formation Involving Cabbeling and Frontogenetic Strain at Thermohaline Fronts. Part II: Numerical Simulations”. *Journal of Physical Oceanography* 47.7 (2017), pp. 1755–1773 (cit. on p. 93).

[Siegelman, 2020] Lia Siegelman, Patrice Klein, Pascal Rivière, Andrew F. Thompson, Hector S. Torres, Mar Flexas, et al. “Enhanced upward heat transport at deep submesoscale ocean fronts”. *Nature Geoscience* 13.1 (2020), pp. 50–55 (cit. on p. 40).

[Small, 2008] R.J. Small, S.P. deSzoeke, S.P. Xie, L. O’Neill, H. Seo, Q. Song, et al. “Air-sea interaction over ocean fronts and eddies”. *Dynamics of Atmospheres and Oceans* 45.3 (2008), pp. 274–319 (cit. on p. 42).

[Smith, 1997] Walter H. F. Smith and David T. Sandwell. “Global Sea Floor Topography from Satellite Altimetry and Ship Depth Soundings”. *Science* 277.5334 (1997), pp. 1956–1962 (cit. on p. 136).

[Souza, 2018] Arthur Gerard Quadros de Souza, Rodrigo Kerr, and José Luiz Lima de Azevedo. “On the influence of Subtropical Mode Water on the South Atlantic Ocean”. *Journal of Marine Systems* 185 (2018), pp. 13–24 (cit. on pp. 133, 134, 137).

[Spall, 1995] Michael A. Spall. “Frontogenesis, subduction, and cross-front exchange at upper ocean fronts”. *Journal of Geophysical Research: Oceans* 100.C2 (1995), pp. 2543–2557 (cit. on pp. 53, 133).

[Speer, 2013] Kevin Speer and Gael Forget. “Chapter 9 - Global Distribution and Formation of Mode Waters”. *Ocean Circulation and Climate*. Vol. 103. International Geophysics. Academic Press, 2013, pp. 211–226 (cit. on pp. 29, 91, 93, 115).

[Speer, 2000] Kevin Speer, Stephen R. Rintoul, and Bernadette Sloyan. “The Diabatic Deacon Cell”. *Journal of Physical Oceanography* 30.12 (2000), pp. 3212–3222 (cit. on p. 25).

[Speer, 1992] Kevin Speer and Eli Tziperman. “Rates of Water Mass Formation in the North Atlantic Ocean”. *Journal of Physical Oceanography* 22.1 (1992), pp. 93–104 (cit. on pp. 21, 22, 44, 57).

[Speer, 1993] Kevin G. Speer. “Conversion among North Atlantic surface water types”. *Tellus A* 45.1 (1993), pp. 72–79 (cit. on p. 22).

[Speer, 1997] Kevin G. Speer. “A note on average cross-isopycnal mixing in the North Atlantic ocean”. *Deep Sea Research Part I: Oceanographic Research Papers* 44.12 (1997), pp. 1981–1990 (cit. on p. 57).

[Speich, 2007] Sabrina Speich, Bruno Blanke, and Wenju Cai. “Atlantic meridional overturning circulation and the Southern Hemisphere supergyre”. *Geophysical Research Letters* 34.23 (2007) (cit. on pp. 127, 129, 142).

[Speich, 2002] Sabrina Speich, Bruno Blanke, Pedro de Vries, Sybren Drijfhout, Kristofer Döös, Alexandre Ganachaud, et al. “Tasman leakage: A new route in the global ocean conveyor belt”. *Geophysical Research Letters* 29.10 (2002), pp. 55-1–55–4 (cit. on p. 127).

[Sprintall, 1992] Janet Sprintall and Matthias Tomczak. “Evidence of the barrier layer in the surface layer of the tropics”. *Journal of Geophysical Research: Oceans* 97.C5 (1992), pp. 7305–7316 (cit. on p. 96).

[Stern, 1965] Melvin E. Stern. “Interaction of a Uniform Wind Stress with a Geostrophic Vortex”. *Deep Sea Research and Oceanographic Abstracts* 12.3 (1965), pp. 355–367 (cit. on p. 42).

[Stevens, 2021] B. Stevens, S. Bony, D. Farrell, F. Ament, A. Blyth, C. Fairall, et al. “EUREC^{4}A”. *Earth System Science Data* 13.8 (2021), pp. 4067–4119 (cit. on pp. 102, 103).

[Stommel, 1948] Henry Stommel. “The westward intensification of wind-driven ocean currents”. *Eos, Transactions American Geophysical Union* 29.2 (1948), pp. 202–206 (cit. on pp. 4, 10).

[Stommel, 1957] Henry Stommel. “A survey of ocean current theory”. *Deep Sea Research (1953)* 4 (1957), pp. 149–184 (cit. on p. 10).

[Stommel, 1979] Henry Stommel. “Determination of water mass properties of water pumped down from the Ekman layer to the geostrophic flow below”. *Proceedings of the National Academy of Sciences* 76.7 (1979), pp. 3051–3055 (cit. on pp. 28, 55, 91).

[Stramma, 1999] Lothar Stramma and Matthew England. “On the water masses and mean circulation of the South Atlantic Ocean”. *Journal of Geophysical Research: Oceans* 104.C9 (1999), pp. 20863–20883 (cit. on p. 148).

[Stramma, 2008] Lothar Stramma, Gregory C. Johnson, Janet Sprintall, and Volker Mohrholz. “Expanding Oxygen-Minimum Zones in the Tropical Oceans”. *Science* 320.5876 (2008), pp. 655–658 (cit. on p. 170).

[Su, 2020] Zhan Su, Hector Torres, Patrice Klein, Andrew F. Thompson, Lia Siegelman, Jinbo Wang, et al. “High-Frequency Submesoscale Motions Enhance the Upward Vertical Heat Transport in the Global Ocean”. *Journal of Geophysical Research: Oceans* 125.9 (2020), e2020JC016544 (cit. on p. 40).

[Suga, 1990] Toshio Suga and Kimio Hanawa. “The mixed-layer climatology in the northwestern part of the North Pacific subtropical gyre and the formation area of Subtropical Mode Water”. *Journal of Marine Research* 48.3 (1990), pp. 543–566 (cit. on p. 133).

[Sverdrup, 1947] H. U. Sverdrup. “Wind-Driven Currents in a Baroclinic Ocean; with Application to the Equatorial Currents of the Eastern Pacific*”. *Proceedings of the National Academy of Sciences* 33.11 (1947), pp. 318–326 (cit. on pp. 4, 10).

[Talley, 2011] Lynne D. Talley, George L. Pickard, William J. Emery, and James H. Swift. “Chapter 14 - Global Circulation and Water Properties”. *Descriptive Physical Oceanography (Sixth Edition)*. Ed. by Lynne D. Talley, George L. Pickard, William J. Emery, and James H. Swift. Sixth Edition. Academic Press, 2011, pp. 473–511 (cit. on pp. 15, 25, 27, 136).

[Talley, 2001] Lynne D. Talley and Jae-Yul Yun. “The Role of Cabbeling and Double Diffusion in Setting the Density of the North Pacific Intermediate Water Salinity Minimum”. *Journal of Physical Oceanography* 31.6 (2001), pp. 1538–1549 (cit. on p. 46).

[Thomas, 2008a] Leif N. Thomas. “Formation of intrathermocline eddies at ocean fronts by wind-driven destruction of potential vorticity”. *Dynamics of Atmospheres and Oceans* 45.3 (2008), pp. 252–273 (cit. on p. 102).

[Thomas, 2010] Leif N. Thomas and Terrence M. Joyce. “Subduction on the Northern and Southern Flanks of the Gulf Stream”. *Journal of Physical Oceanography* 40.2 (2010), pp. 429–438 (cit. on pp. 53, 68).

[Thomas, 2002] Leif N. Thomas and Peter B. Rhines. “Nonlinear stratified spin-up”. *Journal of Fluid Mechanics* 473 (2002), pp. 211–244 (cit. on p. 42).

[Thomas, 2015] Leif N. Thomas and Callum J. Shakespeare. “A New Mechanism for Mode Water Formation involving Cabbeling and Frontogenetic Strain at Thermohaline Fronts”. *Journal of Physical Oceanography* 45.9 (2015), pp. 2444–2456 (cit. on pp. 45, 46).

[Thomas, 2008b] Leif N. Thomas, Amit Tandon, and Amala Mahadevan. “Submesoscale Processes and Dynamics”. *Ocean Modeling in an Eddying Regime*. 2008, pp. 17–38 (cit. on p. 40).

[Trenberth, 1989] Kevin E. Trenberth, William G. Large, and Jerry G. Olson. “The Effective Drag Coefficient for Evaluating Wind Stress over the Oceans”. *Journal of Climate* 2.12 (1989), pp. 1507–1516 (cit. on p. 5).

[Tsubouchi, 2010] T. Tsubouchi, T. Suga, and K. Hanawa. “Indian Ocean Subtropical Mode Water: its water characteristics and spatial distribution”. *Ocean Science* 6.1 (2010), pp. 41–50 (cit. on pp. 100, 104, 123).

[Tsubouchi, 2007] Takamasa Tsubouchi, Toshio Suga, and Kimio Hanawa. “Three Types of South Pacific Subtropical Mode Waters: Their Relation to the Large-Scale Circulation of the South Pacific Subtropical Gyre and Their Temporal Variability”. *Journal of Physical Oceanography* 37.10 (2007), pp. 2478–2490 (cit. on pp. 100, 104).

[Tsubouchi, 2016] Takamasa Tsubouchi, Toshio Suga, and Kimio Hanawa. “Comparison Study of Subtropical Mode Waters in the World Ocean”. *Frontiers in Marine Science* 3 (2016) (cit. on pp. 93, 100, 133, 163).

[Uehara, 2003] Hiroki Uehara, Toshio Suga, Kimio Hanawa, and Nobuyuki Shikama. “A role of eddies in formation and transport of North Pacific Subtropical Mode Water”. *Geophysical Research Letters* 30.13 (2003) (cit. on pp. 133, 155).

[Urakawa, 2012] L. Shogo Urakawa and Hiroyasu Hasumi. “Eddy-Resolving Model Estimate of the Cabbeling Effect on the Water Mass Transformation in the Southern Ocean”. *Journal of Physical Oceanography* 42.8 (2012), pp. 1288–1302 (cit. on p. 46).

[Vallis, 2006] Geoffrey K. Vallis. “Simplified Equations for Ocean and Atmosphere”. *Atmospheric and Oceanic Fluid Dynamics: Fundamentals and Large-scale Circulation*. Cambridge University Press, 2006, pp. 197–244 (cit. on p. 34).

[Vu, 2018] Briac Le Vu, Alexandre Stegner, and Thomas Arsouze. “Angular Momentum Eddy Detection and Tracking Algorithm (AMEDA) and Its Application to Coastal Eddy Formation”. *Journal of Atmospheric and Oceanic Technology* 35.4 (2018), pp. 739–762 (cit. on p. 133).

[Walin, 1982] GÖSTA Walin. “On the relation between sea-surface heat flow and thermal circulation in the ocean”. *Tellus* 34.2 (1982), pp. 187–195 (cit. on pp. 21, 57, 68, 91).

[Wenegrat, 2017] Jacob O. Wenegrat and Leif N. Thomas. “Ekman Transport in Balanced Currents with Curvature”. *Journal of Physical Oceanography* 47.5 (2017), pp. 1189–1203 (cit. on p. 42).

[Wenegrat, 2018] Jacob O. Wenegrat, Leif N. Thomas, Jonathan Gula, and James C. McWilliams. “Effects of the Submesoscale on the Potential Vorticity Budget of Ocean Mode Waters”. *Journal of Physical Oceanography* 48.9 (2018), pp. 2141–2165 (cit. on p. 93).

[Williams, 1995] Richard G. Williams, John C. Marshall, and Michael A. Spall. “Does Stommel’s Mixed Layer “Demon” Work?” *Journal of Physical Oceanography* 25.12 (1995), pp. 3089–3102 (cit. on pp. 55, 87).

[Wong, 2003] Annie P. S. Wong and Gregory C. Johnson. “South Pacific Eastern Subtropical Mode Water”. *Journal of Physical Oceanography* 33.7 (2003), pp. 1493–1509 (cit. on p. 133).

[Woods, 1985] J.D. Woods. “Chapter 34 The physics of Thermocline Ventilation”. *Coupled Ocean-Atmosphere Models*. Ed. by J.C.J. Nihoul. Vol. 40. Elsevier Oceanography Series. Elsevier, 1985, pp. 543–590 (cit. on pp. 28, 55, 87).

[Worthington, 1958] L.V. Worthington. “The 18° water in the Sargasso Sea”. *Deep Sea Research (1953)* 5.2 (1958), pp. 297–305 (cit. on pp. 29, 91, 92, 118).

[Wu, 2020] Baolan Wu, Xiaopei Lin, and Lisan Yu. “North Pacific subtropical mode water is controlled by the Atlantic Multidecadal Variability”. *Nature Climate Change* 10.3 (2020), pp. 238–243 (cit. on pp. 100, 104).

[Wunsch, 2018] Carl Wunsch and Raffaele Ferrari. “100 Years of the Ocean General Circulation”. *Meteorological Monographs* 59 (2018), pp. 7.1–7.32 (cit. on p. 2).

[Xu, 2016] Lixiao Xu, Peiliang Li, Shang-Ping Xie, Qinyu Liu, Cong Liu, and Wendian Gao. “Observing mesoscale eddy effects on mode-water subduction and transport in the North Pacific”. *Nature Communications* 7.1 (2016), p. 10505 (cit. on pp. 93, 133).

[Xu, 2017] Lixiao Xu, Shang-Ping Xie, Qinyu Liu, Cong Liu, Peiliang Li, and Xiaopei Lin. “Evolution of the North Pacific Subtropical Mode Water in Anticyclonic Eddies”. *Journal of Geophysical Research: Oceans* 122.12 (2017), pp. 10118–10130 (cit. on pp. 100, 104).

[Xu, 2014] Lixiao Xu, Shang-Ping Xie, Julie L. McClean, Qinyu Liu, and Hideharu Sasaki. “Mesoscale eddy effects on the subduction of North Pacific mode waters”. *Journal of Geophysical Research: Oceans* 119.8 (2014), pp. 4867–4886 (cit. on p. 68).

[Yasuda, 1997] Tamaki Yasuda and Kimio Hanawa. “Decadal Changes in the Mode Waters in the Midlatitude North Pacific”. *Journal of Physical Oceanography* 27.6 (1997), pp. 858–870 (cit. on p. 91).

[Yu, 2008] Lisan Yu, Xiangze Jin, and Robert Weller. “Multidecade Global Flux Datasets from the Objectively Analyzed Air-sea Fluxes (OAFlux) Project: Latent and Sensible Heat Fluxes, Ocean Evaporation, and Related Surface Meteorological Variables”. *OAFlux Project Technical Report* (2008) (cit. on pp. 113, 143).

[Zhai, 2012] Xiaoming Zhai, Helen L. Johnson, David P. Marshall, and Carl Wunsch. “On the Wind Power Input to the Ocean General Circulation”. *Journal of Physical Oceanography* 42.8 (2012), pp. 1357–1365 (cit. on pp. 5, 42).

[Zhang, 2019] Zhengguang Zhang, Bo Qiu, Patrice Klein, and Seth Travis. “The influence of geostrophic strain on oceanic ageostrophic motion and surface chlorophyll”. *Nature Communications* 10.1 (2019), p. 2838 (cit. on p. 40).

ABSTRACT

Within the Earth's climate system, the ocean is engaged as a huge reservoir of important properties such as heat and carbon, predominantly resulting from exchanges with the atmosphere on timescales from hours to millennia. Such large volume of storage in the ocean interior thus questions the mechanisms of water property transport and distribution, leading to the concept of ocean ventilation, a process that connects ocean surface waters with the interior. Commonly associated with an increase in density of surface waters, ventilation is typically interpreted as a downward transfer of water masses due to stability and other fine-scale processes. Understanding the dynamics and thermodynamics of water mass formation, ventilation and dissipation, is therefore one of the key scientific challenges confronting the entire climate community.

In this thesis, several processes related to ventilation have been discussed and a specific attention has been given to the mesoscale whose typical length is less than 100 km and timescale spans on the order of a month. The largest proportion of mesoscale kinetic energy is contained by coherent vortices, known as mesoscale eddies, which are nearly geostrophic and can have the vertical extent down to the thermocline. Aimed at a combination between the ventilation theory and mesoscale dynamics, the first part of this thesis has been devoted to a revisit to the theory of subduction at the bottom of mixed layer that quantifies long-term (permanent) transport of surface water masses into the main thermocline. Interpreted as a transient state in the subduction process, mode waters are a specific type of water mass homogeneous in properties (i.e., characterized by low potential vorticity) and residing between the seasonal and main thermoclines. Such transiency of mode waters is associated with their formation mechanism largely due to surface buoyancy forcing that is season-dependent. The second part of this thesis is thus related to an algorithm development to detect more precisely than other available methods the surface mixed layers and mode waters from several profiling databases. By co-locating mode waters with mesoscale eddies identified from the satellite altimetry, it is possible to quantify 1) the percentage of mode waters carried by eddies in an Eulerian sense, and 2) anomalies of temperature, salinity and others transported within eddies in a Lagrangian framework. Accordingly, a revisit to global mode water distribution has been provided, in terms of their dynamics and thermodynamics at the mesoscale. The South Atlantic Subtropical Mode Water has been considered as a special example and brought into details in the last chapter, since it is not only formed according to the typical baroclinity at the western boundary, but also develops due to a large amount of inter-basin transport carried by anticyclonic Agulhas Rings shedding from the Indian Ocean.

Apart from the thermohaline perspective of ocean circulation and ventilation, i.e., surface convection and its significance on mode water formation and renewal, this thesis also provides an assessment on the wind-driven aspect and a combination of these two components. In specific, we extended the Ekman dynamics to allow for an influence from geostrophic motions and self-advection. A brief discussion on diapycnal and more complex physics of ventilation at the mesoscale is also presented.

KEYWORDS

ocean ventilation theory, mesoscale dynamics, mode water, heat uptake

RÉSUMÉ

Dans le système climatique de la Terre, l'océan constitue un énorme réservoir de chaleur et carbone, résultant principalement des échanges avec l'atmosphère sur des échelles de temps allant des heures aux millénaires. Les mécanismes d'absorption de la chaleur et du carbone, leur transport et distribution dans l'océan intérieur sont conceptualisés en tant que ventilation de l'océan, un processus qui relie la formation des masses d'eau à la surface de l'océan et leur propagation et transformation en profondeur. Typiquement associée à une augmentation de la densité des eaux de surface, la ventilation est généralement interprétée comme un transfert verticale des masses d'eau dû à la stabilité de la colonne d'eau, à leur transport horizontal et à d'autres processus à petite échelle. Comprendre la dynamique et la thermodynamique sous-jacentes à la formation, transport et transformation des masses d'eau est donc l'un des principaux défis scientifiques en sciences du climat.

Dans cette thèse, l'accent a été mis sur plusieurs processus liés à la ventilation avec un focus particulier sur la dynamique à méso-échelle de l'océan caractérisée par des échelles horizontales de l'ordre de 100 km et des échelles de temps de l'ordre des mois. La plus grande partie de l'énergie cinétique à méso-échelle est contenue dans des tourbillons cohérents, connus sous le nom de tourbillons de méso-échelle, dont les écoulements sont proches de l'équilibre géostrophique et peuvent avoir une étendue verticale allant de la surface jusqu'à la thermocline. Visant une combinaison entre la théorie de la ventilation et la dynamique à méso-échelle, la première partie de cette thèse a été consacrée à une revisite de la théorie de la subduction au fond de la couche de mélange qui quantifie le transport à long terme des masses d'eau de surface dans le thermocline principale. Interprétées comme un état transitoire dans le processus de ventilation, les eaux modales sont des masses d'eau aux propriétés homogènes (c'est-à-dire caractérisées par une faible vorticité potentielle) et résidant entre les thermoclines saisonnières et principales. Cette éphémérité des eaux modales est associée à leur mécanisme de formation dû au forçage saisonnier de flottabilité de surface. La deuxième partie de cette thèse porte donc sur le développement d'un algorithme permettant de détecter les couches de mélange de surface et les eaux modales avec plus de précision que les autres méthodes disponibles. En associant les eaux modales aux tourbillons de méso-échelle identifiés par altimétrie satellitaire, c'était possible de quantifier 1) le pourcentage d'eaux modales transportées par les tourbillons au sens eulérien, et 2) les anomalies de température, de salinité et d'autres transportées dans les tourbillons dans un cadre lagrangien. Par conséquent, une révision de la distribution globale des eaux modales a été proposée, en termes de leur dynamique et thermodynamique à la méso-échelle. Les eaux modales subtropicales de l'Atlantique Sud ont été considérées comme un exemple particulier et détaillées dans le dernier chapitre, parce qu'elles ne se forment pas seulement selon la baroclinité typique à la limite ouest, mais elles se développent également en raison d'une grande quantité de transport inter-bassin transporté par des tourbillons anticycloniques se déversant de l'océan Indien.

Outre la perspective thermohaline de la circulation et de la ventilation océanique, c'est-à-dire la convection de surface et son importance sur la formation et le renouvellement des eaux modales, cette thèse fournit également une évaluation du forçage par vent de la circulation océanique et une combinaison de ces deux composantes. C'est-à-dire la théorie d'Ekman et son couplage avec la dynamique géostrophique de l'océan. Une brève discussion sur les processus de mélange diapycnal et d'autres processus plus complexe de la ventilation à la méso-échelle a également été fournie.

MOTS CLÉS

théorie de la ventilation océanique, dynamique à méso-échelle, eaux modales, absorption de chaleur